# Gravitational-wave background: detection and implications

Martinovic, Katarina

*Awarding institution:*
King's College London

# Gravitational-wave background: detection and implications

*Katarina Martinovic*

A dissertation submitted in fulfillment

of the requirements for the degree of

**Doctor of Philosophy**

at

**King's College London**

Theoretical Particle Physics & Cosmology Group

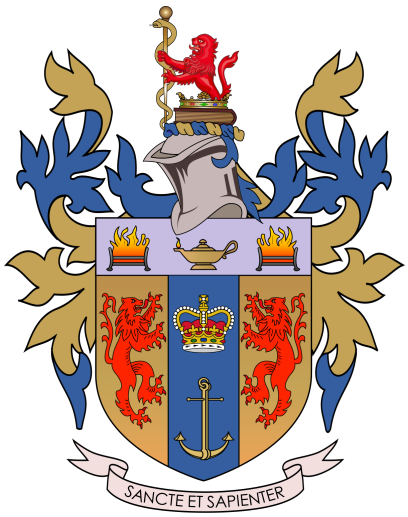


August 7, 2023

# Declaration

I hereby declare that except where specific reference is made to the work of others, the contents of this dissertation are original and have not been submitted in whole or in part for consideration for any other degree or qualification in this, or any other university. This dissertation is my own work and contains the outcome of work done in collaboration with others including the following publications:

- Detecting a stochastic gravitational-wave background in the presence of correlated magnetic noise, *Phys. Rev. D 102 (2020) 10, 102005*,
- Upper limits on the isotropic gravitational-wave background from Advanced LIGO and Advanced Virgo's third observing run, *Phys. Rev. D 104 (2021) 2, 022004*,
- Impact of Schumann resonances on the Einstein Telescope and projections for the magnetic coupling function, *Phys. Rev. D 104 (2021) 12, 122006*,
- Simultaneous estimation of astrophysical and cosmological stochastic gravitational-wave backgrounds with terrestrial detectors, *Phys. Rev. D 103 (2021) 4, 043023*,
- Dictionary learning: a novel approach to detecting binary black holes in the presence of Galactic noise with LISA, *Phys. Rev. Lett. 130 (2023) 9, 091401*,
- Footprints of population III stars in the gravitational-wave background, *Astrophys. J. 940 (2022) 1, 29*,
- Implications for First-Order Cosmological Phase Transitions from the Third LIGO-Virgo Observing Run, *Phys. Rev. Lett. 126 (2021) 15, 151301*,
- Probing Early Universe Supercooled Phase Transitions with Gravitational Wave Data, *Phys. Rev. D 107 (2023) 2, 023511*,

- Searching for parity violation with the LIGO-Virgo-KAGRA network, *Phys. Rev. D 104 (2021) 8, L081101*,
- Constraints on Quasi-dilaton Massive Gravity, *Phys. Rev. D 100 (2019) 12, 124016*,
- Measuring the propagation speed of gravitational waves with LISA, *Journal of Cosmology and Astroparticle Physics 08 (2022) 08, 031.*

# Acknowledgements

To Mairi, thank you for your endless support and help over the last four years. Thank you for always being a message away and always ready to discuss matters of Physics or life. Your drive and determination shaped me into the researcher that I am today and I will be forever grateful.

A big thank you to Pat Meyers, whose immense knowledge on gravitational-wave background and data analysis opened up endless doors in my own research.

To everyone in the Stochastic group, and with special thanks to Andrew Matas, thank you for showing me how collaborative and impactful science can be.

My fellow PhDs of Theoretical Particle Physics and Cosmology Group, thank you for the welcomed distractions from work. My journey would not have been nearly as fun without you.

To Francis Hickenbottom, thank you for lighting a spark for Physics in me and making me curious about the Universe. Your inspirational teaching has stayed with me through the years.

A huge thank you to Dom and his dad, whose kindness and philanthropy made it possible to get this far.

From Montenegro to the UK, and all around the world, thank you to all of my friends for showing endless enthusiasm for my work and keeping me sane when the going got tough. I appreciate you.

A big thanks to Katie, Sue and Robin, for welcoming me into the family and giving me a home away from home.

To Sam, my proof-reader, my audience for practising talks, thank you for sharing in my excitement for gravitational waves from day one. Thank you for being by my side through it all and helping me grow.

Finally, I dedicate this work to Vladimir, Žaklina and Miško - I am lucky to call you my family. Thank you for always being so supportive and making Podgorica-Vienna-London work so well all these years.

# Abstract

The gravitational-wave background (GWB) is a superposition of many astrophysical and cosmological sources, such as unresolved compact binaries, cosmic strings, and phase transitions in the early universe. The first three observing runs by LIGO/Virgo/KAGRA (LVK) have not made a detection of the background. Nonetheless, the existing stringent upper limits can be used to constrain theoretical models and study the early Universe.

In this thesis we explore the various aspects of the GWB - from its detection to implications. We start with a careful treatment of correlated magnetic noise sources that could limit our intrinsic detector sensitivity, and even yield a false detection. In a separate study, we highlight the importance of source separation in the case of a detection. By separating the individual sources we may reveal remnants of early Universe processes. The gravitational radiation that decoupled soon after the Big Bang is a window into physics at energy scales inaccessible to particle colliders. We search for GWB from a first-order phase transition in the LVK frequency range, and in this way place constraints on couplings and masses of particles beyond the Standard Model. New physics could also present itself in the form of parity violation in the early Universe and we search for hints of a polarised GWB. Additionally, we study mergers of remnants formed by the hypothetical first stars in the Universe, and the GWB they create. We look ahead and investigate detection prospects with proposed detector upgrades, providing strong motivation for the next generation of detectors. Finally, we test general relativity using data on rotation curves of the surrounding galaxies, and by measuring the speed of gravitational waves.

# List of acronyms

**ASD** amplitude spectral density

**BBH** binary black hole

**BNS** binary neutron star

**BPL** broken power-law

**CBC** compact binary coalescence

**CE** Cosmic Explorer

**CL** confidence level

**CMB** cosmic microwave background

**ET** Einstein Telescope

**FOPT** first-order phase transition

**GW** gravitational wave

**GWB** gravitational-wave background

**GR** General Relativity

**LVK** LIGO-Virgo-KAGRA

**ORF** overlap reduction function

**PE** parameter estimation

**PV** parity violation

**PSD** power spectral density

**QDMG** quasi-dilaton massive gravity

**SNR** signal-to-noise ratio

# Contents

# List of Figures

# List of Tables

## Chapter 1

# Introduction & Motivation

The first direct detection of gravitational waves (GWs) occurred on September 14th 2015 [1]. Advanced LIGO [2], a detector on Earth, was sensitive to the stretching and shrinking of space-time from GWs emitted during a merger of two black holes. This extreme event took place over a billion years ago, at a luminosity distance of 410 Mpc. The discovery verified predictions from Einstein's theory of general relativity (GR) and allowed us to study the strong-gravity regime of the theory [3, 4]. It has also resulted in the emergence of gravitational-wave astronomy, with numerous GW detections following the first one [5].

During their first two observational runs, O1 and O2, Advanced LIGO and Advanced Virgo [6] detected gravitational wave signals from 10 binary black hole (BBH) mergers, and one binary neutron star (BNS) merger [7]. During the third observation run (O3), numerous low-latency alerts for binary black hole, binary neutron star, and neutron star-black hole mergers were sent out to astronomers [8]. Exceptional events from O3 have been published, including new compact neutron star-black hole mergers [9, 10, 11]. All of the compact binary coalescences (CBCs) during the first three observing runs mount to a staggering 90 GW events [12, 13, 14]. These detections have already made a broad-reaching impact on stellar astrophysics, the study of dense nuclear matter, and beyond [15].

Looking ahead, GWs may allow us to probe the earliest epochs of the

Universe. Take for instance the precise measurement of the cosmic microwave background (CMB) [16] — although a very powerful tool, it can only reveal information about the Universe up to the surface of last scattering, 380,000 years after the Big Bang. Before this, the Universe was opaque to electromagnetic radiation since it had not cooled down enough for electrons and protons to combine into hydrogen atoms, and the hot plasma contained free electrons that scattered photons [17, 18]. Gravitational waves, however, were free to roam, and with sensitive enough instruments we could detect this relic radiation.

The focus of this thesis is the fraction of energy-density of the Universe contained in gravitational waves, known as gravitational-wave background (GWB). In Chapter 1 we define gravitational waves within the framework of GR. We elaborate on the detectors that have been built to detect gravitational waves, as well as future detector proposals. We then describe the GWB and its detection methods, highlighting the well-studied astrophysical contribution to the background. We finish with a discussion on some of the difficulties due to the presence of correlated noise sources.

In Chapter 2 we dive into the GWB search strategy and novel methods that we have developed to remove correlated magnetic noise. We present an application of our methods to the third observing run O3. We finish with the first detailed study on the impact of magnetic noise sources on the sensitivity of the proposed Einstein Telescope, where we made projections for necessary improvements in future GW detectors. Chapter 3 tackles source separation of a GWB signal. Once a detection is made, we will face the difficult task of identifying its origin. With the use of Bayesian and machine learning tools, we find limits to separating sources in current and future detectors. We study possible astrophysical and cosmological implications of GWB detection in Chapter 4, ranging from primordial stars, early Universe phase transitions to signs of parity violation. In Chapter 5 we investigate modifications to GR theory of gravity, and whether these

leave an imprint on astrophysical and GW data. Concluding remarks can be found in Chapter 6.

Throughout we adopt common notation, with Greek letters representing space-time indices and Roman letters representing spatial indices. Repeating indices are summed over under Einstein notation, e.g. a scalar product of two $n$-dimensional vectors $\vec{a}$ and $\vec{b}$ is $a_i b_i = \sum_{i=1}^{n} a_i b_i$.

## 1.1 Gravitational waves

General relativity describes the fabric of space-time as a manifold with a metric on it, $g_{\mu\nu}$. The metric is a function of the coordinates, $x^\mu = (ct, x, y, z)$, and it defines lengths and times on the manifold [1]. To define covariant derivatives on the manifold, one requires Christoffel symbols:

$$\Gamma^{\rho}_{\mu\nu} = \frac{1}{2} g^{\rho\sigma} (\partial_\mu g_{\sigma\nu} + \partial_\nu g_{\sigma\mu} - \partial_\sigma g_{\mu\nu}) \,, \tag{1.1}$$

where $\partial_\mu = \frac{\partial}{\partial x^\mu}$. Curvature of space-time is captured by the Riemann tensor,

$$R^{\mu}_{\nu\rho\sigma} = \partial_\rho \Gamma^{\mu}_{\nu\sigma} - \partial_\sigma \Gamma^{\mu}_{\nu\rho} + \Gamma^{\mu}_{\eta\rho} \Gamma^{\eta}_{\nu\sigma} - \Gamma^{\mu}_{\eta\sigma} \Gamma^{\eta}_{\nu\rho} \,, \tag{1.2}$$

the Ricci tensor, $R_{\mu\nu} = R^{\eta}_{\mu\eta\nu}$, and the Ricci scalar, $R = g_{\mu\nu} R^{\mu\nu}$. The Ricci scalar defines the gravitational action

$$S = \frac{c^3}{16\pi G} \int \mathrm{d}^4x \sqrt{-g}\, R + \int \mathrm{d}^4x \sqrt{-g}\, \mathcal{L}_\mathrm{m} \,, \tag{1.3}$$

with $\mathcal{L}_\mathrm{m}$ as the matter Lagrangian, and $g$ as the determinant of the metric. Varying the action with respect to $g_{\mu\nu}$, one finds Einstein's field equations

$$R_{\mu\nu} - \frac{1}{2} g_{\mu\nu} R = \frac{8\pi G}{c^4} T_{\mu\nu} \,, \tag{1.4}$$

[1] Here we highlight the most important ideas of GR. Further reading on the topic can be explored in the many graduate textbooks, e.g. [19, 20, 21].

where the matter part of the action defines the energy-momentum tensor $T^{\mu\nu}$, namely $\delta(\int \mathrm{d}^4x\sqrt{-g}\,\mathcal{L}_\mathrm{m}) \equiv \int \frac{1}{2c}\mathrm{d}^4x\sqrt{-g}T^{\mu\nu}\delta g_{\mu\nu}$. The Einstein's equations are invariant under diffeomorphism, i.e. coordinate transformation

$$g_{\mu\nu}(x) \to g'_{\mu\nu}(x') = \frac{\partial x^\rho}{\partial x'^\mu}\frac{\partial x^\sigma}{\partial x'^\nu}g_{\rho\sigma}(x). \tag{1.5}$$

If there is no matter present $T^{\mu\nu} = 0$, the simplest solution to Einstein's equations is the Minkowski flat-space metric, $\eta_{\mu\nu} = \mathrm{diag}(-1,1,1,1)$, leading to the special theory of relativity.

### 1.1.1 Linearised gravity

In this thesis we study GWs originated from distant sources, hence we can work in the weak-gravity regime. For very small perturbations around flat space-time, $|h_{\mu\nu}| \ll 1$, one can write

$$g_{\mu\nu} = \eta_{\mu\nu} + h_{\mu\nu}. \tag{1.6}$$

There are several subtleties between symmetries of the full versus the linearised theory of gravity and we discuss these briefly here. Note that the diffeomorphism covariance is broken in linearised gravity because only a limited choice of coordinates satisfies $|h_{\mu\nu}| \ll 1$. Instead, linearised gravity is invariant under infinitesimal coordinate transformation, $x^\mu \to x'^\mu = x^\mu + \xi^\mu(x)$, provided that derivatives of $\xi^\mu(x)$ are at most of the order $|h_{\mu\nu}|$, giving

$$h_{\mu\nu}(x) \to h'_{\mu\nu}(x') = h_{\mu\nu}(x) - (\partial_\mu\xi_\nu + \partial_\mu\xi_\nu). \tag{1.7}$$

The linearised theory exhibits the Poincaré symmetry of translations, boosts and rotations. The two latter transformations are often referred to as Lorentz transformations,

$$x'^\mu \to \Lambda^\mu_\nu x^\nu. \tag{1.8}$$

These transformations leave the Minkowski metric unchanged

$$\eta_{\mu\nu} = \Lambda^{\rho}_{\mu}\Lambda^{\sigma}_{\nu}\eta_{\rho\sigma}, \tag{1.9}$$

leading to Lorentz invariance of special theory of relativity. Therefore, every infinitesimal space-time region obeys Lorentz covariance locally, with physical laws independent of the inertial frame of reference.

Keeping only terms up to linear order in $h_{\mu\nu}$, the Riemann tensor is

$$R_{\mu\nu\rho\sigma} = \frac{1}{2}(\partial_\nu\partial_\rho h_{\mu\sigma} + \partial_\mu\partial_\sigma h_{\nu\rho} - \partial_\mu\partial_\rho h_{\nu\sigma} - \partial_\nu\partial_\sigma h_{\mu\rho}). \tag{1.10}$$

Rewriting the perturbation in its trace-reversed form, $\bar{h}_{\mu\nu} = h_{\mu\nu} - \frac{1}{2}\eta_{\mu\nu}h$, the Einstein's field equations become

$$\Box\bar{h}_{\mu\nu} + \eta_{\mu\nu}\partial^\rho\partial^\sigma\bar{h}_{\rho\sigma} - \partial^\rho\partial_\nu\bar{h}_{\mu\rho} - \partial^\rho\partial_\mu\bar{h}_{\nu\rho} = -\frac{16\pi G}{c^4}T_{\mu\nu}. \tag{1.11}$$

With existing gauge freedom, we can simplify equations by fixing the Lorenz gauge

$$\partial^\nu\bar{h}_{\mu\nu} = 0. \tag{1.12}$$

The Einstein's field equations are then a set of wave equations:

$$\Box\bar{h}_{\mu\nu} = -\frac{16\pi G}{c^4}T_{\mu\nu}. \tag{1.13}$$

Combining the Lorentz gauge with the transverse-traceless (TT) gauge,

$$h^{0\mu} = 0, \qquad h^i_i = 0, \qquad \partial^j h_{ij} = 0, \tag{1.14}$$

leads to the following solution to the wave equations (1.13)

$$h_{\mu\nu}^{\mathrm{TT}}(t,z) = \begin{pmatrix} 0 & 0 & 0 & 0 \\ 0 & h_+ & h_\times & 0 \\ 0 & h_\times & -h_+ & 0 \\ 0 & 0 & 0 & 0 \end{pmatrix} \cos[\omega(t - z/c)], \tag{1.15}$$

where $\omega$ is the angular frequency of the wave. The GW perturbation is a plus- (+) and cross- ($\times$) polarised plane wave travelling along the z-direction at the speed of light $c$. In the following section we describe how GWs are generated, highlighting the merging of compact objects that has been observed in Advanced LIGO/Virgo detectors.

### 1.1.2 Sources of gravitational radiation

For a system with mass density $\rho(\vec{x})$ to radiate away gravitational energy, it must have a non-zero quadrupole moment, $I_{ij}$, with the traceless part of the quadrupole moment

$$I_{ij}^T = \int \rho(\vec{x}) \left[ r_i r_j - \frac{1}{3} r^2 \delta_{ij} \right] \mathrm{d}^3 r. \tag{1.16}$$

The gravitational waves emitted are then given by

$$h_{ij}^{TT}(t,r) = \frac{2G}{c^4 r} \frac{\partial^2 I_{ij}^T(t - r/c)}{\partial t^2}, \tag{1.17}$$

and the energy radiated away in gravitational waves is

$$\frac{\mathrm{d}E}{\mathrm{d}t} = -\frac{G}{5c^5} \left( \frac{\mathrm{d}I_{ij}^T}{\mathrm{d}t^3} \right)^2. \tag{1.18}$$

The nature of GW radiation can be broadly divided into three categories:

- transient,
- continuous,

- and background.

Transient GWs can be in the form of short bursts or the inspiral of two compact objects (black hole/neutron star) orbiting one another [22]. Continuous waves are emitted by highly-spinning neutron stars, pulsars, that slow down over time due to the loss of gravitational-wave energy. Finally there are gravitational waves that originate from random, unresolved and independent sources and combine to create a background, e.g. the gravitational radiation from the early Universe. Below we discuss in more detail the different types of GWs and what sources them.

### Transient GW sources

Bursts of GWs may be emitted by cosmic strings, hypothetical 1-D topological defects, and their features i.e. cusps and kinks [23]. Cosmic strings cannot be avoided in case of spontaneous symmetry breaking from a grand-unified theory to the Standard Model [24]. Cusps, kinks and kink-kink collisions have well-modelled waveforms that have been used to search for cosmic strings in the existing GW data [25]. In contrast, core-collapse supernovae and gamma ray bursts are among sources of transient GWs that are difficult to model. Great uncertainty in our theoretical understanding of these events has motivated the "unmodelled" pipelines that search for a wide range of sources [26]. If there are any unexpected sources of GWs, we may identify them in the unmodelled searches.

Transient gravitational waves emitted from two compact objects merging are the only direct detection channel for GWs to date, and we now demonstrate how they are modelled. A binary system of compact objects (e.g. black holes) orbiting one another radiates away gravitational waves. Let us consider two masses in the $x-y$ plane on a circular trajectory with frequency $f$ and at a distance $R$, with the relative coordinate $\vec{x} = R(\cos(2\pi ft), \sin(2\pi ft), 0)$. Reducing the problem to a single object of mass $\mu = m_1 m_2/(m_1+m_2)$, we find non-zero components of the mass quadrupole moment, $I_{11}$, $I_{22}$ and $I_{12}$. Evaluating these and plugging into

(1.17), the plane wave for each polarisation is

$$h_+(t) = \frac{2(G\mathcal{M}_c)^{5/3}}{c^4 R}(\pi f_{\rm GW})^{2/3}(1+\cos^2\iota)\cos(2\pi f_{\rm GW}t+\phi_0), \tag{1.19}$$

$$h_\times(t) = \frac{2(G\mathcal{M}_c)^{5/3}}{c^4 R}(\pi f_{\rm GW})^{2/3}\cos\iota\sin(2\pi f_{\rm GW}t+\phi_0), \tag{1.20}$$

where $\mathcal{M}_c = (M_1M_2)^{3/5}/(M_1+M_2)^{1/5}$ is the chirp mass, and $\iota$ is the inclination. Note that the frequency of emitted gravitational waves is twice that of the orbital frequency, $f_{\rm GW} = 2f$. As GW radiation leaves the system, the orbit shrinks and the compact objects speed up. Eventually the compact objects become close enough to merge and leave behind a single (more massive) compact object. The frequency of the GWs evolves over time as

$$\dot{f}_{\rm GW} = \frac{96}{5}\left(\frac{G\mathcal{M}_c}{c^3}\right)^{5/3}\pi^{8/3}f_{\rm GW}^{11/3}\,. \tag{1.21}$$

Consider the first GW event detected, GW150914 [27]. Figure 1.1 shows the strain in the LIGO Hanford detector, overlaid with fitted waveform templates for merging of two black holes. The chirp mass of the system was deduced from the evolution of the frequency using (1.21).

So far we have discussed the first direct detection of GWs. Note, however, there was indirect evidence for their existence 40 years prior. The Hulse-Taylor binary system of a neutron star and a pulsar orbiting each other was discovered in 1974 [28], and its orbit decay due to GW emission agrees with predictions from GR [29].

## Continuous GW sources

Current detectors, in addition to the transient merger events, "listen out" for continuous GWs from compact objects in orbit long before they merge or from pulsars with large irregularities that give a quadrupole moment. The GWs emitted have constant (or very slowly-varying) frequency and last over long timescales. There has been no detection of these long-duration coherent waves but stringent limits have been placed on the maximum

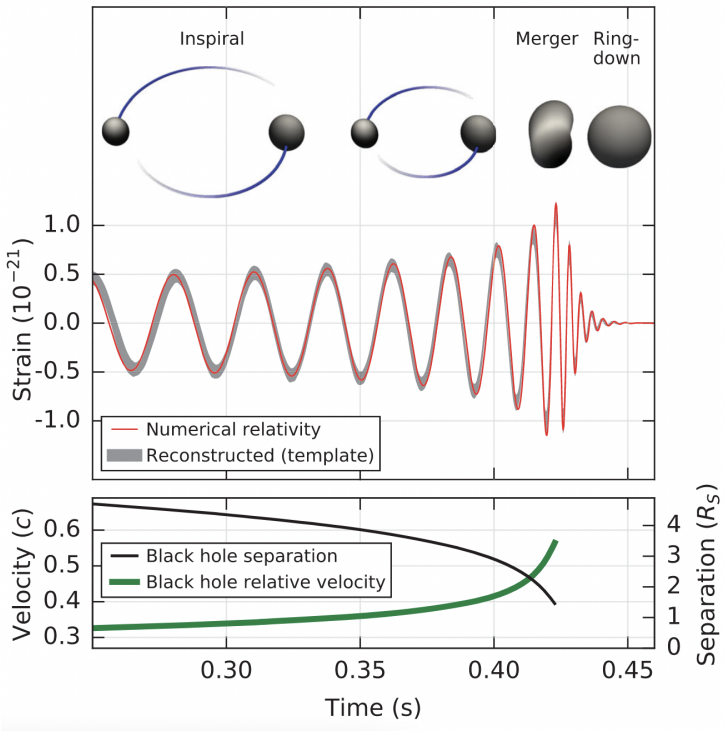


**Figure 1.1:** Top panel: Reconstructed waveform for a system of two black holes coalescing with parameters consistent with GW150914 event (strain projected onto LIGO Hanford arms). Bottom panel: total mass of the system and GW frequency associated with the matched waveform template lead to relative velocity and effective separation of black holes curves. Plot included in the original discovery paper [27].

strain amplitude, and in turn on pulsars' ellipticity and r-mode amplitude [30, 31].

## Background GW sources

In the coming years, one of the main targets of GW detectors will be a detection of the GWB. We expect GWB from unresolved binary mergers to be detectable by the time Advanced LIGO and Advanced Virgo reach design sensitivity [32]. Other sources, both astrophysical and cosmological, can contribute to the GWB, the most of exciting of which include primordial GWs from the early Universe [33]. The background searches can also complement transient GW searches, through, e.g. searching for alternative polarisations of GWs [34, 35, 36], and they

can be used together with transient detections to constrain the star

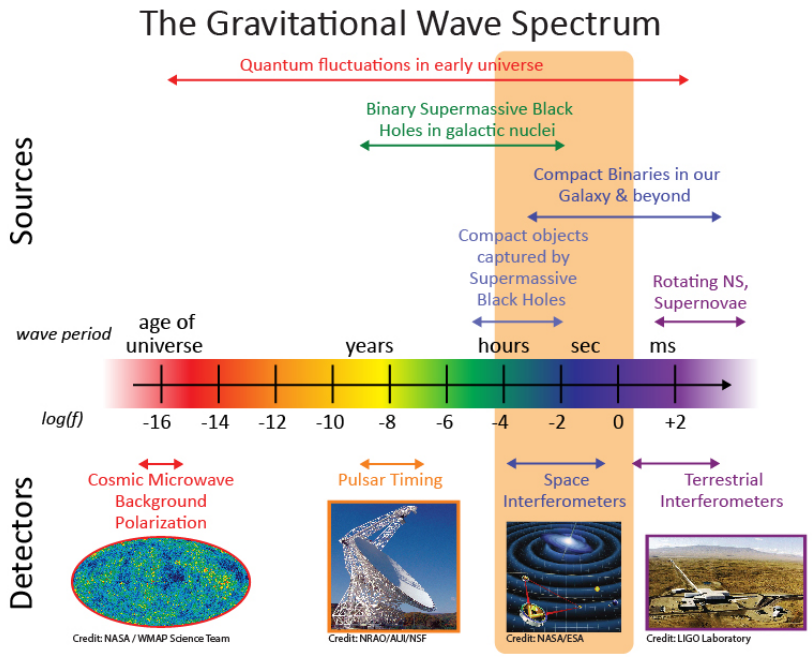


**Figure 1.2:** Frequency span of a range of GW sources, from compact binaries and pulsars to quantum fluctuations. Terrestrial interferometers have access only to the very high frequencies, while the millihertz range will be probed by the space-based detectors. Arrays of pulsars in the galaxy are sensitive to the nanohertz GWs, while CMB B-mode will help study primordial waves redshifted to as low as $10^{-15}$ Hz. This image is presented in [38].

formation history of the Universe [37]. Most of the work in the upcoming chapters of this thesis concerns background GW radiation.

All the categories of gravitational waves discussed thus far span a wide range of frequencies depending on what sources them. Detectors have been built (and proposed) to probe the different frequencies, see Figure 1.2. We now discuss current and future detectors, and their sensitivity to specific sources of gravitational waves.

## 1.2 Gravitational-wave detectors

Gravitational radiation is very weak and therefore extremely difficult to detect. Consider a human-built experiment designed to generate GWs: two objects of equal mass 1000 kg, orbiting each other 1 km away from the detectors. The prefactor in (1.20) is then $2(G\mathcal{M}_c)^{5/3}/(c^4 R) \sim \mathcal{O}(10^{-50})$. Such

minute changes in length are impossible to detect, which is why we turn to the massive astrophysical objects as GW factories in the sky. Two stellar-mass black holes merging into a single black hole give out GW radiation with a typical strain of $\mathcal{O}(10^{-20})$. To detect a strain 100 000 smaller than the size of the atomic nucleus, extremely sensitive apparatus needed to be designed and built. The interferometry used by Michelson and Morley in the 1887 experimental setup to determine Earth's velocity in aether - a medium believed to carry light waves - proved a useful starting point [39].

In a Michelson-Morley interferometer light emitted by a laser passes through a beam splitter, then travels down two perpendicular arms of equal length, reflects and travels back to recombine in the beam splitter. The recombined light is then directed towards a photodetector. Assuming a stationary, unperturbed system, with perfectly aligned reflected light beams, the photodetector should detect constant (zero) intensity of light. This is due to destructive interference of the two out-of-phase light beams. Should the lengths of the interferometer arms change, the beams no longer cancel out perfectly, and we have a signal. For the purpose of GW searches, the photodetector would "see" a signal for the duration of the GW passing through the detector, while the light storage arms experience stretching and contracting.

Strain sensitivity scales with interferometer arm length and the square root of the power of the laser on the beam splitter. The existing GW interferometers represent a far more advanced implementation of the Michelson interferometer design, namely dual-recycled, Fabry-Pérot Michelson [40]. The modifications are necessary to make the detector sensitive to tiny changes in distance caused by GWs. Dual-recycled refers to recycling of light to increase laser power and improve the resolution of the instrument, which is achieved with power recycling mirrors placed between the laser and the beam splitter. The Fabry-Pérot resonator cavities increase the light-beam travel distance with additional mirrors in each arm near

the beam splitter, forcing the light to bounce back between them and the mirrors at the arms' ends. The distance light travels in LIGO and Virgo detector arms, each 4 km and 3 km in length, increases to 1200 km and 200 km respectively with the use of Fabry-Pérot cavities.

Note that, to obtain (1.15) we fixed a gauge, in other words we choose a specific frame of observation. We need to be careful when considering GW detectors in this frame, since it is typically more useful to discuss results in the detector frame. In the TT frame, particles originally at rest remain at rest as the gravitational wave passes by. To understand this, let us examine the equation for geodesics $x^\mu$ - paths that non-accelerating particles would follow,

$$\frac{\mathrm{d}^2 x^\mu}{\mathrm{d}\tau^2} + \Gamma^\mu_{\nu\rho}\frac{\mathrm{d}x^\nu}{\mathrm{d}\tau}\frac{\mathrm{d}x^\rho}{\mathrm{d}\tau} = 0. \tag{1.22}$$

In the TT gauge $\Gamma^i_{00}$ vanishes, hence if $dx^i/d\tau = 0$ then $d^2x^i/d\tau^2 = 0$. This does not mean that all hope is lost in detecting GWs since they have no physical effect on particles they pass through. After all, we are not interested in coordinate distance $L$ in the TT frame, but in the frame-independent proper distance $s$ between two test particles. This distance changes due to a GW of frequency $\omega$ travelling by since

$$s = \sqrt{g_{\mu\nu}dx^\mu dx^\nu} \approx L[1 + \frac{1}{2}h_+ cos(\omega t)]. \tag{1.23}$$

Examining geodesics in the TT frame reveals that this reference frame can be in effect reproduced by a freely-falling experimental setup [41]. Ground-based detectors, however, due to Earth's gravitational pull and rotation come with many complications. At all times, in the detector frame we observe an acceleration of $9.81\,\mathrm{ms}^{-2}$, and relativistic rotating frame effects e.g. Coriolis force. These effects mount to dominate any small changes in the detector frame due to a passing gravitational wave by multiple orders of magnitude. Existing detectors avoid these limitations by tracking movement of freely-suspended test masses in a frequency window where gravi-

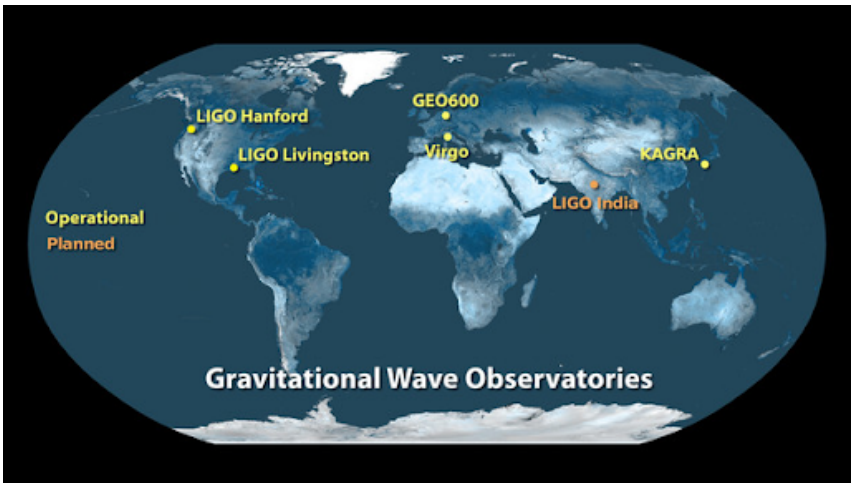


**Figure 1.3:** The currently operational network of GW detectors, along with planned LIGO India.

tational waves dominate, and any detector-frame effect can be neglected.

The advanced optics in GW interferometers make the detectors sensitive enough to faint GW signals. They also make the detectors extremely sensitive to human-produced vibrations, bound to contaminate the photodetector output. Therefore, any GW detector should be positioned at a remote site, far from any human activity to ensure minimum pollution. Furthermore, when building a detector network, individual interferometers should be located far from one another to avoid any coinciding noise sources mimicking GWs. If two far-apart interferometers output identical changes in strain (almost) simultaneously, this could be a smoking gun for a GW that passed both of them. With this in mind, locations of the current GW interferometer are reasonable: LIGO Hanford in the deserts of Washington, USA, LIGO Livingston in the vast pine forest in Louisiana, USA, Virgo in a quiet village in Tuscany, Italy, and KAGRA [42] in the underground Kamioka mine, Japan, see Figure 1.3.

### Generations of GW detectors

The original LIGO and Virgo detectors, with shorter detector arms and less sophisticated design, belong to the first generation of GW interferome-

ters which did not detect gravitational waves [2] [43]. Currently operational Advanced LIGO (aLIGO), Advanced Virgo, KAGRA, are part of the second generation of detectors (2G). Future upgrades of these detectors are planned, with each upgrade approaching the design sensitivity. The success of existing detectors has motivated discussion and planning for more sensitive detectors. Third generation of detectors (3G) is expected to improve strain sensitivity by an order of magnitude compared to 2G detectors. The most developed proposal to date is the Einstein Telescope (ET) [44], a triangular configuration [3] of three baseline pairs. Furthermore, the proposal for another L-shaped interferometer with 20 and 40 km arms (compare it to e.g. LIGO's 4 km arms) is underway, referred to as the Cosmic Explorer (CE) [45]. There is also LISA [46], following the success of LISA pathfinder, which will be the first GW detector in the sky. We compare the sensitivity curves between these detectors and showcase their science goals.

### 1.2.1 Comparing detector sensitivities

A typical representation of GW detector sensitivity is a plot of the noise power spectral density (PSD), or the amplitude spectral density (ASD=$\sqrt{\text{PSD}}$) as a function of frequency. The one-sided noise PSD, $S_n(f)$, is defined only over a physical range of frequencies ($f \geq 0$) as the ensemble average [4]

$$\langle \tilde{n}_i^*(f)\tilde{n}_i(f')\rangle = \frac{1}{2}\delta(f-f')S_n(f), \tag{1.24}$$

where $\tilde{n}_i(f)$ is noise of detector $i$ in the frequency domain. Another useful quantity is characteristic strain

$$h_c(f) = \sqrt{fS_n(f)}. \tag{1.25}$$

[2] The GEO600 detector in Germany and TAMA 300 detector in Japan were part of the first generation as well.

[3] There are ongoing discussions on the geometry and design of ET, but for the purpose of this thesis we assume a triangular, cryogenic, high-frequency instrument.

[4] For example, over observation time period T, we denote $\langle a(t)b(t)\rangle = \int_0^T a(t)b(t)\mathrm{d}t$.

On a characteristic strain against frequency graph, the area between the signal and the detector sensitivity is the signal-to-noise ratio (SNR) of the source.

From Figure 2 in [47] we can see that the cryogenic LIGO upgrade, Voyager, is expected to increase sensitivity by a factor of 2 compared to the current aLIGO sensitivity. Note that Advanced Virgo is less sensitive than Advanced LIGO Hanford and LIGO Livingston, and as such has made fewer detections. Having a third detector in the network, however, becomes important in localising sources, studies of source polarisation and treatment of correlated magnetic noise [48]. Einstein Telescope and Cosmic Explorer detector proposals span the same frequency range as Advanced LIGO and Advanced Virgo and they are expected to see an order of magnitude improvement in sensitivity relative to Advanced LIGO.

Until now, we have been able to explore the local Universe and detect BBH mergers up to a redshift of about 2, and BNS mergers up to a redshift of about 0.1. Note that due to lower progenitors' masses, we are only sensitive to the nearby neutron stars. Cosmic Explorer and Einstein Telescope extend the astrophysical horizon to colossal $z \sim 40$ for BBHs and $z \sim 10$ for BNSs [49, 50]. If operational, ET and CE detectors could reveal a large proportion of stellar-mass BBH mergers in the distant Universe [51]. One may even find first direct evidence for existence of the elusive primordial population of stars, which will be discussed in a later chapter.

The prospect of these 3G detectors will certainly lead to more frequent detections of coalescence events, but we can look for other sources of gravitational radiation in an unexplored range of frequencies. LISA detector is expected to start collecting data in mid-2030s, and it will provide access to the millihertz range. Similarly to the ET proposal, LISA consists of three baseline pairs forming an equilateral triangle. Short for Laser Interferometer Space Antenna, it will have three spacecrafts containing two test masses and two lasers to measure precisely the distance between the spacecrafts.

A space-based GW detector has no limitations from e.g. seismic and magnetic noise sources on Earth. We are also not limited with the scale of the detector and we can significantly extend the detectors arms. Separation between LISA test masses will be on the order of $10^6$ km compared to $1 - 10$ km here on Earth.

The long arms result in great sensitivity at the low-frequency, millihertz range. This unexplored frequency domain brings with it the prospect of discovering new GW sources, notably mergers of supermassive black hole binaries, as well as extreme-ratio inspirals from objects captured by supermassive black holes with mass ratios of $10000 : 1$. There are also continuous waves from inspiralling white-dwarf binaries, which for most part are treated as confusion noise in the detector. Later in this thesis we show methods that we developed to separate massive black hole merger signals from the Galactic white dwarf noise. The early inspiral signals from stellar-mass binaries detected with LISA may be used to predict merger events later observed with the high-frequency, Earth-based detectors.

There are other planned experiments, e.g. AION [52], AEDGE [53], that use atom interferometry for measuring GWs, or ones that search for changes in Earth's position due to GWs using time measurements from pulsars in the galaxy, referred to as Pulsar Timing Array projects, e.g. NANOGrav [54]. The GWs detected in these experiments will be complementary to the traditional optical interferometer data, with AION and AEDGE filling the "frequency gap" between LISA and LIGO, and NANOGrav experiment searching for GWs in the nanohertz range.

In this section we have seen that current 2G GW detectors can only probe the local Universe. The many CBCs that are too distant and therefore too weak to be detected individually, combine into GWB in the detectors. We now describe how to detect this background and other sources that contribute to it.

## 1.3 Gravitational-wave background

Gravitational-wave background [5] is a superposition of many astrophysical and cosmological sources, and it contains information about the distant Universe. If we assume the background to be isotropic [6], Gaussian, stationary, and unpolarised, then it is fully characterised by the dimensionless energy density per logarithmic frequency interval

$$\Omega_{\rm GW}(f) = \frac{1}{\rho_c}\frac{{\rm d}\rho_{\rm GW}(f)}{{\rm dln}(f)}, \tag{1.26}$$

where ${\rm d}\rho_{\rm GW}$ is the GW energy density in the frequency interval $\ln f$ to $\ln f + {\rm d}\ln f$, and $\rho_c = 3H_0^2c^2/(8\pi G)$ is the critical energy density to close the Universe. It is common to model the GWB spectrum as a power law:

$$\Omega_{\rm GW}(f) = \Omega_{\rm ref}\left(\frac{f}{f_{\rm ref}}\right)^{\alpha}, \tag{1.27}$$

where $\Omega_{\rm ref}$ is the amplitude at a reference frequency, $f_{\rm ref}$, and $\alpha$ is the spectral index. Unresolved CBCs in the LIGO frequency band are expected to create a background spectrum with $\alpha = 2/3$; whereas slow roll inflation models and cosmic strings [7] are likely to be flat in frequency, i.e. with $\alpha = 0$. It is also common to consider a model that is flat in GW power, which corresponds to $\alpha = 3$, to mimic signals like those from e.g. supernovae [33]. For an overview of the types of expected GWB spectra, we refer the reader to Fig. 1 of [58]. We will expand on the GWB astrophysical and cosmological sources in future sections. Recent estimates suggest that the GWB could be detected by the Advanced LIGO and Advanced Virgo detector network once these detectors reach design sensitivity and integrate strain data for $\mathcal{O}(\text{years})$ [32].

[5] Often referred to as the *stochastic* GWB [55].

[6] In the case of an anisotropic background, similarly to the treatment of CMB anisotropies, one should study the angular power spectrum decomposed into spherical harmonics or correlation between neighbouring pixels on a GW intensity sky map [56, 57].

[7] The GWB spectrum from cosmic strings is expected to plateau to a constant value in the LVK frequency range, see Fig. 1 in [23].

The combined data from the first three observing runs show no detection of the GWB. From the data, one can place upper limits on the background that are model-dependent, e.g. [59]:

- for a flat cosmological background, $\alpha = 0$, the upper limit on the amplitude at 95% confidence level (CL) is

$$\Omega_{\mathrm{GW}} < 5.8 \times 10^{-9}, \tag{1.28}$$

- for a background sourced by CBCs, $\alpha = \frac{2}{3}$, the upper limit on the amplitude at 25 Hz and at 95% CL is

$$\Omega_{\mathrm{GW}} < 3.4 \times 10^{-9}. \tag{1.29}$$

Let us look more closely at the background detection methods and how to obtain upper limits such as (1.28) and (1.29).

### 1.3.1 Detecting a background

The observed strain in GW detector $i$, $s_i(t)$, is a combination of the GW signal $h_i(t)$ and the underlying noise $n_i(t)$,

$$s_i(t) = h_i(t) + n_i(t). \tag{1.30}$$

Unlike for transient signals, searches for a GWB require long integration times because the signal is below the intrinsic detector noise. We search for the GWB by cross-correlating outputs from two or more widely-separated detectors, and in the case of no correlated noise sources between the detectors, the only limiting factor of the search is total observation time [60, 38].

Working in the frequency regime, let us assume that the signal observed by GW detectors, $\tilde{s}_i(f)$, can be written as

$$\tilde{s}_i(f) = \tilde{h}_i(f) + \tilde{n}_i(f), \tag{1.31}$$

where $\tilde{n}_i(f)$ is the Fourier transform of the instrument noise in detector $i$, and

$$\tilde{h}_i(f) = \sum_A \int \mathrm{d}^2\hat{r}\, F_i^A(f,\hat{r})\tilde{h}_A(f,\hat{r})e^{-2\pi i f \vec{x}_i\cdot\vec{r}/c} \tag{1.32}$$

is the total GW signal in detector $i$ located at $\vec{x}_i$. Here $F_i^A(f,\hat{r})$ is the response of detector $i$ to a plane-wave travelling in direction $\hat{r}$ with polarisation $A$, and $\tilde{h}_A(f,\hat{r})$ is the Fourier amplitude of that plane wave. Consequently,

$$\begin{aligned}\langle \tilde{s}_i^*(f)\tilde{s}_j(f')\rangle &= \langle \tilde{h}_i^*(f)\tilde{h}_j(f')\rangle + \langle \tilde{h}_i^*(f)\tilde{n}_j(f')\rangle \\ &\quad + \langle \tilde{n}_i^*(f)\tilde{h}_j(f')\rangle + \langle \tilde{n}_i^*(f)\tilde{n}_j(f')\rangle.\end{aligned} \tag{1.33}$$

If we assume that the GWB is isotropic, Gaussian, stationary and unpolarised, then it is well-described by a single power spectral density $S_{\mathrm{GW}}(f)$,

$$\langle \tilde{h}_i^*(f)\tilde{h}_j(f')\rangle = \frac{1}{2}\delta_T(f-f')\Gamma_{ij}(f)S_{\mathrm{GW}}(f), \tag{1.34}$$

where $\delta_T(f-f')$ is the finite-time approximation to the Dirac delta function, and $S_{\mathrm{GW}}(f)$ is the GW strain PSD related to the dimensionless energy density as follows

$$S_{\mathrm{GW}}(f) = \frac{3H_0^2}{10\pi^2}\frac{\Omega_{\mathrm{GW}}(f)}{f^3}. \tag{1.35}$$

Note that, for the existing detectors, the overlap reduction function (ORF), $\Gamma_{ij}(f)$, accounts for all the relevant geometric factors when cross-correlating data from different detectors [60, 61], as shown in Figure 1.4. For a pair of co-located and co-aligned detectors, the ORF is equal to unity at all frequencies.

In what follows, we consider a GWB search that uses a cross-correlation estimator that is optimal for a Gaussian, stationary, unpolarised and isotropic background. Our estimator, $\hat{C}_{ij}(f)$, for the GWB measured

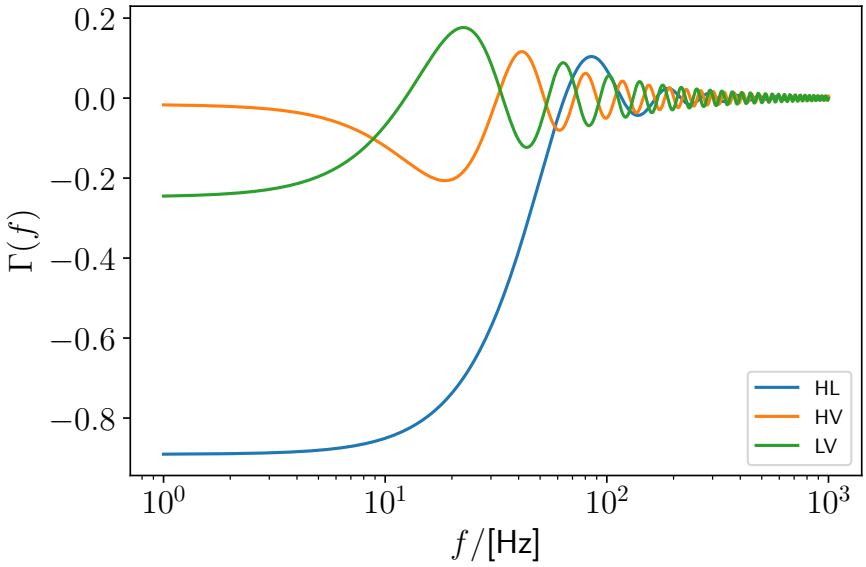


**Figure 1.4:** Overlap reduction function for LIGO Hanford (H), LIGO Livingston (L) and Virgo (V) detectors.

from detectors $i$ and $j$ is

$$\hat{C}_{ij}(f) = \frac{2}{T_{\rm obs}} \frac{\mathrm{Re}[\tilde{s}_i^*(f)\tilde{s}_j(f)]}{\Gamma_{ij}(f)S_0(f)}, \tag{1.36}$$

where $T_{\rm obs}$ is the duration over which the Fourier transform is taken, and $S_0(f)$ is the spectral shape for a GWB that is flat in energy density, $S_0(f) = 3H_0^2/(10\pi^2 f^3)$. Note we only use the cross correlation, and not auto-correlation, in the search because the noise PSD is not known precisely enough to be subtracted accurately, and therefore in practice the cross correlation is nearly optimal [8].

In the limit where the total GW strain amplitude in detector $i$, $\tilde{h}_i(f)$, is much less than the intrinsic detector noise, $\tilde{n}_i(f)$, the variance of $\hat{C}_{ij}(f)$ is given by

$$\sigma_{ij}^2(f) = \frac{1}{2\Delta f T_{\rm obs}} \frac{P_i(f)P_j(f)}{\Gamma_{ij}(f)^2 S_0(f)^2}, \tag{1.37}$$

[8] In the case of space-based LISA, however, we expect the noise PSD to be well known and dominated by the background from Galactic white dwarf binaries. Hence auto-correlation can prove useful when searching for GWB with LISA [56].

where $P_i(f)$ is the one-sided PSD of detector $i$ between times $t$ and $t + T_{\rm obs}$, and $\Delta f$ is the frequency resolution.

In general, (1.36) and (1.37) are estimated for many short time-segments of $T_{\rm obs} = 192$ s and these segments are optimally combined in a post-processing step given by

$$\hat{C}_{ij}(f) = \frac{\sum_k \hat{C}_{ij,k}(f)\sigma^{-2}_{ij,k}(f)}{\sum_k \sigma^{-2}_{ij,k}(f)}, \tag{1.38}$$

$$\sigma_{ij}(f) = \left(\sum_k \sigma^{-2}_{ij,k}(f)\right)^{-1/2}, \tag{1.39}$$

where $k$ indexes the time segments. Combining (1.33)–(1.35) and substituting into (1.36) we find

$$\langle \hat{C}_{ij}(f)\rangle = \Omega_{\rm GW}(f) + 2\,{\rm Re}\left[\frac{\langle \tilde{n}^*_i(f)\tilde{n}_j(f)\rangle}{T_{\rm obs}\,\Gamma_{ij}(f)S_0(f)}\right], \tag{1.40}$$

where we have assumed that the GW signal and the intrinsic noise are uncorrelated, $\langle \tilde{h}^*_i(f)\tilde{n}_j(f')\rangle = 0$, and that the noise in each frequency bin is independent. It is clear from (1.40) that in the absence of correlated noise, $\langle \hat{C}_{ij}(f)\rangle$ is an estimator for $\Omega_{\rm GW}(f)$. However, this is not the case when $\langle \tilde{n}^*_i(f)\tilde{n}_j(f)\rangle \neq 0$. The treatment above is only an accurate description of the cross-correlated data if there are no sources of correlated noise. Provided this is the case, the largest contribution to the GWB is expected to arise from unresolved binary mergers.

### 1.3.2 Astrophysical foreground

The transient signals from mergers of distant compact binary objects were the first (and only) GW triggers in our interferometers. We were able to detect these events because the masses of the compact objects involved and distances from Earth lead to signals above the noise of the GW interferometers. As discussed in 1.2.1, current detectors only "see" the local Universe, i.e. redshift $z \lesssim 2$ for BBH and redshift $z \lesssim 0.1$ for BNS coalescences. Merg-

ers of compact objects that are further away produce GW signals that are too weak to be detected by the interferometers. Individually, these events are buried in the noise of the detectors. Superimposing contributions from all unresolved CBC events, however, leads to a GWB that may be picked up by our detector networks

$$\Omega_{\rm GW}(f) = \frac{f}{\rho_c H_0} \int {\rm d}\theta p(\theta) \int {\rm d}z \frac{R(z,\theta)\frac{{\rm d}E_{\rm GW}(f_s,\theta)}{{\rm d}f_s}}{(1+z)E_z(z)}, \tag{1.41}$$

where $p(\theta)$ is the probability distribution of the source parameters, ${\rm d}E_{\rm GW}/{\rm d}f_{\rm s}$ in the energy density emitted by a single source at a redshift $z$ with parameters $\theta$, and $f_{\rm s}$ is the emitted frequency in the source frame $f_{\rm s} = f(1+z)$. The merger rate $R(z,\theta)$ gives the number of coalescences per unit volume per unit time as a function of redshift. The factor $(1+z)$ in the denominator converts the merger rate from the source to the detector frame, and $E_z(z)$ accounts for the considered cosmology, i.e. the expansion history of the Universe, $E_z(z) = \sqrt{\Omega_{\rm m}(1+z)^3 + \Omega_\Lambda}$, with $\Omega_{\rm m} = 0.31, \Omega_\Lambda = 0.69$ [62]. The unresolved CBCs contribution is expected to dominate GWB and is often referred to as the astrophysical "foreground".

The energy spectrum is obtained by integrating over a sphere

$$\frac{{\rm d}E_{\rm GW}}{{\rm d}f} = \frac{\pi c^3}{2G} f^3 r^2 \int d\Omega \left( |\tilde{h}_+(f)|^2 + |\tilde{h}_\times(f)|^2 \right), \tag{1.42}$$

and for a detailed treatment we refer the reader to [41]. Substituting the GW strain from compact objects spiralling towards each other, we have

$$\frac{{\rm d}E_{\rm GW}}{{\rm d}f_{\rm s}}(f_{\rm s}) = \frac{5(G\pi)^{2/3}\mathcal{M}_{\rm c}^{5/3}F_\iota}{12} f_{\rm s}^{-1/3} \times \begin{cases} (1+\sum_{i=2}^{3}\alpha_i v^i)^2 & \text{if } f_s < f_{\rm merg} \\ f_{\rm s} w_{\rm m}(1+\sum_{i=1}^{2}\epsilon_i v^i)^2 & \text{if } f_{\rm merg} \le f_{\rm s} < f_{\rm ring} \\ f_{\rm s}^{1/3} w_{\rm r} \mathcal{L}^2(f_{\rm s}, f_{\rm ring}, \sigma) & \text{if } f_{\rm ring} \le f_{\rm s} < f_{\rm cut} \end{cases} \tag{1.43}$$

where $f_{\rm merg}$, $f_{\rm ring}$ and $f_{\rm cut}$ are the frequencies at the start of merger, start of ringdown and end of emission in the source frame, respectively. $F_\iota$ is dependent on the source's inclination, $F_\iota = (1+\cos^2\iota)^2/(4+\cos^2\iota)$. $\mathcal{L}(f_{\rm s}, f_{\rm ring}, \sigma)$ is the Lorentzian function centred at $f_{\rm ring}$, with width $\sigma$, and $w_m$, $w_r$ are the normalisation constants ensuring the continuity between the three phases. The factors $\epsilon_i$ and $\alpha_i$ and the frequencies $f_{\rm merg}$, $f_{\rm ring}$ and $f_{\rm cut}$ follow from analytical waveforms detailed in [63] and depend on the symmetric mass ratio $\eta = (m_1 m_2)/(m_1+m_2)^2$ of the progenitors' masses, and the effective spin of the system $\chi = [(m_1\vec{s}_1 + m_2\vec{s}_2)/(m_1+m_2)]\vec{L}/L$.

The CBC events detected by LVK so far have stellar-mass black hole progenitors of average mass 30 $M_\odot$. For two non-spinning black holes of mass 30 $M_\odot$, the merging frequency is estimated to be $f_{\rm merg}$ = 121 Hz [63]. The GWB searches, however, have low sensitivity at high frequencies above 100 Hz, due to the ORFs for HLV network baseline pairs going to zero at these frequencies and the $f^3$ factor in (1.36). This is clearly seen in Table I of [59] which lists the frequency up to which 99% sensitivity of each O3 baseline pair is contained. Therefore, we conclude that current detectors are most likely to detect the inspiral part of the coalescence in the GWB, $f^{2/3}$, represented by the first coalescence regime in (1.43). The astrophysical foreground is hence typically modelled as a power law with a spectral index 2/3.

It is worth noting that the GWB is obtained by integrating over all redshift and therefore depends on the cosmic evolution of our Universe. One must also integrate over the source parameters such as masses and spins, making the above expression sensitive to properties of the entire CBC population. This may prove particularly useful in interpreting burst events that come from tails of probability distributions of CBC parameters.

A common assumption is that compact binary formation follows cosmic star formation, leading to a binary merger rate that peaks at redshift around $z \approx 2$ for high-metallicity progenitors, see Figure 1.5. Uncertainties

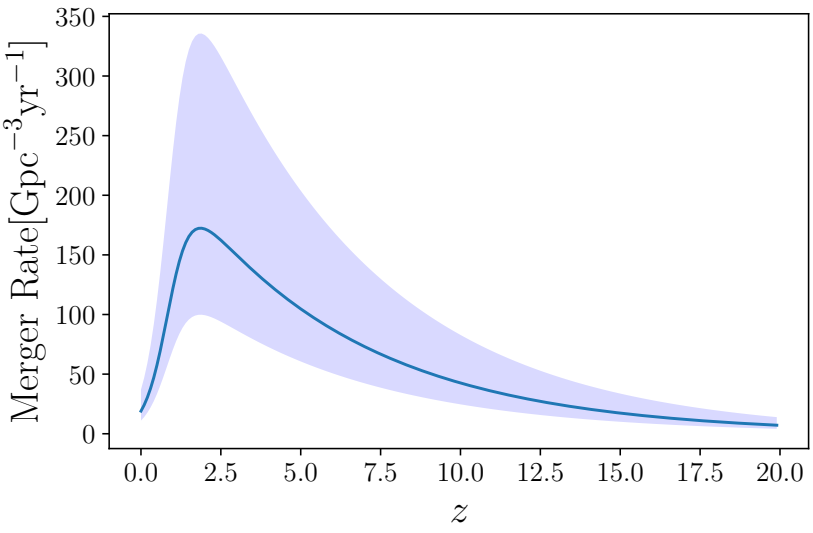


**Figure 1.5:** A simplified model for the merger rate of black hole binaries detected by Advanced LIGO/Virgo. We assume the merger rate is proportional to the star formation rate in [64], and we use the local merger rate from the O3 transient catalogue, $R_{\rm BBH}(z=0) = 19^{+18}_{-8}{\rm Gpc}^{-3}{\rm yr}^{-1}$ [12]. The shaded region captures the uncertainty in the local merger rate measurement.

in stellar formation and evolution models translate directly into uncertainties in the astrophysical GWB [59]. There are further uncertainties in mass and spin distributions of compact objects creating the background. A recent and detailed analysis of astrophysical population properties can be found in the inference studies of the LVK transient catalogues [65].

Carefully taking into account systematic and theoretical uncertainties, and using the information from catalogues of individual CBCs detected in the first three observing runs, one can make "forecasts" of the astrophysical foreground. Detection of the GWB from unresolved CBCs could be achieved by Advanced LIGO and Advanced Virgo at their design sensitivities, see Figure 1.6. However, it is possible for magnetic noise that is correlated between spatially separated ground-based detectors to mimic a GWB signal. We finish this chapter with a discussion on a well-studied source of correlated magnetic noise in detector strain.

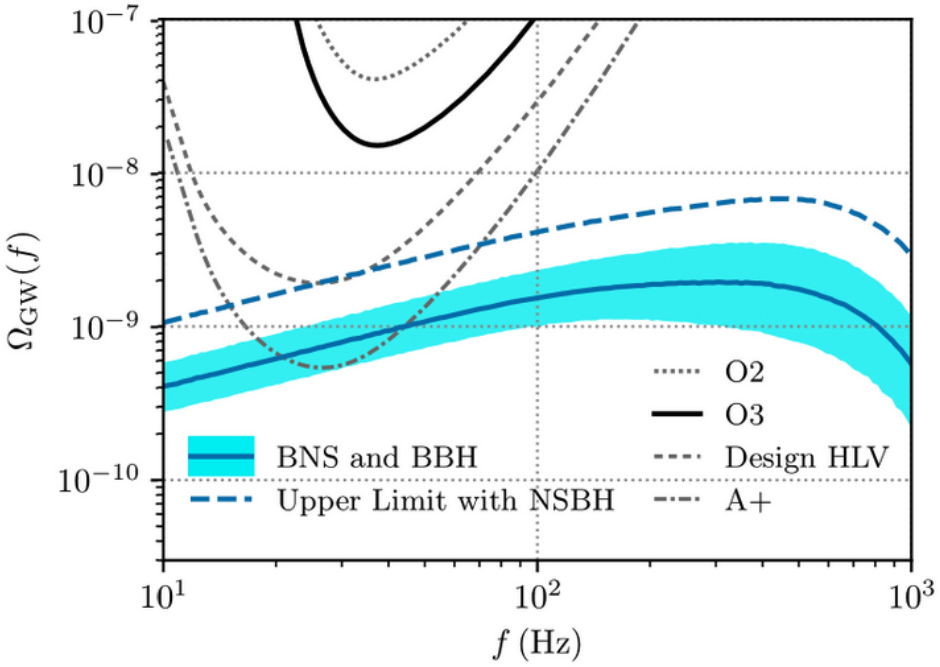


**Figure 1.6:** Predictions for $\Omega_{\rm GW}(f)$ from binary black holes, binary neutron stars and black hole-neutron star binaries using the fiducial astrophysical model in [59]. The sensitivity curves from completed O2, O3 runs confirm no detection of a background yet, but projections for future detector upgrades, Design and A+ sensitivities, show these may probe the astrophysical background. Figure presented in [59].

### 1.3.3 Correlated magnetic noise

When searching for an isotropic GWB, one uses cross-correlation techniques between spatially separated interferometers to detect a correlated signal that is below the local noise of either individual instrument. However, globally correlated noise sources remain present in the cross-correlated data and can therefore affect the analysis. An example of such a source is Schumann resonances [66, 67]. Schumann resonances are extremely low-frequency ($< 50$ Hz) electromagnetic excitations in the cavity formed by the Earth's surface and the ionosphere, driven by lightning strikes across the globe. Given their global character, Schumann resonances are correlated over distances of several thousands of kilometers and longer.

In 1952, Winfried Otto Schumann predicted the existence of global extremely low frequency peaks in the electromagnetic field of the Earth,

which were subsequently observed [68, 69]. The resonances are eigenmodes of the conducting spherical cavity formed by the surface of the Earth and its ionosphere, and are excited by lightning discharges [70]. They are expected to couple magnetically to GW interferometers via, e.g. the mirror suspension systems, electric cables and the electronics, thereby inducing a correlated signal of terrestrial origin [71, 72, 73, 74]. Correlated noise in GW detectors caused by Schumann resonances could be comparable to the sensitivity of GWB searches performed by the advanced detector network in the near future [60, 71, 72]. Analytic models of the impact of correlated noise in GW detectors have been explored in recent work, such as [75, 76]. The first harmonic, which corresponds to the circumference of the Earth, is at 7.8 Hz, and the subsequent harmonics are at 14 Hz, 20.8 Hz and 27.3 Hz. The first mode has the strongest resonance peak, with each consecutive peak being weaker than the previous one.

In Figure 1.7, we show the PSD seen in low-noise magnetometers on-site at the Advanced Virgo detector. We can clearly see the first five harmonics of the Schumann resonances. There is a diurnal variation in the amplitude of the Schumann resonances that corresponds to electrical storms that start at similar times and places each day [77, 78]. The amplitude of the resonance peaks can vary by as much as a factor of two between the loudest and quietest times of the day, depending on the time of year and the location [78, 79, 70]. What is shown in Figure 1.7 represents a trough in the height of the peaks over the course of the day at Virgo. Despite this diurnal variation, the spectrum is typically modelled as stationary for simplicity.

If left untreated, this correlated magnetic noise in the interferometers is a threat to the detection of a GWB. Can there be a successful detection of GWB in the presence of correlated magnetic noise, both with current and future GW detectors? We seek to answer this question in Chapter 2.

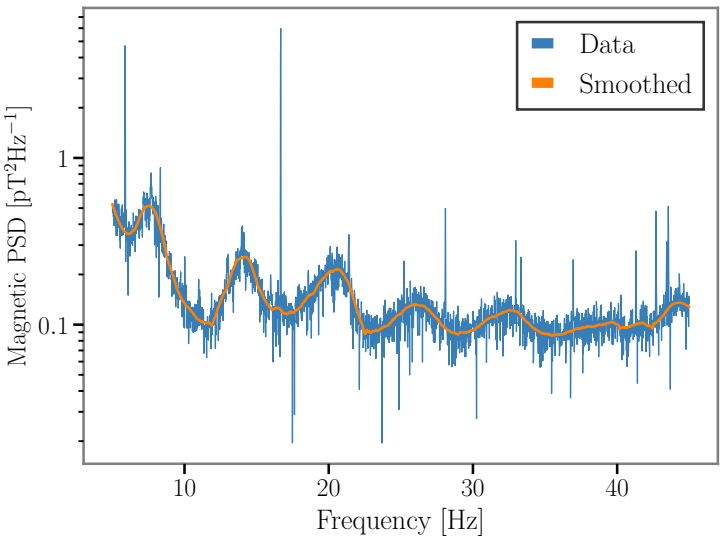


**Figure 1.7:** Power spectral density of magnetometer data near the Advanced Virgo detector. The blue is the inverse-averaged power spectral density for many 32 s chunks of data for the period from 00:00–02:00 UTC on July 9th, 2019. We use inverse averaging to account for possible magnetic transients that occur during this time. We produce the orange curve by removing the large, narrow spectral features and applying a smoothing filter. We can clearly see five harmonics of the Schumann resonances. The large, narrow spectral features are caused by local magnetic noise on site at Virgo.

# Chapter 2

# Gravitational-wave background detection

## 2.1 Foreword

As plethora of model builders design theories and simulate the GWs that could be produced as a result, instrumentalists are hard at work to reduce noise in GW detectors. Without this important step, there would be no data to guide us and inform us of the nature of our Universe. Before we study the implications of GW data on physical theories, we should ensure that the data we are analysing is gravitational, and not some terrestrial contamination.

A common method for reducing noise in the presence of a stationary signal is Wiener filtering and it has been employed at LIGO to remove sources of environmental noise [80, 81, 82]. In Wiener filtering, a *target* station is defined, and noise measurements at other *witness* stations (and correlations therein), are used to predict and subtract noise at the target station. For the purpose of noise subtraction from GW interferometers, the interferometer is the target station and the witness stations are e.g. nearby seismometers or magnetometers probing the ambient seismic or magnetic fields. If the witness sensors had infinite SNR, Wiener filtering would remove all of the correlated noise, but low SNR in the witness sensors leads

to imperfect subtraction. Furthermore, Wiener filtering can only be applied to linear coupling of external noise to GW strain, missing out on potential non-linearities [83]. More recently, machine learning methods have been developed that match performance of Wiener filters for linearly coupled noise. The deep learning algorithms go beyond Wiener filtering since they can learn arbitrarily high order couplings of the input data and subtract non-linear couplings [84].

Another method to determine whether a signal is terrestrial or gravitational in origin is the geodesy [85, 86]. Geodesy relies on inferring the relative separation and orientation of GW detectors from an estimate of GWB, and checking if this is consistent with the actual geometry of the detector network. Provided the two agree, one can deduce that the signal is gravitational in origin. If there are inconsistencies, the detected signal is not the GWB, but merely an artefact of terrestrial correlations.

Complementary to these existing studies of correlated noise in GW detectors, we develop a Bayesian approach to detect a GWB in the presence of correlated magnetic noise presented in 2.2. Like the Wiener filtering technique, we rely on witness sensors in the form of magnetometers located in the vicinity of the GW detectors. Coherences between magnetometer measurements at Hanford, Livingston and Virgo are used to model correlated magnetic fields at the interferometer sites. With models of magnetic coupling into the strain channels, we construct the correlated magnetic noise contribution to the background for each baseline pair. We outline the model selection methods used to establish if there is preference for magnetic correlated noise over white Gaussian noise in simulated data. Next we investigate scenarios where both magnetic and GW signals are injected, and test our method to search for presence of GWB in the data when there is magnetic contamination. In 2.3 we apply this Bayesian analysis to magnetic noise in data from O3, confirming there was no magnetic contamination during the run. We finish the chapter by investigating magnetic noise

in the 3G detector, Einstein Telescope, in 2.4. Here we make projections for upper limits on coupling of magnetic fields to the detector strain channel and we conclude by commenting on necessary improvements in noise reduction for next-generation detectors.

## 2.2 Detecting a GWB in the presence of correlated magnetic noise

Schumann resonances are a potential source of correlated magnetic noise. An estimate of the correlated magnetic noise budget in the isotropic GWB search using data from the first, second and third observing run indicates that it is not yet an issue for GWB studies [87, 59]. However, as detectors grow more sensitive, this will likely change, and the magnetic noise budget could dominate the signal [72]. Hence, a careful treatment of correlated magnetic noise is of vital importance.

### 2.2.1 Simulating GW data with correlated noise

In this section, we discuss how we simulate GW data that is contaminated with correlated noise due to the Schumann resonances. In 2.2.1 we present a model for the coupling of magnetic fields into GW detectors. In 2.2.1 we show how to simulate multiple data streams that have correlated Gaussian noise components, and then we apply that method to our specific use case.

The Schumann resonances, being global excitations, are coherent across the $\mathcal{O}(1000\ \mathrm{km})$ distance scales between GW detectors [80, 88]. We model the time-series induced in magnetometers from the Schumann resonances as Gaussian, stationary, and unpolarised, with a PSD that can be described by a set of Lorentzians centred around the main harmonics. We assume that the data in two magnetometers, $\tilde{m}_i(f)$ and $\tilde{m}_j(f)$, have a cross-spectral density given by

$$\langle \tilde{m}_i^*(f)\tilde{m}_j(f')\rangle = \frac{1}{2}\delta_T(f-f')\gamma_{ij}^M(f)M(f), \tag{2.1}$$

where $M(f)$ is the correlated power spectral density and $\gamma_{ij}^{M}(f)$ is the magnetic analogue to the gravitational overlap reduction function, $\Gamma_{ij}$. This model is equivalent to expression (23) of [75], and we refer the reader to that paper for an in-depth discussion of the model.

## Coupling to detectors

Magnetic fields can induce noise in GW detectors by coupling to metallic materials in the suspension system of the detector, or by inducing currents in the cabling. The magnetic coupling is estimated by injecting magnetic noise into the detector, and measuring the detector's response, and the response of the witness magnetometers near the detectors. Peaks in the detectors' strain channels are related to the peaks in the magnetometer channels via the coupling function, $T(f)$ [71]:

$$\tilde{n}(f) = T(f)\tilde{m}(f). \tag{2.2}$$

The exact frequency dependence of the coupling function is uncertain, and it can change over the course of a long observation run [89]. Despite our knowledge of the magnetic sources to a great precision, this uncertainty in the detector response to terrestrial magnetic sources makes magnetic noise challenging to study. Throughout this analysis, we will assume that the coupling is constant in time, is well-described by a power law, and is real. It takes the form

$$T(f) = \kappa \left(\frac{f}{10\ \text{Hz}}\right)^{-\beta} \times 10^{-23}\ \text{strain/pT}, \tag{2.3}$$

where $\kappa$ is the amplitude of the coupling at 10 Hz and $\beta$ is the spectral index of the power law. In [72], they estimated a coupling function with $\kappa = 2$, $\beta = 2.67$ for LIGO Hanford Observatory (LHO). Measurements made after the second observation run found $\kappa = 0.38$ at LHO and $\kappa = 0.25$ at LIGO Livingston Observatory (LLO), and $\beta = 3.55, 4.61$ [89] at LHO and LLO respectively. Meanwhile for Virgo, post-O2 measurements indicate $\kappa$=0.275

and $\beta$=2.50 [90]. These measurements highlight that the coupling functions differ in both shape and amplitude at each site.

We made three simplifying assumptions in defining (2.3), and relaxing each of these assumptions could be explored further in future work. For example, it is known that the strength of the coupling function can change as a function of time due to things like routine maintenance on the detectors. Next, recent measurements at LHO indicate that $T(f)$ has a more complicated frequency structure than a simple power law. There is evidence, for example, of a shift to a positive spectral index at higher frequencies. Finally, the assumption that $T(f)$ is real will also need to be revisited in the future. It could be modelled by multiplying (2.3) by a frequency-dependent phasor term, $e^{i\phi(f)}$, but there are no measurements at present for the frequency structure of that phase or how it behaves as a function of time. It is possible to generalise the simulations we perform to inject signals that relax these assumptions and evaluate the effect they have on the method we discuss later.

## Simulating data

In this section, we first discuss how we generate correlated synthetic magnetometer data streams with a specific ORF and cross-power. We then discuss how we translate that into strain data using a coupling function. We close with a discussion of the parameters we use to simulate the data.

### Simulating correlated Gaussian signals

We discuss simulating a correlated Gaussian signal with a specific $M(f)$ and $\gamma_{ij}^{M}(f)$ between detectors. Let us consider a network of $N$ detectors. Individual on-site magnetometer measurements combine to give an $N$-dimensional column vector, $\tilde{\boldsymbol{m}}(f)$, and the magnetic overlap reduction functions are then a hermitian $N \times N$ matrix, $\boldsymbol{\gamma}^{M}(f)$:

$$\langle \tilde{\boldsymbol{m}}(f)\tilde{\boldsymbol{m}}^{\dagger}(f')\rangle = \frac{1}{2}\delta(f-f')\boldsymbol{\gamma}^{M}(f)M(f). \tag{2.4}$$

The individual elements of the $\gamma^M(f)$ matrix represent the ORF between different baselines, evaluated at $f$. We then decompose $\gamma^M$ using a Cholesky decomposition [91]:

$$\gamma^M(f) = \boldsymbol{L}(f)\boldsymbol{L}(f)^\dagger, \tag{2.5}$$

where $\boldsymbol{L}(f)$ is a lower-triangular matrix. We can use $\boldsymbol{L}(f)$ to construct the correlated magnetometer data,

$$\tilde{\boldsymbol{m}}(f) = \sqrt{\frac{M(f)}{2}}\boldsymbol{L}(f)\tilde{\boldsymbol{\eta}}(f), \tag{2.6}$$

with $\tilde{\boldsymbol{\eta}}(f)$ being white Gaussian noise with a covariance matrix given by the identity matrix:

$$\langle \tilde{\boldsymbol{\eta}}(f)\tilde{\boldsymbol{\eta}}^\dagger(f')\rangle = \mathbf{I}\delta(f - f'). \tag{2.7}$$

Once we obtain $\tilde{\boldsymbol{m}}(f)$, which mimics local magnetometer measurements, we project it onto the detectors using a power law coupling function as in (2.3). We inverse-Fourier transform that strain spectrum to produce $\boldsymbol{h}(t)$, and add it to Gaussian detector noise that is uncorrelated between the separate detectors and has a PSD consistent with design sensitivity for the Advanced LIGO and Advanced Virgo detectors [92].

**Correlated magnetic noise PSD and $\gamma_{ij}^M(f)$ for synthetic data sets**

When constructing a data set with synthetic magnetic noise, we must choose a power-spectral density of the correlated magnetic signal between sites, $M(f)$. This PSD should include the first several harmonics of the Schumann resonances. Throughout the rest of this study, we model each peak as a separate Lorentzian, with the fundamental peak having an amplitude of 1 $\mathrm{pT}^2/\mathrm{Hz}$. A plot of the simulated PSD is shown in Figure 2.1. We only include harmonics below 30 Hz for this study. While the true correlated magnetic PSD does not fall off as rapidly as our simulated version, the steep coupling functions we consider in 2.2.3 will make higher frequen-

cies negligible when the magnetic noise is projected onto the detectors.

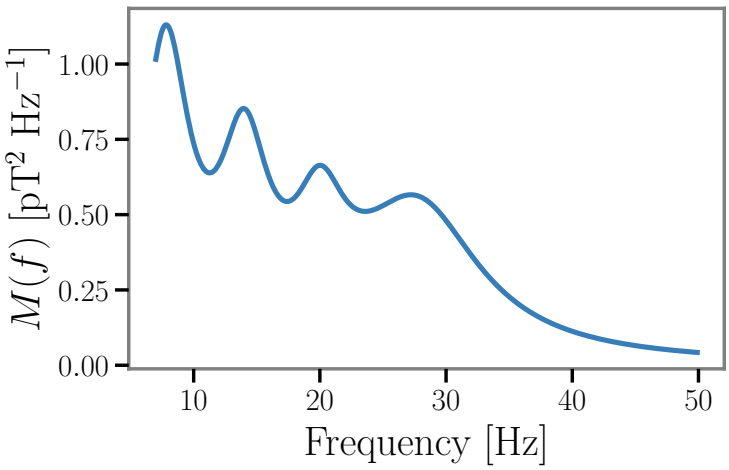


**Figure 2.1:** Injected $M(f)$ spectrum. We simulate the first four Schumann peaks as Lorentzians with reasonable amplitudes and widths.

We use the real part of coherence measurements between magnetometers located on site at LHO, LLO and Virgo to estimate $\gamma_{ij}^{M}(f)$ for each detector pair, and we use these measurements throughout the rest of this work when creating synthetic data sets. Our use of the real part of the coherences in this case does not affect the results. This can be seen by substituting (2.2) into (1.40). A term like (2.1) comes out, multiplied by $T_i(f)$ and $T_j(f)$, which are assumed to be real. A similar, explicit calculation along these lines is done in Section 2.2.2. If $T_i(f)$ were not real, then we would need to use the full, complex coherences for $\gamma_{ij}^{M}(f)$. More details related to these measurements are discussed in Appendix A.1. A plot of the measured $\gamma_{ij}^{M}(f)$ is shown for the three detector pairs of interest in Figure 2.2. For comparison, we also include $\Gamma_{ij}(f)$, which is the analogous quantity for GWs. The differences between $\gamma_{ij}^{M}(f)$ and $\Gamma_{ij}(f)$ help us to discriminate between correlated magnetic noise and a GWB in Section 2.2.2.

### 2.2.2 Simultaneous estimation of correlated noise and GWs

Various techniques have been proposed to address correlated noise due to Schumann resonances in the output of GW detectors. The most prominent of these techniques is Wiener filtering [71, 72, 80, 88]. The downside of

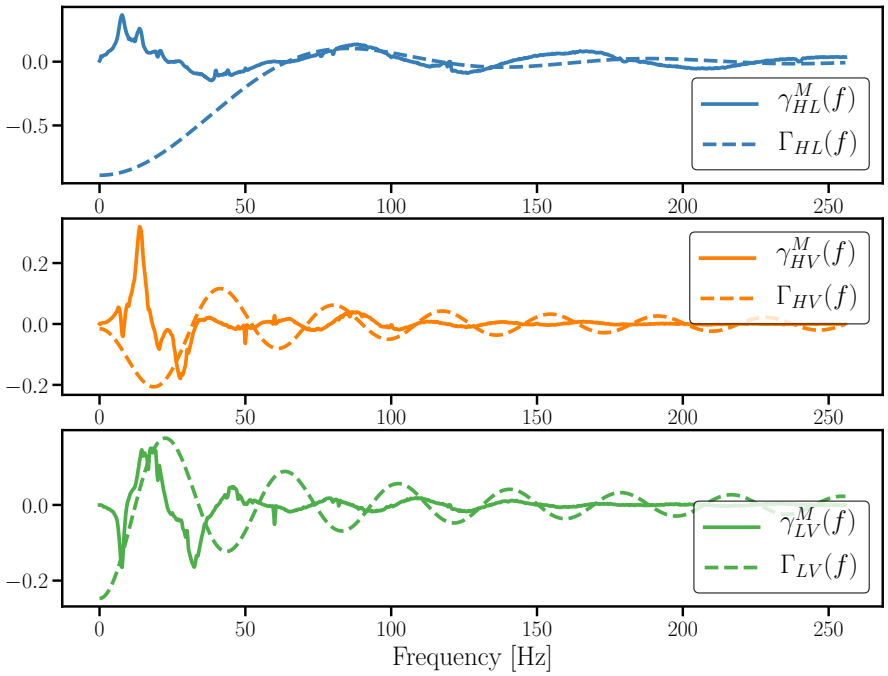


**Figure 2.2:** From top to bottom we show $\gamma^M_{ij}(f)$ (solid) and $\Gamma_{ij}(f)$ (dashed) for $ij$ = HL, HV, and LV. We discuss how we measure $\gamma^M_{ij}(f)$ in Appendix A.1.

Wiener filtering is that it requires a large coherence between the witness and target channels, which means that for weakly coupled signals it can be difficult to completely subtract the noise [80, 88].

We propose an alternative method to address correlated noise, specifically as it pertains to a search for a GWB. We model the correlated magnetic noise in GW detectors using the data collected by the magnetometers placed near the detector sites, and a parameterised model for the magnetic field to GW detector coupling. We then include this model as a contribution to the estimator, $\hat{C}_{ij}(f)$ in (1.36), together with a GWB model. The way we treat magnetometer data here is reminiscent of the "a priori" subtraction scheme presented in [72], except that here we offer a straightforward way to handle uncertainty in the measurement of the coupling functions by treating them as nuisance parameters that we marginalise over.

## Correlated noise model

We can rewrite (1.35) to include separate correlated magnetic and uncorrelated noise terms

$$\tilde{s}_i(f) = \tilde{h}_i(f) + \tilde{n}_i^{\mathrm{u}}(f) + T_i(f)\tilde{m}_i(f), \tag{2.8}$$

where $\tilde{n}_i^{\mathrm{u}}(f)$ is the uncorrelated noise in detector $i$, and $T_i(f)\tilde{m}_i(f)$ represents the correlated magnetic noise. Substituting (2.8) and (2.3) into (1.36) we find

$$\langle \hat{C}_{ij}(f) \rangle = \Omega_{\mathrm{GW}}(f) + \Omega_{\mathrm{M},ij}(f), \tag{2.9}$$

where $\Omega_{\mathrm{M},ij}(f)$ represents the magnetic contribution, which we derive next.

We construct the magnetic model, $\Omega_{M,ij}(f)$, by first treating local magnetometer data the same way we analyse GW strain data. We break the magnetometer data into $T_{\mathrm{obs}} = 192$ s data chunks, and we calculate the cross-power term in the same way as (1.36), replacing the strain data with local magnetometer data. That is, for the data between $t_k$ and $t_k + T_{\mathrm{obs}}$ we calculate

$$\hat{M}_{ij,k}(f) = \frac{2}{T_{\mathrm{obs}}} \frac{\mathrm{Re}\left[\tilde{m}_{i,k}^*(f)\tilde{m}_{j,k}(f)\right]}{\Gamma_{ij}(f)S_0(f)}. \tag{2.10}$$

We post-process the magnetometer data with the same weights used for post-processing the GW data, viz.

$$\hat{M}_{ij}(f) = \frac{\sum_k \hat{M}_{ij,k}(f)\sigma_{ij,k}^{-2}(f)}{\sum_k \sigma_{ij,k}^{-2}(f)}. \tag{2.11}$$

The weights, $\sigma_{ij,k}(f)$, are the same as those expressed in (1.39). They are calculated using *GW strain data* and not magnetometer data. This way we treat the magnetometer data the same way the magnetic contribution to the final $\hat{C}_{ij}(f)$ statistic is treated. We then use this final measurement to

construct the magnetic contribution to the model, which is given by

$$\Omega_{\mathrm{M},ij}(f) \;=\; \kappa_i\kappa_j\left(\frac{f}{10\ \mathrm{Hz}}\right)^{-\beta_i-\beta_j}\hat{M}_{ij}(f)\times 10^{-22}. \tag{2.12}$$

The factor of $10^{-22}$ assumes that the units of $\tilde{m}_i(f)$ are T $\mathrm{Hz}^{-1}$.

## Parameter Estimation and Model Selection

We use a parameter estimation and model selection scheme similar to those set out in [35, 36, 93]. We choose a Gaussian likelihood for $\hat{C}_{ij}(f)$ given by

$$\ln p(\hat{C}_{ij}(f)|\boldsymbol{\theta}_{\mathrm{GW}},\boldsymbol{\theta}_{\mathrm{M}}) = -\frac{1}{2}\sum_f \frac{\left[\hat{C}_{ij}(f)-\Omega_{\mathrm{GW}}(f,\boldsymbol{\theta}_{\mathrm{GW}})-\Omega_{\mathrm{M},ij}(f,\boldsymbol{\theta}_{\mathrm{M}})\right]^2}{\sigma_{ij}^2(f)} - \frac{1}{2}\ln\left(2\pi\sigma_{ij}^2(f)\right), \tag{2.13}$$

where $\boldsymbol{\theta}_{\mathrm{GW}}$ and $\boldsymbol{\theta}_{\mathrm{M}}$ represent parameters for the GW and magnetic models respectively. In the case where we have cross-correlation statistics for multiple baselines, we consider the total likelihood to be the product of the individual likelihoods for each pair of detectors. The resulting multi-baseline likelihood is given by

$$p(\{\hat{C}_{ij}(f)\}_{ij\in\mathrm{pairs}}|\boldsymbol{\theta}_{\mathrm{GW}},\boldsymbol{\theta}_{\mathrm{M}}) = \prod_{ij\in\mathrm{pairs}} p(\hat{C}_{ij}(f)|\boldsymbol{\theta}_{\mathrm{GW}},\boldsymbol{\theta}_{\mathrm{M}}). \tag{2.14}$$

It is straightforward to use (2.14) to estimate the posterior distribution of the parameters, $\boldsymbol{\theta}_{\mathrm{GW}}$ and $\boldsymbol{\theta}_{\mathrm{M}}$, either by brute-force calculation or by Markov chain Monte Carlo methods [94, 95].

We will also compare different models for the data using Bayesian model selection. The four models we consider are:

1. **NOISE:** $\Omega_{\mathrm{M}}(f)=0$, $\Omega_{\mathrm{GW}}(f)=0$,
2. **GW:** $\Omega_{\mathrm{M}}(f)=0$, $\Omega_{\mathrm{GW}}(f)\neq 0$,
3. **SCHU:** $\Omega_{\mathrm{M}}(f)\neq 0$, $\Omega_{\mathrm{GW}}(f)=0$,

4. **GW+SCHU:** $\Omega_{\rm M}(f) \neq 0$, $\Omega_{\rm GW}(f) \neq 0$.

The form of the GWB model, $\Omega_{\rm GW}(f)$, is a power law with amplitude at $f = 25$ Hz, $\boldsymbol{\theta}_{\rm GW} = \Omega_{2/3}$ and spectral index $\alpha = 2/3$ fixed. The form of $\Omega_{\rm M}(f)$ is given by (2.12) with $\boldsymbol{\theta}_{\rm M} = (\kappa_i, \kappa_j, \beta_i, \beta_j)$ when two detectors are involved. Another set of coupling parameters $(\kappa_k, \beta_k)$ are included when a third detector is used.

We compare these models using Bayes factors [96]. For example, comparing the **GW** model to the **NOISE** model we have

$$\mathcal{B}^{\rm GW}_{\rm NOISE} = \frac{\int {\rm d}\boldsymbol{\theta}_{\rm GW} p(\hat{C}_{ij}(f)|\boldsymbol{\theta}_{\rm GW}) p(\boldsymbol{\theta}_{\rm GW})}{\mathcal{N}} \tag{2.15}$$

where $\mathcal{N}$ is given by evaluating (2.13) for $\Omega_{\rm M}(f) = \Omega_{\rm GW}(f) = 0$, and $p(\boldsymbol{\theta}_{\rm GW})$ is the prior on the GW model parameters. When $\mathcal{B}^{\rm GW}_{\rm NOISE} > 1$ there is support for the **GW** model compared to the **NOISE** model. A further discussion of interpretation of Bayes factors can be found in, e.g. chapter 3 of [38]. In this thesis, we will consider "strong" support for one model over another when $\ln \mathcal{B} > 8$. The numerator of (2.15) is referred to as the evidence of the **GW** model and is denoted $\mathcal{Z}_{\rm GW}$. The prior distribution used for each parameter in the model throughout the rest of this study is shown in Table 2.1.

We use the nested sampler `CPNest` [97, 96] through the front-end package `Bilby` [98] to both explore the posterior distribution of each parameter and to estimate the evidences for each model.

### 2.2.3 Results on synthetic data

In this section we show results for end-to-end simulations of a GWB search using GW data with correlated magnetic noise. In 2.2.3 we briefly review data simulation schemes in the time- and frequency-domains. In the rest of this section we seek to answer three main questions:

1. How does including three detectors aid in our ability to detect the correlated magnetic noise and constrain parameters associated with

| Parameter | Prior |
|---|---|
| $\Omega_{2/3}$ | LogUniform($10^{-12}$, $10^{-7}$) |
| $\kappa_H$ | Uniform(0, 10) |
| $\kappa_L$ | Uniform(0, 10) |
| $\kappa_V$ | Uniform(0, 10) |
| $\beta_H$ | Uniform(0, 10) |
| $\beta_L$ | Uniform(0, 10) |
| $\beta_V$ | Uniform(0, 10) |

**Table 2.1:** List of prior distributions used for each parameter for results presented in 2.2.3.

it?

2. Can we detect GWs in the context of correlated magnetic noise? How is the significance of the detection affected by the presence of that noise?

3. Can a noisy measurement of $\hat{M}_{ij}(f)$ or a strong correlated magnetic signal lead to a false GWB detection?

## Synthetic data and parameters

We simulate the strain time-series for the LHO, LLO, and Virgo detectors with correlated magnetic noise using the techniques described in Section 2.2.1. We then run the standard pipeline used by LIGO-Virgo for the isotropic search for a GWB to calculate $\hat{C}_{ij}(f)$ and $\hat{M}_{ij}(f)$ for all possible detector pairs [1]. All GWB injections are made in the frequency domain on those data products and assume a power law spectrum with $\alpha = 2/3$ to mimic an astrophysical GWB from unresolved CBCs.

The three different year-long synthetic data sets we consider are described in Table 2.2. We consider data sets with no correlated magnetic noise (**none**), realistic correlated magnetic noise (**realistic**) based on post-O2 measurements [89, 90], and strong correlated magnetic noise (**strong**). The **strong** data set corresponds to a larger coupling strength than we currently observe, but is meant to be a stand-in for situations where we do

[1] `https://git.ligo.org/stochastic-public/stochastic`

| Run name | $\kappa_H$ | $\beta_H$ | $\kappa_L$ | $\beta_L$ | $\kappa_V$ | $\beta_V$ |
|---|---|---|---|---|---|---|
| **None** | 0 | 0 | 0 | 0 | 0 | 0 |
| **Realistic** | 0.38 | 3.55 | 0.35 | 4.61 | 0.275 | 2.50 |
| **Strong** | 5 | 3.55 | 5 | 4.61 | 5 | 2.50 |

**Table 2.2:** Correlated magnetic noise parameters for four different synthetic data sets.

observe correlated magnetic noise. This could occur either due to an increase in the sensitivity of detectors or a change in the coupling functions themselves.

For Monte Carlo simulations of many noise realisations we will directly simulate (2.12) in the frequency domain. This simulation method is used in the final two parts of this section, and will also consider the same **none**, **realistic**, and **strong** scenarios detailed in Table 2.2.

## Advantages in detecting correlated magnetic noise using three detector network

We begin by looking at the advantage of having a three-detector, global network as opposed to a simple two-detector network. To evaluate this situation, we use the time-domain data discussed previously. We first look at the effect using three detectors has on model selection, before discussing the advantages of using three detectors when performing parameter estimation.

In Table 2.3 we show log-Bayes factors comparing different models when there is no injected GWB. The first column indicates the strength of the correlated noise injection and the second column indicates which detectors were used in the parameter estimation. The other four columns present Bayes factors comparing different models.

The results for the **none** and **realistic** injections are shown in the first four rows of Table 2.3. The log-Bayes factors indicate that there is no preference for a model with correlated magnetic noise compared to Gaussian noise ($\ln \mathcal{B}^{\mathrm{SCHU}}_{\mathrm{NOISE}}$) or for any model that includes a GWB compared to Gaus-

| **Run Name** | Dets | $\ln \mathcal{B}^{\mathrm{GW}}_{\mathrm{NOISE}}$ | $\ln \mathcal{B}^{\mathrm{SCHU}}_{\mathrm{NOISE}}$ | $\ln \mathcal{B}^{\mathrm{SCHU+GW}}_{\mathrm{NOISE}}$ | $\ln \mathcal{B}^{\mathrm{SCHU+GW}}_{\mathrm{SCHU}}$ |
|---|---|---|---|---|---|
| **None** | HL | -0.65 | -0.26 | -1.0 | -0.74 |
| **None** | HLV | -0.75 | 0.45 | -0.32 | -0.77 |
| **Realistic** | HL | -0.61 | -0.36 | -1.01 | -0.65 |
| **Realistic** | HLV | -0.57 | -0.53 | -1.18 | -0.65 |
| **Strong** | HL | 0.28 | 0.32 | 0.59 | 0.27 |
| **Strong** | HLV | 0.59 | 33.29 | 33.67 | 0.38 |

**Table 2.3:** We show odds ratios that compare different models when no GW injection is made. We show results for all three injected data sets using just the Hanford (H), Livingston (L) pair, as well as the full Hanford, Livingston, Virgo (V) network.

sian noise ($\ln \mathcal{B}^{\mathrm{GW}}_{\mathrm{NOISE}}$ and $\ln \mathcal{B}^{\mathrm{SCHU+GW}}_{\mathrm{NOISE}}$). Thus, insofar as our simple coupling model is accurate, it is unlikely that at design sensitivity Schumann resonances will be detectable after one year of integration time. However, the coupling functions can change as a function of time, and how they impact the search is highly sensitive to the strength and frequency spectrum of the coupling between the magnetic field and the strain channel of the detector.

The **strong** injection results are shown in the fifth and sixth rows of Table 2.3. There is little evidence for correlated magnetic noise with the Hanford-Livingston pair of detectors, but when we include Virgo to the network, we make a clear detection, with $\ln \mathcal{B}^{\mathrm{SCHU}}_{\mathrm{NOISE}} = 33.29$. This is due to a degeneracy between the parameters in the two-detector case. With only a single measurement of magnetic noise $\Omega_{M,ij}$, we cannot break the degeneracy between coupling amplitudes $\kappa_i$ and $\kappa_j$, and the spectral indices $\beta_i$ and $\beta_j$, see again (2.12). However, with three measurements of magnetic noise in the three-detector case, we can recover individual magnetic parameters. While we make a detection of Schumann resonances, $\ln \mathcal{B}^{\mathrm{SCHU+GW}}_{\mathrm{SCHU}} = 0.38$ indicates that there is no preference for a model that also includes a GWB compared to a model that contains just correlated magnetic noise. Including a third detector significantly aids in our ability to detect and characterise correlated magnetic noise in this situation.

It is also important that we are able to accurately recover the correct

parameters for the GWB, even when there is a strong correlated magnetic noise injection. In Figure 2.3, we show a corner plot with 1- and 2-D marginalised posterior distributions for each parameter over which we sample for the **strong** injection (last row of Table 2.2). In this case, there is no GWB. The green posteriors indicate using only LHO and LLO, while the blue include Virgo in the network as well. It is clear that including Virgo significantly improves our estimates of the Schumann parameters. In the two-detector scenario the magnetic parameters are nearly unconstrained. Whereas, when using the three-detector network, we are able to achieve reasonable estimates of $\beta_H$, $\beta_L$ and $\beta_V$. This makes sense given the model selection results (fifth and sixth rows of Table 2.3), which indicate that adding Virgo improved our ability to detect correlated magnetic noise. Furthermore, the posterior on $\Omega_{2/3}$ in Figure 2.3 can be used to set an upper limit on $\Omega_{2/3}$ in the presence of correlated magnetic noise. In Section 2.2.3, where we perform frequency domain injections, we will discuss how upper limits on $\Omega_{2/3}$ are affected by the presence of correlated magnetic noise.

In Figure 2.4 we show the same as Figure 2.3, but with a GWB injection of $\Omega_{2/3} = 10^{-8}$. The strength of this injection is chosen for illustrative purposes. We see that the posterior on $\Omega_{2/3}$ is well-constrained but represents an overestimate of the true injected value by 14%. Due to computational restrictions, we are unable to perform repeated time-domain simulations to evaluate whether this is a systematic bias in our method. However, we did perform repeated frequency-domain simulations with magnetic and gravitational-wave parameters drawn from the priors in Table 2.1. Using probability-probability estimates as a diagnostic [99], we see no evidence of systematic bias on our estimate of $\Omega_{2/3}$.

Including Virgo does not improve our ability to constrain $\Omega_{2/3}$. However, it adds significantly to our ability to detect and constrain parameters in the correlated magnetic noise model. A correlated noise detection that

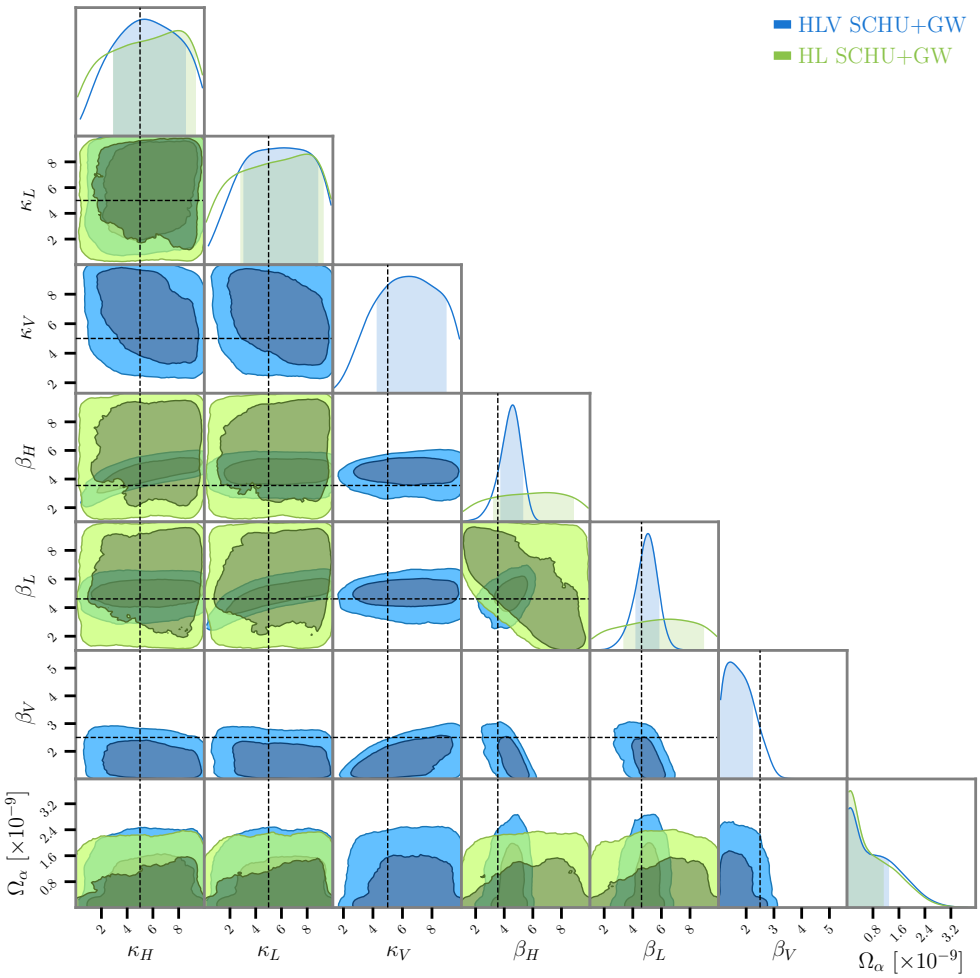


**Figure 2.3:** Parameter estimation results for strong correlated noise injection and no GWB injection. Blue lines and contours correspond to using Hanford, Livingston, and Virgo data. Green lines and contours correspond to using only the Hanford, Livingston pair of detectors. Dashed lines indicate the injected value of each parameter. It is evident that including three detectors improves the recovery of $\kappa$ and $\beta$ for all three detectors. In both cases, the posterior on $\Omega_{2/3}$ is consistent with no GWB.

is dominated by pairs of detectors that include Virgo is still able to constrain the coupling function parameters in all three detectors, which means that a third detector can aid in our ability to model the correlated noise contribution in the detector pair that is most sensitive to a GWB. Finally, this study hints at the advantage of having a network of three detectors for the 3G detectors. Building two Cosmic Explorers, alongside a triangular-

configuration of Einstein Telescope, could greatly improve the modeling of correlated magnetic noise at the individual detector sites.

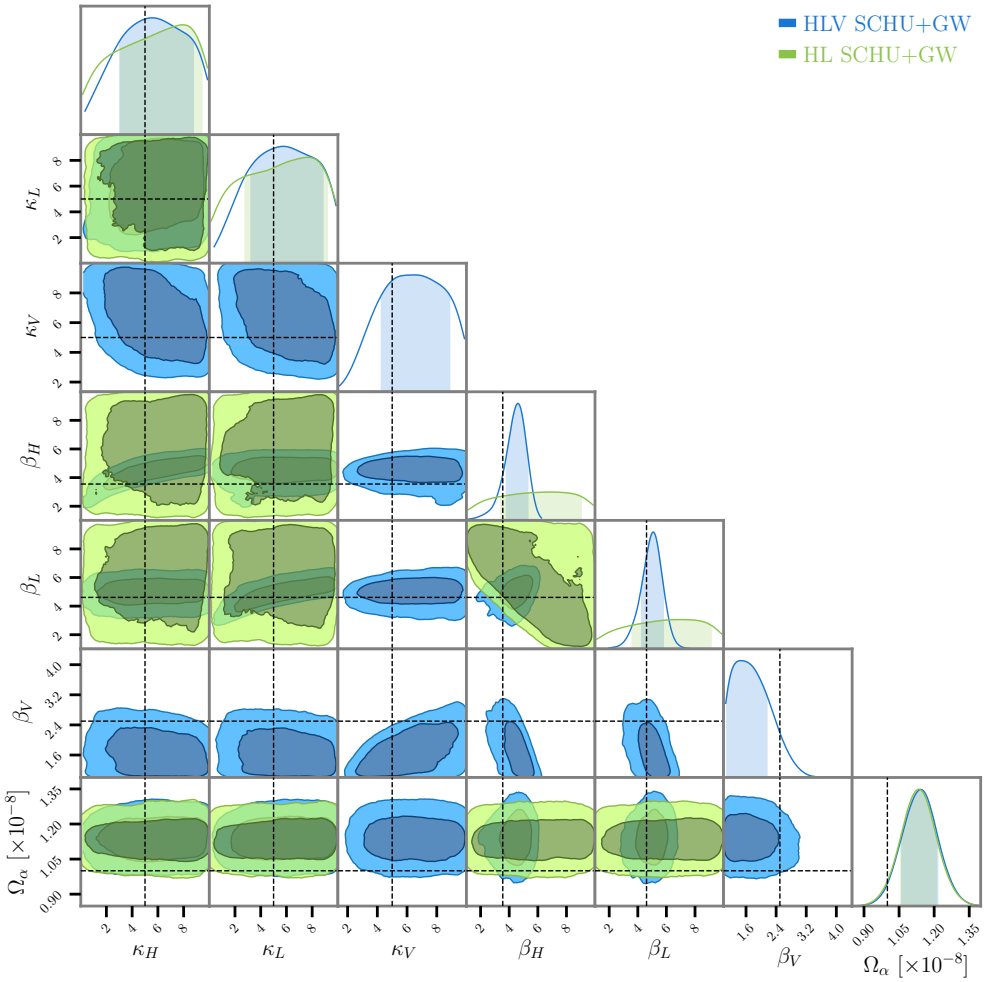


**Figure 2.4:** Parameter estimation results for strong correlated noise injection and $\Omega_{2/3} = 10^{-8}$. Blue lines and contours correspond to using Hanford, Livingston, and Virgo data. Green lines and contours correspond to using only the Hanford, Livingston pair of detectors. Dashed lines indicate the injected value of each parameter. It is evident that including three detectors improves the recovery of $\kappa$ and $\beta$ for all three detectors. The posterior distributions of $\Omega_{2/3}$ for both scenarios are consistent with one another, and indicate a 14% overestimate of $\Omega_{2/3}$.

## GWB detection with correlated magnetic noise

In this section we show we are able to detect GWs when correlated magnetic noise is present and we show how the presence of correlated magnetic noise affects the significance of that detection. We performed 300 Monte Carlo simulations, in the frequency domain, of the **strong** and **none** correlated noise parameters in Table 2.2. We did this for $\Omega_{2/3} = 0, 10^{-8}$, and $3 \times 10^{-9}$, assuming 1 year of integration time. The results are shown in three panels in Figure 2.5, where we show the distribution of $\ln \mathcal{B}^{\text{SCHU+GW}}_{\text{SCHU}}$ for each simulation. Throughout this section we use the full three-detector network and all inference is done with the prior distributions in Table 2.1.

The top left panel of Figure 2.5, where $\Omega_{2/3} = 0$, shows that for both the strong correlated magnetic noise injection (blue, solid) and the no correlated magnetic noise case we see no preference for the model including GWs compared to the one that only includes correlated magnetic noise, as one would expect. In the absence of a detection of $\Omega_{2/3}$, we can use the posterior distribution on that parameter to set 90% upper limits for each of the 300 realisations. The median 90% upper limit on $\Omega_{2/3}$ set for the ensemble of injections is $4.8 \times 10^{-10}$ for both the **strong** and **none** cases.

In the top right panel of Figure 2.5 we show results for $\Omega_{2/3} = 3 \times 10^{-9}$, which is within the range of the expected GWB due to unresolved CBCs [32]. There is mild evidence for a GWB for both distributions, with the **none** distribution (orange, dashed) peaking at $\ln \mathcal{B}^{\text{SCHU+GW}}_{\text{SCHU}} \approx 6$ and the **strong** distribution (blue, solid) peaking at $\ln \mathcal{B}^{\text{SCHU+GW}}_{\text{SCHU}} \approx 4$. It is clear that when strong correlated noise is present the significance is lower than when there is no correlated noise.

In the bottom panel of Figure 2.5 we show results for $\Omega_{2/3} = 10^{-8}$. This value is larger than expected for an astrophysical background from unresolved CBCs [32], but is chosen for illustrative purposes. When there is strong correlated magnetic noise present (blue, solid) the distribution peaks at a lower value than when there is no correlated magnetic noise

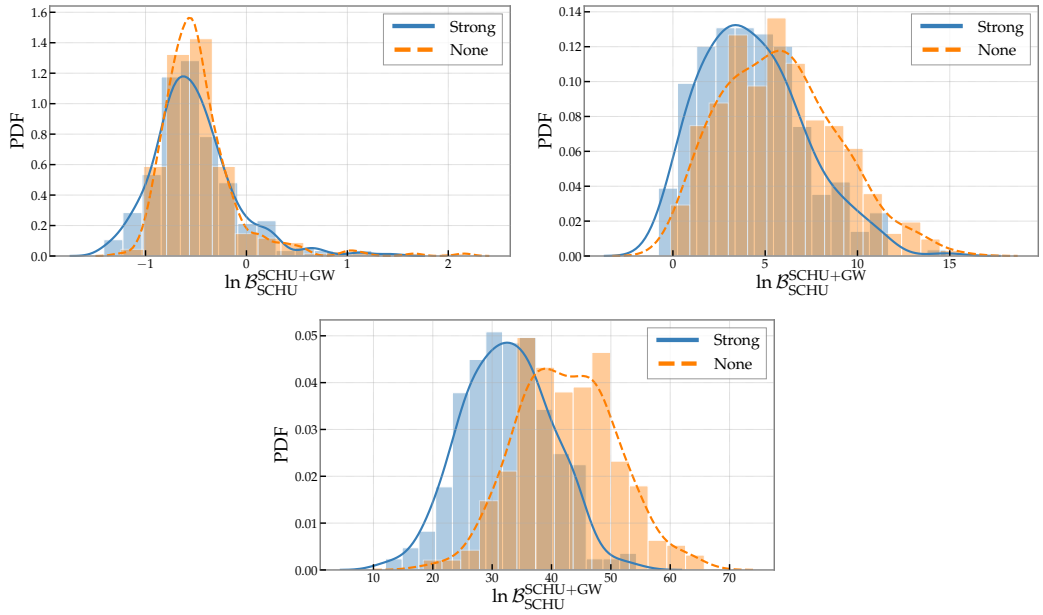


**Figure 2.5:** We show the distribution of $\ln \mathcal{B}^{\mathrm{SCHU+GW}}_{\mathrm{SCHU}}$ for the **strong** (blue, solid) and **none** (orange, dashed) injection parameters, and $\Omega_{2/3} = 0$ (top left), $\Omega_{2/3} = 3 \times 10^{-9}$ (top right) and $\Omega_{2/3} = 10^{-8}$ (bottom). In the top left panel we see no evidence for a GW detection. In the top right and bottom panels we see evidence the presence of a GWB in both cases (although that evidence is marginal in the top right panel). The presence of correlated magnetic noise has clearly shifted the Bayes factor distributions downward.

injected (orange, dashed), indicating a drop in the significance of the GWB detection when correlated magnetic noise is present. The median of the simulations with **strong** correlated magnetic noise is $\ln \mathcal{B}^{\mathrm{SCHU+GW}}_{\mathrm{SCHU}} = 32.2$ compared to $\ln \mathcal{B}^{\mathrm{SCHU+GW}}_{\mathrm{SCHU}} = 42.2$ for the **none** simulation, corresponding to a 31% drop in the detection statistic.

Figure 2.5 shows that the presence of correlated magnetic noise reduces the significance of a GW detection. In Figure 2.6 we show how $\ln \mathcal{B}^{\mathrm{SCHU+GW}}_{\mathrm{SCHU}}$ scales with time for the **strong** (blue, solid) and **none** (orange dashed) cases with an injection of $\Omega_{2/3} = 3 \times 10^{-9}$. We also show a third case where we consider a noisy measurement of $\hat{M}_{ij}(f)$, which we will discuss in Section 2.2.3. The **strong** and the **none** cases are clearly different, and the time-to-detection (in this case the time to reach $\ln \mathcal{B}^{\mathrm{SCHU+GW}}_{\mathrm{SCHU}} = 8$) is increased to $2.1^{+1.7}_{-0.7}$ years for the **strong** case compared to $1.5^{+0.9}_{-0.6}$ years for

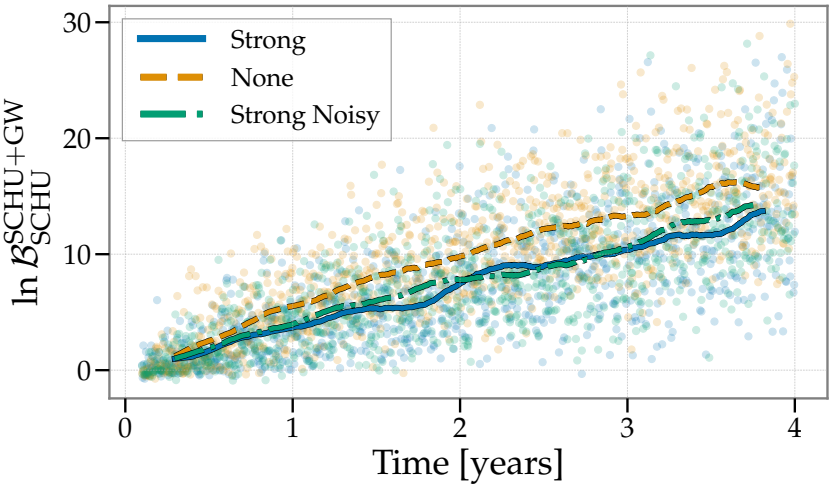


**Figure 2.6:** We show how $\ln \mathcal{B}^{\mathrm{SCHU+GW}}_{\mathrm{SCHU}}$ scales as a function of time using 1000 injections in the frequency domain with increasing observation time with a GWB injection of $\Omega_{2/3} = 3 \times 10^{-9}$. The **strong** case (blue, solid) is clearly below the **none** case (orange, dashed). We also show the **strong** case with a noisy measurement of $\hat{M}_{ij}(f)$ with a magnetic SNR of 5 (green, dash-dot). It does not appear that a noisy measurement of $\hat{M}_{ij}(f)$ significantly hinders our ability to detect a GWB.

the **none** case (values given define the 68% confidence regions).

## Can a poor measurement of $\hat{M}_{ij}(f)$ lead to a false GWB detection?

To this point, we have not considered the effect of local magnetometer noise, which can reduce the significance with which we measure the noise that is correlated between the detectors. In this section, we address whether a low-SNR measurement of $\hat{M}_{ij}(f)$, defined in (2.11), or very strong correlated noise could lead to a false GW detection. To evaluate this question, we perform frequency-domain injections with increasing values of $\kappa$ from 0 to 9 for each detector, and the same $\beta$ values for LHO, LLO, and Virgo that were used for the **realistic** and **strong** injections in Table 2.2. For this test, we use the full three detector network and we extend the upper range of the priors, shown in Table 2.1, on $\kappa$ from 10 to 20.

We also vary the confidence with which we measure $\hat{M}_{ij}(f)$. We perform our frequency domain injection using $M(f)$ presented in Figure 2.1.

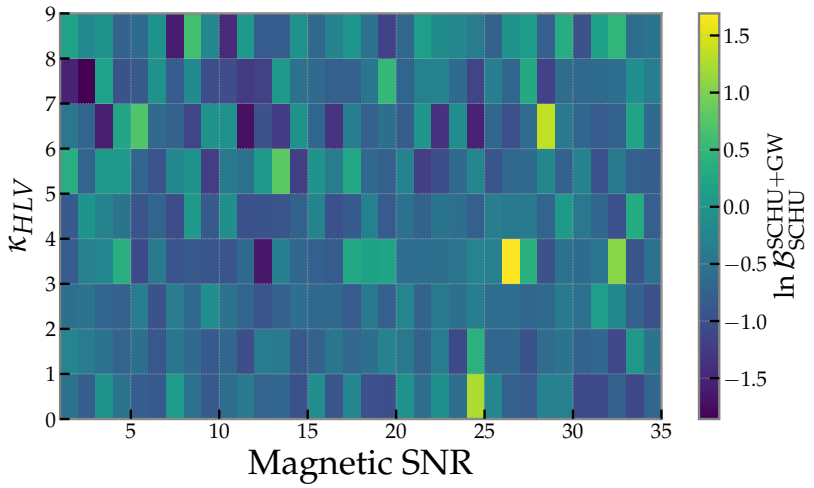


**Figure 2.7:** We show a grid of $\ln \mathcal{B}^{\mathrm{SCHU+GW}}_{\mathrm{SCHU}}$ for different values of $\kappa$ (the same $\kappa$ is used for all three detectors) and the magnetic SNR defined in (2.16). The range of $\ln \mathcal{B}^{\mathrm{SCHU+GW}}_{\mathrm{SCHU}}$ across the whole grid is consistent with no GWB detection. This indicates it is unlikely that a false GWB detection could be caused by a noisy measurement of $\hat{M}_{ij}(f)$ or the presence of strong correlated magnetic noise.

We then simulate a "measurement" at a chosen SNR in each frequency bin by drawing $\hat{M}_{ij}(f)$ from a normal distribution with mean $\gamma^M_{ij}(f)M(f)$ and variance $\sigma^2_M(f)$. Due to the fact that the SNR and $M(f)$ are chosen a priori, we re-arrange the definition of the SNR to set the standard deviation in each frequency bin,

$$\sigma_M(f) = \frac{\gamma^M_{ij}(f)M(f)}{\mathrm{SNR}}. \tag{2.16}$$

We perform frequency domain injections with SNRs ranging from 1 to 35.

In Figure 2.7 we show $\ln \mathcal{B}^{\mathrm{SCHU+GW}}_{\mathrm{SCHU}}$ for the range of $\kappa$ and magnetic SNR values we inject and with $\Omega_{2/3} = 0$. The Bayes factors in Figure 2.7 are consistent with no detection–they span a similar range to those in the top panel of Figure 2.5, where we assumed a perfect measurement of $\hat{M}_{ij}(f)$. This result indicates that a false detection of a GWB is unlikely, even with an uncertain measurement of the Schumann resonances.

We also test whether a noisy measurement of $\hat{M}_{ij}(f)$ could increase

time-to-detection of a GWB. We do this by showing how $\ln \mathcal{B}^{\text{SCHU+GW}}_{\text{SCHU}}$ scales with time for $\kappa = 5$ (**strong** case) and SNR=5 in Figure 2.6 with the green dash-dot curve. There is a not a clear reduction in detection strength compared to the blue solid curve, which is the same correlated magnetic noise strength but with a no-noise measurement of $\hat{M}_{ij}(f)$. The time-to-detection for the noisy measurement case is $2.1^{+1.2}_{-0.9}$ years, which is around 50% longer than the case with no correlated noise and comparable to the case where we make a noiseless measurement of the magnetic field.

## Discussion

In this study we performed realistic simulations of correlated magnetic noise in interferometric gravitational-wave detectors, and proposed a new method to detect a GWB in the presence of that correlated magnetic noise. The method reliably separates a GWB from correlated magnetic noise, although the significance of a detection can be reduced - either by the presence of strong correlated noise, or through a noisy measurement of the correlated magnetic fields. We also showed that a three-detector network improves our ability to detect, estimate, and subtract the correlated magnetic noise compared to just a single detector pair.

The method presented here is an alternative to Wiener filtering, but could also be used in tandem with Wiener filtering. For example, this method could be used to find correlated noise that was not successfully subtracted using Wiener filtering. Besides, any proposed GWB signal could be verified using the geodesy methods discussed in [85]. In that scenario, the maximum a posteriori parameters could be used to subtract off the correlated magnetic noise, and the proposed remaining GWB signal could be analysed using geodesy.

Improvements on the work could be achieved by using a model for the magnetic coupling functions that is more flexible than a simple power law. It should make direct comparisons with other proposed methods, and work towards incorporating the time-variability of both coupling functions and

Schumann resonances. This method is easily applicable to current searches for GWB, and should help make a reliable detection of GWB using ground-based interferometric detectors. In the following section we demonstrate how our method was applied to the data from the O3 run to search for signs of correlated magnetic noise.

## 2.3 Correlated magnetic noise during O3

The O3 run has set the most stringent upper limits to date on the gravitational-wave background [59]. In the following section we will show the results of applying the Bayesian methods mentioned in 2.2.2 to the O3 data, and summarise the magnetic noise study in [59].

Magnetometer data collected throughout the observing run, $m_i(t)$, can be used to construct a magnetic correlations budget

$$\hat{C}_{\mathrm{mag},ij}(f) = \frac{2}{T_{\mathrm{obs}}} \frac{|T_i(f)||T_j(f)|\mathrm{Re}[\tilde{m}_i^\star(f)\tilde{m}_j(f)]}{\Gamma_{ij}(f)S_0(f)}. \tag{2.17}$$

Here $\tilde{m}_i(f)$ are the Fourier transforms of the magnetometer channels, $T_i(f)$ the coupling of magnetic fields to the detector and $S_0(f)$ the usual normalisation factor. The coupling functions were monitored throughout the run by magnetic injections (of varying frequency and amplitude) and measurements of the strain response in each detector. Figure 2.8 demonstrates that even with the most pessimistic estimates of the magnetic budget, correlated magnetic noise contribution to the background is well below the sensitivity of the O3 detector network. Therefore magnetic contamination was not concerning in the third LVK run. Further, for the first time we used a Bayesian framework to complement the study of the magnetic budget and we were able to confirm that magnetic noise did not limit the sensitivity of the GW detectors.

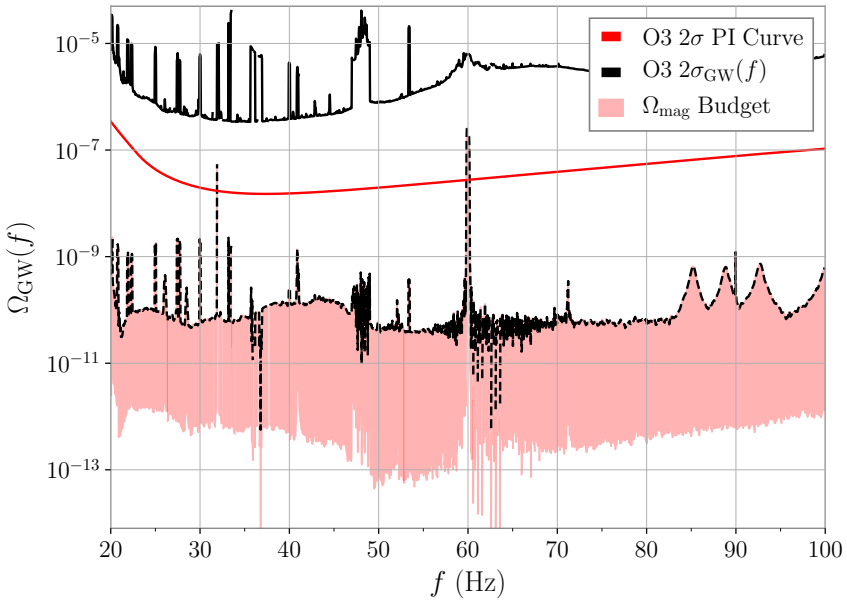


**Figure 2.8:** Correlated magnetic noise budget, $\Omega_{\rm mag}$, constructed using (2.17). The uncertainty in the measurements of the coupling functions leads to uncertainty in the magnetic budget. The most conservative estimate of the budget remains two orders of magnitude below the power law integrated curve and 4 orders of magnitude below the standard deviation of the cross-correlator estimated in O3.

### 2.3.1 Measurements of the magnetic coupling functions

We use weekly magnetic injections performed in O3 [100] to construct more informative priors on magnetic parameters $\kappa$ and $\beta$ than the ones listed in Table 2.1. Figures 2.9, 2.10, 2.11 show measurements of the coupling functions at Hanford, Livingston and Virgo respectively. The magnetic coupling as a function of frequency for all three detectors can be approximated as a power law [2]. We set priors on magnetic parameters such that the upper and lower limit for $T(f)$ encapsulate all of the measurements – the two extremes are showed in Figure 2.9 - 2.11. The orange line in the figures corresponds to $T(f)$ evaluated using the upper limit of $\kappa$ and $\beta$ priors, while the blue line corresponds to $T(f)$ evaluated using the lower prior limits. For $\kappa_i$ the chosen prior distributions were chosen to

[2]Note that the power law approximation breaks down for high frequencies and we see an increase in magnetic coupling to the strain channel at frequencies larger than 100 Hz. This is not a problem for 2G detectors, since most of their GWB sensitivity lies in the frequency range up to 100 Hz [59].

be log-uniform from 0.01 to 10 for all of the detectors. The uniform priors on the spectral indices varied between detectors, namely the $\beta$ priors chosen for the study were (0, 12), (1, 10) and (0, 7), for LHO, LLO and Virgo respectively.

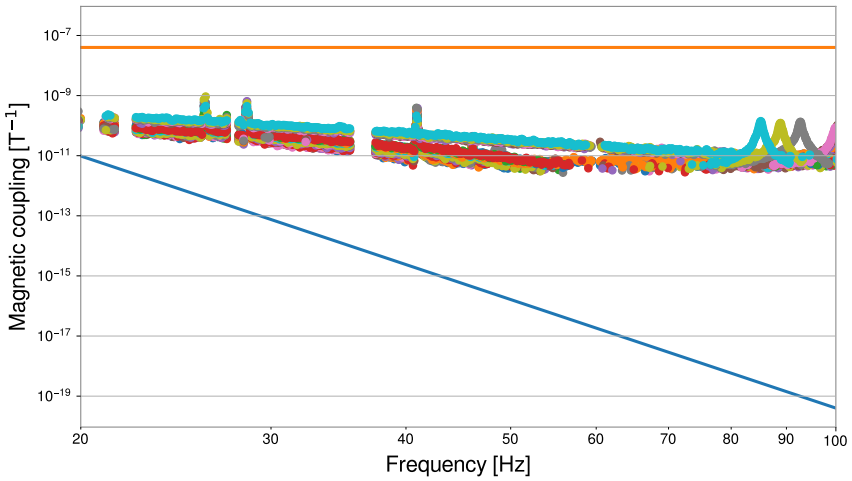


**Figure 2.9:** Measurements of the LHO magnetic coupling function recorded throughout the O3 run. The two lines plotted show the lower and upper limit for the coupling function used as prior knowledge in our Bayesian analysis.

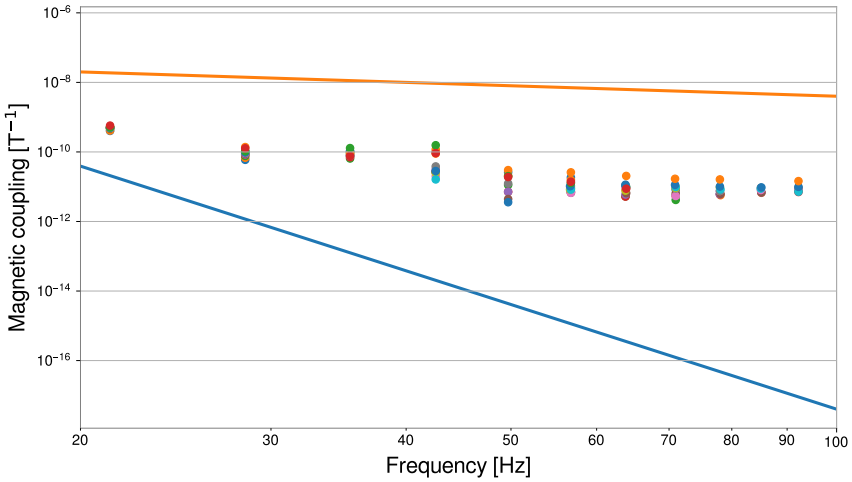


**Figure 2.10:** Measurements of the LLO magnetic coupling function recorded throughout the O3 run. The two lines plotted show the lower and upper limit for the coupling function used as prior knowledge in our Bayesian analysis.

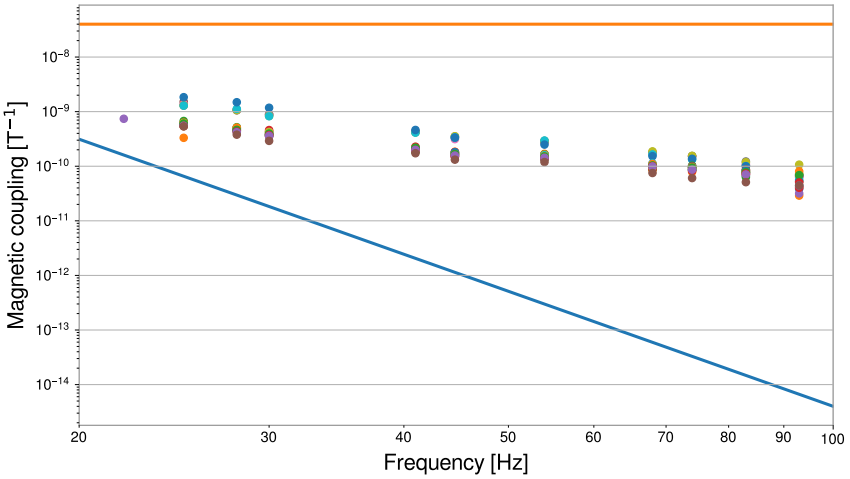


**Figure 2.11:** Measurements of the Virgo magnetic coupling function recorded throughout the O3 run. The two lines plotted show the lower and upper limit for the coupling function used as prior knowledge in our Bayesian analysis.

Following the Bayesian framework developed in 2.2.2 and applying the above-mentioned priors, we search for correlated magnetic noise in the O3 data. We find no preference for correlated magnetic noise over instrumental Gaussian noise, with $\log_{10}\mathcal{B}^{\mathrm{MAG}}_{\mathrm{N}} = -0.03$. Our results agrees with the estimates of the magnetic budget and confirms that there was no significant magnetic contamination in the O3 run.

Additionally, we search for simultaneous presence of a gravitational-wave background and a magnetic correlated noise background. We use a simple power law (1.27) to model $\Omega_{\mathrm{GW}}(f)$ and set a log-uniform prior on the amplitude from $10^{-13}$ to $10^{-5}$ along with a Normal distribution (centred at 0, with standard deviation 3.5) as the prior distribution on the spectral index. We find $\log_{10}\mathcal{B}^{\mathrm{MAG+PL}}_{\mathrm{N}} = -0.3$, suggesting there is no significant evidence of a GWB in the data, consistent with the main results of [59].

### 2.3.2 Future LVK runs and `pygwb`

The LVK Stochastic group [3] has designed a Python pipeline, `pygwb`, that will serve the purpose of processing output from the strain channels and

[3] Following an initiative from Andrew Matas.

producing the cross-correlator statistics in the upcoming observing runs. This pipeline includes a parameter estimation module which I lead and designed, with a careful treatment on correlated magnetic noise presented thus far. Specifically, the parameter estimation module represents a catalogue of $\Omega_{\rm GW}(f)$ models one can search for in the data using the hybrid frequentist-Bayesian approach [59]. The module consists of a parent class with generic definitions of likelihood and noise, and model-dependent child classes that include details of the model parameters. It represents a user-friendly and accessible interface for running parameter estimation on GWB data. The details on `pygwb` are summarised in a technical note included in Appendix B.

The latest results in a search for an isotropic GWB showed that Schumann resonances are below the detector sensitivity; however as the sensitivity increases they could limit the search. More importantly, one should study their effect on searches with future Earth-based interferometers which aim to have approximately one order of magnitude improvement in sensitivity compared to current instruments. In the following section we explore magnetic correlations in the context of ET and set targets (upper limits) on ET's magnetic coupling functions.

## 2.4 Correlated magnetic noise in Einstein Telescope

The next-generation detectors will shine a light on GW events at higher redshifts. Due to significant improvements in sensitivity compared to the current-generation detectors, magnetic correlated noise in the form of Schumann resonances could present a grave limitation. In this study we focus on the European proposal for a 3G GW interferometer: the Einstein Telescope [101]. We consider recorded magnetic activity at a candidate site for the Einstein Telescope, and forecast the necessary measures to ensure that magnetic contamination will not pose a threat to the science goals of

this 3G detector. In addition to global magnetic effects, we study local magnetic noise and the impact it might have on co-located interferometers. We express our results as upper limits on the coupling function of magnetic fields to the interferometer arms, implying that any larger values of magnetic coupling into the strain channel would lead to a reduction in the detectors' sensitivity.

The current ET proposal consists of three interferometers with an opening angle $\pi/3$ forming an equilateral triangle. The no-longer operational Sos Enattos mine in Sardinia, Italy, is one of the possible locations to host the future ET interferometer, another being the Euregio Rhein-Maas at the intersection of the Belgian, Dutch and German borders [102]. Please note that this work does not contain a site comparison and typical magnetic spectra will be used to make statements on the impact of magnetic fields on ET, regardless of its exact location.

The research and development, and design phase of ET is ongoing. With this consideration we investigate the impact of fundamental magnetic noise sources, such as Schumann resonances, on the ET interferometers. We construct the maximal allowed magnetic coupling function so that the fundamental magnetic sources are not limiting the sensitivity of ET, either as an instrument itself or in its use for a search for an isotropic GWB.

In addition to low-frequency Schumann resonances, there are high-frequency correlated magnetic fields from individual lightning strikes [103], mainly situated in the frequency range 100 Hz - 1 kHz [104]. We will investigate the impact of these on ET's sensitivity, as well as consider possible limitations due to infrastructural noise.

In 2.4.1 we describe coupling of magnetic fields into ET. Section 2.4.2 focuses on the different magnetic data sets that will be used to make projections about the magnetic coupling function for ET. In 2.4.3 the magnetic coupling functions are constructed and we will discuss the impact of our results and their interpretation.

### 2.4.1 Einstein Telescope configuration

We approximate ET as three interferometers and ignore the details of the xylophone configuration [105]; this does not affect our results.

In what follows, we assume the three co-located, 10 km long arm interferometers in triangle configuration of ET, namely $\mathrm{ET}_1$,$\mathrm{ET}_2$,$\mathrm{ET}_3$, as having identical sensitivity, and we take the unbiased estimator of $\Omega_{\mathrm{GW}}(f)$ to be (1.36). Furthermore, we neglect the difference in $\Gamma_{ij}$ between the baseline pairs $ij = \mathrm{ET}_1\mathrm{ET}_2$,$\mathrm{ET}_1\mathrm{ET}_3$,$\mathrm{ET}_2\mathrm{ET}_3$, where we will be using $\Gamma_{\mathrm{ET}_1\mathrm{ET}_2}$ from now on. For frequencies under 1 kHz the relative differences are [106]:

$$\frac{|\Gamma_{\mathrm{ET}_1\mathrm{ET}_2} - \Gamma_{\mathrm{ET}_1\mathrm{ET}_3}|}{\Gamma_{\mathrm{ET}_1\mathrm{ET}_2}} < 5 \times 10^{-7},$$

$$\frac{|\Gamma_{\mathrm{ET}_1\mathrm{ET}_2} - \Gamma_{\mathrm{ET}_2\mathrm{ET}_3}|}{\Gamma_{\mathrm{ET}_1\mathrm{ET}_2}} < 2 \times 10^{-7},$$

justifying our choice to neglect the difference between baseline pairs. The normalisation factor $S_0(f)$ is given by $S_0(f) = (9H_0^2)/(40\pi^2 f^3)$ and $T_{\mathrm{obs}}$ is the total observation time of the data-collecting period [4].

Equivalent to the cross-correlation statistic (1.36), one can construct a magnetic cross-correlation statistic as in (2.17),

$$\begin{aligned} \hat{C}_{\mathrm{mag},\mathrm{ET}_1\mathrm{ET}_2}(f) &= |\mathcal{K}_{\mathrm{ET}}(f)|^2 M_{\mathrm{ET}_1\mathrm{ET}_2}, \\ \text{where} \quad M_{\mathrm{ET}_1\mathrm{ET}_2} &= \frac{2}{T_{\mathrm{obs}}} \frac{|\tilde{m}^*_{\mathrm{ET}_1}(f)\tilde{m}_{\mathrm{ET}_2}(f)|}{\Gamma_{\mathrm{ET}_1\mathrm{ET}_2}(f)S_0(f)}, \end{aligned} \tag{2.18}$$

and $\mathcal{K}_{\mathrm{ET}}(f)$ describes the coupling from magnetic fields to interferometer $\mathrm{ET}_1$, where we have used $\mathcal{K}_{\mathrm{ET}}(f) = \mathcal{K}_{\mathrm{ET}_1}(f) = \mathcal{K}_{\mathrm{ET}_2}(f)$. To construct a conservative magnetic cross-correlation statistic we take the modulus of $\tilde{m}^*_{\mathrm{ET}_1}(f)\tilde{m}_{\mathrm{ET}_2}(f)$ rather than taking only the real part into account [107, 59].

When analysing data in a search for an isotropic GWB using inter-

[4] The form of $S_0(f)$ for ET differs from that one of e.g. LIGO by a factor of 3/4. This is due to the difference in opening angle between interferometers' arms ($\pi/2$ for LIGO and $\pi/3$ for ET) that leads to different normalisation factors in the ORF of LIGO and ET baseline pairs [38].

ferometers $i$ and $j$, the magnetic coupling functions $\mathcal{K}_{i,j}(f)$ are measured by injecting magnetic fields with known amplitude and frequency and observing their impact on the output in the GW data $s_{i,j}(t)$ [73, 74] (as discussed in 2.3 for O3 data). However, in this study we will consider a different approach: given a desired sensitivity and a magnetic spectrum $|\tilde{m}^*_{\mathrm{ET}_1}(f)\tilde{m}_{\mathrm{ET}_2}(f)|$, we estimate the maximal allowed magnetic coupling function $\mathcal{K}_{\mathrm{ET}}(f)$ such that ET will not be limited by this magnetic noise.

The sensitivity for a GWB search is different to the instantaneous sensitivity of the ET interferometer, i.e. the one-sided ASD $P_{\mathrm{ET}}(f) = P_{\mathrm{ET}_1}(f) = P_{\mathrm{ET}_2}(f) = P_{\mathrm{ET}_3}(f)$. In the case of an isotropic GWB search, the sensitivity is given by the standard deviation on the cross-correlation statistic defined in (1.37). This $\sigma_{\mathrm{ET}_1\mathrm{ET}_2}(f)$ defines our uncertainty and therefore our sensitivity in a single frequency bin used in the analysis. However, when searching for an isotropic GWB, one typically expects a broadband signal and often assumes a power law GWB model. Hence, a useful measure of GWB sensitivity is also the power law integrated (PI) curve. The PI curve, $\Omega^{\mathrm{PI}}_{\mathrm{ET}_1\mathrm{ET}_2}(f)$ is constructed using $\sigma_{\mathrm{ET}_1\mathrm{ET}_2}(f)$ so that its tangent at any frequency represents the sensitivity at which one could detect a power law $\Omega_{\mathrm{GW}}(f)$ with an SNR of 1 for the $\mathrm{ET}_1\mathrm{ET}_2$ baseline [108]. Therefore, it serves as a good figure of merit to identify broadband noise sources that could limit the sensitivity of a GWB search.

To ensure that magnetic noise does not obstruct the isotropic search for a GWB, we construct an upper limit on the magnetic coupling function that we label "GWB," in the following way. We use (2.18) and take the upper limit for the magnetic cross-correlation $\hat{C}_{\mathrm{mag},\mathrm{ET}_1\mathrm{ET}_2}(f)$ to be the $1\sigma$-PI sensitivity curve – $\Omega^{\mathrm{PI}}_{\mathrm{ET}_1\mathrm{ET}_2}$ – after one year of taking data:

$$\mathcal{K}^{\mathrm{GWB}}_{\mathrm{ET}}(f) \equiv \sqrt{\frac{\Omega^{\mathrm{PI}}_{\mathrm{ET}_1\mathrm{ET}_2}}{M_{\mathrm{ET}_1\mathrm{ET}_2}}}\,. \tag{2.19}$$

In addition, we explore a complimentary method for computing upper

limits of the magnetic coupling function $\mathcal{K}_{\mathrm{ET}}(f)$. To investigate the impact of magnetic noise sources on the ASD of an individual interferometer, we construct what we refer to as the "ASD" upper limit:

$$\mathcal{K}_{\mathrm{ET}}^{\mathrm{ASD}}(f) \equiv k \, \frac{P_{\mathrm{ET}}(f)}{P_{\mathrm{mag}}(f)} \, , \tag{2.20}$$

where $k$ is set to be $1/10$ to require any single technical noise contribution to be a factor of 10 lower than ET's ASD, $P_{\mathrm{ET}}(f)$. $P_{\mathrm{mag}}(f)$ is the one-sided ASD of the magnetometers witnessing the local noise of ET, assuming the magnetic noise to be the same for the three individual ET interferometers $\mathrm{ET}_1$, $\mathrm{ET}_2$ and $\mathrm{ET}_3$. If magnetic fields couple significantly at this level, they will limit the expected sensitivity of the interferometer. The "ASD" upper limit should be investigated to prevent magnetic noise from drastically impacting *all* science goals of the GW interferometer.

To make full use of ET's capabilities when searching for an isotropic GWB, one should use $\mathcal{K}_{\mathrm{ET}}^{\mathrm{GWB}}(f)$. On the contrary, to find the level at which magnetic fields might directly impact the instantaneous sensitivity achieved by ET, then $\mathcal{K}_{\mathrm{ET}}^{\mathrm{ASD}}(f)$ is the relevant measure.

### 2.4.2 Magnetic data in Einstein Telescope

In this analysis we use observed, rather than simulated, magnetic data. However, since the location and exact positioning of ET is unknown we will estimate $|\tilde{m}^*_{\mathrm{ET}_1}(f)\tilde{m}_{\mathrm{ET}_2}(f)|$ using a variety of observed magnetic spectra that we describe below.

As a part of site characterisation of the Sos Enattos mine for ET [109, 110], magnetic field measurements were taken from 5 Hz to 100 Hz in the exceptionally quiet environment inside the unused mine. We use 48 days of data taken from Nov 14 2019 to Dec 31 2019, using a single-axis Metronix MFS-06e magnetometer positioned inside the Sos Enattos mine about 200 m below ground level. The magnetometer is sampled at 250 Hz. Given these on-site measurements are available for Sos Enattos but not

for the Euregio Rhein-Maas ET-candidate site, we will use the magnetic spectrum observed at Sos Enattos as a reference estimate for the magnetic spectrum at the future ET site: $\tilde{m}_{\mathrm{ET}}(f) = 2\tilde{m}_{\mathrm{SosEnattos}}(f)$. The factor 2 allows for higher magnetic fields at the final site and to be more conservative. Further investigations into magnetic noise at Euregio Rhein-Maas could help compare the two currently proposed sites, but we do not make any statement about which site will be used as the actual location of the ET detector. Site-specific amplifying or reducing ambient magnetic fields are typically a second order effect that can be ignored. However, as shown by measurements at KAGRA, local amplification of ambient magnetic fields may not always be negligible [111, 42].

We show in Figure 2.12 percentiles of the magnetic ASD as measured at Sos Enattos. We use the shape of the 10% magnetic percentile curve, since it captures the peaks of the Schumann spectrum very well. We then scale the amplitude to match the amplitude of the 95%-percentile curve at 7.8 Hz, the first Schumann mode. This gives a good prediction for the Schumann resonance spectrum at Sos Enattos.

This low-frequency range is where most of the sensitivity is for the ongoing isotropic GWB searches, with the most recent LIGO-Virgo observing run containing 99% sensitivity to a flat $\Omega_{\mathrm{GW}}$ spectrum below 100 Hz [59]. The sensitivity at high frequencies is suppressed since the ORF for the LIGO and Virgo baseline pairs drops significantly with frequency and approaches zero at a few hundreds of Hz. The same, however, may not be true for the ET detectors, whose geometry leads to no suppression at high frequency, and the anticipated ORF remains approximately constant up to 1 kHz, e.g. $\gamma_{\mathrm{ET_1ET_2}}(1\ \mathrm{kHz})/\gamma_{\mathrm{ET_1ET_2}}(1\ \mathrm{Hz}) = 99.48\%$. We therefore look to place upper limits on the magnetic coupling function at high frequencies.

We estimate the correlated magnetic noise spectrum above 100 Hz by computing the cross spectral density (CSD) between magnetometers at LIGO Hanford and LIGO Livingston. The separation of several thou-

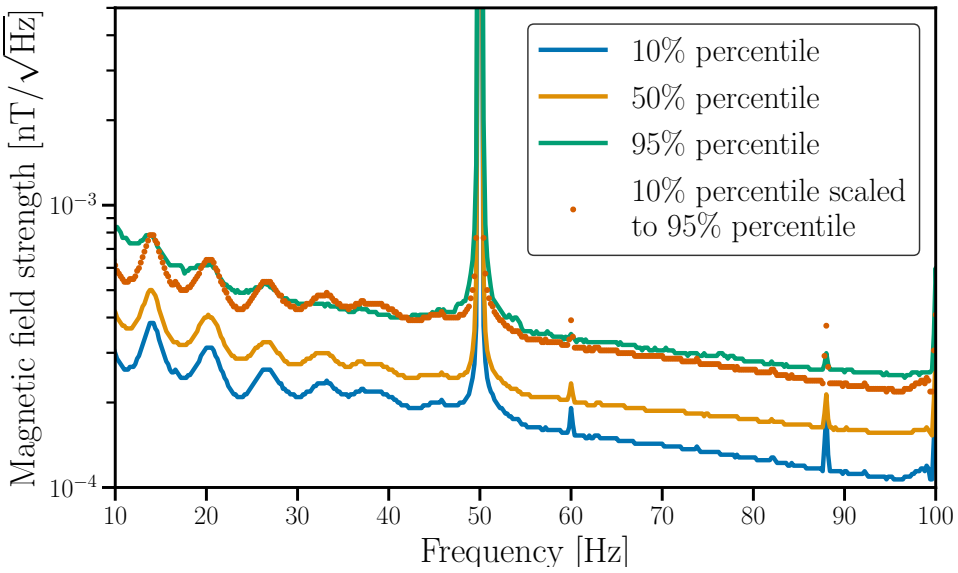


**Figure 2.12:** Sos Enattos magnetic ASD constructed using 48 days of data from Nov 14 2019 to Dec 31 2019. A one-directional magnetometer was employed to collect the data in the mine approximately 200 m below ground level. The line at 50 Hz is coming from the power mains.

sands of kilometers between the two sites ensures that the estimated spectrum only contains fundamental, global effects rather than local contributions. We consider the Hanford-Livingston baseline as the most conservative choice for magnetic CSD since these are the closest interferometers and the impact of individual lightning strikes at frequencies above $\sim$ 100 Hz drastically attenuates with increasing distance. Hanford and Livingston both have two low-noise magnetometers on site, positioned at low-noise locations orientated along the interferometers arms. We make use of an "omni-directional" magnetic CSD, where we take into account all possible cross-correlation combinations between the magnetometer pairs at both interferometer sites,

$$\begin{aligned} \mathrm{CSD_{HL}} = [\, &|\tilde{m}^*_{H_x}(f)\tilde{m}_{L_x}(f)|^2 + |\tilde{m}^*_{H_x}(f)\tilde{m}_{L_y}(f)|^2 \\ &+ |\tilde{m}^*_{H_y}(f)\tilde{m}_{L_x}(f)|^2 + |\tilde{m}^*_{H_y}(f)\tilde{m}_{L_y}(f)|^2 \,]^{1/2} \,. \end{aligned} \tag{2.21}$$

Here $H_x, H_y$ $(L_x, L_y)$ represent the two orthogonal magnetometers at Han-

ford (Livingston) pointing along the interferometer's $x$- and $y$-arms. We use data recorded from Apr 2 2019 to Mar 27 2020, which approximately matches the O3 run. We assume $\mathrm{CSD}_{\mathrm{HL}}$ is a realistic estimation for the magnetic noise at ET, where we include an additional factor of 2 reflecting our uncertainty on the magnetic spectrum [5]: $|\tilde{m}^{*}_{\mathrm{ET}_1}(f)\tilde{m}_{\mathrm{ET}_2}(f)| = 4\mathrm{CSD}_{\mathrm{HL}}$.

We also investigate the impact of local magnetic noise. One should study local magnetic noise carefully as this could be a correlated noise source as well because each local corner station for the triangular ET set-up will likely house mirrors for two of the three interferometers (separated by $\sim 300$ m and in different vacuum tubes). To model local magnetic fields of a GW interferometer, we consider the local magnetic noise measured in the central building (CEB) at Virgo site [73]. We use the 90% magnetic percentile of data collected between Feb 10 2020 and Feb 16 2020 - during the second half of the third observing run, O3b. This spectrum is quite similar to the one observed in the Virgo CEB during O2 [112]. We assume the local noise at Virgo is a realistic estimation for the local magnetic noise at ET, where we include an additional factor of 2 reflecting our uncertainty on the magnetic spectrum: $\tilde{m}_{\mathrm{ET}_1}(f) = 2\tilde{m}_{\mathrm{V}_{\mathrm{CEB}}}(f)$.

### 2.4.3 Limits on magnetic coupling in Einstein Telescope

We construct two complementary measures—$\mathcal{K}^{\mathrm{GWB}}_{\mathrm{ET}}(f)$ and $\mathcal{K}^{\mathrm{ASD}}_{\mathrm{ET}}(f)$—of the magnetic coupling function. In our analysis, we use two preliminary design studies, called $\mathrm{ET}_{\mathrm{Single}}$ and $\mathrm{ET}_{\mathrm{Xylophone}}$ [6] [113, 105]. In the remainder of this work we will use the notation ET-S and ET-X as abbreviations to refer to $\mathrm{ET}_{\mathrm{Single}}$, respectively $\mathrm{ET}_{\mathrm{Xylophone}}$. In Figure 2.13 we show the sensitivity curves for both of these design options in the left panel. In the right panel we show the PI curves for each of these design options for 1 year of integration time. The ET-X configuration is an order of magnitude

[5] A factor of 2 at the level of individual magnetic fields $\tilde{m}_{\mathrm{ET}}(f)$, corresponds to a factor of $2^2$ at the level of $|\tilde{m}^{*}_{\mathrm{ET}_1}(f)\tilde{m}_{\mathrm{ET}_2}(f)|$.

[6] In previous literature $\mathrm{ET}_{\mathrm{Single}}$ and $\mathrm{ET}_{\mathrm{Xylophone}}$ have also been referred to as respectively ET-B, ET-D.

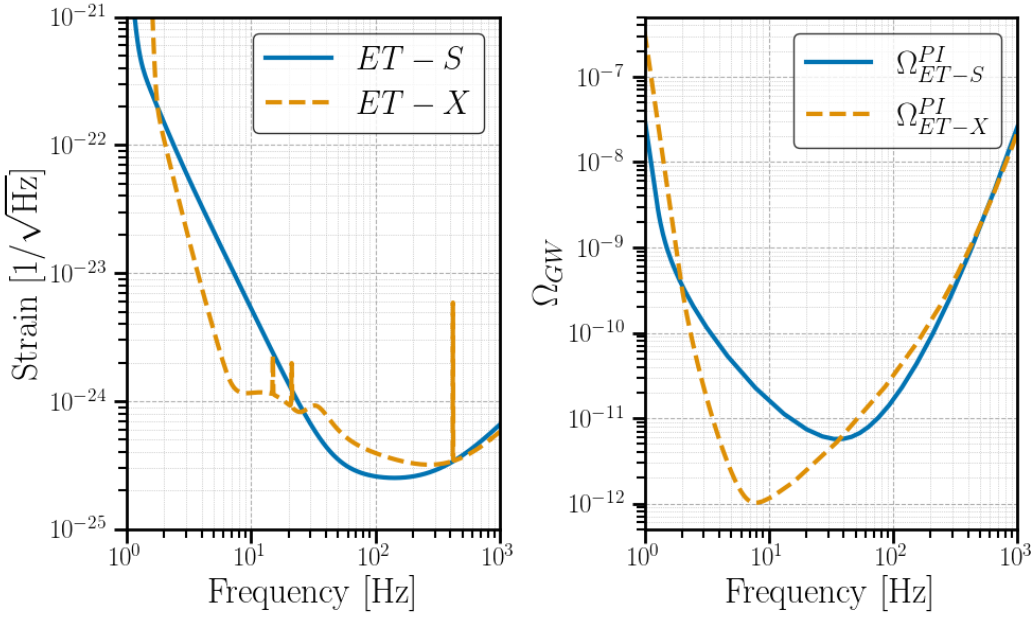


**Figure 2.13:** The ET configurations – ET-S, ET-X [113, 105] – and their anticipated sensitivity curves (left panel) as well as their power law integrated curves after a year-long observation (right panel).

more sensitive at low frequencies as compared to ET-S. Figure 2.13, shows ET-X could be sensitive to a GWB at the $\Omega_{\text{GW}}(f) \sim 10^{-12}$ range, with an SNR=1 after 1 year of observation. This seems to be consistent with earlier investigations stating a GWB with strength $\Omega_{\text{GW}}(f) = 2 \times 10^{-12}$ would be detected with an SNR=5 after 1.3 years of observation time [114].

The upper limits presented here assume the reduction of the magnetic coupling is the only pursued method to prevent magnetic fields from coupling significantly to the interferometer. Methods such, as the use of Wiener filters [115], could also be used to reduce the effects of correlated magnetic noise. However, the best strategy for ET will be to design the magnetic isolation to be as good as possible.

In Figure 2.14 we show limits on the coupling imposed by our target sensitivity measures. The $\mathcal{K}_{\text{ET}-\text{X}}^{\text{GWB}}(f)$ limits are indicated by the solid blue curve, while $\mathcal{K}_{\text{ET}-\text{X}}^{\text{ASD}}(f)$ limits are denoted by the dash-dotted yellow curve. The average coupling measurements made at Virgo [73, 116], LIGO Hanford and Livingston [117, 118, 119, 100] during the O3 run are indicated

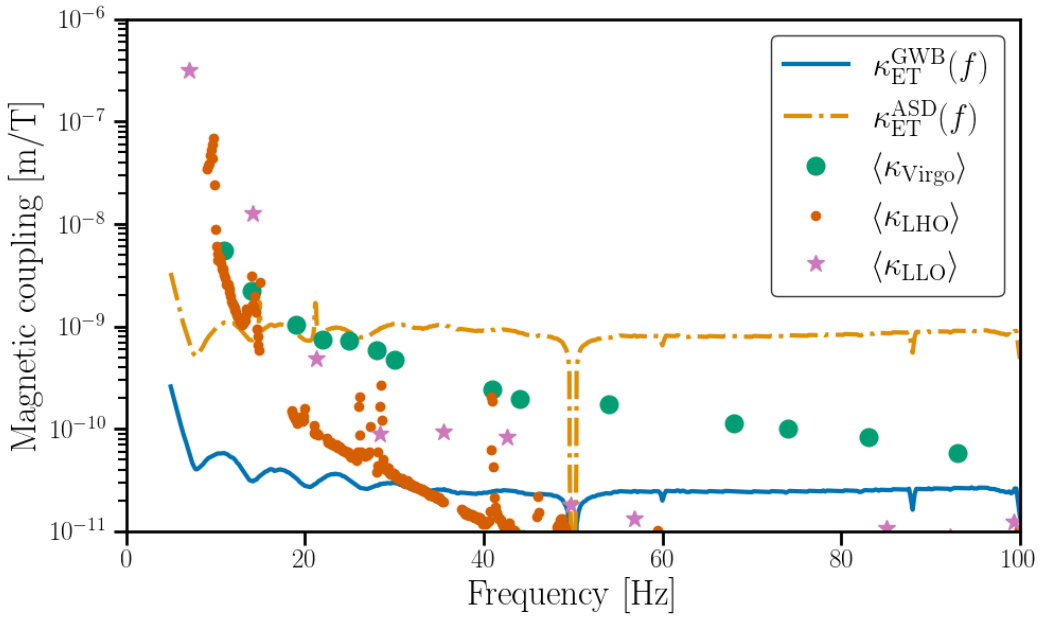


**Figure 2.14:** "ASD" and "GWB" magnetic coupling function upper limits for ET − X design sensitivity. Also included are the average of the measurements of the coupling functions at LIGO Hanford, LIGO Livingston and Virgo during the O3 run for comparison.

by the green circles, smaller orange circles, and magenta stars respectively. Please note that the magnetic coupling measurements only start from 11 Hz, 9 Hz and 7 Hz for respectively the Virgo, LIGO Hanford and LIGO Livingston interferometers. In Figure 2.15 and Figure 2.16 we show high and low-frequency coupling limits, $\mathcal{K}_{\rm ET}^{\rm GWB}(f)$, respectively for each of the design options (solid blue for ET-S, yellow dashed for ET − X). The average coupling measurements at Virgo, Hanford, and Livingston are the same as in Figure 2.14.

We notice that the upper limit on the magnetic coupling at certain frequencies is allowed to be greater than the magnetic coupling at current observatories [7], for example $\gtrsim 30$ Hz in the $\mathcal{K}_{\rm ET-X}^{\rm ASD}(f)$ curve in Figure 2.14. This means that one can be less concerned about Schumann resonance magnetic noise coupling into ET as compared to LIGO/Virgo detectors.

[7] Above 100 Hz the weekly measurements of the magnetic coupling are often upper limits rather than an actual measurements. However during some periods of "extreme" magnetic coupling such high values are actually measured as well [73].

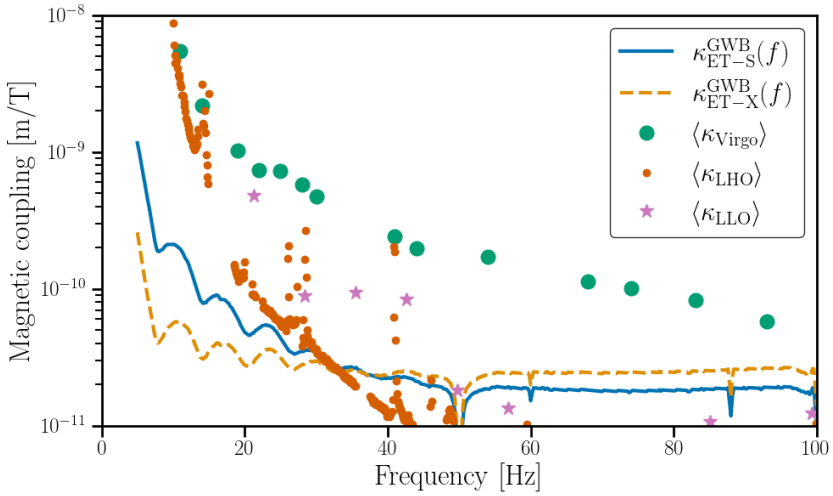


**Figure 2.15:** Variation in the "GWB" magnetic coupling function upper limits for the different ET designs. Also included are the average of the measurements of coupling functions at LIGO Hanford, LIGO Livingston and Virgo during the O3 run for comparison.

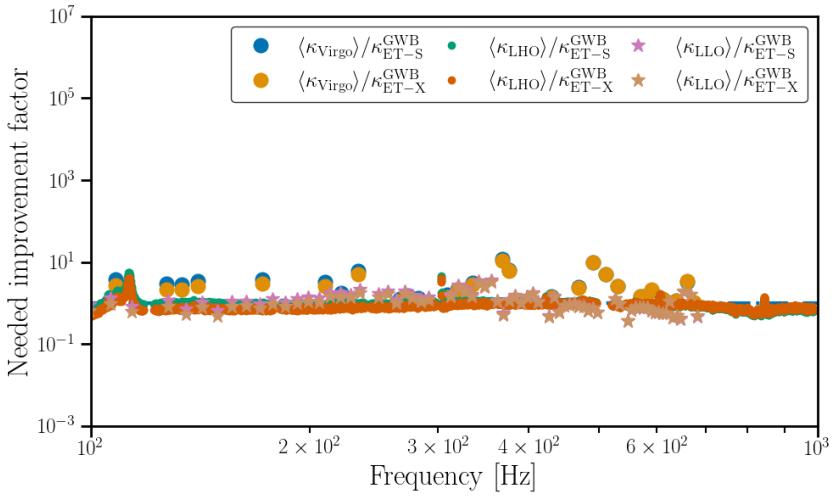


**Figure 2.16:** Upper limits on "GWB" magnetic coupling function of ET-S and -X at high frequencies. Also included is the average of the measurements of coupling functions at LIGO Hanford, LIGO Livingston and Virgo during the O3 run for comparison.

The reason for this result can be seen by considering the difference between the magnetic coupling measured in units of [$T^{-1}$] [8] and in units of [m $T^{-1}$]. The latter takes into account the arm-length of the interferometer, $L_{\rm arm}$,

$$\mathcal{K}[T^{-1}] = \frac{\mathcal{K}\,[\mathrm{m\ T^{-1}}]}{L_{\rm arm}[\mathrm{m}]}\ .$$

Since ET is planned to have a 10 km arm-length, instead of 4 km (LIGO) or 3 km (Virgo), the test masses displacements due to magnetic effects measured in the units [m $T^{-1}$] is allowed to be larger compared to existing interferometers.

We emphasise that Figure 2.14 and Figure 2.15 use data measured at the Sos Enattos candidate site for ET. However, given the similar amplitude of the Schumann resonances around the globe, these results could be transferable to another location and more specifically a second candidate site in the Euregio Rhein-Maas. That is assuming there is no extreme magnification of magnetic fields due to local effects, as observed at KAGRA [111, 42]. To account for such a possibility we introduced a factor of 1/2 in our estimates of the coupling upper limits.

We illustrate in Figure 2.16 the effect of magnetic fields at ET above a 100 Hz. An example of an analysis that could target a signal at these higher frequencies is the study of a GWB from unresolved millisecond pulsars. This search is complementary to the standard continuous-wave search of individual pulsars, and can help constrain ellipticity of rotating neutron stars [120, 121, 30]. Current forecasts predict an improvement of one to two orders of magnitude in the sensitivity to ellipticity going from LIGO-Virgo to ET. However, correlated magnetic noise at high frequencies could weaken the ellipticity constraints (see, Figure 6 in [122]), and should thus be treated carefully.

In our high-frequency analysis we have used the magnetic CSD measured between LIGO Hanford and LIGO Livingston, two widely separated

[8] The unit of magnetic coupling function [$T^{-1}$] is often referred to as [strain $T^{-1}$].

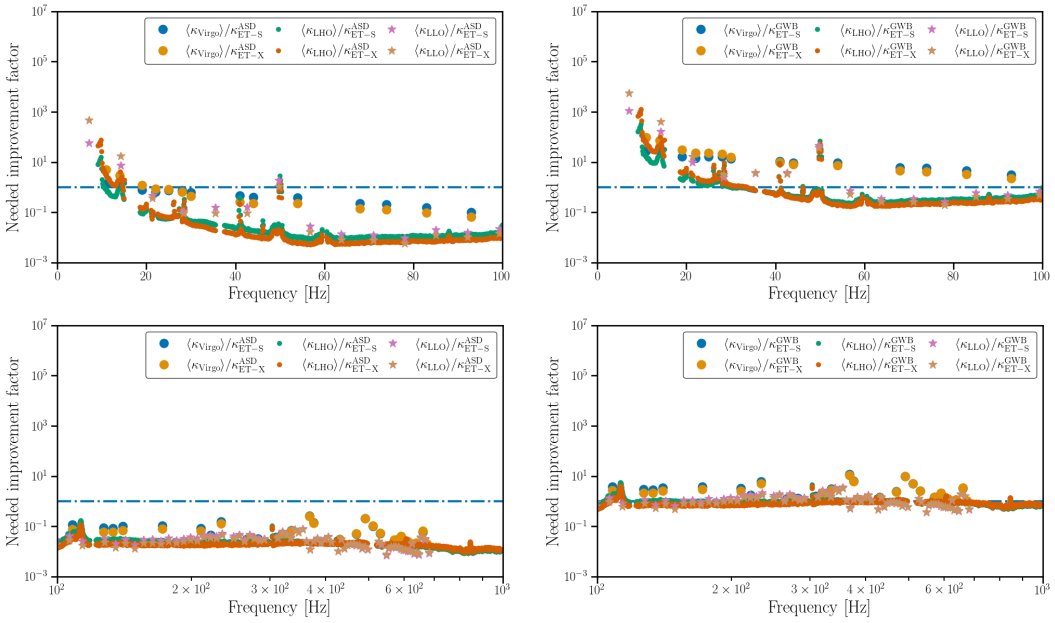


**Figure 2.17:** Needed improvement factor as a function of frequency for the "ASD" (left panels) and "GWB" (right panels) upper limits on the ET magnetic coupling function. The low-frequency (top panels) magnetic coupling poses a greater challenge for the operation of ET compared to the high-frequency (bottom panels) magnetic coupling, while "GWB" upper limits on the magnetic coupling are more constraining than the "ASD" ones. In all panels, the dash-dotted blue line indicates the line where no improvement is necessary.

sites, to ensure we are not dominated by local effects. However, since magnetic fields from the sources contributing to this magnetic noise (e.g. individual lightning strikes [104]) are attenuated over long distances, the fundamental magnetic spectrum at ET could be stronger compared to our predictions. Therefore one should be cautious interpreting the upper limits presented in Figure 2.16. For the magnetic coupling above 100 Hz, we do not show the upper limits calculated using the "ASD" formalism, (2.20), since these limits are less stringent than the measured magnetic coupling at present day interferometers.

We summarise these results in Figure 2.17, where we express the estimated "ASD" and "GWB" upper limits as a factor of improvement needed in the ET coupling function relative to Hanford, Livingston and Virgo coupling functions. We show how this factor varies with frequency, as well as

how it changes with the choice of ET design sensitivity. For frequencies below $\sim 30$ Hz, the magnetic coupling would need to drastically reduced, with factors of improvement of the order $10^2 - 10^4$ needed for the isotropic GWB search, see top right panel. High-frequency coupling, on the other hand, would only require up to a factor of 10 reduction in magnetic coupling to run a successful GWB search (bottom right panel). Meanwhile, from the "ASD" upper limits we do not require any improvement in coupling function at frequencies above 30 Hz, see two left panels, confirming that this is a less conservative constraint on the magnetic coupling.

Note that above 30 Hz Advanced LIGO's magnetic coupling is dominated by induction of currents in cables [74]. One mitigation strategy that could be followed in this scenario is using, as much as possible, a cabling network of optical fibers. The implementation of a large-scale optical fiber network has been investigated and implemented at CERN [123]. An important factor for the reduced magnetic coupling for Advanced LIGO compared to Advanced Virgo is that LIGO uses an electrostatic test mass actuators whereas Virgo uses magnetic actuation [74, 116]. Further reducing the number of magnets attached to the suspensions should reduce magnetic coupling. Additional magnetic shielding can be a complementary method to reduce the magnetic coupling [112]. Ultimately, if methods for magnetic coupling reduction are insufficient one could consider the cancellation of magnetic noise, similar to what is considered in the context of Newtonian Noise [124, 125], albeit using magnetometers instead of seismometers.

Finally, if one is unable to reduce the effect from local magnetic fields originating from e.g. used infrastructure, local magnetic noise sources will dominate the fundamental magnetic noise discussed above. This leads to the most stringent coupling upper limits, reported in Figure 2.18. To construct these upper limits the magnetic noise as observed in the Virgo central building is used. This represents a realistic magnetic environment in present-day interferometers, however it may not be the most conservative.

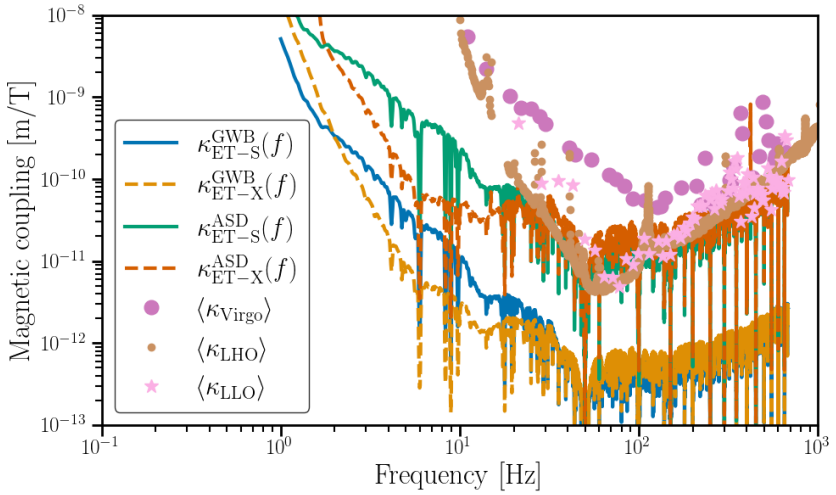


**Figure 2.18:** "ASD" and "GWB" magnetic coupling function upper limits of all ET design sensitivities in the case the local magnetic noise is the same level as the CEB at Virgo during O3. Also included are the average of the measurements of coupling functions at LIGO Hanford, LIGO Livingston and Virgo during the O3 run for comparison.

In the case of Virgo this local noise does not pose a serious problem in the GWB search since it is uncorrelated with local magnetic noise at far-away Hanford and Livingston detectors. Between co-located ET interferometers, however, the local noise could become correlated. This can lead to drastically more stringent upper limits on the magnetic coupling. If one wants to fully utilise the data for GWB searches, the magnetic coupling should be well below the magnetic coupling measured at Hanford, Livingston and Virgo, see Figure 2.18. Below $\sim$ 30 Hz, the instantaneous detector sensitivity will be limited by magnetic noise if the coupling is not reduced below the current day magnetic coupling of Hanford, which is already significantly smaller compared to the coupling measured at Livingston and Virgo.

## Discussion

Einstein Telescope is a powerful and promising instrument for detecting a GWB, with an unprecedented low-frequency sensitivity compared to LIGO and Virgo [122]. The ability to detect a GWB through correlation methods between multiple detectors assumes the absence of correlated noise [126].

However, globally coherent magnetic fields have been identified as a limiting noise source for the present GW detector network [71, 72, 48]. As we have shown, this is also the case for ET. More precisely, we have shown that the magnetic coupling functions for ET must be better than those of LIGO and Virgo by a factor of $10^2 - 10^4$ for frequencies below 30 Hz, in order to avoid correlated noise from Schumann resonances affecting GWB searches.

Reducing the magnetic coupling to prevent a significant impact on the interferometers, and also to ensure that local magnetic noise is as small as possible, is the best strategy for ET. This could be achieved by reducing the number of magnets attached to the suspensions [74], additional shielding [112], and using optical fibers as much as possible for signal transmission [74]. There could also be a synergy with noise subtraction methods, such as Wiener filters [115, 124, 125]. However they also could be used to reduce the effects of correlated magnetic noise and loosen the requirements on the magnetic coupling, as presented here.

Not reaching the reported upper limits on the magnetic coupling functions could have a direct impact on the search for a GWB with ET. Note, however, that reaching these upper limits is not necessarily a guarantee that there are no effects by magnetic fields on the search for a GWB. The importance of correlated magnetic noise coupling will need to be considered as ET is designed and constructed.

## 2.5 Afterword

In this chapter we discussed at length the impact of correlated magnetic noise on sensitivity of current and future GW detectors. In addition to already existing methods, such as Wiener filtering, we consider statistical Bayesian tools to treat correlated noise present in the data. We described the Bayesian framework and demonstrated its success in separating a GW signal from correlated magnetic noise. This framework was used in the O3 run, and it proved that magnetic noise was not present in the data.

Finally, we made projections for the coupling functions in the future ET detector and pointed to improvement needed to ensure ET's sensitivity is not limited by magnetic noise. For gravitational-wave background searches below $\sim 30$ Hz it will be necessary for the Einstein Telescope magnetic isolation coupling to be two to four orders of magnitude better than that measured in the current Advanced LIGO and Virgo detectors.

When we detect a GWB signal, we will have the tools at hand to confirm that it is gravitational in nature, and not an artefact of correlated magnetic noise sources. The question naturally arises: If we have detected a GWB, can we determine its components?

# Chapter 3

# Source separation

## 3.1 Foreword

Gravitational-wave background is a random signal produced by many weak, independent and unresolved sources; it can be of cosmological or astrophysical origin. A variety of early Universe processes, like quantum vacuum fluctuations during inflation, post-inflationary preheating, first order phase transitions, or topological defects (in particular cosmic strings) can lead to a GWB [127, 128, 129].

An astrophysical contribution to the GWB comes from the superposition of unresolved GW sources of stellar origin. This includes burst sources, like core collapse supernovae and the final stage of CBCs, together with quasi-periodic long-lived sources like pulsars and the early inspiral phase of compact binaries [130, 33]. A detection of a GWB can provide important astrophysical information about, for instance, the mass range for neutron star and black hole progenitors, or the rate of compact binaries [32]. It also sheds light on particle physics models beyond the Standard Model and the early stages of our Universe.

Once a GWB is successfully detected, there will be the challenge of identifying the sources that contribute to it. Untangling these signals will deepen our knowledge of merger rates and population models [131, 132, 133, 134], our understanding of exotic objects [135, 136, 137, 138] and in

particular early Universe models [139, 140, 129, 141].

Extensive literature on separation of GWB sources confirms the importance of this step in GW data analysis. Broadly, separation techniques rely on non-gaussianity or temporal variation of the astrophysical background, as well as use singular value decomposition of the signal, see e.g. terrestrial [142, 143, 144, 145, 146, 147] and space-based GW detector source separation studies [148, 149, 150, 151]. This chapter consists of two parts; 3.2 tests separation of an astrophysical CBC background from a cosmological background in terrestrial detectors using our Bayesian tools described in the previous chapter, while 3.3 reflects on separating Galactic confusion noise from CBC signals in space-based LISA using a novel machine-learning method.

## 3.2 Terrestrial GW detectors

In this section, we consider backgrounds that comprise CBCs and additional cosmological sources for terrestrial detectors, and we set simultaneous upper limits on these backgrounds. We find that the Advanced LIGO, Advanced Virgo network, operating at design sensitivity, will not allow for separation of the sources we consider. Third-generation detectors, sensitive to many more individual compact binary mergers, can reduce the astrophysical GWB via subtraction of individual sources, and potentially reveal a cosmological background [152, 153].

In this study, we adapt the parameter estimation analysis from 2.2.2, which is based on techniques already present in the literature [154, 155, 156], to separate the astrophysical and cosmological contributions to the GWB. We first discuss 2G detectors Advanced LIGO and Advanced Virgo. We then move to 3G detectors, namely Einstein Telescope and Cosmic Explorer, and comment on how the study could be adapted to the space-based LISA detector. The future detector networks require subtraction of the "loud" CBCs from the GWB, prior to the parameter estimation

[157, 146, 158, 159, 114], to ensure that the cosmological background is not obscured by the astrophysical one. In 3.2.1 we discuss the individual sources we choose for this study. We describe the GW signals injected and the analysis we perform in 3.2.2. We summarise our results in 3.2.3 and make concluding remarks.

### 3.2.1 Astrophysical and cosmological sources

#### CBC background

The CBC background is likely to be the largest contribution to the GWB [32]. Therefore, any attempt to measure other contributions to the background should be done in such a way as to simultaneously measure a CBC background and other contributions. The analytic model describing the CBC background depends on quantities such as redshift and merger rates [130, 32]; the inspiral phase can be approximated as

$$\Omega_{\rm CBC}(f) = \Omega_{2/3}\left(\frac{f}{25\,\rm Hz}\right)^{2/3}. \tag{3.1}$$

In the case of 2G detectors, we can use this approximation freely [160, 161]. When it comes to future GW detectors, however, the approximation cannot be applied to the entire frequency band. Instead, one must also include the contributions from the merger and ringdown phases that cause measurable deviations from this approximation, as shown in (1.43) [146, 161]. For the purpose of this study, we restrict ourselves to the range $(10-100)$ Hz, the frequency range over which the approximation in (3.1) is valid, even after individual source subtraction [146].

The current estimate of the amplitude of the CBC spectrum from individual sources over the Advanced LIGO and Advanced Virgo frequency range places an upper bound $\Omega_{\rm CBC} = 1.9 \times 10^{-9}$, at a reference frequency of 25 Hz [59]. This estimate includes contributions from binary black holes, binary neutron stars, and black hole-neutron star systems.

There are numerous studies on subtracting resolvable CBC signals

from the data, and these can lead to a reduction in their contribution to the GWB by as much as two orders of magnitude for binary black hole signals and one order of magnitude for binary neutron star signals [157, 146, 158, 159, 114]. When considering future detectors like Einstein Telescope and Cosmic Explorer, we assume a scenario where such a subtraction has already been made – following the results from [146]. Note that the imperfect subtraction of CBC sources may pose a serious threat to digging out a cosmological background, and extensive research must be done to improve the subtraction methods [152, 153].

### Cosmic Strings

A phase transition followed by a spontaneously broken symmetry can leave behind topological defects as remnants of a previous more symmetric phase. One particular class of such defects is cosmic strings, line-like defects, generically formed within the context of grand unified theories [162].

A network of cosmic strings is mainly characterised by the string tension $G\mu$, where $G$ is Newton's constant, and $\mu$ is the mass per unit length. The dynamics of a string network are driven by the formation of loops and the emission of bursts of GWs, predominantly from cusps and kinks, and kink-kink collisions [163, 25]. The superposition of these bursts leads to a GWB over a large range of frequencies, making it a target for GW searches from pulsar timing arrays in the nanohertz band as well as the ground-based detectors we consider here [164, 165, 166].

In the high-frequency regime we consider, $(10 - 100)$ Hz, the spectrum of the GWB is flat, i.e. $\Omega_{\rm CS}(f) = \text{const}$ [167], and it only depends on the averaged total power emitted by a loop, and the total number of loops. A GWB analysis can thus put a limit on the string tension, and consequently on the energy scale of the phase transition leading to the formation of these objects.

The 95% credible upper limit placed after the first three LIGO obser-

vation runs, assuming a uniform prior, is $\Omega_{CS} = 1.3 \times 10^{-8}$ [107, 59]. This implies upper bounds to the string tension [25], $G\mu \leq 4 \times 10^{-15}$, for the loop distribution model in [168].

### First Order Phase Transitions

If a phase transition occurred at temperatures $(10^5 - 10^{10})$ GeV, the corresponding GW spectrum would be observed in the $(10 - 100)$ Hz frequency range we consider [169]. The phase transition associated with the breaking of Peccei-Quinn symmetry, for instance, could have happened at such high temperatures, leading to the QCD axion, a well motivated extension to the Standard Model. In this scenario, the growth of the true vacuum bubbles, and their subsequent collisions, give out GWs due to several effects [170]. The strongest of those is most likely due to sound waves from bubble growth in plasma. The turbulence of the plasma in which the bubbles grow can also produce GWs. Finally, GWs are emitted due to collision of the scalar wall profiles. There exist numerical [171, 172, 173] and analytical [174, 175] models for the shape of $\Omega_{GW}$ as a function of frequency for each of these contributions.

The frequency spectrum of the GWB produced by most models can be captured by a smoothed broken power law:

$$\Omega_{BPL} = \Omega_* \left(\frac{f}{f_*}\right)^{\alpha_1} \left[1 + \left(\frac{f}{f_*}\right)^{\Delta}\right]^{(\alpha_2 - \alpha_1)/\Delta}. \tag{3.2}$$

For example, numerical simulations find the GW spectrum due to the sound waves in the plasma [176]

$$h^2\Omega_{SW}(f) = F(\beta, H_*, \kappa_{SW}, \alpha, g_*, v_w) \, \frac{(f/f_{SW})^3}{[1 + 0.75(f/f_{SW})^2]^{7/2}}, \tag{3.3}$$

where $\beta$ is the transition strength, $H_*$ is the Hubble constant at the time of GW production, $\kappa_{SW}$ is the efficiency factor, $\alpha$ is the ratio of latent heat

released in the phase transition to the heat of the radiation bath, $g_*$ is the number of relativistic degrees of freedom, $v_w$ is the bubble wall velocity, and $f_{\rm SW} = f_{\rm SW}(\beta, H_*)$ is the peak frequency.

If we use (3.2) to approximate (3.3), then we have $\alpha_1 = 3$, $\alpha_2 = -4$ and $\Delta = 2$. Relating $\Omega_*$ and $f_*$ to the long list of physical parameters that control the phase transition is beyond the scope of this study. We will discuss GWB from first-order phase transitions in greater detail in the next chapter.

### 3.2.2 Bayesian simultaneous estimation method

We undertake a Bayesian parameter estimation and model selection study. For a single GW detector pair, $ij$, the log-likelihood is obtained by setting $\Omega_{{\rm M},ij} = 0$ in (2.13) [1], resulting in

$$\log p(\hat{C}_{ij}(f)|\boldsymbol{\theta}_{\rm GW}) = -\frac{1}{2}\sum_f \left( \frac{\left[\hat{C}_{ij}(f) - \Omega_{\rm GW}(f, \boldsymbol{\theta}_{\rm GW})\right]^2}{\sigma_{ij}^2(f)} - \log\left[2\pi\sigma_{ij}^2(f)\right] \right), \tag{3.4}$$

where $\Omega_{\rm GW}(f)$ is the model spectrum and $\boldsymbol{\theta}_{\rm GW}$ are the parameters that define the model. We extend this analysis to include three GW detectors by adding log-likelihoods for the individual pairs to construct a multiple-baseline log-likelihood. To compare two models, $\mathcal{M}_1$ and $\mathcal{M}_2$, and make statements about which is more favourable by the data, we utilise Bayes factors.

While the posterior distribution of $\boldsymbol{\theta}_{\rm GW}$ is evaluated in conjunction with Bayes factors, we can also analytically calculate a bound on covariance between model parameters using the information matrix. This has been used for estimating parameter covariance for GWB models in other studies as well [177, 178, 161]. For the case of a Gaussian likelihood with uncorrelated measurements (frequency bins) with an unbiased estimator,

[1] We assume the correlated magnetic noise to be reduced to a level that is below the sensitivity of our detectors.

the information matrix is given by

$$\mathcal{I}_{ij}(\boldsymbol{\theta}) = \sum_f \sigma(f)^{-2} \left( \frac{\partial \Omega_{\rm GW}(f,\boldsymbol{\theta})}{\partial \theta_i} \right) \left( \frac{\partial \Omega_{\rm GW}(f,\boldsymbol{\theta})}{\partial \theta_j} \right). \tag{3.5}$$

The covariance between model parameters is theoretically bounded below by the inverse of the information matrix

$$\mathrm{cov}_{\boldsymbol{\theta}}\left(\theta_i,\theta_j\right) \geq \left[\mathcal{I}^{-1}(\boldsymbol{\theta})\right]_{ij}. \tag{3.6}$$

This bound, known as the Cramér-Rao lower bound, can be exceeded by including, e.g. informative prior information. However, the structure of the information matrix can still offer valuable insight into the degeneracy of certain model parameters with one another and offer an intuitive picture of the parameter estimation problem.

### Injected Signal

We consider two types of injections: one containing a CBC and a cosmic strings background, and another one containing a CBC and a background due to phase transitions, see Table 3.1. The background labelled here as CBC refers to what is left once we subtract the known CBC contribution, i.e. it is the residual astrophysical background. For the second injection, we choose a broken power law with exponents $\alpha_1 = 3$, $\alpha_2 = -4$, and $\Delta = 2$ which best describes $\Omega_{\rm SW}$, the sound wave contribution to $\Omega_{\rm GW}$. In this case our Bayesian search estimates the peak frequency, $f_*$, as well as the amplitude of the smooth broken power law, $\Omega_*$.

The injection strengths we choose vary from one detector network to another. The instrumental noise is included at the level of the design sensitivity curves of the detectors. We consider O4 sensitivity for Advanced LIGO and Advanced Virgo [179], $ET_{\rm Xylophone}$ for the Einstein Telescope [105] and CE Wideband for the Cosmic Explorer [180]. The same prior is used for the recovered amplitudes, $\Omega_{2/3}, \Omega_{\rm CS}, \Omega_*$, all of them log-uniformly

distributed between $10^{-15}$ and $10^{-8}$. All results are presented for 1 year observation time.

| | $\Omega_{\rm GW}(f)$ | GW parameters, $\boldsymbol{\theta}_{\rm GW}$ |
|---|---|---|
| Injection 1 | $\Omega_{\rm CBC}(f) + \Omega_{\rm CS}(f)$ | $(\Omega_{2/3}, \Omega_{\rm CS})$ |
| Injection 2 | $\Omega_{\rm CBC}(f) + \Omega_{\rm BPL}(f)$ | $(\Omega_{2/3}, \Omega_*, f_*)$ |

**Table 3.1:** GW spectra injected, and the parameters estimated in the analysis.

### 3.2.3 Limits on sensitivity to cosmological backgrounds

We present results on source separation for a GWB detection with different sets of GW detector networks.

#### Advanced LIGO and Advanced Virgo

In this section we consider separation of a cosmic strings signal from a CBC signal with the current detector network operating at design sensitivity. We vary injection strengths, with 25 injections log-uniformly distributed between $\Omega_{2/3} \in (10^{-9.4}, 10^{-8.4})$. These values were chosen by using 90% limits on CBC background from [32]. We explore the flat cosmic strings spectrum with 35 injections log-uniformly distributed between $\Omega_{\rm CS} \in (10^{-9.4}, 10^{-7.4})$. The upper limit of the injection range is consistent with constraints placed on a cosmic strings GWB spectrum from data in the first three observational runs [59]. The Bayes factors we find are too low to differentiate between the signals, with values ranging between -0.1 and 0.1, indicating that one cannot distinguish models that include both spectra from models that include only a CBC background. Other methods, which seek to model the contribution from individual CBCs on shorter time-scales, along with an isotropic, flat background propose ways of overcoming these obstacles [144, 145].

#### Third Generation Detectors

Operating at their anticipated O4 sensitivity, the Advanced LIGO, Advanced Virgo network cannot achieve source separation of a detected GWB signal. We therefore pursue studies in future detectors. As was done in

[146], we consider a network of Cosmic Explorer detectors at the Hanford and Livingston locations, and Einstein Telescope at the Virgo site. Figure 1 in [146] estimates that after individual source subtraction, the residual CBC contribution to the GWB is dominated by unresolved binary neutron star mergers at the level of $\sim 10^{-11}$ at 10 Hz. We therefore use a log-uniformly distributed range of $\Omega_{2/3} \in (10^{-11.8}, 10^{-10.8})$ at 25 Hz in the top panel of Figure 3.1, and fix $\Omega_{2/3} = 1 \times 10^{-11}$ for all the injections in the bottom panel. We then use comparable signal strengths for the cosmological contributions, in particular $\Omega_{\rm CS} \in (10^{-12.8}, 10^{-11.8})$ and $\Omega_* \in (10^{-11.6}, 10^{-10.6})$.

The GW selection effect could favour the detection of the best oriented and located sources, especially at larger redshift, disqualifying the assumption of an isotropic GWB in the standard cross-correlation statistic. This leads to a systematic bias in the residual background and hence to a correction for the overlap reduction function [181, 182]. This could provide another way for discriminating between an astrophysical from a cosmological background.

From the top panel of Figure 3.1, we see that we start to confidently separate a flat spectrum from the residual CBC signal for $\Omega_{\rm CS} = 4.5 \times 10^{-13}$. Cosmic strings backgrounds lower than this get lost in the unrecovered CBCs and cannot be singled out. Our sensitivity allows constraints to be placed on the string tension as low as $G\mu \leq 3.0 \times 10^{-17}$ and $G\mu \leq 4.0 \times 10^{-19}$, for the cosmic string loop distribution models [183] and [168], respectively. Similar sensitivity to a cosmic strings spectrum is expected from the space-based LISA detector, whereas the Square Kilometer Array is expected to at most probe $G\mu$ values 3 or 4 orders of magnitude less sensitive [23].

As for a broken power law background due to an early Universe phase transition, we find that the Cosmic Explorer and Einstein Telescope network's sensitivity is highly dependent on the break frequency of the spectrum, see bottom panel of Figure 3.1. The most conservative estimate we

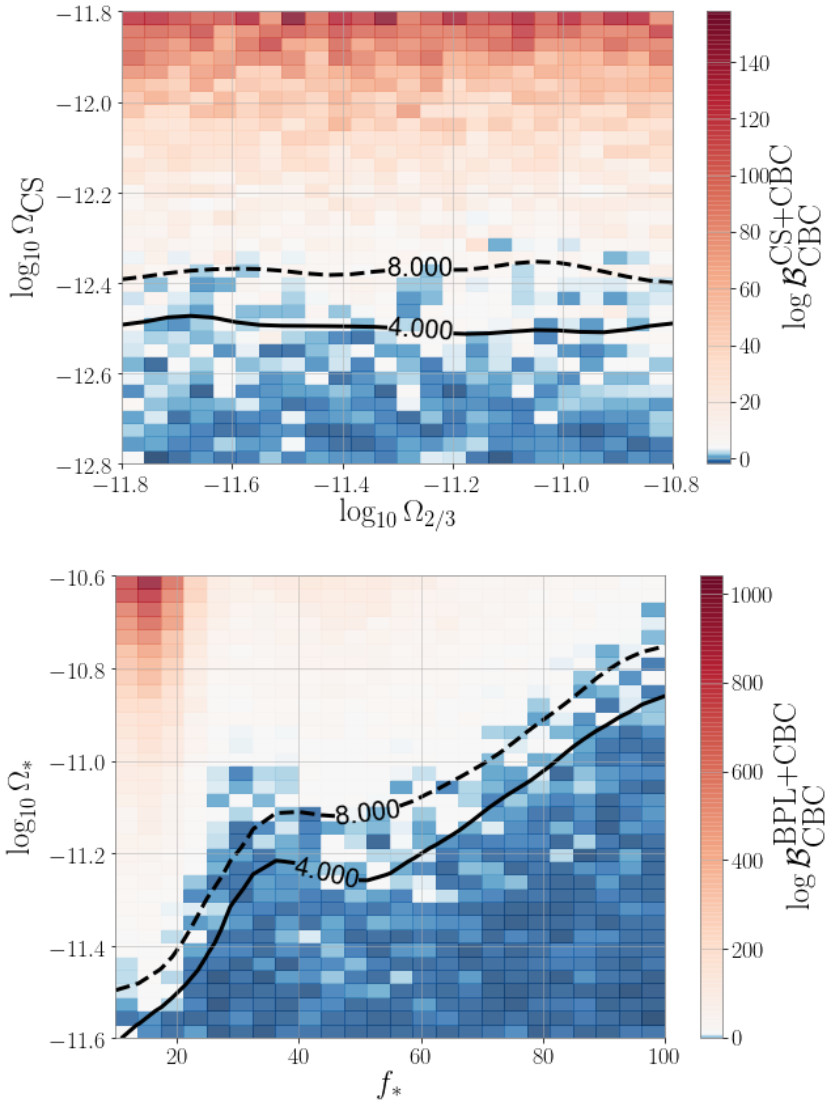


**Figure 3.1:** Variation of log Bayes factor with the injected power laws for cosmic strings (top panel) and a first order phase transition (bottom panel) for third-generation detectors. The residual CBC amplitude for the bottom panel is $\Omega_{2/3} = 1 \times 10^{-11}$ for all of the injections. The contour plots show values of $\log \mathcal{B} = 4$ or $\log \mathcal{B} = 8$, which is roughly when we start to see significant preference for one of the models, since $\log \mathcal{B} = 8$ corresponds to approximately SNR = 4.

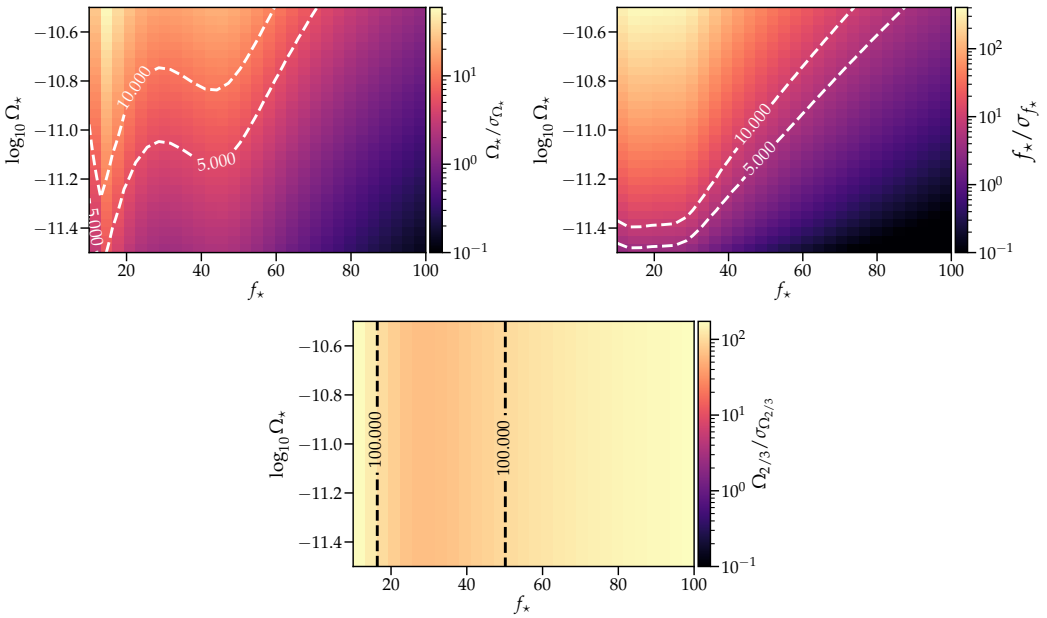


**Figure 3.2:** Precision with which we can measure $f_*$, $\Omega_*$, and $\Omega_{2/3}$ for the broken power law model, where $\sigma$ for each parameter is estimated using the bound in (3.6). The model parameter used for $f_*$ and $\Omega_*$ is given by the value of the $x$- and $y$-axes respectively. The residual CBC injection is $\Omega_{2/3} = 1 \times 10^{-11}$ for all simulations.

find of a detectable BPL signal (i.e. with $\log \mathcal{B} = 8$), is the one associated with $f_* = 100$ Hz, $\Omega_* = 1.8 \times 10^{-11}$. Taking into account injected values for $\alpha_1, \alpha_2, \Delta, f_*$, we estimate a signal of amplitude $\Omega_{\rm BPL} = 2.2 \times 10^{-13}$ at 25 Hz.

We also look at the precision with which we can measure $\Omega_*, f_*$ and $\Omega_{2/3}$ using the covariance bound in (3.6). We use $f_*/\sigma_{f_*}$ as a proxy for the precision of our $f_*$ measurement, with $\sigma_{f_*} = [\mathrm{cov}(f_*, f_*)]^{1/2}$ estimated from (3.6) (and analogous expressions for $\Omega_*$ and $\Omega_{2/3}$). In Figure 3.2, we show the theoretical bound on this precision for $\Omega_*, f_*, \Omega_{2/3}$ as a function of the strength and shape of the broken power law background. In all three panels, the horizontal axis is $f_*$ and the vertical axis is $\log_{10}\Omega_*$. The colour is the precision statistic discussed above. For all three panels, we have fixed $\Omega_{2/3} = 1 \times 10^{-11}$. The broken power law model parameters are best estimated when $f_* \approx 20$ Hz and are improved as $\Omega_*$ increases. Interestingly, the theoretical precision with which we measure $\Omega_{2/3}$ is independent of $\Omega_*$, but is dependent upon the shape, which is governed by

$f_*$. This is because elements of the information matrix in (3.5) that involve derivatives of $\Omega_*$ and $\Omega_{2/3}$ are independent of both $\Omega_*$ and $\Omega_{2/3}$ because these variables appear linearly in separate terms of the combined model $\Omega_{\rm BPL}(f) + \Omega_{\rm CBC}(f)$. This means that the variance of $\Omega_*$ and $\Omega_{2/3}$, and the covariance between them are independent of these amplitudes. These variables are still correlated with each other – merely the covariance between them is independent of the values themselves.

### Discussion

We have looked at current, and future, terrestrial GW detectors to see if we can successfully perform source separation of a detected GWB signal. This is an important task, since it allows us to relate a detection to physical theories underlying it and perhaps give us a hint of beyond Standard Model physics. Although Advanced LIGO and Advanced Virgo sensitivity is not sufficient to separate sources, we find promising results for 3G detectors such as the Einstein Telescope and Cosmic Explorer [184, 185].

This analysis can be additionally extended by considering other cosmological sources of a GWB. One can for instance consider the minimal Pre-Big-Bang model for which $\Omega_{\rm GW}(f)$ today scales as $f^3$ at the low frequency end of the spectrum, whereas in the high frequency range its behaviour depends on a dimensionless free parameter of the model [186]. Furthermore, one can consider the full analytical model for a CBC background (1.43), thereby expanding the studied frequency range.

Our study concerns the frequency range for ground based detectors. The LISA observational band offers an exciting possibility to observe GWs from phase transitions [170]. Much work has been done to develop methods to characterise an arbitrary GWB spectrum [187], as well as techniques to distinguish a cosmologically produced GWB from Galactic binaries [148], a binary black hole produced background [144], and instrumental noise [188, 148].

In the following section we investigate the impact of Galactic binaries

on the detection of CBCs with the LISA detector. The noise produced by the inspiral of millions of white dwarf binaries in the Milky Way may pose a threat to one of the main goals of LISA mission: the detection of massive black hole binary mergers. We present a novel study for reconstruction of merger waveforms in the presence of Galactic confusion noise using *dictionary learning*.

## 3.3 LISA detector

The space-based GW interferometer LISA will be sensitive to GWs in the millihertz range. Other GW sources will be detectable at these frequencies: inspiralling Galactic white dwarf binaries, inspiralling binaries with extreme mass-ratio, or colliding true vacuum bubbles formed at the electroweak phase transition [189, 190, 191]. The tens of millions of double white dwarf binaries in the Galaxy could have an impact on detectability of massive black hole binaries coalescing in the LISA frequency band [192]. LISA will observe continuous GWs from inspiraling white dwarfs, and although it may be sensitive to individual sources, most will remain unresolved and these are referred to as Galactic confusion noise [193, 194, 195]. It has been shown that modulation of the Galactic noise could lead to a reduction in SNR of other GW sources by a factor of 4 [196]. A LISA Data Challenge [2] is underway to study the impact of overlapping Galactic sources on the sensitivity to massive black hole mergers [197], and attempts to separate the foreground from other GW sources have been conducted [148, 198, 199, 200].

In this section we apply a dictionary learning method to separate CBCs from the Galactic confusion noise in the LISA frequency band. Such a method has been successfully applied in GW data analysis to classify and denoise Advanced LIGO's "blip" noise transients [201] and effectively improve the performance of the detector. More precisely, we assess the suit-

[2] `https://lisa-ldc.lal.in2p3.fr`.

ability of the dictionary learning method for the classification and reconstruction of massive binary black hole merger signals in the presence of Galactic noise.

Previous studies focused on the inspiral of loud CBC sources and demonstrated that SNR accumulated over time is sufficiently large to overcome the noise from Galactic binaries [202]. In other literature, detectability of CBCs was investigated for equal-mass and non-spinning binaries [203, 204, 46], confirming the largest SNR is expected from binaries with combined mass $\sim (10^5 - 10^6)M_\odot$. In particular, Figure 3 in [46] presents two mass ranges with low SNR that could be affected by Galactic confusion noise, namely $(10^2 - 10^4)M_\odot$ and $(10^7 - 10^9)M_\odot$.

Here we consider all of the mass ranges, along with varying spins and redshifts, and we study their waveforms around coalescence time. The dictionary learning method reconstructs CBC signals with ease in the trivial case where the CBCs are above the Galactic noise, i.e. for the $(10^5 - 10^6)M_\odot$ mass range. We find the dictionary learning method to be too computationally expensive for very heavy mergers in the range $(10^7 - 10^9)M_\odot$. However, our method succeeds in separating low-SNR binaries in the range $(10^2 - 10^4)M_\odot$ from the Galactic noise. Hence, the dictionary learning method could significantly assist the detection of this prime LISA source.

### 3.3.1 Dictionary learning

Any CBC signal in the LISA band will be overlaid with continuous waves from the inspiral of double white dwarfs. Therefore, we can model the detector strain, $y(t)$, as a superposition of the CBC signal $u(t)$ and the Galactic confusion noise $n(t)$:

$$y(t) = u(t) + n(t). \tag{3.7}$$

We express the loss function as

$$J(u) = ||y - u||^2_{L_2} + \lambda \mathcal{R}(u), \tag{3.8}$$

and search for a solution $u_\lambda$ that minimises $J(u)$, where $||\cdot||_{L_2}$ is the $L_2$ norm. The first term in the loss function, often referred to as the *error term*, measures how well the solution fits the data, while the regularisation term $\mathcal{R}(u)$ captures any imposed constraints. The regularisation parameter $\lambda$ tunes the weight of the regularisation term relative to the error term; it is a hyperparameter of the optimisation process.

The goal of the dictionary learning method [205] is to find the sparse vector $\alpha$ that reconstructs the true signal $u$ as a linear combination of columns of a dictionary $\mathbf{D}$,

$$u \sim \mathbf{D}\alpha, \tag{3.9}$$

with $\mathbf{D}$ a matrix of prototype signals (atoms) trained to reconstruct a given set of signals, which for our study is CBCs. Sparsity of the vector $\alpha$ is imposed via the regularisation term $\mathcal{R}(u) = ||\alpha||_{L_1}$, using the $L_1$ norm. Therefore, the constrained variational problem in (3.8) reads

$$\alpha_\lambda = \underset{\alpha}{\operatorname{argmin}} \left\{ ||y - \mathbf{D}\alpha||^2_{L_2} + \lambda ||\alpha||_{L_1} \right\}, \tag{3.10}$$

and is called "basis pursuit" [206] or "least absolute shrinkage and selection operator" (LASSO) [207].

The basis pursuit can be improved significantly if, instead of using a predefined dictionary, we apply a learning process where the dictionary is trained to fit a given set of signals. The procedure starts by selecting templates of CBC waveforms and whitening the data. The waveforms are aligned at the strain maximum and divided into patches, with the number of patches ($p$) much larger than the length of each patch ($d$). To train the dictionary we solve (3.10) considering both the sparse vector $\alpha$ and the

dictionary **D** as variables:

$$\alpha_\lambda, \mathbf{D}_\lambda = \underset{\alpha,\mathbf{D}}{\operatorname{argmin}} \left\{ \frac{1}{d} \sum_{i=1}^{p} ||\mathbf{D}\alpha_i - x_i||_{L_2}^2 + \lambda ||\alpha_i||_{L_1} \right\}, \tag{3.11}$$

with $x_i$ denoting the $i$-th training patch. This problem is not jointly convex unless the variables are considered separately as outlined in [208].

In our study we create training signals that contain CBC waveforms only and no noise. The dictionary created is then tested on signals that include new CBC waveforms *combined* with Galactic noise. We describe briefly the massive black hole and white dwarf binary waveforms used in our datasets below.

### 3.3.2 Training and testing datasets

We utilise the `IMRPhenomD` approximant [209] provided by the LISA Data Challenge to model waveforms of binary black holes detectable by LISA, capturing inspiral, merger and ringdown of the signal. Binaries with total mass $(10^5 - 10^6)M_\odot$ are expected to have SNR $\geq 150$, making separation from Galactic noise a trivial problem. CBCs in the mass range $(10^7 - 10^9)M_\odot$ have small frequencies, making it difficult for the dictionary learning to reconstruct their sinusoidal behavior. We thus, study reconstruction capabilities of binary black holes with total mass ranging from $(10^2 - 10^4)M_\odot$. The dictionary is trained on a set of 100 noiseless CBC signals, simulated over one day with cadence $\Delta t = 2$ s [3]. Table 3.2 lists the relevant parameters of the `IMRPhenomD` waveform and the corresponding ranges of values we choose for the CBC sources. We simulate the data by drawing randomly from the probability distribution of the parameters. The redshift for all sources is fixed to $z = 2$, since changing the redshift leads to a simple rescaling of the amplitude that has no impact on our whitened data in the training set. Note that the same does not hold for the testing

[3] The cadence was chosen low enough to have a high sampling rate that avoids aliasing, but high enough to allow for reasonable computational time.

| Parameter | Distribution |
|---|---|
| Total mass ($M_\odot$) | logUniform[$10^2$,$10^4$] |
| Mass ratio | Uniform[1,10] |
| Primary spin | Uniform[-1,1] |
| Secondary spin | Uniform[-1,1] |
| Redshift | 2 |
| Luminosity Distance (Mpc) | 15975 |

**Table 3.2:** Parameters used to construct training CBC signals with the `IMRPhenomD` waveform approximant. We choose values randomly from the uniform distributions indicated in the right column, keeping redshift and luminosity distance fixed.

data, since changing redshift would change the relative amplitude of the CBCs to the Galactic noise.

Consider two white dwarfs of mass $M_1$ and $M_2$ on a quasi-circular orbit with inclination $\iota$ at a distance $R$. They emit GWs with amplitude [210]

$$A_+(\mathcal{M}_c, R, f_{\rm GW}, \iota) = \frac{2G^{5/3}\mathcal{M}_c^{5/3}}{c^4 R}(\pi f_{\rm GW})^{2/3}(1+\cos^2\iota), \quad (3.12)$$

$$A_\times(\mathcal{M}_c, R, f_{\rm GW}, \iota) = -\frac{4G^{5/3}\mathcal{M}_c^{5/3}}{c^4 R}(\pi f_{\rm GW})^{2/3}\cos\iota, \quad (3.13)$$

for the $+$ and $\times$ polarisations, respectively. The resulting plane wave has a slight frequency shift over time, and for each polarisation reads

$$h_+(t) = A_+\cos\left(2\pi f_{\rm GW}t + \dot{f}_{\rm GW}t^2 + \phi_0\right), \quad (3.14)$$

$$h_\times(t) = A_\times\sin\left(2\pi f_{\rm GW}t + \dot{f}_{\rm GW}t^2 + \phi_0\right), \quad (3.15)$$

where $\phi_0$ stands for the initial phase and $\dot{f}_{\rm GW}$ for the GW frequency time derivative

$$\dot{f}_{\rm GW} = \frac{96}{5}\left(\frac{G\mathcal{M}_c}{c^3}\right)^{5/3}\pi^{8/3}f_{\rm GW}^{11/3}. \quad (3.16)$$

To simulate the LISA Galactic confusion noise we sum over GW signals

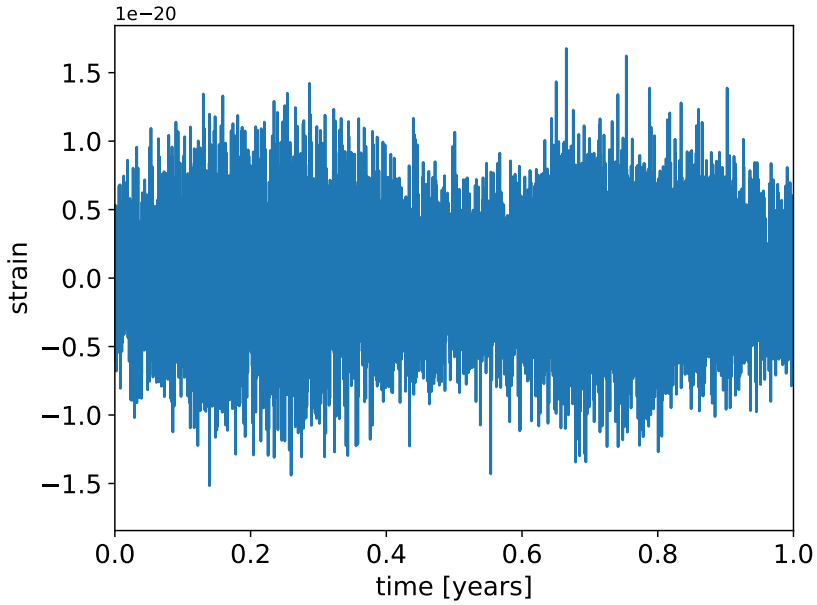


**Figure 3.3:** Strain due to the inspiral of binary white dwarfs in the Galaxy as measured by LISA over a 1 year orbit. The modulation from LISA's orbit creates peaks at $1/4$ and $3/4$ of the year, when the normal of LISA's constellation plane is pointed at or away from the Galactic center.

from the white dwarf binaries in our galaxy:

$$n(t) = \sum_{i=1}^{N} \sum_{A=+,\times} \frac{\sqrt{3}}{2} F_A h_{A,i}(t), \tag{3.17}$$

where $F_{+,\times}$ stands for the detector response function [211]. The masses, location, and orbital frequency of nearly 5 million white dwarf binaries in the Milky Way are taken from [212].

We present the resulting Galactic confusion noise in Figure 3.3. The orbit of LISA around the Sun introduces a modulation in the Galactic noise (3.17), with maximum value when the normal of the LISA constellation plane is closest to the binary location, as expected since white dwarfs are supposed to cluster near the Galactic center. In our analysis, we will first consider the Galactic noise at a time of the year when it is maximum. We subsequently consider testing signals that combine Galactic noise and a CBC signal.

### 3.3.3 Results

The hyperparameters of dictionary learning, namely the regularisation parameter $\lambda$, the atom (and patch) length $d$ and the number of patches $p$, have an impact on the quality of the signal reconstruction. We fix $p = 3d/2$ to ensure a complete dictionary (one where the number of atoms is greater than atom length) and choose $d \in [2^2, 2^7]$. Independently of our choice of $d$, we find the optimal regularisation parameter to lie in the range $\lambda_{\rm opt} \in [10^{-3}, 10^{-2}]$ (see Appendix C for a detailed study). For the remainder of the analysis we fix $\lambda = 10^{-3}$, as little quantitative differences to our results are found with the choice of $\lambda = 10^{-2}$.

To find the best dictionary size, for each reconstruction we calculate the so-called overlap between the injected CBC waveform $h_i(f)$ and the recovered waveform $h_r(f)$,

$$\mathcal{O} = \frac{(h_i|h_r)}{\sqrt{(h_i|h_i)(h_r|h_r)}}, \tag{3.18}$$

with

$$(x|y) = 2\int_0^\infty \frac{x(f)y^*(f) + x^*(f)y(f)}{S_n(f)}\mathrm{d}f \tag{3.19}$$

where $S_n(f)$ is the one-sided noise PSD. The overlap $\mathcal{O}$ can range between -1 and 1, with 1 reflecting perfectly matched signals, and -1 implying perfect anti-correlation. The overlap is widely used in the GW community for identifying transient CBC signals through matched filtering using waveform approximants template banks [213, 214, 215, 216]. We track this metric across the testing dataset and choose the optimal atom length $d_{\rm opt}$ that maximises it, namely $d_{\rm opt} = 4$ (see Appendix C).

To have a metric for error, we also calculate the overlap between the recovered CBC and the present Galactic noise $n$, which we denote as $\mathcal{O}(h_r, n)$. In addition, we define the overlap difference $\Delta\mathcal{O} = \mathcal{O}(h_r, h_i) - \mathcal{O}(h_r, n)$ to evaluate how much more the reconstructed signal has in common with the injected signal than with Galactic noise.

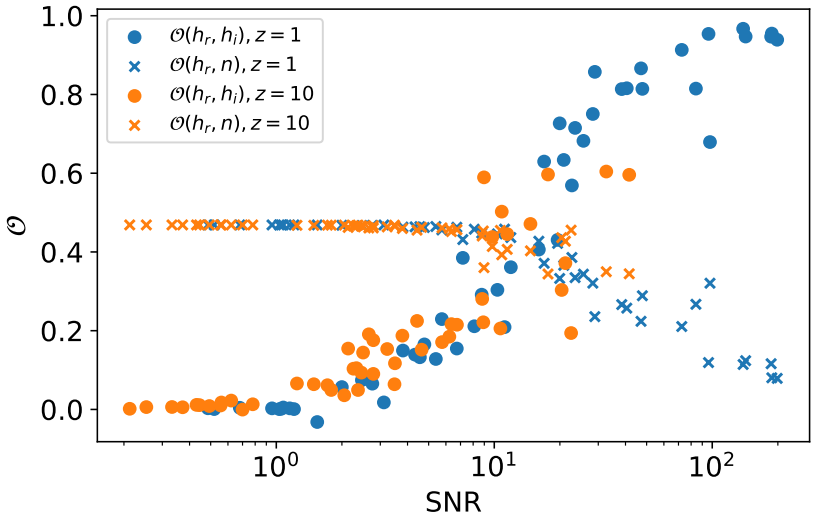


**Figure 3.4:** Overlap between reconstructed signal and injected CBC waveform as a function of SNR for redshift $z = 1, 10$ and fixed atom length $d = 4$, overlayed with recovery overlap between reconstructed signal and noise for the same data.

We now study how well the CBCs can be reconstructed using a dictionary with $d = 4$ and $\lambda = 10^{-3}$. Specifically, we create two sets of 50 signals with CBCs at redshift $z = 1$ and $z = 10$, and investigate how their reconstruction varies with SNR. From Figure 3.4 we see that the overlap between reconstructed signal and injected CBC waveform increases with SNR, while the overlap between reconstructed signal and noise decreases with SNR, as expected. Interestingly, the noise overlap is approximately constant until SNR $\approx 10$, where it starts to decrease, while the reconstruction starts to improve significantly, with $\mathcal{O}(h_r, h_i) = 1$ for some of the $z = 1$ waveforms. Note that the $z = 1$ and $z = 10$ data sets do not differ greatly in overlap, and when they do it is between sources of very different mass. Therefore, we turn to study how overlap changes as a function of both redshift and total mass of the CBC.

We begin by fixing mass ratio to 1 and both black holes' spins to 1, for simplicity, and we create a dataset of 400 CBC events with uniform spacing $1 \leq z \leq 20$ and log-uniform spacing for total mass of the binary $10^2 M_\odot \leq M_{\text{tot}} \leq 10^4 M_\odot$. Each event is overlayed with Galactic noise at a yearly

modulation maximum and minimum (see Figure 3.3), and reconstructed. Resulting contours of signal overlap $\mathcal{O}(h_r,h_i) = 0.5$, 0.9, overlap difference $\Delta\mathcal{O} = 0$, 0.75 and SNR $= 5$, 15, 25 are plotted in Figure 3.5. Although generally speaking increasing SNR improves reconstruction capabilities, reconstruction success is more dependent on the CBC's total mass and redshift.

In strong (maximum) Galactic noise scenarios, binaries with total mass greater than 1330 $M_\odot$ can be reconstructed with $\mathcal{O}(h_r,h_i) > 0.5$ for the redshift range. Reconstructions with $\mathcal{O}(h_r,h_i) > 0.5$ in weak (minimum) Galactic noise scenarios can be achieved for binaries with total mass greater than 355 $M_\odot$. Extremely good signal reconstruction, with overlap greater than 0.9, can be achieved for sources with total mass greater than 1350 $M_\odot$ up to redshifts of 3 in the pessimistic case, and up to redshifts as large as 7.5 in the optimistic case. From Figure 3.5 one can also track how the overlap difference $\Delta\mathcal{O}$ varies with binary mass and redshift. All sources that lie in the parameter space at the right of the $\Delta\mathcal{O} = 0$ contour lead to reconstructed signals that are more similar to the true, injected signal than the Galactic noise. In the pessimistic case this is true for total masses greater than 1000 $M_\odot$, and in the optimistic case for total masses as small as 315 $M_\odot$.

## Discussion

Gravitational-wave signals from the inspiral of white dwarf binaries in the Galaxy must be considered when studying detection of CBC signals with LISA [192]. In this work we have modelled this Galactic confusion noise and studied its impact on the reconstruction of massive black hole binary merger signals using an approach based on learned dictionaries. We have found dictionary learning to be a promising technique for detection of such signals in the presence of Galactic noise. Reconstructing the CBC waveforms with dictionary learning can be optimised with atom length $d = 4$ and regularisation parameter $\lambda \in [10^{-3},10^{-2}]$.

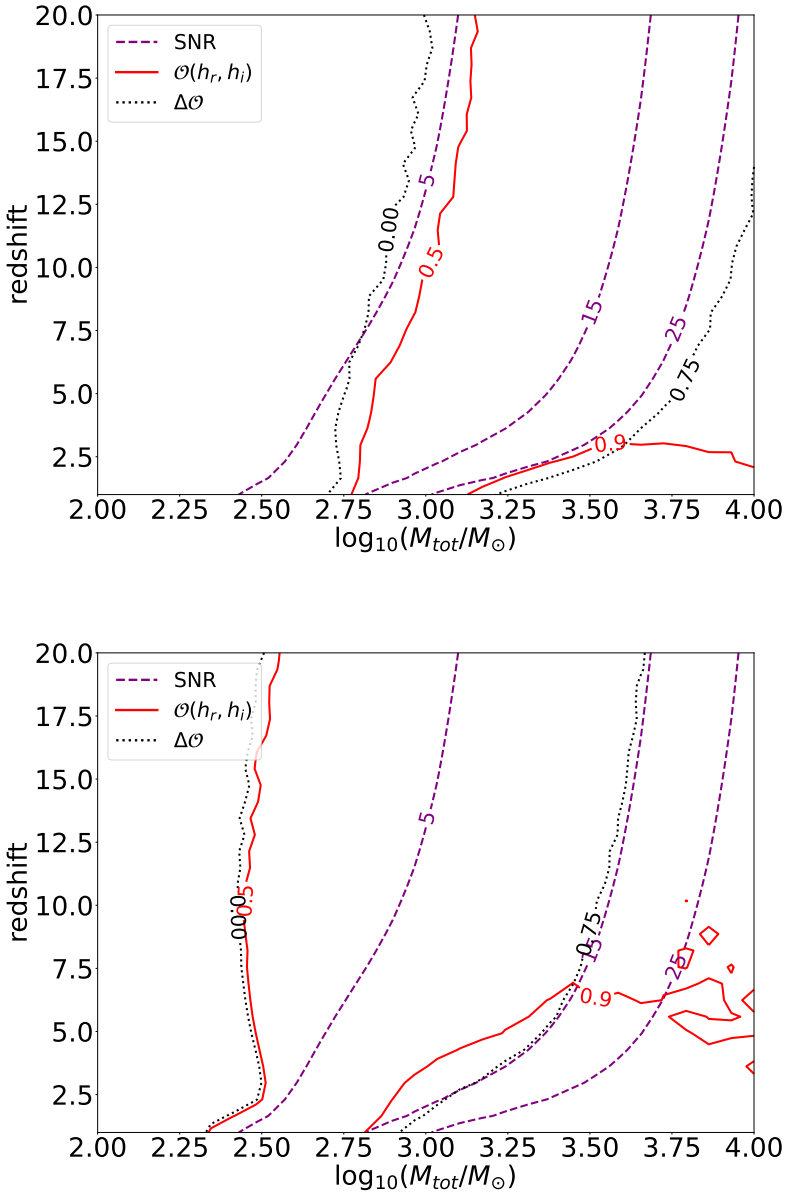


**Figure 3.5:** Overlap between reconstructed signal and injected CBC waveform as a function of total mass and redshift in strong (top) and weak (bottom) Galactic noise scenarios, fixing binary mass ratio to 1 and black hole spins to 1.

The threshold overlap between the injected and the reconstructed signal, typically chosen to be $\mathcal{O}(h_r,h_i) = 0.5$, can be achieved for binaries with mass $M_{\rm tot} > 1330\,M_\odot$ in strong Galactic noise, and with mass $M_{\rm tot} > 355\,M_\odot$ in weak Galactic noise at all redshifts. For CBCs with total mass $M_{\rm tot} > 3150\,M_\odot$, the reconstructed waveform and the true waveform overlap greatly with $\mathcal{O}(h_r,h_i) > 0.9$ up to redshift $z = 3$ and $z = 7.5$ in the case of strong and weak Galactic noise, respectively. For all tested signals, we calculate the overlap between the reconstructed CBC waveform and the Galactic noise, and its difference to the overlap between the reconstructed and injected CBC waveform. We conclude that the reconstructed signal overlaps more with the true CBC signal than with the noise for binaries with $M_{\rm tot} > 1000\,M_\odot$.

## 3.4 Afterword

In this chapter we have demonstrated the success of Bayesian and machine learning tools in source separation at ground-based and space-based detectors respectively. As we await the first detection of a GWB, the great technical challenge of separating the astrophysical and cosmological contributions must be addressed. This will not be plausible with the sensitivity of current 2G detectors, but one needs to utilise the future 3G detector network. For LISA, the continuous GWs emitted by the inspiral of Galactic binaries will create a signal that could limit detection of other GW sources. The dictionary learning method we presented here proved successful at recovering a CBC signal in the presence of white-dwarf noise.

We focus on implications for physical models once we have made a detection of the background in the next chapter. What can a GWB detection teach us about the physical theories governing the Universe?

# Chapter 4

# Gravitational-wave background implications

## 4.1 Foreword

Experimental data is key in determining the laws of physics that govern nature, and in particular experimental GW data has opened up a novel way of studying the near and far Universe. The process that starts with gathering GWB data and finishes with implications on physical theories is complex and intricate. The first step in the pipeline is collecting data and constructing useful and intuitive statistics. In the case of a detection, exhaustive checks are undertaken to ensure the nature of the signal, as was discussed in Chapter 2. The next necessary step is identification of sources in the detected signal, methods for which were the focus of Chapter 3. The final, and crucial, step is translating data constraints into different models, either in the form of constraining the models' parameters or simply ruling them out. Model builders are patiently awaiting a detection, but a detection is only meaningful if we can transform it into meaningful statements about physical models.

Here we explore the parameter space of primordial-star remnants, phase transitions, and search for signs of parity violation in GWB data. We first inspect astrophysical implications, building on the properties of

the CBC background described in 1.3.2. In the event of a strong first-order phase transition (FOPT) that happened at energy scales $\left(10^5 - 10^{10}\right)$ GeV, stochastic GWs produced could form a background detectable by terrestrial detectors. We present constraints on FOPT models with O3 data, and anticipate detectability with 3G detectors. To demonstrate the translation from GW data to constraints on particle physics models, we present our study on GWB from supercooled FOPTs. Finally, we showcase tools for estimating parity violation in the case of a polarised background and their limitations.

## 4.2 Primordial-star remnants

The most recent LVK observing run presented us with dozens of new merger events and has expanded the stellar graveyard. Despite the increase in the number of detections, we are yet to observe with confidence an event that would suggest that the progenitor compact objects are remnants of the oldest stars in the Universe [65] - the theoretically-postulated population III (pop III) stars [1]. Pop III stars are thought to have formed at high redshifts at a time when the Universe was mostly made up of hydrogen and helium, and as such have low metallicity compared to the more recently formed, population I/II (pop I/II) stars [218, 219, 220]. These old stars have hitherto evaded sky surveys [221, 222, 223], and their detection remains an objective for upcoming experiments, such as the James Webb Space Telescope [224].

Pop III stars may help understand the early epochs of the Universe and solve some puzzles in black hole formation [225, 226, 227]. Numerical simulations show that these primordial stars could have led to the formation of super-massive black holes at high redshifts [228, 229, 230]. Mergers of such heavy remnants would appear in the millihertz frequency range explored by space-based detectors such as LISA [231]. The scope of our

[1] GW150914 could be a potential candidate [217].

study, however, is detection prospects of terrestrial detector networks; we focus on models that predict a pop III signal in the LVK frequency range. The pop III formation channels and evolution mechanisms [232, 233] lead to mass and redshift distributions different to that of pop I/II [234]. Consequently, the contribution to the GWB from a superposition of unresolved pop III-seeded CBCs may deviate significantly from that of unresolved pop I/II sources [235, 236].

In this study, for the first time, we consider the possibility of separating pop I/II and pop III GWB contributions. A previous study [237] suggests that the total CBC background is dominated by pop I/II. However, pop III can be uncovered using subtraction techniques and studying the residual backgrounds [238, 132, 239, 143, 146]. As the sensitivity of detectors increases and GW interferometers *see* more individual CBC events, a pop III residual background emerges as the dominant signal over pop I/II residual background [237].

We first study how to detect the GWB from pop III stars, and in the case of a successful detection, we explore subsequent implications about masses and redshifts of the population. We use the widely accepted StarTrack (ST) simulation data [240] and apply our detection methods, ultimately showing consistency of our implications analysis with the underlying population. The ST data is the most recent extensive catalogue of merging binaries from pop I, II, III stars leading to a GWB in the LVK frequency range [237].

### 4.2.1 GWB from population III remnants

The GWB is defined as the superposition of GWs from all unresolved sources. We concentrate on the CBC (from pop I/II and III stars) contribution to the GWB, and express it as $\Omega_{\rm GW}(f)$ defined in (1.41). For binary neutron stars and neutron star-black hole mergers, we only consider the inspiral phase and assume that the GW emission stops at the last stable orbit. For binary black holes, we consider the three regimes of the coales-

cence (inspiral, merger, ringdown phase) given by the corresponding phenomenological waveforms [63] for circular orbits [241], as defined in (1.43). Once the spectrum of $\Omega_{\rm GW}$ is calculated, we estimate the corresponding SNR for a network of $N$ detectors [38]:

$$\mathrm{SNR} = \frac{3H_0^2}{10\pi^2}\sqrt{2T}\left[\int_0^\infty \mathrm{d}f \sum_{i=1}^{N}\sum_{j>i}\frac{\Gamma_{ij}^2(f)\Omega_{\rm GW}^2(f)}{f^6 P_i(f)P_j(f)}\right]^{1/2}, \tag{4.1}$$

with $T$ the observational time, $P_i$ and $P_j$ the one-sided noise PSDs of detectors $i$ and $j$, $\Gamma_{ij}$ the previously-defined normalised overlap reduction function characterising the distance and the relative orientation between $i$ and $j$ for sources isotropically distributed in the sky.

We consider the StarTrack population synthesis code which models stellar evolution [2], and in particular the FS1 model which concerns the evolution of pop III stars [233], discussed in detail in [243]. It assumes that pop III stars were formed in large gas clouds with a star formation rate that peaks at redshift $z \sim 12$, while the star formation rate for pop I/II stars peaks at $z \sim 2$ (see Fig. 4 in [233]). The corresponding background and its detectability have been calculated [237] using a catalogue of sources rather than the analytical expression (1.41). The calculation of the residual GWB from the catalogue of sources is described in Appendix D.1.

If pop III exists, its signal will be superposed with a pop I/II signal. For a dominant pop I/II signal, the pop III signal will remain hidden underneath it, and one can only place upper limits on the amplitude of the pop III contribution to $\Omega_{\rm GW}(f)$. If, however, a pop III signal is the dominant one, then we could detect deviations from the characteristic CBC 2/3 power law, and even get insight on the mass and redshift distribution of pop III stars.

[2]The StarTrack model considers the low-metallicity approximation of Pop II stars for the stellar evolution of Pop III. Recently [242] explored the impact of large uncertainties in parameters governing the stellar modelling. It was found that these uncertainties in numerous parameters overshadow any effects a low-metallicity approximation may have on the final population.

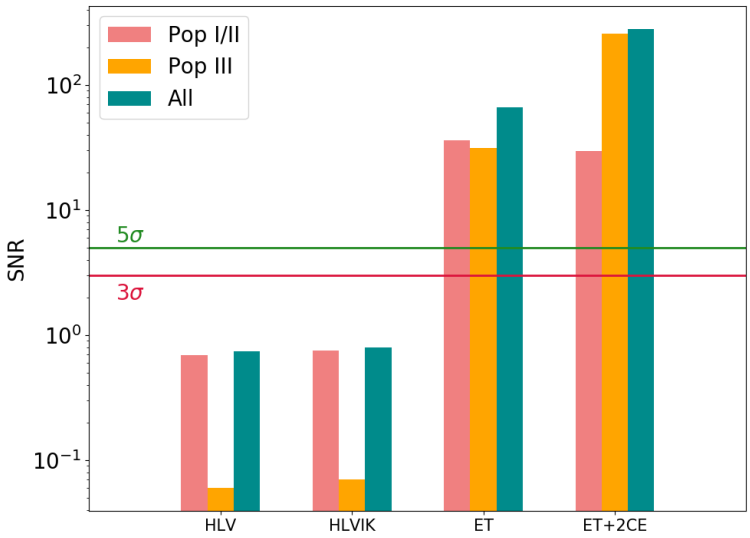


**Figure 4.1:** SNR obtained for *residual* CBC backgrounds considering design sensitivities of Hanford (H), Livingston (L), Virgo (V), LIGO-India (I), KAGRA (K), Einstein Telescope (ET) and Cosmic Explorer (CE). The pink bars correspond to SNR from pop I/II sources, the yellow from pop III sources, and the green ones represent SNR from the combined residual background (pop I/II and pop III sources).

Estimates of CBC contributions to $\Omega_{\rm GW}(f)$ from ST simulations suggest that pop III signal is lost in the pop I/II foreground. For 2G detector networks – even by including LIGO, Virgo, LIGO-India, and KAGRA – pop III is practically invisible and its contribution to the global SNR is negligible [237]. Third-generation terrestrial detectors, Einstein Telescope and Cosmic Explorer, may reveal a pop III GWB. These future detectors will have unprecedented sensitivity and they will be able to discover a great number of individual CBCs, thereby reducing the GWB originating from unresolved CBCs. Being more difficult to resolve, binaries from pop III persist, resulting in a large contribution to the residual CBC background in 3G detectors, see Figure 4.1. Detectors such as ET and CE may reveal a pop III background after the subtraction of individually resolved merger events, since subtraction methods are less efficient to detect the high-redshift and low-frequency pop III CBCs.

We compare in Figure 4.2 the total and residual background for two 3G networks: a pessimistic scenario with only ET (top) and an optimistic scenario ET+2CE (bottom), with ET at the current Virgo site, and the two CEs at LIGO Hanford and Livingston sites. It is worth noting that these detector sites are chosen out of convenience and the discussion for where 3G detectors would be constructed is ongoing. Ultimately, our results are qualitatively the same regardless of final detector location. The pop III contribution in ET has a very small impact on the combined residual background from pop I/II and III, but in ET+2CE the pop III residual background clearly dominates for frequencies below $\sim 20$ Hz. Figure 4.2 shows a change in the shape of the background. The peak frequency of pop III spectrum changes slightly while the slope characterising the end of emission decreases dramatically when we remove individually detected sources.

To demonstrate the impact of subtraction of resolved CBCs on the population, we show in Figure 4.3 the probability density of the total redshifted mass, $M^z_{\rm tot} = (1+z)(m_1+m_2)$, and the merger rate as a function of redshift, $R(z)$, for the whole catalogue and the residual one for ET+2CE network.

The sources remaining in the residual catalogue are the ones with the highest redshift, affecting the total corrected mass distribution which is in turn responsible for the changes in the GWB spectrum. We note that for masses and redshifts lower than the ones provided by the StarTrack model, the resulting GWB spectrum peak shifts to higher frequencies and the 2/3 power law dominates in the LVK frequency range.

We estimate the ET+2CE residual pop III parameters by searching for the background using an optimal filter and performing a Bayesian analysis. In our model, we include only isolated binaries in pop I/II, i.e. progenitors coupled at formation that orbit one another for a billion years before merging. However, taking into account dynamical binaries brought together in dense star clusters instead, will not affect our results. Indeed, even if

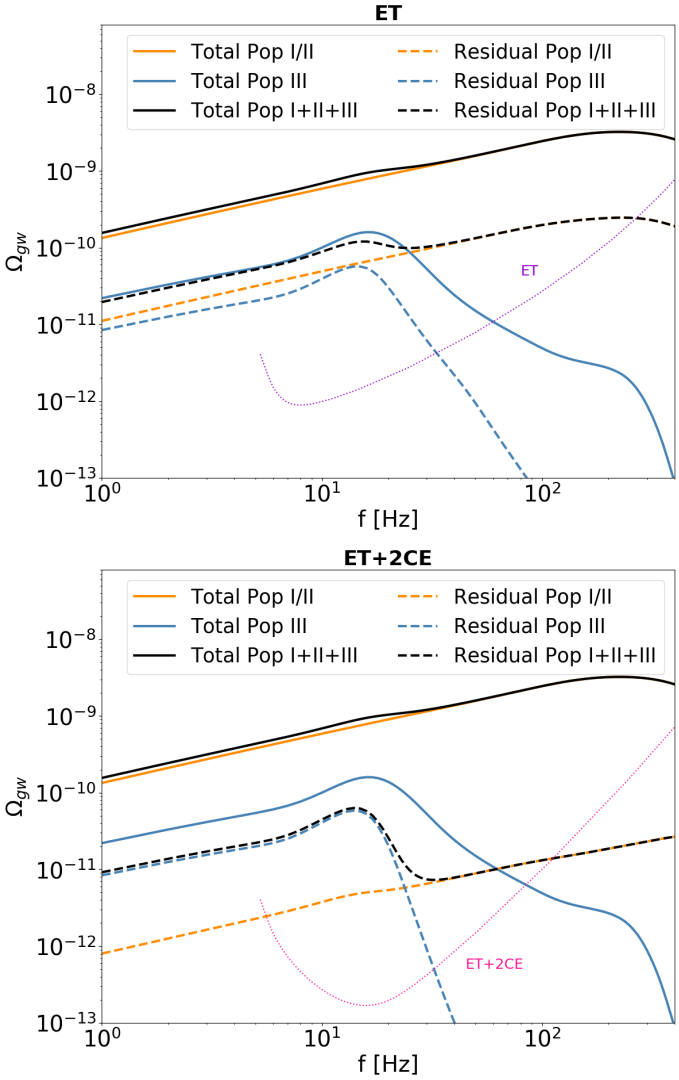


**Figure 4.2:** Total and residual GWB of ET (top) and ET+2CE (bottom) detector networks. The pop I/II and pop III contributions are shown in green and red, respectively, with the combined residual signal shown in black.

the masses can be larger, the redshift of dynamical binaries is similar to that of isolated binaries. Consequently, dynamical binary sources can be subtracted as efficiently as the isolated ones and the shape of the energy density spectrum also follows the power law $f^{2/3}$ below 100 Hz. This is discussed in [244] for 2G detectors (the results for 3G detectors will be presented in an upcoming study).

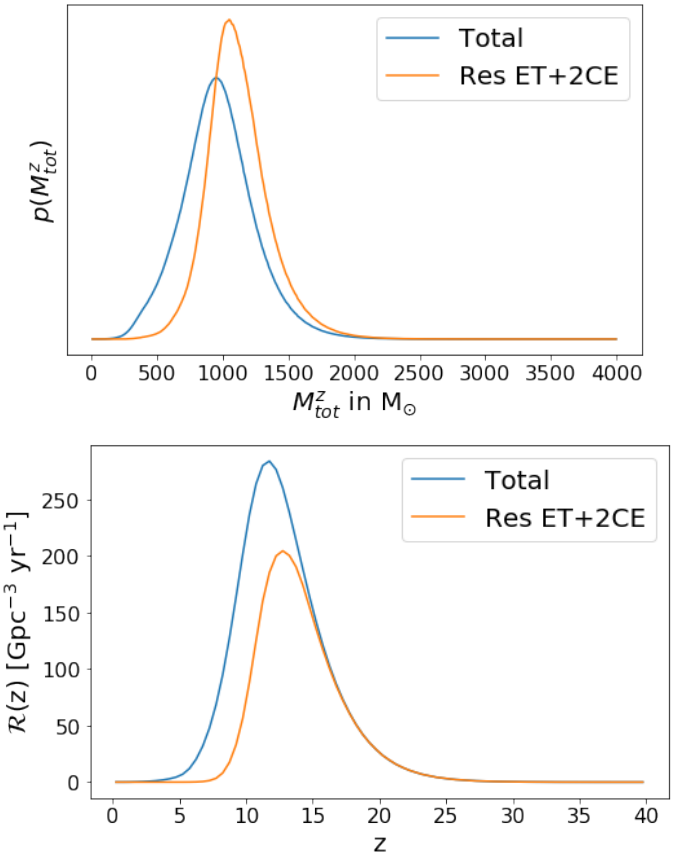


**Figure 4.3:** Comparison between the total (blue) and ET+2CE residual (orange) catalogue for redshifted total mass distributions (top) and merger rates (bottom).

### 4.2.2 Modelling of the background

The stochastic pipeline takes strain data $\tilde{s}_{i,j}$ from detectors, $i, j$, and constructs cross-correlation statistics using optimal filters as described in 1.3.1. Let us construct a Gaussian log-likelihood such as (3.4), which allows us to estimate the model parameters by finding the best-fit to the cross-correlation data and minimising the likelihood function. To compare models and find which ones fit data better, we perform model selection with Bayes factors.

We model a pop I/II CBC signal as a power law defined in (1.27), setting $f_{\rm ref}$ = 25 Hz and spectral index 2/3, since CBCs detected thus far lead to an inspiral signal in the low-frequency range. This can be seen in Figure 4.2 where the total GWB from pop I/II and III in 3G detectors is

presented. The pop III spectrum shows clear deviation from a 2/3 power law, because signals from further away stars would be more redshifted and would therefore be detected in their merger and ringdown phases. We test search filters different from a 2/3 power law to investigate if the deviation from pop I/II signal can be identified in a parameter estimation study. Motivated by the shape of the residual pop III GWB in Figure 4.2, we consider:

- power law with varying spectral index (PL), previously defined in (1.27),
- broken power law (BPL)

$$\Omega_{\rm GW}^{\rm BPL}(f) = \begin{cases} \Omega_{\rm peak} \left(\frac{f}{f_{\rm peak}}\right)^{\alpha_1} & \text{for } f \leq f_{\rm peak}, \\ \Omega_{\rm peak} \left(\frac{f}{f_{\rm peak}}\right)^{\alpha_2} & \text{for } f > f_{\rm peak}, \end{cases} \tag{4.2}$$

- triple BPL

$$\Omega_{\rm GW}^{\rm TBPL}(f) = \begin{cases} \Omega_{\rm peak} \left(\frac{f}{f_{\rm peak}^{(1)}}\right)^{\alpha_1} & \text{for } f \leq f_{\rm peak}^{(1)}, \\ \Omega_{\rm peak} \left(\frac{f}{f_{\rm peak}^{(2)}}\right)^{\alpha_2} & \text{for } f_{\rm peak}^{(1)} < f \leq f_{\rm peak}^{(2)}, \\ k\,\Omega_{\rm peak} \left(\frac{f}{f_{\rm peak}^{(2)}}\right)^{\alpha_3} & \text{for } f > f_{\rm peak}^{(2)}\ ; \end{cases} \tag{4.3}$$

  $k = (f_{\rm peak}^{(2)}/f_{\rm peak}^{(1)})^{\alpha_2}$ ensures continuity of the piecewise function, and

- smooth BPL, previously defined in (3.2).

The priors for each model's parameters can be found in Appendix D.2. If any of the filters above are preferred over a 2/3 filter, this could be an indication of the presence of a pop III signal.

### 4.2.3 Implications on the redshifted mass of the population

In the case of a detection, we examine whether we can constrain the mass/redshift distribution from the optimal search parameters. Equation (1.41) shows that the parameters impacting the background shape are the redshift-dependent merger rate and the progenitors' mass distribution. To understand how these population characteristics relate to model parameters, such as peak frequency and slope, we generate multiple spectra. We assume spinless, equal-mass binaries [245]. We fix the merger rate and vary the intrinsic mass input, observing how the shape of the GWB spectrum changes. Our results, however, depend on the choice of merger rate (see Appendix D.3). This is due to a degeneracy between the effects that merger rate and mass distribution have on the GWB [236]. We thus study the dependence of $\Omega_{\rm GW}$ on the *redshifted* total mass of each binary in the population, $M^{z}_{\rm tot}$, and find a relationship between the mass and the peak frequency of the spectrum.

We generate GW spectra with a merger rate from ST, varying the redshifted total mass, and find agreement (within 10%) between redshifted ringdown frequency and the peak of the spectrum, see Table 4.1. We obtain the same agreement if we use the merger rate in [236], suggesting again that an estimate of the peak frequency can be used to constrain the redshifted total mass of the population. This relationship, therefore, holds independently of the evolution model of the pop III binaries.

| $M^{z}_{\rm tot}$ | $f_{\rm peak}$ | $f^{z}_{\rm ring}$ | % difference |
|---|---|---|---|
| 100 | 166.2 | 165.8 | 0.20 |
| 200 | 83.7 | 82.9 | 1.0 |
| 300 | 56.5 | 55.3 | 2.1 |
| 400 | 43.1 | 41.4 | 3.9 |
| 500 | 35.2 | 33.2 | 5.7 |

**Table 4.1:** Variation of the peak of GWB spectra with a change in redshifted total binary mass. We find agreement between the peak frequency and the redshifted ringdown frequency.

Current models of pop III remnant mergers are subject to great uncer-

tainties, leading to merger rates of varying amplitude peaking at redshifts between 7 and 15 [233, 246, 247, 248]. Since the amplitude of the background is proportional to the merger rate, a factor of $\sim 10$ reduction in the merger rate amplitude would make pop III GWB contribution undetectable. If the peak of the merger rate appears at a lower redshift, the background may be invisible, e.g. close to or below the pop I/II residual. To quantify this statement we derive the GWB obtained for a toy model based on StarTrack simulations by shifting the merger rate peak (see Appendix D.4). We conclude that for pop III merger rates that peak at redshifts below $z < 6$, the pop III contribution is likely lost to the pop I/II residual.

### 4.2.4 Detection prospects with a 3G network

We simulate one year of observation time with the ET+2CE network, taking the CBC background from the ST catalogue. We find the best-fit models to the *residual* GWB that remains after subtracting the individual sources. A model selection study shows preference for other filters over a 2/3 PL, see Table 4.2. The models with a broken power law shown in the last 3 rows are clearly favoured over a single power law model. However, we do not observe a great increase in Bayes factor for the triple and smooth BPL over just a BPL. Hence, a BPL filter is sufficient for a residual pop III GWB search.

| model, $\mathcal{M}$ | $\ln \mathcal{B}^{\mathcal{M}}_{2/3}$ |
|---|---|
| PL | 28782 |
| BPL | 45825 |
| triple BPL | 46341 |
| smooth BPL | 46792 |

**Table 4.2:** Log Bayes factor of pop III filters compared to the 2/3 power law filter.

Already with a varying-index PL search we deduce that the 2/3 filter is not appropriate, since the estimated power law index is $\alpha = -0.6$ (we provide the corner plot in Appendix D.2). The more intricate filters, however, fit the $\Omega_{\rm GW}$ spectrum well and capture the presence of the peak success-

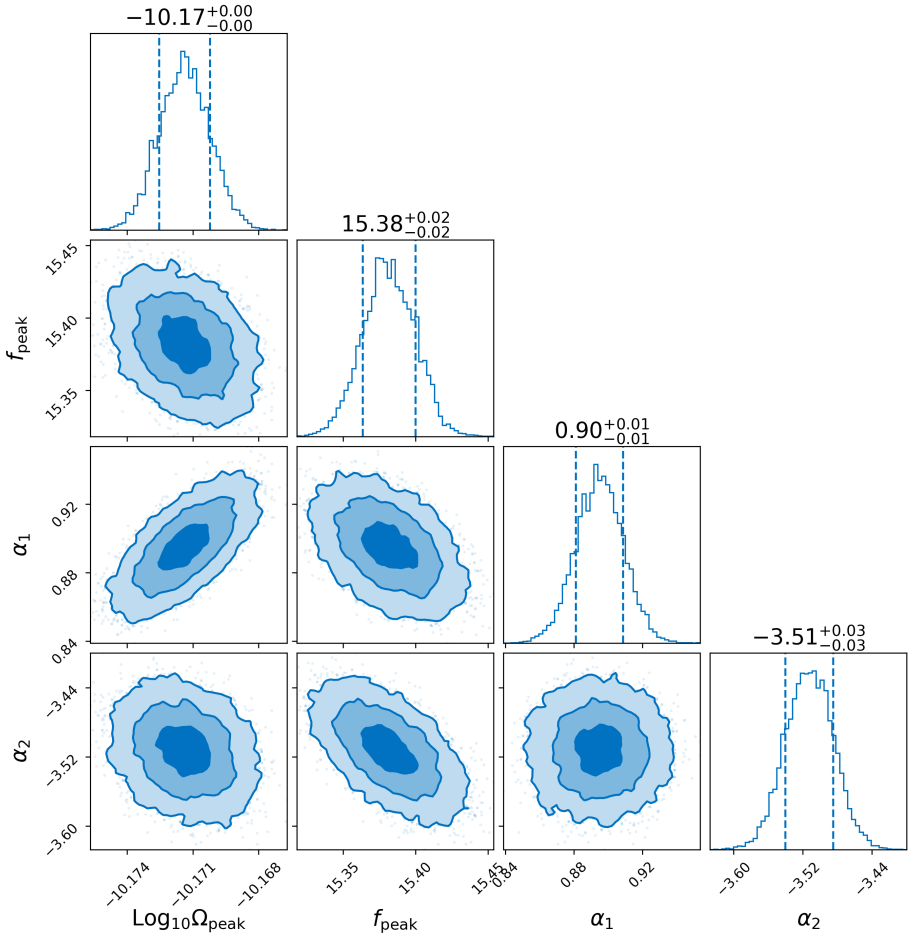


**Figure 4.4:** BPL fit to residual GWB spectrum of pop I+II+III from the ST simulation. The peak frequency is estimated to $f_{\rm peak} = 15.4$ Hz.

fully. To understand the redshifted mass distribution of pop III creating the GWB, we investigate the peak frequency of the signal. We obtain a good estimate of the peak frequency using a BPL search filter, shown in Figure 4.4, $f_{\rm peak} = 15.4$ Hz. The redshifted ringdown frequency that matches the peak frequency, $f^z_{\rm ring} = 15.4$ Hz, corresponds to $M^z_{\rm tot} = 1076 M_\odot$. The ST redshifted mass distribution shown in the top panel of Figure 4.3, gives an average redshifted total mass of the residual population, $< M^z_{\rm tot} >= 1121 M_\odot$. Therefore, our estimate of average $M^z_{\rm tot}$ agrees well with the true value.

## Discussion

Gravitational waves emitted from CBCs formed by pop III stars could represent a promising detection channel of the first stars formed in the Uni-

verse. Although 2G detectors are unable to detect the GWB from pop III stars, we have demonstrated that future GW interferometers could lead to a detection. Employing the ET+2CE 3G detector network, we could successfully subtract enough individual merger events to unravel the elusive pop III GWB. Subtraction methods are more effective for nearby sources, so the residual pop I/II signal can become sub-dominant to the pop III residual. The 2/3 power law approximation of GWB energy density for the CBC background breaks in this case due to the higher redshifted masses of pop III. Instead of the 2/3 power law, the GWB spectrum peaks in the low-frequency LVK range.

A model selection study showed that we could observe the peak caused by the unresolved merger and ringdown GWs from pop III stars. With a good estimate of the peak frequency, we could deduce the average redshifted total binary mass distribution of the residual population. Using the ST catalogue of binary sources, we have demonstrated the effectiveness of our Bayesian analysis combined with implications for the retrieved parameters. We have derived the relationship between peak frequency and redshifted total mass assuming equal-mass and non-spinning binaries. Combining our study with possible future detections of individual Pop III mergers will help confirm existence of such primordial, low-metallicity stars and obtain information about their characteristics.

In the following section we travel back in time and look at first-order phase transitions in the very early stages of the Universe, when it was too hot for primordial stars to form. We analyse the GWs generated by particles beyond the Standard Model as the Universe expands and cools down, allowing for symmetry breaking and phase transitions.

## 4.3 GWB from phase transitions

The Universe might have undergone a series of phase transitions (see, e.g. [249, 250]). In the case of a first-order phase transition, once the

temperature drops below a critical value, the Universe transitions from a meta-stable phase to a stable one, through a sequence of bubble nucleation, growth, and merger. During this process, a GWB is expected to be generated [251, 252].

Since the inception of the Standard Model, particle physicist have searched for a simpler, grand unified theory whose symmetry breaking gives us the Standard Model. We now know that the electromagnetic and weak nuclear force combine into a single electroweak force at energies above $T_{EW} \sim 100$ GeV. Upcoming LHC runs and future accelerators will probe such high energy scales in hope to study the nature of the electroweak transition. The Standard Model predicts a smooth crossover at the electroweak scale [253] , but singlet extensions can offer a strong FOPT (see e.g. review [254]). If a strong FOPT took place and bubbles of true vacuum expanded and collided, the resulting milliHertz GWB could be detected by LISA. This would represent an exceptional case of complementarity between high-energy colliders and GW interferometers.

Many compelling extensions of the Standard Model predict strong FOPTs in addition to grand unification models [255, 256, 257], e.g. supersymmetric models [258, 259, 260, 261, 262, 263], extra dimensions [264, 265], composite Higgs models [266, 267, 268, 269, 270, 271, 272] and models with an extended Higgs sector (see, e.g. [273, 274]). Generally there might exist symmetries beyond the ones of the Standard Model, which are spontaneously broken through a FOPT; for example the Peccei-Quinn symmetry [275, 276, 169, 277, 278], the $B - L$ symmetry [279, 280, 281, 282], or the left-right symmetry [283]. The nature of cosmological phase transitions depends strongly on the particle physics model at high energy scales.

The GWB sourced by a FOPT spans a wide frequency range. The peak frequency is mainly determined by the temperature at which the FOPT occurs. Interestingly, if that temperature is in the range $(10^5 - 10^{10})$ GeV – an energy scale not accessible by any existing terrestrial accelerators – the

produced GWB is within the frequency range of Advanced LIGO and Advanced Virgo [284, 285]. Such an energy scale is well-supported by either the Peccei-Quinn axion model [286], which solves the strong CP problem and provides a dark matter candidate, or high-scale supersymmetry models [287, 288, 289], among others. Especially, for axion-like particles, the upper end of the $T_{\rm pt}$ we probe is at the energy scale where astrophysical constraints, such as stellar cooling, lose their sensitivities [290]. In addition, the lower end of the $T_{\rm pt}$ fits well in minisplit SUSY models where the Higgs mass is explained.

In what follows we place constraints on the normalised energy density in GWs from first-order strong phase transitions using data from Advanced LIGO and Virgo's first, second and third observing runs. We then focus on the supercooling family of first-order phase transitions since these give a particularly strong GW signal, before briefly commenting on GWs from turbulence in the early Universe plasma.

### 4.3.1 Phase transition models

As the temperature of the Universe decreases, a new (true) vacuum with a lower energy density may appear, along with a potential barrier separating it from the high-temperature (false) vacuum. The transition between the two states corresponds to the formation of bubbles of true vacuum in various patches of the Universe, and their subsequent expansion. The nucleation rate per unit volume of such bubbles can be roughly estimated as [291]

$$\Gamma(T) \sim T^4 \exp\left(-\frac{S(T)}{T}\right), \tag{4.4}$$

where $S(T)$ is the Euclidean action following a Wick rotation $t \to it$, evaluated on the bubble solution interpolating between the false and true vacuum. The onset of a FOPT occurs at the nucleation temperature $T_{\rm pt}$ at which $\Gamma(T_{\rm pt}) \approx H_{\rm pt}^4$, with $H_{\rm pt}$ denoting the Hubble parameter at that time,

$H_{\rm pt} = H(T_{\rm pt})$.

A FOPT can be described by four parameters: the bubble wall velocity $v_w$, the nucleation temperature $T_{\rm pt}$, the inverse of the transition's duration in Hubble units $\beta/H_{\rm pt}$,

$$\frac{\beta}{H_{\rm pt}} = T_{\rm pt}\frac{d}{dT}\left(\frac{S(T)}{T}\right)\Big|_{T=T_{\rm pt}}, \tag{4.5}$$

and the strength of the transition $\alpha$,

$$\alpha = \frac{\rho_{\rm vac}(T_{\rm pt})}{\rho_{\rm rad}(T_{\rm pt})}, \tag{4.6}$$

which is the ratio of the vacuum energy density to the radiation energy density at nucleation temperature. It is well established that GWs can be produced by mainly three sources: bubble collisions, sound waves, and magnetohydrodynamic turbulence (see [191, 292, 176, 250] for recent reviews). The GWB thus produced is described by the energy density spectrum $\Omega_{\rm GW}(f)$. Each spectrum can be well approximated by a broken power law, with its peak frequency determined by the typical length scale at the transition, the mean bubble separation $R_{\rm pt}$ (which is related to $\beta$), and also by the amount of redshifting determined by $T_{\rm pt}$ and the cosmic history. The amplitude of each contribution is largely determined by the energy released normalised by the radiation energy density $\alpha$, its fraction going into the corresponding source and $v_{\rm w}$. For now we do not consider the contribution from magnetohydrodynamic turbulence as it always happens together with sound waves and is subdominant. In addition, we note that its spectrum is the least understood and might witness significant changes in the future [191, 293, 294, 295, 296, 297, 298].

The dominant source for GW production in a thermal transition, as most commonly encountered in the early Universe, is the sound waves in the plasma induced by the coupling between the scalar field and the thermal bath [173, 172, 141]. A good analytical understanding of this spectrum

has been achieved through the sound shell model [299, 300, 301], though it still does not capture all the physics [141, 302, 250] to match perfectly the result from numerical simulations [191, 173]. We use the spectrum from numerical simulations:

$$\begin{aligned}\Omega_{\rm SW}(f)h^2 = 2.65\times10^{-6}\left(\frac{H_{\rm pt}}{\beta}\right)\left(\frac{\kappa_{\rm SW}\alpha}{1+\alpha}\right)^2\left(\frac{100}{g_*}\right)^{1/3} v_{\rm w} \\ \times\left(\frac{f}{f_{\rm SW}}\right)^3\left(\frac{7}{4+3(f/f_{\rm SW})^2}\right)^{7/2}\Upsilon(\tau_{\rm SW})\,,\end{aligned} \tag{4.7}$$

where $\kappa_{\rm SW}$ is the fraction of vacuum energy converted into the kinetic energy of the bulk flow, a function of $v_{\rm w}$ and $\alpha$ [303, 304]; $g_*$ is the number of relativistic degrees of freedom, chosen to be 100 in our analysis; $h$ is the dimensionless Hubble parameter; $f_{\rm SW}$ is the present peak frequency,

$$f_{\rm SW} = 19\frac{1}{v_{\rm w}}\left(\frac{\beta}{H_{\rm pt}}\right)\left(\frac{T_{\rm pt}}{100{\rm GeV}}\right)\left(\frac{g_*}{100}\right)^{\frac{1}{6}}\mu{\rm Hz}, \tag{4.8}$$

and $\Upsilon = 1-(1+2\tau_{\rm SW}H_{\rm pt})^{-1/2}$ [301] which is a suppression factor due to the finite lifetime [301, 305], $\tau_{\rm SW}$, of sound waves. $\tau_{\rm SW}$ is typically smaller than a Hubble time unit [306, 307] and is usually chosen to be the timescale for the onset of turbulence [176], $\tau_{\rm SW}\approx R_{\rm pt}/\bar{U}_f$, with $R_{\rm pt} = (8\pi)^{1/3}v_{\rm w}/\beta$ for an exponential nucleation of bubbles [300, 301], and $\bar{U}_f^2 = 3\kappa_{\rm SW}\alpha/[4(1+\alpha)]$ [176].

When sound waves, and thus also magnetohydrodynamic turbulence, are highly suppressed or absent, bubble collisions can become dominant, e.g., for a FOPT in vacuum of a dark sector which has no or very weak interactions with the standard plasma. The resulting GW spectrum can be well modelled with the envelope approximation [308, 309, 175], which assumes an infinitely thin bubble wall and neglects the contribution from overlapping bubble segments. In the low-frequency regime, $\Omega_{\rm GW}\propto f^3$ from causality [174, 310, 311], and for high-frequencies $\Omega_{\rm GW}\propto f^{-1}$ [171] due to the dominant single bubble contribution as revealed by the analytical

calculation [175]. The spectrum is [171, 175, 176]

$$\Omega_{\rm COLL}(f)h^2 = 1.67\times10^{-5}\Delta(v_{\rm w})\left(\frac{H_{\rm pt}}{\beta}\right)^2\left(\frac{\kappa_\phi\alpha}{1+\alpha}\right)^2\left(\frac{100}{g_*}\right)^{1/3}S_{\rm env}(f), \tag{4.9}$$

where $\kappa_\phi = \rho_\phi/\rho_{\rm vac}$ denotes the fraction of vacuum energy converted into gradient energy of the scalar field. The amplitude $\Delta$ is $\Delta(v_{\rm w}) = 0.48v_{\rm w}^3/(1+5.3v_{\rm w}^2+5v_{\rm w}^4)$ and the spectral shape is $S_{\rm env} = 1/(c_l\tilde{f}^{-3}+(1-c_l-c_h)\tilde{f}^{-1}+c_h\tilde{f})$ where $c_l = 0.064$, $c_h = 0.48$ and $\tilde{f} = f/f_{\rm env}$ with $f_{\rm env}$ the present peak frequency

$$f_{\rm env} = 16.5\left(\frac{f_{\rm BC}}{\beta}\right)\left(\frac{\beta}{H_{\rm pt}}\right)\left(\frac{T_{\rm pt}}{100\ {\rm GeV}}\right)\left(\frac{g_*}{100}\right)^{\frac{1}{6}}\mu{\rm Hz}, \tag{4.10}$$

and $f_{\rm BC}$ the peak frequency right after the transition $f_{\rm BC} = 0.35\beta/(1+0.069v_{\rm w}+0.69v_{\rm w}^4)$. More recent simulations going beyond the envelope approximation show a steeper shape $f^{-1.5}$ for high frequencies [312], and it also varies from $f^{-1.4}$ to $f^{-2.3}$ as the wall thickness increases [313] (see also [314, 315, 316]).

### 4.3.2 Searching for phase transitions in GWB data

Here we take two analysis approaches. First, we consider an approximated broken power law including main features of the shape and its peak. We then consider the phenomenological models (4.9) and (4.7), for contributions from bubble collisions and sound waves.

*I. Broken power law model*: The spectrum can be approximated by a broken power law as (3.2). Here $\alpha_1 = 3$, from causality, and $\alpha_2$ takes the values $-4$ and $-1$, for sound waves and bubble collisions, respectively. We fix the $\alpha_1$ parameter in our search, but we let $\alpha_2$ vary uniformly between -8 and 0, allowing for the values motivated by both contributions. The value for $\Delta$ is set to 2 for sound waves and 4 for approximating bubble collisions. We run a Bayesian search for both values, but present results

only for $\Delta = 2$, since it gives more conservative upper limits. In addition to a search for the broken power law, we undertake a study on simultaneous estimation of a CBC background and a broken power law background, because current estimates of the CBC background [32, 317] show it as a non-negligible component of any GWB signal.

The log-likelihood for a single detector pair is Gaussian, as previously defined in (3.4). The search for an isotropic signal showed no evidence of correlated magnetic noise, and a pure Gaussian noise model is still preferred by the data [317]. Therefore, here, a contribution from Schumann resonances [71, 88, 318] is neglected. The model we fit to the data is $\Omega_{\rm GW}(f, \boldsymbol{\theta}_{\rm GW})$, with parameters $\boldsymbol{\theta}_{\rm GW}$. The set of GW parameters depends on the type of search we perform.

The CBC spectrum is modelled as (1.27), with $\alpha = 2/3$ and $f_{\rm ref} = 25$ Hz. We consider three separate scenarios: contributions from unresolved CBC sources, with $\boldsymbol{\theta}_{\rm GW} = (\Omega_{\rm ref})$; broken power law contributions, with $\boldsymbol{\theta}_{\rm GW} = (\Omega_*, f_*, \alpha_2)$; and the combination of CBC and broken power law contributions, for which $\boldsymbol{\theta}_{\rm GW} = (\Omega_{\rm ref}, \Omega_*, f_*, \alpha_2)$. The priors used are summarised in Table 4.3. To compare GW models and assess which provides a better fit, we use Bayes factors. In particular, we consider $\log \mathcal{B}^{\rm CBC+BPL}_{\rm noise}$ and $\log \mathcal{B}^{\rm CBC+BPL}_{\rm CBC}$ as indicative detection statistics.

*II. Phenomenological model*: Two scenarios are considered, corresponding to dominant contributions from bubble collisions or sound waves, respectively, following an approach similar to [169]. The analysis procedure follows closely that of the broken power law search, with $\boldsymbol{\theta}_{\rm GW} = (\Omega_{\rm ref}, \alpha, \beta/H_{\rm pt}, T_{\rm pt})$ including CBC background $\Omega_{\rm CBC}$, and $\Omega_{\rm GW}$ from bubble collisions and sound waves described by (4.9) and (4.7), respectively.

For bubble collisions, $v_{\rm w}$ and $\kappa_\phi$ are set to unity (for a detailed discussion of the possible choices see [303, 191]). The remaining model parameters are varied in the ranges in Table 4.3. We note that the GW spectra in (4.7) and (4.9) may not be applicable when $\alpha \gtrsim 10$, e.g. in the case of su-

| **Broken power law model** | |
|---|---|
| Parameter | Prior |
| $\Omega_{\rm ref}$ | LogUniform($10^{-10}$, $10^{-7}$) |
| $\Omega_*$ | LogUniform($10^{-9}$, $10^{-4}$) |
| $f_*$ | Uniform(0, 256) Hz |
| $\alpha_1$ | 3 |
| $\alpha_2$ | Uniform(-8,0) |
| $\Delta$ | 2 |
| **Phenomenological model** | |
| Parameter | Prior |
| $\Omega_{\rm ref}$ | LogUniform($10^{-10}$, $10^{-7}$) |
| $\alpha$ | LogUniform ($10^{-3}$, 10) |
| $\beta/H_{\rm pt}$ | LogUniform ($10^{-1}$, $10^{3}$) |
| $T_{\rm pt}$ | LogUniform ($10^{5}$, $10^{10}$) GeV |
| $v_{\rm w}$ | 1 |
| $\kappa_\phi$ | 1 |
| $\kappa_{\rm SW}$ | $f(\alpha, v_{\rm w}) \in [0.1 - 0.9]$ |

**Table 4.3:** List of prior distributions used for all parameters in the various searches. The narrow, informative prior on $\Omega_{\rm ref}$ stems from estimates of the CBC background [32], and encompasses uncertainties on the mass and redshift distributions of CBCs [317, 319]. The frequency prior is uniform across the frequency range considered since we have no further information about it.

percooling, and also a large $\alpha$ does not translate into a significant increase in the GW amplitude since $\alpha/(1+\alpha) \to 1$. Moreover, $\beta/H_{\rm pt}$ is related to the mean bubble separation, up to an $O(1)$ coefficient, and one should be cautious when it is smaller than 1 [320, 306]. In this study, we conservatively choose $\beta/H_{\rm pt}$ to be larger than 0.1.

For sound waves, we initially set $v_{\rm w} = 1$, and then explore different values for $v_{\rm w}$ in the range (0.7 - 1.0), corresponding to various detonation and hybrid modes of fluid velocity profile [302, 303]. Here $\kappa_{\rm SW}$ is a function of $\alpha$ and $v_{\rm w}$, e.g., for $v_{\rm w} = 1$, $\kappa_{\rm SW}$ increases from 0.1 to 0.9 as $\alpha$ increases from 0.1 to 10. The rest of the parameters are varied as in the case of bubble collisions.

### 4.3.3 Constraints from O3 data

*I. Broken power law model*: In Figure 4.5 we present posterior distributions of parameters in the combined CBC and BPL search. The Bayes factor is

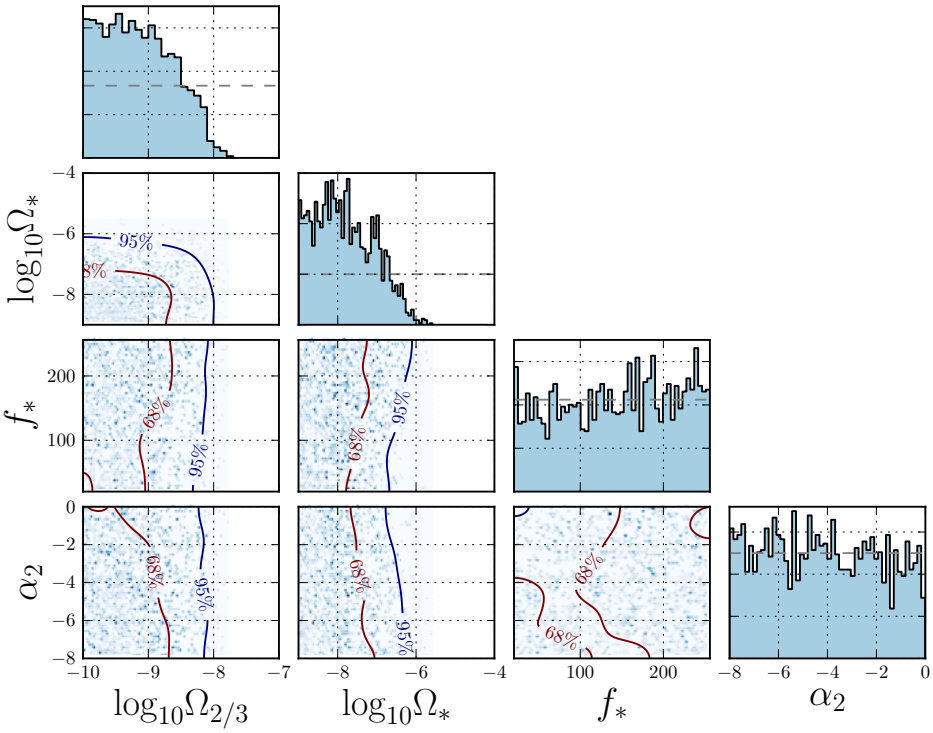


**Figure 4.5:** Posterior distributions for the combined CBC and broken power law search as a function of $\log\Omega_{\rm ref}$ and the different parameters of the model. The 68% and 95% CL exclusion contours are shown. The horizontal dashed line in the posteriors indicate the flat priors used in the analysis.

$\log\mathcal{B}^{\rm CBC+BPL}_{\rm noise} = -1.4$, demonstrating no evidence of such a signal in the data from the three observing runs. The 2-D posterior of $\Omega_{\rm ref}$ and $\Omega_*$ allows us to place simultaneous estimates on the amplitudes of the two spectra. The 95% CL upper limits are $\Omega_{\rm ref} = 6.1 \times 10^{-9}$ and $\Omega_* = 5.6 \times 10^{-7}$, respectively. If we take individual posterior samples of $\Omega_*$, $f_*$ and $\alpha_2$ from Figure 4.5, and combine them to construct a posterior of $\Omega_{\rm BPL}$, we estimate at 95% CL $\Omega_{\rm BPL}(25\,{\rm Hz}) = 4.4 \times 10^{-9}$. The width of the $\alpha_2$ posterior suggests no preference for a particular value by the data, and we are unable to rule out any part of the parameter space at this time. Other searches give Bayes factors $\log\mathcal{B}^{\rm BPL}_{\rm noise} = -0.78$ and $\log\mathcal{B}^{\rm CBC+BPL}_{\rm CBC} = -0.81$, once again giving no evidence for a BPL signal, with or without CBCs considered.

To demonstrate the dependence of GW amplitude constraints on other parameters, we present 95% CL upper limits on $\Omega_*$ for a set of $\alpha_2$ and $f_*$

in Table 4.4. We choose representative values of $\alpha_2$, for bubble collisions, $\alpha_2 =$ -1 and -2, and for sound waves, $\alpha_2 =$ -4. The $f_*$ values are chosen to represent broken power laws that peak before, at, and after the most sensitive part of the LVK band, $f_* = 25\,\mathrm{Hz}$. As expected, the most constraining upper limits are obtained for a signal that peaks at 25 Hz. For the signal in the first column that peaks at 1 Hz, the faster it decays, the weaker it is at 25 Hz. Therefore, the more negative $\alpha_2$ values give less constraining upper limits on the amplitude. Finally, the signal that peaks at 200 Hz gives similar $\Omega_*$ upper limits for all values of $\alpha_2$ since it resembles a simple $\alpha_1 = 3$ power law in the range with largest SNR. Note the upper limits in Table 4.4 are fundamentally different from results in Figure 4.5. In the former case we fix $f_*$ and $\alpha_2$ and find $\Omega_*^{95\%}$, while in the latter we marginalise over all parameters to obtain $\Omega_*^{95\%}$.

| **Broken power law model** | | | |
|---|---|---|---|
| | $f_* = 1\,\mathrm{Hz}$ | $f_* = 25\,\mathrm{Hz}$ | $f_* = 200\,\mathrm{Hz}$ |
| $\alpha_2 = -1$ | $3.3 \times 10^{-7}$ | $3.5 \times 10^{-8}$ | $2.8 \times 10^{-7}$ |
| $\alpha_2 = -2$ | $8.2 \times 10^{-6}$ | $6.0 \times 10^{-8}$ | $3.7 \times 10^{-7}$ |
| $\alpha_2 = -4$ | $5.2 \times 10^{-5}$ | $1.8 \times 10^{-7}$ | $3.7 \times 10^{-7}$ |

**Table 4.4:** Upper limits for the energy density amplitude, $\Omega_*^{95\%}$, in the broken power law model for fixed values of the peak frequency, $f_*$, and negative power law index, $\alpha_2$.

*II. Phenomenological model*: We now estimate 95% CL upper limits on $\Omega_{\mathrm{COLL}}$ and $\Omega_{\mathrm{SW}}$ from bubble collisions and sound waves respectively. The Bayesian analysis is repeated separately for $\Omega_{\mathrm{COLL}}$ and $\Omega_{\mathrm{SW}}$ contributions, with priors stated in Table 2.1, leading to Bayes factors $\log \mathcal{B}^{\mathrm{CBC+COLL}}_{\mathrm{noise}}$= -0.74 and $\log \mathcal{B}^{\mathrm{CBC+SW}}_{\mathrm{noise}}$= -0.66, respectively.

In Figure 4.6 we present exclusion regions as a function of the different parameters of the CBC+FOPT model, now under the assumption that contributions from bubble collisions dominate, with $v_{\mathrm{w}} = 1$ and $\kappa_\phi = 1$. In general, with the chosen prior, the data can exclude part of the parameter space at 95% CL, especially when $T_{\mathrm{pt}} > 10^8$ GeV, $\alpha > 1$, or $\beta/H_{\mathrm{pt}} < 1$.

Table III presents 95% CL upper limits on $\Omega_{\mathrm{COLL}}$(25 Hz) for several

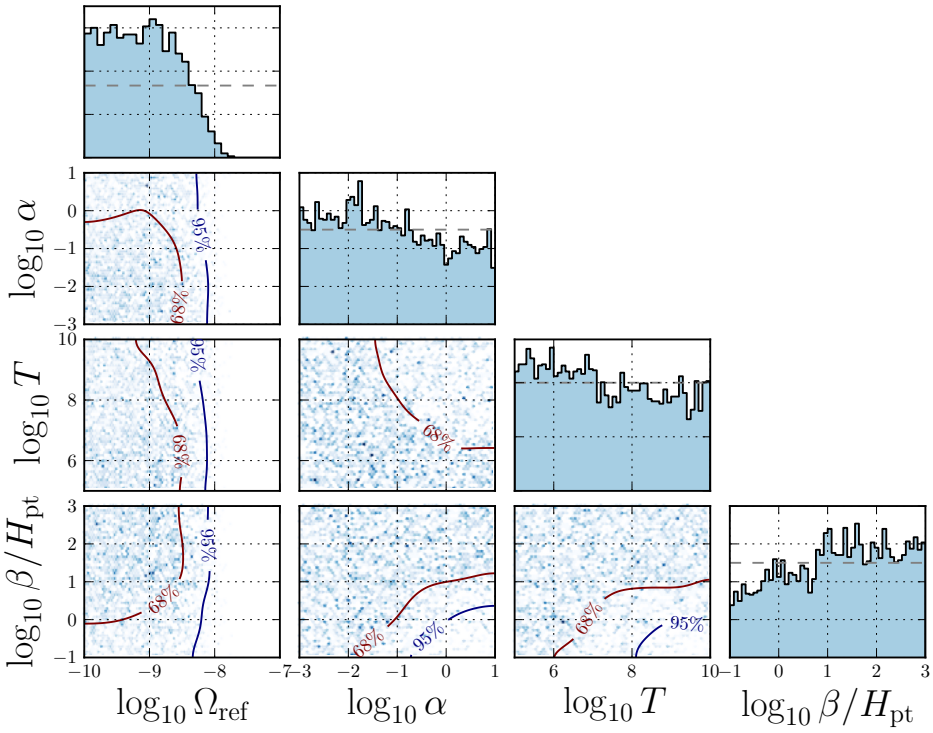


**Figure 4.6:** Posterior distributions for the CBC+FOPT search in the case of a phenomenological model with dominant bubble collision contributions as a function of $\log\Omega_{\rm ref}$ and the different parameters of the model. The 68% and 95% CL exclusion contours are shown. The horizontal dashed line in the posteriors indicate the flat priors used in the analysis.

$\beta/H_{\rm pt}$ and $T_{\rm pt}$, where $\alpha$ is left as a free parameter to be inferred from the data. We consider three values for $\beta/H_{\rm pt}$, namely 0.1, 1, and 10, and four for $T_{\rm pt}$: $10^7$, $10^8$, $10^9$, and $10^{10}$ GeV. Our constraints on $\Omega_{\rm COLL}(25\ {\rm Hz})$, as computed at the reference frequency of 25 Hz, vary in the range $4.0\times10^{-9}$ to $1.0\times10^{-8}$, with more stringent limits at large $\beta/H_{\rm pt}$ or large $T_{\rm pt}$. At the largest values of $\beta/H_{\rm pt}$ and $T_{\rm pt}$ there is not enough sensitivity to place constraints to the model. In all cases, the inferred upper limits on the CBC background range between $\Omega_{\rm ref} = 5.3\times10^{-9}$ and $6.1\times10^{-9}$.

Similarly, in Figure 4.7 we present the results for the CBC+FOPT hypothesis in which the sound waves dominate with $v_{\rm w}=1$ and $\kappa_{\rm SW}$ a function of $v_{\rm w}$ and $\alpha$. The Bayesian analysis shows sensitivity at large values of $\alpha$ and $T_{\rm pt}$, but does not exclude regions in the parameter space at

| Phenomenological model (bubble collisions) | | | | |
|---|---|---|---|---|
| $\Omega^{95\%}_{\rm COLL}$ (25 Hz) | | | | |
| $\beta/H_{\rm pt} \setminus T_{\rm pt}$ | $10^7$ GeV | $10^8$ GeV | $10^9$ GeV | $10^{10}$ GeV |
| 0.1 | $9.2 \times 10^{-9}$ | $8.8 \times 10^{-9}$ | $1.0 \times 10^{-8}$ | $7.2 \times 10^{-9}$ |
| 1 | $1.0 \times 10^{-8}$ | $8.4 \times 10^{-9}$ | $5.0 \times 10^{-9}$ | – |
| 10 | $4.0 \times 10^{-9}$ | $6.3 \times 10^{-9}$ | – | – |

**Table 4.5:** The 95% CL upper limits on $\Omega^{95\%}_{\rm COLL}(25\ {\rm Hz})$ for fixed values of $\beta/H_{\rm pt}$ and $T_{\rm pt}$, and $v_{\rm w} = \kappa_\phi = 1$. The dashed lines denote no sensitivity for exclusion.

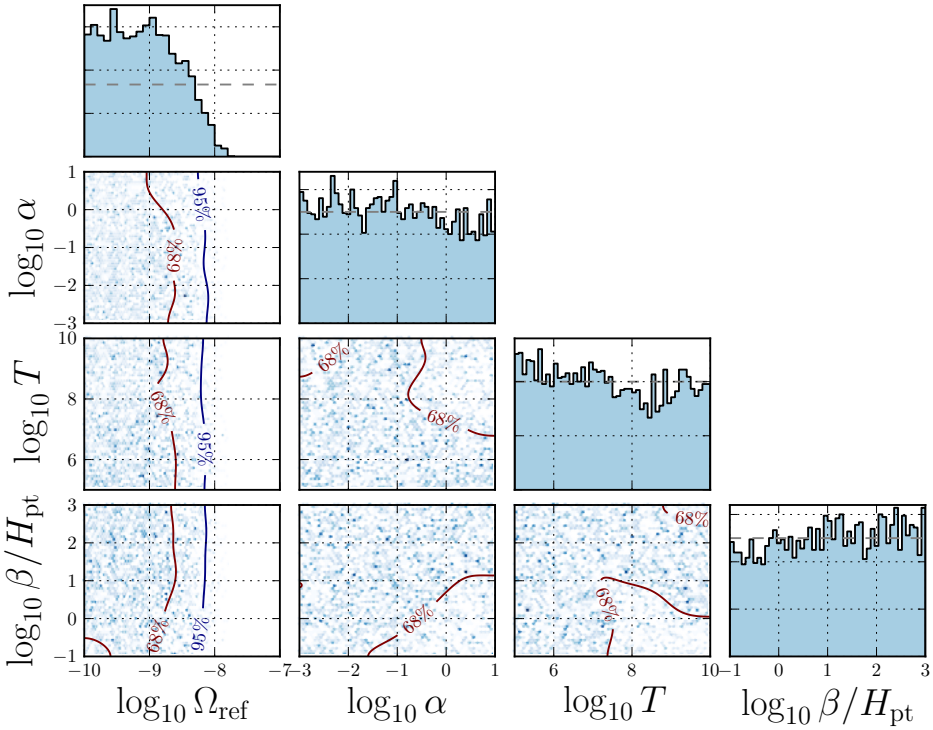


**Figure 4.7:** Posterior distributions for the CBC+FOPT search in the case of a phenomenological model with dominant sound wave contributions ($v_{\rm w} = 1$), as a function of $\log\Omega_{\rm ref}$ and the different parameters of the model. The 68% and 95% CL exclusion contours are shown. The horizontal dashed line in the posteriors indicate the flat priors used in the analysis.

95% CL. The analysis is then performed for given values of $\beta/H_{\rm pt}$ and $T_{\rm pt}$ leaving $\alpha$ as a free parameter. As a result, a 95% CL upper limit on $\Omega_{\rm SW}(25\ {\rm Hz})$ of $5.9 \times 10^{-9}$ is obtained for $\beta/H_{\rm pt} < 1$ and $T_{\rm pt} > 10^8$ GeV. The analysis is repeated for models with reduced velocities of $v_{\rm w} = 0.9$, $v_{\rm w} = 0.8$, and $v_{\rm w} = 0.7$, with Bayes factor $\log\mathcal{B}^{\rm CBC+SW}_{\rm noise} = -0.60$ and upper

limit $\Omega_{\rm ref} \approx 5.9 \times 10^{-9}$, with no significant $v_w$ dependence. In all studied cases, the models with reduced $v_w$ lead to significantly lower sound waves predicted energy densities, and with no 95% CL exclusions.

## Discussion

We have searched for signals from FOPTs in the early Universe, potentially leading to a GWB in the LVK frequency band. The analysis is based on the data from the three observation periods, for which no generic signals above the detector noise has been observed.

We use the results to deduce implications for models describing GWB. We first consider a generic broken power law spectrum, describing its main features in terms of the shape and the peak amplitude. We place 95% CL upper limits simultaneously on the normalised energy density contribution from unresolved CBCs and a FOPT, $\Omega_{\rm CBC}(25\,{\rm Hz}) = 6.1 \times 10^{-9}$ and $\Omega_{\rm BPL}(25\,{\rm Hz}) = 4.4 \times 10^{-9}$, respectively.

The results are then interpreted in terms of a phenomenological model describing contributions from bubble collisions or sound waves, showing that the data can exclude a part of the parameter space at large temperatures. In a scenario in which bubble collision contributions dominate, with $v_{\rm w} = 1$ and $\kappa_\phi = 1$, part of the phase space with $T_{\rm pt} > 10^8$ GeV, $\alpha > 1$, and $\beta/H_{\rm pt} < 1$ is excluded at 95% CL. For fixed values of $\beta/H_{\rm pt} = 0.1$, 1 or 10 and $T_{\rm pt} = 10^7, 10^8, 10^9$ or $10^{10}$ GeV, the 95% CL upper limits on $\Omega_{\rm COLL}(25{\rm Hz})$ vary in the range between $4.0 \times 10^{-9}$ and $1.0 \times 10^{-8}$ which depends on the $\beta/H_{\rm pt}$ and $T_{\rm pt}$ values considered. In the case where sound waves dominate, several scenarios are explored considering different $v_w$. The data only shows a limited sensitivity, and a 95% CL upper limit on $\Omega_{\rm SW}(25{\rm Hz})$ of $5.9 \times 10^{-9}$ is placed in the case of $v_{\rm w} = 1$, for $\beta/H_{\rm pt} < 0.1$ and $T_{\rm pt} > 10^8$ GeV. Altogether, the results indicate the importance of using LIGO-Virgo GW data to place constraints on new phenomena related to strong FOPTs in the early Universe.

We now move away from the general class of first-order phase tran-

sitions, and study the special case of supercooled first-order phase transitions, since these can lead to GWs with greater amplitude.

### 4.3.4 Supercooled phase transitions

A particularly interesting scenario is when the FOPT is supercooled, which often increases the duration of the FOPT, leading to an enhancement of the GW signal. These strong GW signals are more likely to be observed compared to the non-supercooled ones.

A prolonged period of supercooling can arise in theories with Coleman-Weinberg-type symmetry breaking [321] or in strongly-coupled scenarios. Some models of this type are discussed in [322, 323, 324, 325, 326, 327, 328, 329]. The phenomenon of supercooling occurs when the nucleation temperature is much lower than the scale of the symmetry breaking triggering the FOPT, leading to a large FOPT strength, $\alpha \gg 1$. A supercooled phase transition may have occurred during the inflationary period, when the hot universe rapidly expanded and supercooled to very low temperatures. Given the current sensitivity of LVK detectors, one may expect that FOPT GW signals in reach of the experiment would most probably come from a supercooled FOPT. In what follows we apply our analysis of the LVK data to the theoretically well-motivated supercooled models described in [306, 277], and derive the corresponding constraints on their parameter space.

Our analysis is the first time the LVK data from the first three observing runs is being used to set limits on parameters of particle physics models through a FOPT search. In particular, in the current analysis we apply our priors *directly* at the level of the particle physics parameters, e.g. particle masses and couplings. This presents a novel way of bridging the gap between data analysis and theoretical particle physics model building. For details on the modifications to GW spectra from supercooled phase transitions and the generic constraints we can place on those with LVK data, please refer to Appendices E.1 and E.2.

## Two well-motivated particle physics models

The phenomenon of supercooling occurs in theories with Coleman-Weinberg-type symmetry breaking [321] or strong coupling. Several models of this type have been investigated in the literature in light of their enhanced GW signals [306, 277, 325, 279, 315, 271, 305, 329, 324, 326, 323, 327]. In this study, we focus on Model I [306] and Model II [277], which exhibit approximate conformal symmetry. They are both well-motivated from a particle physics point of view and have a minimal particle content. We note, however, that our analysis can be applied to any other model with supercooling. The general goal is to assess the detectability of signals from supercooled FOPTs with the LVK detectors, and determine the regions of parameter space that can be excluded with current GW data.

## Model I

### Theoretical framework

The first model we consider is based on a theoretically attractive minimal $\mathrm{U}(1)_{B-L}$ extension of the Standard Model gauge group [325, 306, 327]. Upon introducing three right-handed neutrinos, the theory is anomaly-free, realises the seesaw mechanism, and can be incorporated into $\mathrm{SO}(10)$ grand unification. The model includes only two new bosonic fields: a real scalar $\phi$ and a gauge boson $Z'$.

The zero temperature scalar potential is given by

$$V_0(\phi) = \frac{1}{4}\lambda_\phi \phi^4 + \sum_{i=\phi,G,Z'} \frac{n_i}{64\pi^2} \left\{ m_i^4(\phi) \left[ \log\left( \frac{m_i^2(\phi)}{\mu^2} \right) - c_i \right] \right\} , \tag{4.11}$$

where $n_i$ is the number of degrees of freedom, $c_{\phi,G} = 3/2$, $c_{Z'} = 5/6$, $\mu$ is the renormalisation scale, and $G$ denotes the Goldstone boson. The field-dependent masses are:

$$m_{Z'}^2(\phi) = 4g^2\phi^2 , \quad m_\phi^2(\phi) = 3\lambda_\phi \phi^2 , \quad m_G^2(\phi) = \lambda_\phi \phi^2 , \tag{4.12}$$

where $g$ is the gauge coupling. The finite temperature part of the effective potential is

$$\begin{aligned} V_{\rm T}(\phi,T) &= \frac{T^4}{2\pi^2}\sum_{i=\phi,G,Z'} n_i \int_0^\infty dy\, y^2 \log\left(1-e^{-\sqrt{m_i^2(\phi)/T^2+y^2}}\right) \\ &+ \frac{T}{12\pi}\sum_{j=\phi,G,Z'_L} n'_j \left\{ m_j^3(\phi) - [m_j^2(\phi)+\Pi_j(T)]^{\frac{3}{2}} \right\}, \end{aligned} \tag{4.13}$$

with the thermal masses given by

$$\begin{aligned} &\Pi_\phi(T) = \Pi_G(T) = \left(g^2 + \tfrac{1}{3}\lambda_\phi\right) T^2 \,, \\ &\Pi_{Z'_L}(T) = 4g^2T^2 \,, \end{aligned} \tag{4.14}$$

where the subscript $L$ denotes longitudinal components.

This model has only two free parameters relevant for the GW signal: the vacuum expectation value $v$ of the scalar field $\phi$, and the $\mathrm{U}(1)_{B-L}$ gauge coupling $g$. Trading $v$ for the the gauge boson mass $m_{Z'}$, related via

$$m_{Z'} = 2gv \,, \tag{4.15}$$

the two parameters describing Model I are $(m_{Z'}, g)$.

**Constraints from LVK O1+O2+O3 data**

For each point $(m_{Z'}, g)$ of the parameter space, one can compute the parameters describing the phase transition, i.e., $T_{\rm RH}$ and $\beta/H_{\rm RH}$, and the resulting GW spectrum. We note that the temperature of the thermal bath at the time when the GWs are produced is not $T_{\rm pt}$, but rather the reheating temperature $T_{\rm RH}$, approximately given by

$$T_{\rm RH}^4 \simeq \frac{30}{\pi^2 g_*}\Delta V, \tag{4.16}$$

where $\Delta V$ is the potential difference between the true and false vacuum, and $g_*$ is the number of relativistic degrees of freedom. It is often the case

| Model I | | Model II | |
|---|---|---|---|
| $\Omega_{\rm ref}$ | LogU[$10^{-10}$, $10^{-7}$] | $\Omega_{\rm ref}$ | LogU[$10^{-10}$, $10^{-7}$] |
| $m_{Z'}$ | LogU[$10^4$,$10^{11}$] (GeV) | $F$ | LogU[$1.4\times10^9$,$10^{11}$] (GeV) |
| $g$ | U[0.3, 0.4] | $\lambda$ | U[0.325, 0.6] |

**Table 4.6:** Summary of the priors used for parameter estimation for Model I and Model II, where U stands for a uniform and LogU for a log-uniform prior. The narrow prior on $\Omega_{\rm ref}$ stems from estimates of the CBC background [330].

that $T_{\rm RH} \gg T_{\rm pt}$, especially for supercooled phase transitions. However, for sufficiently fast reheating one has $H(T_{\rm pt}) \simeq H(T_{\rm RH})$, which implies that $\beta/H_{\rm pt} \simeq \beta/H_{\rm RH}$ [191].

We restrict ourselves to $m_{Z'} \in [10^4,\ 10^{11}]$ GeV and $g \in [0.3,\ 0.4]$, which corresponds to FOPTs where the GW signal is dominated by sound waves [327]. If the gauge coupling $g$ is chosen to be larger than 0.4, the FOPT is not supercooled and $\alpha \sim 1$. Furthermore, we are not exploring values of $g$ below 0.3, as these correspond to a regime where both bubble collisions and sound waves contribute considerably to the GW spectrum, as discussed in [327].

We perform a parameter estimation search over this parameter space, and include the contribution of the CBC background. The likelihood is given by (3.4), with $\Omega_{\rm GW} = \Omega_{\rm CBC} + \Omega_{\rm SW}$, where $\Omega_{\rm SW}$ is calculated from (4.7) using the model parameters $(m_{Z'},g)$. Thus, the parameters of the search are $\boldsymbol{\theta}_{\rm GW} = (\Omega_{\rm ref},\ m_{Z'},\ g)$. The priors are summarised in Table 4.6 and the results are shown in Figure 4.8 (upper panel) which depicts the resulting posteriors. The upper limits on the amplitude of the astrophysical CBC background are consistent with [331, 332]. Furthermore, a region of parameter space around $m_{Z'} \sim \mathcal{O}(10^8\ \text{GeV})$ is excluded, and corresponds to FOPT GW signals peaked within the frequency range of the LVK detectors.

## Model II

### Theoretical framework

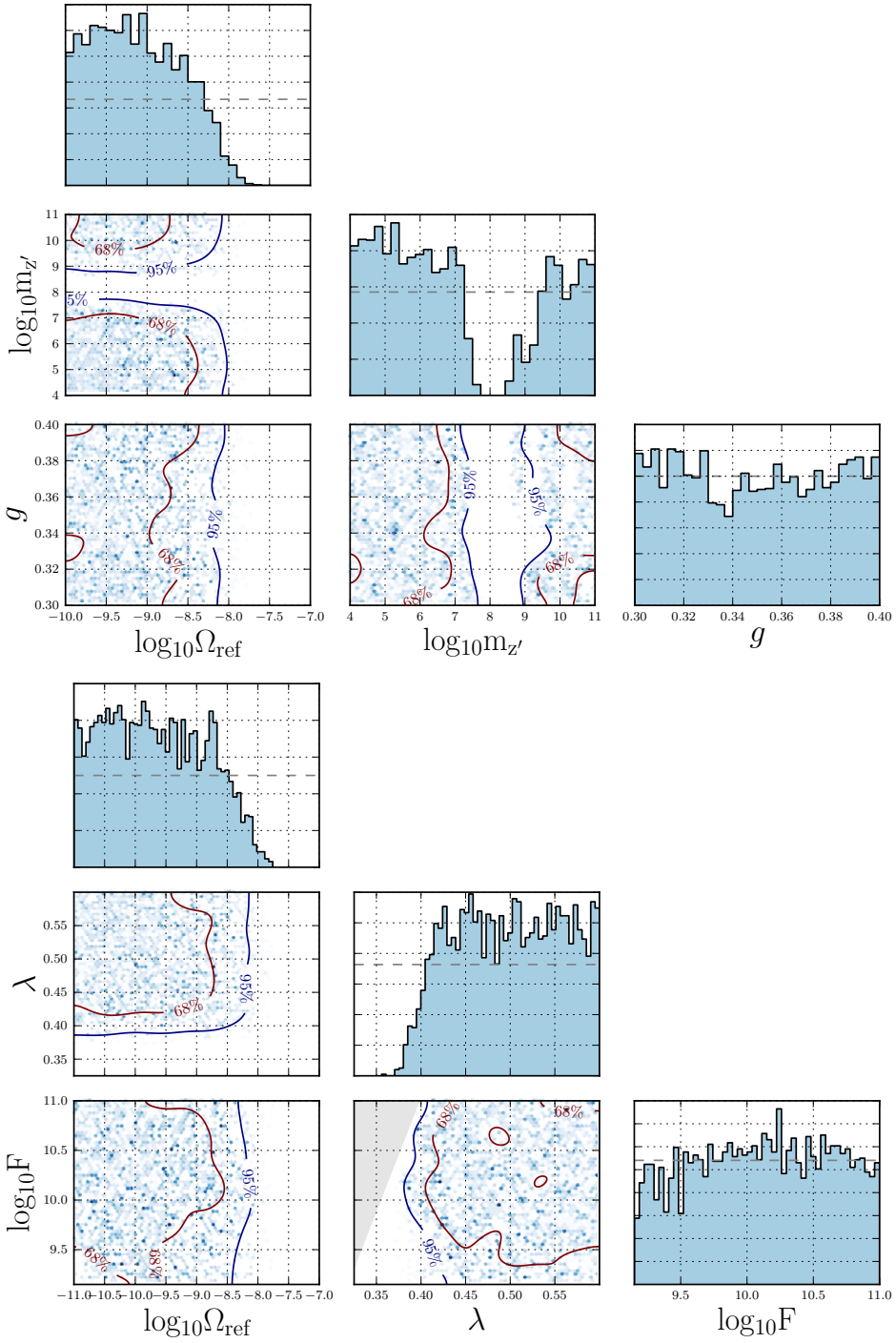


**Figure 4.8:** Constraints on the parameter space $(m_{Z'}, g)$ for Model I (top panel) and on the parameters $\lambda$ and $F$ for Model II (bottom panel), together with constraints on the astrophysical CBC background amplitude $\Omega_{\rm ref}$ using LVK data. The grey region in the bottom plot corresponds to a region where nucleation does not occur and the phase transition does not complete.

This model is based on a radiatively broken U(1) Peccei-Quinn symmetry [277], introduced to solve the strong CP problem, and leading to the appearance of a dark matter candidate – the axion. It extends the Standard Model by including just two new complex scalar fields, $S$ and $X$, which are Standard Model singlets, and both carry Peccei-Quinn charges.

The tree-level scalar potential is

$$V_{\text{tree}} = \lambda_S |S|^4 + \lambda_X |X|^4 + \lambda_{SX} |S|^2 |X|^2 \,. \tag{4.17}$$

It exhibits a flat direction for $\lambda_{SX} = -2\sqrt{\lambda_S \lambda_X}$, which can be parameterised by

$$(S, X) = (\sin\alpha, \cos\alpha)\frac{\sigma}{\sqrt{2}} \,, \;\; \sin^2\alpha = \frac{\sqrt{\lambda_X}}{\sqrt{\lambda_S} + \sqrt{\lambda_X}} \,. \tag{4.18}$$

The mass of the field along the direction orthogonal to $\sigma$ is

$$m_\tau = (4\lambda_S \lambda_X)^{1/4} \sigma \,. \tag{4.19}$$

Assuming that the condition for the flat direction holds at the renormalisation scale $\Lambda$, and switching the parameter $\Lambda$ for the field value at the minimum of the potential $F$, the zero temperature scalar potential is given by

$$V_0(\sigma) = \frac{2\lambda_S \lambda_X}{16\pi^2} \sigma^4 \left( \log \frac{\sigma}{F} - \frac{1}{4} \right) \,. \tag{4.20}$$

At the minimum $\sigma$ has a loop-suppressed mass, whereas the phase of $X$ is massless up to QCD anomalies, and becomes the axion with a decay constant $F_a = F \cos\alpha$. The finite temperature part of the effective potential is given by a formula analogous to (4.13), but with just a single term involving $m_\tau$. To prevent the finite temperature effects from moving the true vacuum

away from the flat direction, we set

$$\lambda_X = \lambda_S \equiv \lambda \ , \tag{4.21}$$

which is equivalent to imposing a $\mathbb{Z}_2$ symmetry at the level of the Lagrangian. As a result, Model II is described by just two parameters: $(\lambda, F)$.

**Constraints from LVK O1+O2+O3 data**

Similarly as for Model I, one can compute the FOPT parameters $\beta/H_{\rm RH}$ and $T_{\rm RH}$, and determine the GW spectrum. The ranges of parameters we consider are: $F \in [1.4 \times 10^9,\ 10^{11}]$ GeV and $\lambda \in [0.325, 0.6]$. A value of $F$ smaller than $1.4 \times 10^9$ GeV (corresponding to an axion decay constant of $10^9$ GeV) is experimentally excluded [333], whereas values of $\lambda$ lower than 0.325 correspond to cases when the phase transition does not complete, i.e., no nucleation occurs.

We again conduct a parameter estimation directly on the parameters of the model. In the case of Model 2 the dominant GW contribution comes from bubble collisions [277]. In the likelihood given by (3.4), $\Omega_{\rm GW} = \Omega_{\rm CBC} + \Omega_{\rm COLL}$, where $\Omega_{\rm COLL}$ is given by (4.9) and can be obtained from the underlying model parameters $(\lambda, F)$. The parameters used for the search are $\boldsymbol{\theta}_{\rm GW} = (\Omega_{\rm ref},\ F,\ \lambda)$ and the priors on $\Omega_{\rm ref}$, $F$ and $\lambda$ are summarised in Table 4.6. The lower panel in Figure 4.8 displays the exclusion regions implied by the current LVK data. The grey region represents part of the parameter space where no nucleation occurs and the phase transition does not complete. As shown in Figure 4.8, part of the parameter space can be excluded at a 95% CL. This mostly puts constraints on the values of $\lambda$, excluding smaller values, as these are the ones that give rise to the strongest GW signals. Furthermore, one notes consistency with the usual CBC upper limits found in this work, and in [331, 332]. We present a comparison between constraints on particle physics couplings from Models I and II using different parameter estimation approaches in Appendix E.3.

### 4.3.5 Future outlook

We complete our study by looking ahead and making projections for the sensitivity of 3G interferometers to a supercooled FOPT that could have occurred at energies inaccessible to particle colliders. The proposed Einstein Telescope and Cosmic Explorer are expected to extend our astrophysical horizon to distant redshift, revealing the majority of CBCs in the Universe. This will help subtract individual sources and reduce the astrophysical contribution to the GW background, in hope of revealing a cosmological background.

We simulate 400 signals containing the residual CBC background [146] and a bubble collision dominated supercooled phase transition for a range of $\beta/H_{\rm RH}$ and $T_{\rm RH}$ values. We then compute the log Bayes factor of a CBC+FOPT model to noise, and a CBC model only to noise; subtracting the two determines the preference for the presence of a FOPT signal in the data. The analysis is then repeated for the case of a dominant sound wave contribution to the FOPT signal. The 3G network used places ET at Virgo and two CEs at the Hanford and Livingston locations.

Our results are presented in Figure 4.9. With the future 3G detectors, we find that a significant part of the parameter space can be probed in both cases. Sound waves and bubble collisions dominated supercooled phase transition scenarios are depicted in the top and bottom panels of Figure 4.9, respectively.

#### Discussion

To demonstrate the huge opportunity for particle physics arising from GW searches, we carried out the pioneering study in which we used the data from the O1, O2 and O3 runs to perform a Bayesian analysis and set direct limits on the parameter space of particle physics models. In our analysis we focused on supercooled FOPTs, since they are naturally characterised by an enhanced signal strength, potentially already within the reach of current LVK detectors.

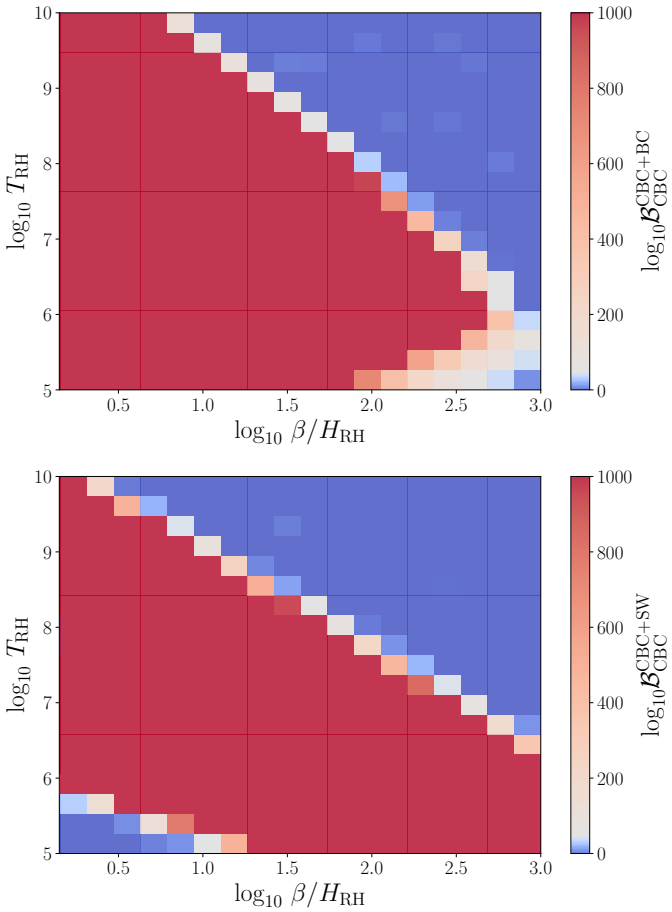


**Figure 4.9:** Preference for a model containing a supercooled phase transition and an astrophysical CBC background over a model with an astrophysical background only. Injections of a bubble collision (BC) dominated FOPT show great constraining power of such a signal with a network of 3G detectors (top), and similarly for injections of a sound waves (SW) dominated FOPT (bottom).

We applied our analysis to two well-motivated particle physics models, which address some of the most intriguing open questions about the Universe: the dark matter puzzle, the strong CP problem, the origin of the neutrino masses, and unification of forces. We place the Bayesian 95% upper limits on the parameter space of those models, providing valuable insight into the available room for new physics. The same strategy can be used to impose limits on other models exhibiting supercooled FOPTs. Apart from conducting the analysis using the available LVK O1-O3 data, we provide an outlook on the reach of 3G detectors. This methodology

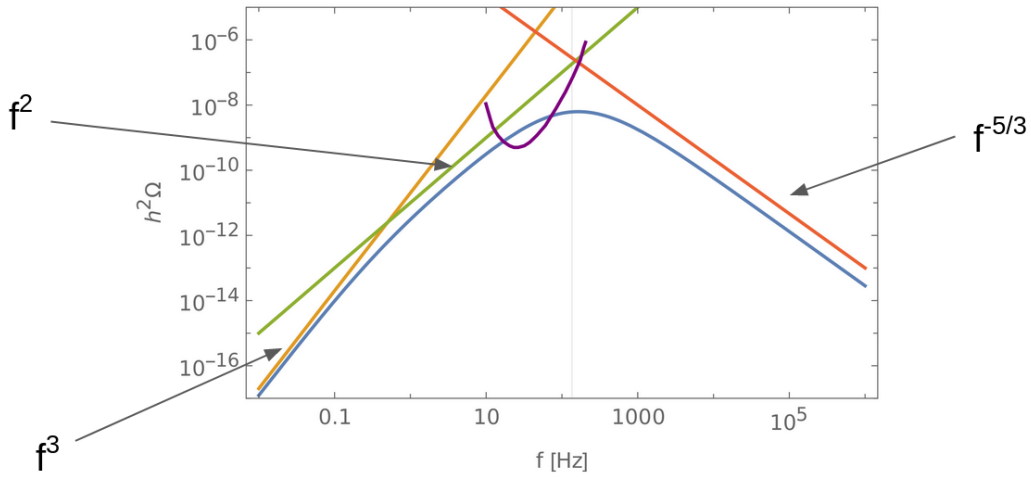


**Figure 4.10:** GWB spectrum from turbulence in the plasma during a FOPT as a function of frequency.

can also be applied to future LVK upgrades, as well as next-generation detectors.

We conclude the discussion on first-order phase transitions by commenting briefly on the typically subdominant FOPT contribution to the GWB - turbulence in the early Universe plasma.

### 4.3.6 Turbulence

The third, and final contribution to $\Omega_{\rm GW}$ from a first-order phase transition is turbulence. Simulations show that bubble collisions induce magnetohydrodynamic turbulence in the plasma. If the turbulence cascade follows a Kolmogorov spectrum, the GWs sourced are of the form [191]

$$\begin{aligned}\Omega_{\rm turb}h^2 &= 3.35\times10^{-4}v_{\rm w}\left(\frac{\beta}{H_{\rm pt}}\right)^{-1}\left(\frac{\kappa_{\rm turb}\alpha}{1+\alpha}\right)^{3/2}\left(\frac{100}{g_*}\right)^{1/3}\\ &\quad\times\left(\frac{f}{f_{\rm turb}}\right)^3\left(1+\frac{f}{f_{\rm turb}}\right)^{-11/3}\left(1+\frac{8\pi f}{h_{\rm pt}}\right)^{-1},\end{aligned}\tag{4.22}$$

with

$$f_{\rm turb}=2.7\times10^{-5}\frac{1}{v_{\rm w}}\frac{\beta}{H_{\rm pt}}\left(\frac{T_{\rm pt}}{100{\rm GeV}}\right)\left(\frac{g_*}{100}\right)^{1/6}{\rm Hz}.\tag{4.23}$$

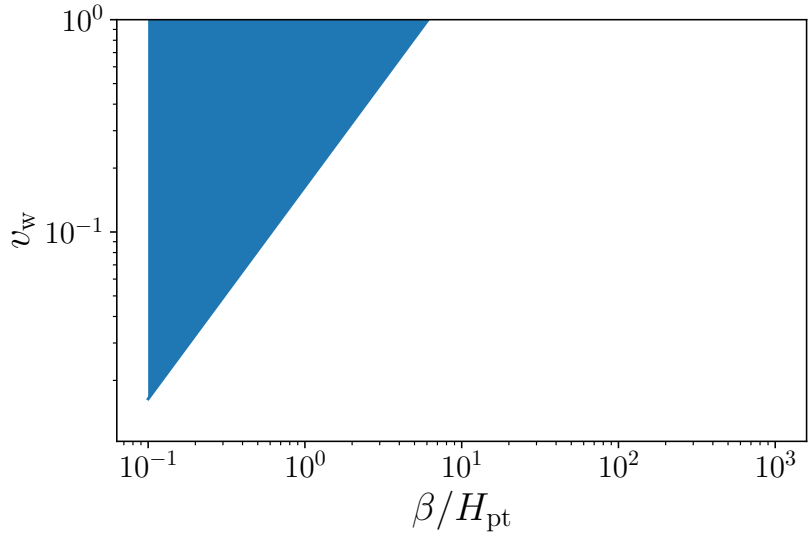


**Figure 4.11:** The blue shaded region represents the parameter space for which $\Omega_{\rm turb}$ goes as $f^3$ and not $f^2$ near the spectrum peak.

The turbulence component of the GWB is expected to be subdominant to both bubble collisions and sound waves.

In Figure 4.10 we can see that the frequency dependence differs from the other FOPT contributions, namely low-frequency spectrum does not scale as $f^3$ close to the peak, but $f^2$ instead. We investigate if there is a parameter space that leads to $f^3$ dependence closer to the peak frequency instead of $f^2$ as shown in Figure 4.10. We find this to be the case only for very large values of $v_w$ and extremely low values of $\beta/H_{\rm pt}$, see Figure 4.11. Since such a choice of parameters is not typical for an FOPT signal, we assume that the low-frequency spectral index of $\Omega_{\rm turb}$ is 2 and not 3. This particular behaviour is a consequence of cascading of energy to smaller scales in the turbulent plasma. Recent numerical simulations confirm a further plateauing of the infrared GW background [334] to a linear scaling with frequency followed by $f^{-8/3}$ at high frequencies. Furthermore, various numerical simulations produce varied high-frequency behaviour, e.g. $f^{-3/2}$ , $f^{-2}$ and $f^{-8/3}$ [335].

The large uncertainty in the shape of the turbulence GWB spectrum, and its anticipated subdominance to both sound wave and bubble collisions

contributions in the FOPT make it very difficult to search for this signal. However, there may be another way of searching for turbulence-sourced GWs. In the following section we focus on a highly probable attribute of the turbulent GWB - its non-zero polarisation, and we investigate if we can detect it with terrestrial interferometers.

## 4.4 Parity-violating GWB

Searches for an *unpolarised* isotropic GWB have been conducted in the past using data gathered by ground-based interferometer detectors LIGO [2] and Virgo [6], and this allowed upper limits on GWB energy density to be placed [107, 336, 337]. However, a multitude of mechanisms in the early Universe can create parity violation [338] that may manifest itself in the production of asymmetric amounts of right- and left-handed circularly polarised isotropic GWs. Since astrophysical sources of the GWB are unlikely to have this circular polarisation, a detection of such a signal can allow cosmologically sourced GWs to be distinguished from the astrophysically sourced component of the GWB. A closer analysis of polarised GWB can place constraints on parity-violating theories.

Numerous parity-violating effects on the GWB have been studied in the literature, including those resulting from the Chern-Simons gravitational term [339, 340, 341] and axion inflation [342]. Another potential chiral source for early Universe GWB is turbulence in the primordial plasma induced either from cosmological first-order (electroweak or QCD) phase transitions [343, 344, 345], or from the primordial magnetic fields that are coupled to the cosmological plasma [346, 347, 348, 349, 350]. Parity-violating effects on the GWB have been explored in detail before [351] from a previous LIGO-Virgo observing run [352], as well as studied in the context of current and future detector capabilities [353, 354, 355, 356, 357].

Since turbulence is a stochastic process, the GWs produced in the process are stochastic as well. Similarly, a parity-violating turbulent source

will produce circularly polarised GWs. Depending on the helicity strength of the source, there are two types of turbulence GW spectra [358, 359]. Turbulence dominated by energy dissipation at small scales leads to a helical Kolmogorov (HK) spectrum, whereas turbulence dominated by helicity dissipation at small scales leads to a helicity transfer (HT) spectrum. We focus on models that result in an HK spectrum, and consider the polarisation degree associated with them.

In what follows we adopt the formalism of [360] and present a method to detect parity violation in GW data. We first analyse existing GW data to place upper limits on a simple power law parity violation model for the normalised GW energy density $\Omega_{\rm GW}(f)$. We consequently study the GWB produced by turbulence in the primordial plasma and investigate what upper limits can be placed with the inclusion of KAGRA and improved LIGO and Virgo sensitivities.

The rest of the study is organised as follows: in 4.4.1 we present our methodology which we then apply to the parity violation models described in 4.4.2. In 4.4.4 we state our results from existing GW data as well as future prospects.

### 4.4.1 Searching for parity violation in GWB data

We use the plane-wave expansion of the metric $h_{ab}$ at cosmic time $t$ and position vector $\vec{x}$ [56]:

$$h_{ab}(t,\vec{x}) = \sum_A \int_{-\infty}^{\infty} df \int_{S^2} d\hat{\Omega}\, h_A(f,\hat{\Omega}) e^{-2\pi i f(t-\vec{x}\cdot\hat{\Omega})} e^A_{ab}(\hat{\Omega}), \tag{4.24}$$

where $e^A_{ab}(\hat{\Omega})$ is the polarisation tensor for a wave travelling in direction $\hat{\Omega}$. We use the circularly polarised bases $e^R = (e^+ + ie^\times)/\sqrt{2}$ and $e^L = (e^+ - ie^\times)/\sqrt{2}$ to obtain the right- and left-handed modes $h_R = (h_+ - ih_\times)/\sqrt{2}$ and $h_L = (h_+ + ih_\times)/\sqrt{2}$, respectively. Right- and left-handed correlators can then be written as

$$\begin{pmatrix} \langle h_R(f,\hat{\Omega}) h_R^*(f',\hat{\Omega}')\rangle \\ \langle h_L(f,\hat{\Omega}) h_L^*(f',\hat{\Omega}')\rangle \end{pmatrix} = \frac{\delta(f-f')\delta^2(\hat{\Omega}-\hat{\Omega}')}{4\pi} \begin{pmatrix} I(f,\hat{\Omega}) + V(f,\hat{\Omega}) \\ I(f,\hat{\Omega}) - V(f,\hat{\Omega}) \end{pmatrix}, \tag{4.25}$$

where $I, V$ are the Stokes parameters, with $V$ characterising the asymmetry between right- and left-handed polarised waves, and $I(\geq |V|)$ the wave's total amplitude. For $V = 0$, (4.25) would be simply the correlator for unpolarised isotropic GWB (1.34). The standard cross-correlation statistic $\hat{C}_{d_1 d_2}$ in the case of a polarised background estimates a modified GWB spectrum $\Omega'_{\rm GW}$ [361, 56]:

$$\Omega'_{\rm GW} = \Omega_{\rm GW}\left[1 + \Pi(f)\frac{\Gamma_V^{d_1 d_2}(f)}{\Gamma_I^{d_1 d_2}(f)}\right] \tag{4.26}$$

where

$$\begin{aligned} \Gamma_I^{d_1 d_2}(f) &= \frac{5}{8\pi}\int d\hat{\Omega}(F_{d_1}^{+} F_{d_2}^{+*} + F_{d_1}^{\times} F_{d_2}^{\times *}) e^{2\pi i f \hat{\Omega}\cdot\Delta\vec{x}}, \\ \Gamma_V^{d_1 d_2}(f) &= -\frac{5}{8\pi}\int d\hat{\Omega}(F_{d_1}^{+} F_{d_2}^{\times *} - F_{d_1}^{\times} F_{d_2}^{+*}) e^{2\pi i f \hat{\Omega}\cdot\Delta\vec{x}}. \end{aligned} \tag{4.27}$$

We denote by $\Gamma_I^{d_1 d_2}$ the standard overlap reduction function of two detectors $d_1, d_2$, and by $\Gamma_V^{d_1 d_2}$ the overlap function associated with the parity violation term. The polarisation degree, $\Pi(f) = V(f)/I(f)$, takes on values between -1 (fully left polarisation) and 1 (fully right polarisation), with $\Pi = 0$ being an unpolarised isotropic GWB. The variance associated with the estimator $\hat{C}_{d_1 d_2}$ is the same as for the isotropic search, see (1.37).

To proceed we perform parameter estimation and fit GW models to data using a hybrid frequentist-Bayesian approach [362]. We assume that correlated-noise sources have been either filtered out [88] or accounted for [48]. The normalised GW energy density model we fit to the data is $\Omega'_{\rm GW}(f, \boldsymbol{\theta})$, with parameters $\boldsymbol{\theta}$ including both GW parameters as well as parameters of the $\Pi(f)$ model.

### 4.4.2 Sources of parity violation

We will apply our method to two classes of GW models. First, we perform a generic search for a parity violating GWB, with power law behaviour (1.27) and $f_{\rm ref} = 25$ Hz. The amplitude prior we use is log-uniform between $10^{-13}$ and $10^{-5}$, and the spectral index prior is a Gaussian distribution centred at 0 with a standard deviation 3.5, following the priors used in [336]. We will search for this model in the currently available GWB data and place upper limits on its parameters.

Second, we use a broken power law spectral shape, motivated by high energy physics. Since we have not detected a GWB yet, we will investigate detection prospects of this more complicated turbulence model with future improved detector sensitivities and forecast what one can learn about its parameters. Extensions of the Standard Model of particle physics can imply parity violation at the electroweak energy scale being manifested through helical (or chiral) turbulent motion [363, 364]. Parity-violating turbulent sources will produce circularly polarised GWs [365], with a broken power law spectral shape peaking at the characteristic frequency of the source. Recent numerical simulations show that at frequencies below the characteristic frequency $\Omega_{\rm GW} \sim f$ [298]. Above the characteristic frequency, the decaying power law depends on the turbulence model [366]. As an example, in our analysis we focus on choice model [367]:

$$\Omega_{\rm GW}(f) = \begin{cases} \Omega_{\rm peak} \left(\frac{f}{f_{\rm peak}}\right) & , \quad f \leq f_{\rm peak} \\ \Omega_{\rm peak} \left(\frac{f}{f_{\rm peak}}\right)^{-8/3} & , \quad f > f_{\rm peak} \, . \end{cases} \tag{4.28}$$

We set $f_{\rm peak} = 25$ Hz, the most sensitive frequency band of LVK detectors, to find the most optimistic prospects of detecting a broken power law GWB model.

### 4.4.3 Degree of parity violation

In addition to modelling the GW spectrum, we need a model for the amount of polarisation of the turbulence spectrum.

Two factors influence the shape of $\Pi(f)$: type of turbulence and helicity strength (see Fig. 1 in [368]). To understand these factors, let us look at the velocity two-point function of a turbulent fluid

$$\langle u_i^*(\boldsymbol{k}) u_j(\boldsymbol{k}')\rangle = (2\pi)^3 \delta^{(3)}(\boldsymbol{k}-\boldsymbol{k}')[P_{ij}P_S(k) + i\epsilon_{ijl}\hat{k}_l P_H(k)], \tag{4.29}$$

with $P_{ij} = \delta_{ij} - k_i k_j/k^2$ and $\epsilon_{ijk}$ the 3-dimensional Levi-Civita symbol. Here $P_S(k)$ is the symmetrical and $P_H(k)$ is the helical part of the power spectrum. These are modelled as power laws $P_S(k) = S_0 k^{n_S}$ and $P_H(k) = A_0 k_S^{n_S - n_H} k^{n_H}$, where $S_0$ and $A_0$ are the amplitudes for the symmetric and helical parts of the velocity spectrum respectively, and $k_s$ is the turbulence cut-off scale. The ratio of $A_0$ to $S_0$ characterises the helicity strength. Imposing causality ($P_S(k) \geq P_H(k)$), maximum helicity occurs for turbulent motion with $A_0/S_0 = 1$. The spectral indices in the $P_S(k)$ and $P_H(k)$ power law models are determined by the type of turbulence.

An HK spectrum is dominated by energy dissipation at small scales, whereas an HT spectrum is dominated by helicity dissipation at small scales. Depending on helicity strength, we observe either HK or a combination of HK and HT spectra. HK spectrum is observed in weakly helical turbulence at all scales $k$. For strongly helical turbulence, however, HT spectrum is observed at small $k$, and HK at large $k$. For the HK spectrum we have $n_S = -11/3$, $n_H = -14/3$, while for HT the spectral indices are $n_S = n_H = -13/3$.

Previous studies [365, 369] calculated, numerically, the net circular polarisation of GWs for different initial turbulent conditions to get the polarisation degree $\Pi$ over a range of scales, and found frequency-dependent models of $\Pi$. In the following, we will study both the simplified $\Pi = \text{const.}$ model, as well as a frequency-dependent polarisation model. In the former

simplified case, the prior for $\Pi$ is uniform between -1 and 1. For the latter case, we adopt the functional form $\Pi(f) = \pm(f/1\,\mathrm{Hz})^{\beta}$ with a uniform prior on $\beta$ between -2 and 0. This simple functional form is motivated by the theoretical models predicting $\Pi$ to decay with frequency [369, 370]. Furthermore, since we consider frequencies larger than 1 Hz (terrestrial detectors are limited by seismic noise at low frequencies), this choice ensures that $\Pi(f)$ is well defined and remains within the physical range [-1,1].

### 4.4.4 Can we determine the polarisation degree?

We place upper limits on parameters of the simpler, power law, GWB model using LVK data. Following this, we discuss detection prospects of model-dependent, broken power law turbulence spectra as the sensitivity of the interferometers increases and more interferometers are added to the network.

#### O3 results

We search for a power law GWB spectrum, as described in (1.27), with a simple $\Pi$ = const. polarisation model in the recent O3 data [337]. We find no preference for a particular $\Pi$ value in the [-1,1] prior range. We find the upper limit on the amplitude of the power law to be $\Omega_{\mathrm{ref}}^{95\%} = 7.0 \times 10^{-9}$. Calculating the Bayes factor, we find $\ln \mathcal{B}_{\Pi=0}^{\Pi\neq 0} = -0.02$, concluding that there is no preference for parity violation models versus no parity violation ones.

It is worth noting that we found the HLV network to be more sensitive to right-hand polarisations compared to left-hand ones. Plotting the $\Omega_{\mathrm{ref}}$ versus $\alpha$ confidence curve generated from O3 data, one observes that it is easier to constrain $\Omega_{\mathrm{ref}}$ for entirely right-handed polarised GWs ($\Pi = 1$) than it is for left-handed ($\Pi = -1$) ones, see Figure 4.12. Excluding the HL detector baseline however, results to a less obvious polarisation bias for right- or left-handed GWs.

To understand the origin of this bias we investigate the asymmetry in the overlap reduction ratio, $\varsigma^{\mathrm{HL}} \equiv \Gamma_V^{\mathrm{HL}}/\Gamma_I^{\mathrm{HL}}$, for the HL detector pairing

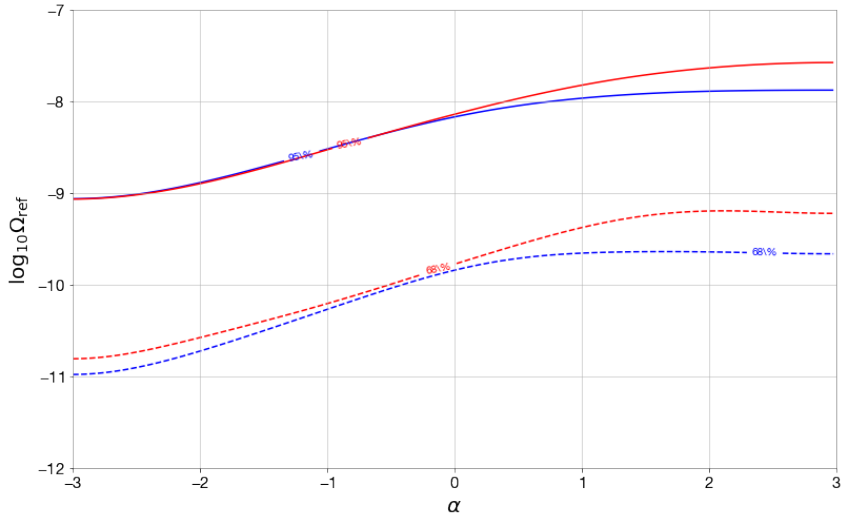


**Figure 4.12:** $\Omega_{\rm ref} - \alpha$ confidence curve at 95% (solid) and 68% (dashed) level for assumed $\Pi = \pm 1$. We see more stringent constraints in the $\Pi = 1$ case (blue) than with the $\Pi = -1$ case (red).

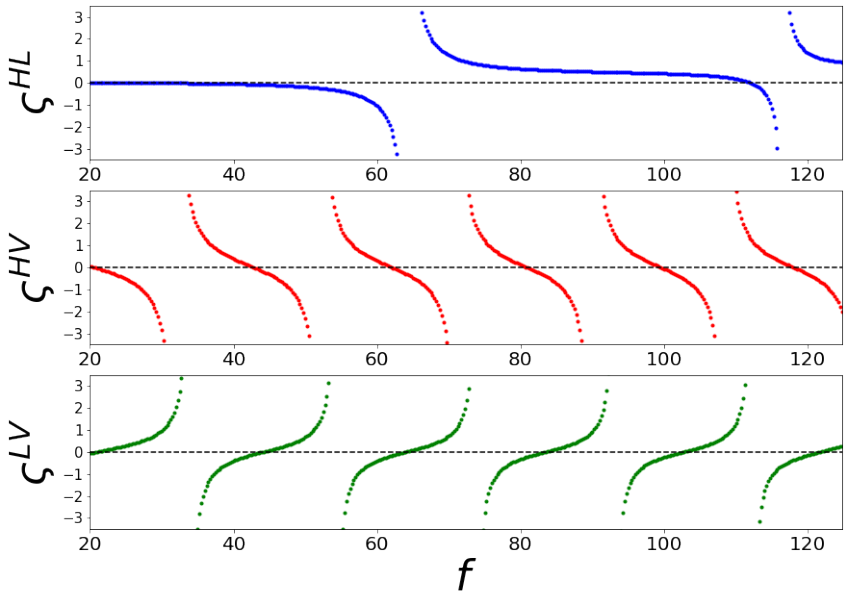


**Figure 4.13:** Overlap reduction function ratio $\varsigma$ for HL (top), HV (middle) and LV (bottom) baselines.

plotted in Figure 4.13, along with the corresponding overlap reduction ratios $\varsigma^{\rm HV}$ and $\varsigma^{\rm LV}$ for the HV and LV baselines, respectively. While $\varsigma^{HV}$ and $\varsigma^{LV}$ are roughly periodic in the considered frequency range ($f \lesssim 130\,$Hz), $\varsigma^{HL}$ is preferentially positive in this frequency range. Preferentially positive $\varsigma^{HL}$ combined with $\Pi > 0$ in (4.27) leads to a larger $\Omega'_{\rm GW}$, hence leading to

stricter constraints on right-hand polarised signals.

In addition to the frequency-independent, $\Pi(f) = \text{const.}$ model, we search for a power law parity violation signal, assuming a right- and left-handed frequency-dependent degree of polarisation $\Pi(f) = \pm(f/1\,\text{Hz})^{\beta}$. There is no detection of a GWB power law signal with frequency-dependent polarisation degree, but for an assumed right- and left-handed polarisation we can place an upper limit on the amplitude, $\Omega_{\text{ref}}^{95\%} = 4.9 \times 10^{-9}$ and $\Omega_{\text{ref}}^{95\%} = 7.4 \times 10^{-9}$, respectively, after marginalising over $\alpha$ and $\beta$. Positive polarisation was expected to have stricter upper bounds based on HLV network's higher sensitivity to entirely right-hand polarisation seen in Figure 4.12. Since more stringent, we only present positive polarisation results. Figure 4.14 shows posterior distribution of amplitude, $\Omega_{\text{GW}}$, and spectral index, $\alpha$, of a power law GW signal, as well as the posterior of the polarisation degree parameter, $\beta$. The $\alpha$ posterior is similar to the Gaussian prior distribution, implying that we cannot deduce anything about the spectral index, $\alpha$, of the GW power law from the O3 data. Finally, with O3 data, we do not constrain the $\beta$ parameter space.

Since we see no detection of a parity-violating signal in O3 data when we use a simple power law model with a frequency-independent polarisation degree, as well as a frequency-dependent one, we do not proceed to search for the broken power law model in (4.28) – such a model would also be undetectable with the data from O3. Instead, we study the prospects of detecting the complex model with a more sensitive GW detector network.

## Future prospects

With each observing LIGO-Virgo run, we see improved upper limits on the GWB, expecting to have a detection in one of the future upgrades of the detector network. Let us therefore investigate the possibility of detecting a parity violation signal with the A+ sensitivity of LIGO, AdV+ sensitivity of Virgo, and including KAGRA at Design sensitivity to the network [179]. We simulate the cross-correlation function that contains a GW signal as

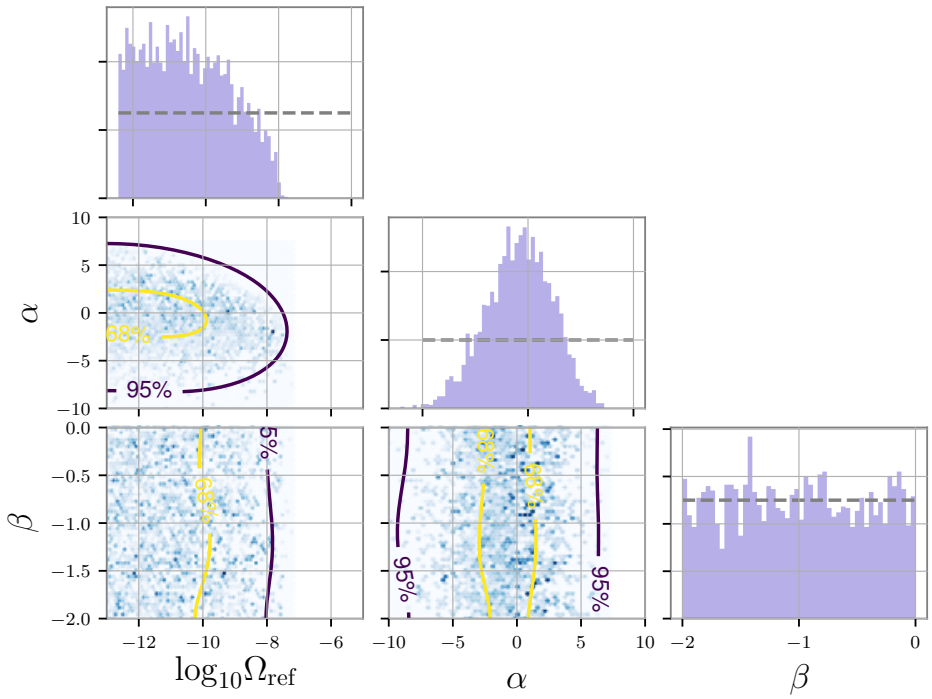


**Figure 4.14:** 95% CL and posterior distribution obtained using O3 data for the model of power law GWB spectrum with parity violation $\Pi(f) = (f/1\,\mathrm{Hz})^{\beta}$.

well as instrumental noise of the detectors. We note that our simulations are for three years observation time. Adding more GW detectors to the network and extending the observation time both lead to improvements in our sensitivity.

Ultimately, we would like to explore the prospects of a detection of a physically motivated, parity-violating signal. This is why in the following section we focus on the detection of a turbulence signal, and not that of a simple power law model. We simulate a broken power law $\Omega_{\rm GW}$, induced by turbulence as described in 4.4.2 [cf. (4.28)]. To investigate the detection prospects of such a signal, we vary the amplitude of the simulated spectrum by doing 1000 simulations log-spaced between $\Omega_{\rm peak} \in [10^{-10}, 10^{-7}]$. Going forward, we assume the polarisation dependence of the simulated spectrum is given by right-handed polarisation $\Pi(f) = (f/1\,\mathrm{Hz})^{-1/2}$, as our results indicated stronger positive polarisation sensitivity in the HLV network. We discuss below our results and their dependence on a devia-

tion of the polarisation parameter $\beta$ from the $-1/2$ value.

Figure 4.15 shows the variation of signal-to-noise Bayes factor, $\mathcal{B}$, of the simulations, focusing particularly in the region $\Omega_{\text{peak}} \in [10^{-10}, 10^{-8}]$. A $\ln \mathcal{B}$ factor of 8 is equivalent to a frequentist SNR of 4 [56], and as such, we take this value to be our detection threshold. Consequently, all points above the solid line in Figure 4.15 will be considered as detected. This leads to an upper limit of $\Omega_{\text{peak}} = 1.5 \times 10^{-9}$; any *louder* signal is expected to be detected with great significance by the A+ detectors.

However, even if we can confidently claim a detection of a turbulent, broken power law GWB, we might not be able to constrain its polarisation. Repeated simulations show that the spectral amplitude $\Omega_{\text{peak}}$ plays the main role in the recovery of the polarisation content. More precisely, we find that stronger signals yield better results for the recovery of the $\Pi(f)$ model, i.e. of the $\beta$ parameter. Our analysis also shows that the inclusion of simulated data from the Virgo and KAGRA detectors is critical in recovering the polarisation of a simulated GWB. We find that for simulations with amplitude $\Omega_{\text{peak}} \geq 5 \times 10^{-8}$, we confidently recover the $\beta = -1/2$ value, see Figure 4.16. We quantify our confidence in recovery of $\beta$ by requiring 95% ($2\sigma$) of its posterior distribution to be within 0.1 of the simulated value.

Therefore, we conclude that the amplitude of the GW spectrum needs to be more than 30 times larger than its detection threshold in order to recover the $\beta = -1/2$ parameter value, and detect a polarisation. Only with such a strong detection, one can study the polarisation model and its implications for parity violation theories.

Weaker GWB may still allow us to place an upper limit on $\beta$. Posteriors for these weak GWB simulations are skewed toward the lower end of the $\beta$ prior. To demonstrate this, Figure 4.17 shows the variation of the median value of $\beta$ posteriors as a function of the simulated spectral amplitude. We find that the median of the posterior starts to deviate downward from $\beta = -1/2$ for $\Omega_{\text{peak}} < 5 \times 10^{-8}$, agreeing with our previously stated definition

of confident recovery. For even weaker simulations, $\Omega_{\rm peak} \lesssim 5 \times 10^{-9}$, the signal becomes too weak to constrain polarisation at all.

To check the dependence of our results on the simulated value of the $\beta$ parameter, we repeat the analysis for $\beta = -1$ and 0 [369]. The detection threshold for each of the data sets is the same as before, $\Omega_{\rm peak} = 1.5 \times 10^{-9}$, suggesting that *when* we claim a detection, it will be independent of the amount of polarisation of the signal. However, the signal strength needed to successfully recover $\beta$ depends on the polarisation model. Namely, the smaller the value of $\beta$ is, the stronger the simulation amplitude is needed. For $\beta = -1$ we are unable to recover it within our simulation range. The $\beta = 0$ simulation, with a frequency-independent polarisation, is recovered with signals of amplitude $\Omega_{\rm peak} = 1 \times 10^{-8}$, only 7 times stronger than the simulation threshold. The only simulation that successfully recovers $\beta$, and is *not* already ruled out by the first three LIGO-Virgo observing runs, is $\beta = 0$, implying that even if we include 4 detectors, and consider 3 years of observation time, it will be challenging to probe frequency-dependent polarisation models.

## Discussion

We searched for GWB generated by sources of parity violation in recent GW data and simulated GW data (future sensitivities of LVK detectors). We found no evidence for such a signal in O3 data and we placed an upper limit on the amplitude of a power law GW model, $\Omega_{\rm ref}^{95\%} = 4.9 \times 10^{-9}$, $7.4 \times 10^{-9}$ for right- and left-hand polarisation, respectively. A bias for constraining right-handed polarised waves was found to be due to the geometry of the LIGO Hanford-Livingston detector baseline, leading to better constraints of $\Pi > 0$ polarisations.

When simulating data for future detection prospects, we considered a chiral turbulence source in the early Universe. The results we obtained are model-dependent. For a GWB modelled as a broken power law (4.28), the LVK detector network is sensitive to peak amplitudes down to

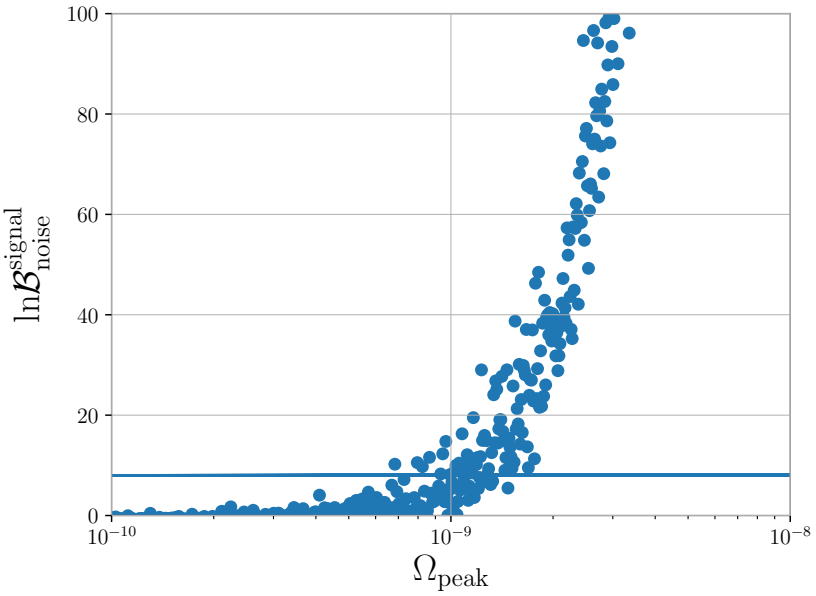


**Figure 4.15:** Bayes factor as a function of amplitude of the simulated signal. Each point represents one of our 1000 simulations. The solid line represents $\ln \mathcal{B}^{\text{signal}}_{\text{noise}} = 8$.

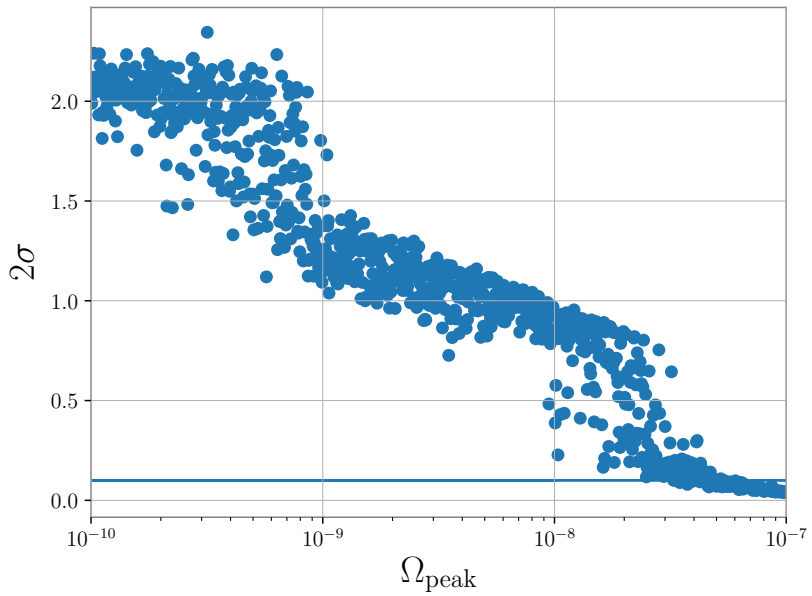


**Figure 4.16:** Variation of $2\sigma$ value of the $\beta$ posterior for each of the 1000 simulations. The solid line represents $2\sigma = 0.1$.

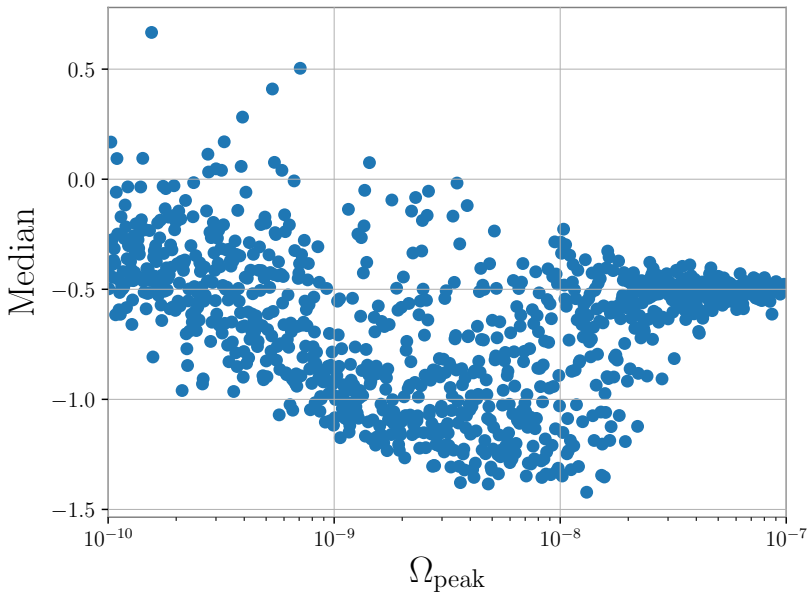


**Figure 4.17:** Variation of the median of the $\beta$ posterior for each of the 1000 simulations.

$\Omega_{\rm peak} = 1.5 \times 10^{-9}$. Our analysis showed that we are able to better estimate the parameters of the parity violation model for stronger simulated GW backgrounds, as well as when the Virgo/KAGRA detectors are included in the analysis, highlighting the importance of having a multi-detector network. For $\beta = -1/2$ we found that successful recovery of $\beta$ requires GWB amplitude of at least $\Omega_{\rm peak} = 5 \times 10^{-8}$, which is excluded by existing GW data. Hence, even if we detect a turbulence signal, we might not be able to deduce its polarisation. The recovery of frequency-independent polarisation ($\beta = 0$) showed more promising results and we might be able to constrain such signals in the future observing runs.

Although this study used the current LIGO and Virgo detectors as well as the upcoming KAGRA detector, it would be interesting to apply the same study to additional ground detectors added to the network such as LIGO-India, as well as next-generation detectors. Note that due to uncertainty in geographical locations (i.e. uncertainty in ORFs) of the planned terrestrial detectors, the study cannot be extended to these at the moment.

## 4.5 Afterword

In this chapter we have demonstrated the wide reach GWB studies can have on different areas of physics: from astrophysics and particle physics to early Universe cosmology.

Astrophysical background from pop III-seeded CBCs presents a complementary tool to the individual detections of these mergers, and it can measure average properties of the population. Detecting a first-order phase transition GWB spectrum would hint at Beyond Standard Model physics at, or above, the electroweak scale. With such a detection we could identify the masses and couplings of the underlying particle physics model, as we showed in the example of a supercooled FOPT. Furthermore, a non-zero polarisation of the GWB may give constraints on inflation or help describe turbulent motion of the plasma in the early Universe. It is certain that as we lower the sensitivity with future upgrades and the next generations of GW detectors, we continue to push the frontiers of theoretical physics.

Until now, we have considered GR to be the correct description of gravity. In the next chapter we will put this assumption to test by exploring modified gravity theories and their astrophysical and GW signatures.

# Chapter 5

# Modifications to gravity

## 5.1 Foreword

General relativity has exhibited immense success in Solar System tests [371], as well as weak-field [372] and strong-field regimes (e.g. merger events [373] and pulsars [374]), in recent years. While the success of GR strongly suggests that this theory is indeed a good description of gravity, exploring modifications to it is an important test of the theory itself. Moreover, a modification of GR may make it UV-complete, or provide a natural explanation of the current accelerated expansion of the Universe without the need of a dark energy component [375].

The widely celebrated gravitational-wave event GW170817 which saw two neutron stars merging, not only in the gravitational spectrum [376], but in the electromagnetic spectrum too, had large consequences on the field of modified gravity. Comparing the time delay between the gravitational and the electromagnetic signal placed a stringent constraint on the difference of the speeds of the two to be less than 1 part in $10^{-15}$ [377]. This constraint ruled out theories of gravity that predicted a significant deviation of the propagation speed of gravitational waves from the speed of light (see constraints placed in e.g. [378], [379], [380]). The challenge and important task is to identify the most promising surviving theories and find ways to test them given the currently available data.

In this chapter we motivate massive gravity, and present constraints we have placed on a particular formulation of it, namely quasi-dilaton massive gravity (QDMG). We finish the chapter with statements on a general class of modified gravity theories that leads to a difference in GW and light speed in the LISA frequency band. All calculations presented below assume natural units, $c = \hbar = 1$.

## 5.2 Introduction to massive gravity

It is widely accepted that the graviton, as Einstein's theory of gravity suggests, is a massless particle of spin-2 with 2 degrees of freedom. Promoting the graviton from a massless to a massive spin-2 field, however, is a challenge that has intrigued physicists for a long time. In fact, the first attempts to write down an action for a massive spin-2 gravity field date back to the 1930s. Fierz and Pauli recognised that the new additional mass term would need to preserve diffeomorphism invariance, hence simply a linear combination of $h^{\mu\nu}h_{\mu\nu}$ and $h^{\mu}_{\mu}h^{\nu}_{\nu}$ would not suffice. They solved this issue by using a method developed by Stückelberg a few years earlier for the case of Proca fields [381]. Adding the so-called Stückelberg field, $\chi_\mu$, they obtained what is now referred to as the Fierz-Pauli term [382]

$$\mathcal{L}_{\rm FP} = -\frac{1}{8}m^2\Big((h_{\mu\nu} + 2\partial_{(\mu}\chi_{\nu)})^2 - (h + 2\partial_\mu\chi^\mu)^2\Big), \tag{5.1}$$

where, under a diffeomorphism given by

$$h_{\mu\nu} \to h_{\mu\nu} + \partial_{(\mu}\epsilon_{\nu)}, \tag{5.2}$$

the fields transform as

$$\chi_\mu \to \chi_\mu - \frac{1}{2}\epsilon_\mu. \tag{5.3}$$

The Stückelberg field is commonly split into its vector and scalar part

$$\chi_\mu = \frac{1}{m}A_\mu + \frac{1}{m^2}\eta_{\mu\nu}\partial^\nu\pi. \tag{5.4}$$

Note that now there are 5 degrees of freedom in total: two tensors, two vectors [1] and one scalar, as is expected for a massive spin-2 field. The helicity-1 modes decouple from external sources, but the helicity-0 mode couples directly to matter and introduces the vDVZ discontinuity [383]. The problem of the discontinuity was solved in 1972, where including non-linear kinetic terms of $\pi$ had the effect of screening the new degree of freedom, a process known as the Vainshtein mechanism [384].

Consequently, the Fierz-Pauli treatment was successfully finalised by the early 1970s. However, this is a treatment of a linearised gravity theory, where the massive spin-2 field is a perturbation to the Minkowski background as discussed in 1.1.1. What we are after, of course, is a full theory of gravity. Enforcing non-linear diffeomorphism invariance introduces further complications in the form of ghost instabilities, higher order derivatives of $\chi_\mu$. The negative kinetic terms lead to energy unbounded from below and therefore an ill-defined theory. It took until 2010 for the problem of ghosts to be resolved by de Rham, Gabadadze and Tolley (dRGT) [385]. But before their work, came the work of Dvali, Gabadadze and Porrati in 2000, with DGP theory representing an important milestone on the road to a ghost-free theory of massive gravity [386].

Developed in 2000, DGP theory is the first attempt at a braneworld approach to massive gravity. A massless spin-2 graviton in 5 dimensions has 5 independent polarisations, the same number of degrees of freedom that a massive spin-2 graviton has in 4 dimensions. Perhaps this coincidence is what inspired the line of reasoning followed by Dvali et al. They started with a 5-D Einstein-Hilbert action, and a 4-D brane located at a single point in the extra dimension with all of the Standard Model confined to it. Projecting the resulting "Einstein's equations" from 5 to 4 dimensions gives rise to the linearised Fierz-Pauli mass term, an exciting discovery for anyone who has ever performed the calculation. The theory contains no

[1] We work in the Coulomb gauge with $\partial_i A^i = 0$.

ghosts, since one starts from a 5-D theory equivalent to GR. Interestingly, the graviton comes out not as a propagator with a pole, but as an infinite sum of free propagators with mass $\mu$, and with a resonance at $\mu = 0$, the so-called "soft mass". This extremely simple and elegant theory goes on to explain late-time acceleration of the Universe in one of the branches of its solution. As tempting as it is, one should not be swayed by the beauty of DGP, because this theory has been ruled out, both by cosmology constraints [387], and more recently by gravitational waves [388]. In fact, DGP is a great example of how much constraints matter: constraining a modified gravity model is just as important as formulating it.

Despite the DGP braneworld model being ruled out, it served its purpose in helping develop crucial ideas for massive gravity since dRGT, bigravity and multigravity, all rely on the existence of a 5th dimension. In these theories, the extra dimension is no longer continuous like in DGP, but it is instead discretised. To every point in the extra dimension, we assign a 4-D metric. If we allow only nearest-neighbour interaction between the metrics, we obtain multigravity. For dRGT and bigravity, the extra dimension is discretised and reduced to only two points, the difference being that in dRGT only one of the metrics is dynamical, whereas in bigravity this is true for both metrics. The interactions between the metrics bring about a mass term in the Lagrangian, which now is in the form of a pole in the propagator, i.e. a "hard mass". The action for dRGT is of the following form:

$$S_{\text{dRGT}} = \int \mathrm{d}^4x\sqrt{-g}\Big[-\frac{M_{\text{Pl}}^2}{2}R(g) + m^2M_{\text{Pl}}^2\sum_{n=0}^{4}\alpha_n\mathcal{L}_n(\mathcal{K}(g,f)) + \mathcal{L}_{\text{m}}(g,\Phi)\Big]. \tag{5.5}$$

The two metrics, $g_{\mu\nu}$ and $f_{\mu\nu}$, are the dynamical and the fiducial metric respectively. The fiducial metric enters the Lagrangian only through the interaction term with the dynamical metric. In other words, it does not directly couple to the matter fields, $\Phi$, and it does not explicitly affect the

geodesics. The fiducial metric is generally defined in terms of the Stückelberg fields, $f_{\mu\nu} = \partial_\mu \phi^a \partial_\nu \phi^b \eta_{ab}$, where $\phi^a = x^a - \frac{1}{M_{\rm Pl}} \chi^a$. The interaction term is parameterised by the matrix $\mathcal{K} = I - \sqrt{g^{-1} f}$, with its eigenvalues in the form of elementary symmetric polynomials, $\mathcal{L}_n$ (explicitly defined in Appendix F.1). The coefficients $\alpha_n$ are chosen such as to avoid any ghost instabilities.

The $\mathcal{K}$ matrix interaction term, with the square root of the two metrics, makes calculations in dRGT significantly non-trivial. In order to attempt any analytic analysis of the theory, one can resort to several different approaches, and the most frequently used are:

- assume proportionality, $g_{\mu\nu} = C^2 f_{\mu\nu}$ [389],
- set $f_{\mu\nu}$ to be the Minkowski metric and $g_{\mu\nu}$ to be a time-dependent Schwarzschild metric [390],
- take the decoupling limit [390].

We resort to taking the decoupling limit, since the second approach is more useful when investigating black holes solutions, and we see no obvious reason why the proportionality condition in the first approach should hold in the most general case.

The name given to the decoupling limit is rather misleading, since it is not an actual limit. It is a scaling that *preserves* all of the physical propagating degrees of freedom, and separates tensor, vector and scalar modes. We expect new interactions in the theory to arise at an energy scale in-between the graviton mass, $m$, and the Planck mass, $M_{\rm Pl}$. The Lagrangian in the decoupling limit is derived by keeping the so-called decoupling scale, $\Lambda_3 = \left(m^2 M_{\rm Pl}\right)^{1/3}$, constant, and letting $M_{\rm Pl} \to \infty$ and $m \to 0$. One can think of it as an expansion in $1/M_{\rm Pl}$, with the relative contribution of the terms in the expansion determined by the above-mentioned scaling relations. Note that in the case $M_{\rm Pl} \to \infty$, the dynamical metric reduces to Minkowski (canonically normalised perturbation, $\frac{1}{M_{\rm Pl}} h_{\mu\nu} \to 0$), and the

Einstein-Hilbert term reduces to its linear form. From here it is clear that the decoupling limit is not appropriate if we are considering non-linear gravity regimes. If, however, we are looking at weak-field gravity systems, this is an acceptable simplification. The resulting Lagrangian, in the absence of any matter, with $\hat{\mathcal{E}}^{\alpha\beta}_{\mu\nu}$ as the linearised Einstein tensor on the Minkowski background,

$$\mathcal{L}^{\rm DL}_{\rm dRGT} = -\frac{1}{4}\Big(h^{\mu\nu}\hat{\mathcal{E}}^{\alpha\beta}_{\mu\nu}h_{\alpha\beta} + \sum_{n=2}^{5}\frac{c_n}{\Lambda_3^{3(n-2)}}\mathcal{L}^{(n)}_{\rm Gal}[\pi] - \frac{2(\alpha_3+4\alpha_4)}{\Lambda_3^6}h^{\mu\nu}X^{(3)}_{\mu\nu}[\Pi]\Big), \tag{5.6}$$

shows the scalar degree of freedom to acquire a galileon symmetry. The new additional symmetry makes it possible to attempt an analytical treatment of the theory. We neglect the vector degrees of freedom as these do not couple to matter, and we show expressions for $\mathcal{L}^{(n)}_{\rm Gal}[\pi]$ in Appendix F.1. The last term is a coupling term between the tensor and the scalar mode (the scalar part of the Stückelberg field), with $\Pi_{\mu\nu} = \partial_\mu\partial_\nu\pi$, and it is also defined in Appendix F.1. Note that the fields $h_{\mu\nu}$ and $\pi$ are canonically normalised. The decoupling limit trick has been used to investigate physical systems such as binary pulsars, and compact object binaries with the two objects far away enough from one another for the weak-field regime to hold [391].

In 2013, quasi-dilaton massive gravity was proposed as a promising solution to the dRGT cosmology problem [392]. In the following section we will discuss this modified gravity theory and study ways to constrain it, before moving to the more general class of gravity theories with frequency-dependent GW speed.

## 5.3 Quasi-dilaton massive gravity

Massive gravity has gained increasing interest over the past years due to the first formulation a ghost-free theory of massive gravity, dRGT [385].

Here we look for ways to test an extension of dRGT theory: quasi-dilaton massive gravity, which is a dRGT theory with an additional quasi-dilaton scalar field [392].

In 5.3.1 we motivate this specific choice of a modified gravity theory and set up the theoretical framework in which we work. In 5.3.2 we consider two different possible approaches to constraining the theory. The first approach is motivated by the ever-growing data in the GW sector and looks at depletion of a GW signal in a massive gravity theory. The second approach considers astrophysical tests of QDMG, in particular changes to the form of the Bardeen potentials, which in turn leads to modifications to the rotation curves of the theory. Bardeen potentials are gauge-invariant and they govern the behaviour of scalar perturbations [393] [2].

### 5.3.1 Theoretical motivation

The theoretical formulation of dRGT gravity was a turning point for all development in the field of massive spin-2 gravity, as it is the first fully complete ghost-free theory of massive gravity. In addition, with its origin in extra dimensional braneworlds, dRGT allows one to entertain even the possibility of a UV completion of the theory [394]. As promising as the theoretical advancements in dRGT are, its phenomenology makes it difficult to practically constrain the theory. It passes all hitherto proposed tests and agrees with GR, making the two indistinguishable. Out of the additional degrees of freedom, the vector modes do not interact with matter, and the scalar mode is Vainshtein-screened close to a source which significantly represses both its production and detection [390]. In addition, a great concern in searching for tests of the theory is that dRGT gravity does not support stable cosmological Friedman-Lemaître-Robertson-Walker (FLRW) solutions. Hence, to promote dRGT to a cosmological theory, one has to add extra degrees of freedom, be it in the form of tensorial modes (e.g. bigravity [395]) or scalar modes (e.g. f(R) massive gravity [396]).

[2] In the Newtonian limit they are simply the Newtonian gravitational potentials.

In what follows, we focus on quasi-dilaton massive gravity, a scalar-extended dRGT theory with a quasi-dilaton field leading to stable FLRW solutions. We note that the existence of a quasi-dilaton type of field is well-founded within string theory and it arises from compactification of the extra dimensions [397]. The action of quasi-dilaton massive gravity is

$$\begin{aligned}\mathcal{S}_{\rm QDMG} &= \int \mathrm{d}^4x\sqrt{-g}\Big[-\frac{M_{\rm Pl}^2}{2}R(g)+\frac{\omega}{2}(\partial\sigma)^2 \\ &\quad +m^2M_{\rm Pl}^2\sum_{n=0}^{4}\alpha_n\mathcal{L}_n(\mathcal{K}(g,f,\sigma))+\mathcal{L}_m(g,\Phi)\Big],\end{aligned} \tag{5.7}$$

where $\sigma$ is the quasi-dilaton, $g$ is the dynamical metric, $f$ is the Stückelbergised fiducial metric, and coefficient $\omega > 0$. The interaction term now includes the quasi-dilation field as follows:

$$\mathcal{K} = I - e^{\sigma/M_{\rm Pl}}\sqrt{g^{-1}f}. \tag{5.8}$$

It is the interaction between the dynamical metric, fiducial metric and the quasi-dilaton field that gives rise to the graviton mass, $m$. Note that the fiducial metric enters the Lagrangian only through the interaction term with the dynamical metric. In other words, it does not directly couple to matter fields, $\Phi$, and it does not explicitly affect the geodesics.

Similarly to dRGT theory, to make calculations simpler, one can take the decoupling limit of the above action [398]. The Lagrangian in the decoupling limit is derived by keeping the so-called decoupling scale, $\Lambda_3 = \left(m^2M_{\rm Pl}\right)^{1/3}$, constant, and letting $M_{\rm Pl}\to\infty$ and $m\to 0$. We remind the reader that taking this decoupling limit allows us to study all of the degrees of freedom of the theory without needing to keep track of GR non-linearities. Note that in our analysis we ignore the vector gravitational degrees of freedom since these do not couple to matter. Interestingly, taking the decoupling limit of QDMG leads to a bi-Galileon theory of gravity, i.e. the scalar gravitational field and the quasi-dilaton field both acquire a

galilean symmetry [392].

The Lagrangian of the theory of interest (i.e in the decoupling limit) then reads

$$\begin{aligned}\mathcal{L}^{\rm DL}_{\rm QDMG} &= -\frac{1}{4}\Big(h^{\mu\nu}\hat{\mathcal{E}}^{\alpha\beta}_{\mu\nu}h_{\alpha\beta}+\sum_{n=2}^{5}\frac{c_n}{\Lambda_3^{3(n-2)}}\mathcal{L}^{(n)}_{\rm Gal}[\pi]-\frac{2(\alpha_3+4\alpha_4)}{\Lambda_3^6}h^{\mu\nu}\mathrm{X}^{(3)}_{\mu\nu}[\Pi]\Big)\\ &\quad -\frac{\omega}{2}(\partial\sigma)^2+\frac{1}{2}\sigma\sum_{n=1}^{4}\frac{(4-n)\alpha_n-(n+1)\alpha_{n+1}}{\Lambda_3^{3(n-1)}}\mathcal{L}_n[\Pi]\\ &\quad +\frac{1}{2M_{\rm Pl}}h_{\mu\nu}T^{\mu\nu}+\frac{1}{2M_{\rm Pl}}\pi T-\frac{2+3\alpha_3}{4M_{\rm Pl}\Lambda_3^3}\partial_\mu\pi\partial_\nu\pi T^{\mu\nu}\,,\end{aligned}\tag{5.9}$$

where $\Lambda_3$ is the decoupling scale (same as for dRGT), $\pi$ is the gravitational scalar degree of freedom and $\sigma$ is the quasi-dilaton field as before. The decoupling limit is valid for typical scales bigger than $1/m$, where $m$ is the graviton mass, and in QDMG we expect this to be of the order of the Hubble scale, $m \approx H_0$ [399]. Note that all of the fields have been canonically normalised.

In the next section we explore two approaches that may constrain quasi-dilaton massive gravity. We firstly estimate the decay probability of helicity-2 to helicity-0 modes, and find that the decay width is too small to leave a trace in the gravitational wave signal. We then investigate the effect that QDMG could have on astrophysical scales, e.g. galaxies and clusters of galaxies. In particular, we investigate whether we can constrain QDMG and its parameters from rotation curves and gravitational lensing. We note that a similar analysis has been done for beyond-Horndeski theories in [400, 401] and more recently in [402].

### 5.3.2 Constraints from GW and astrophysical data

#### Depletion of the gravitational wave signal

One of the unsurprising consequences of working with a massive, instead of a massless, theory of gravity is that the dispersion relation for gravitational waves gets modified. The correction to the dispersion relation in

QDMG looks similar to that in dRGT theory where the tensor mode acquires a mass contribution that is of the order of the mass of the graviton [403]. Current graviton mass bounds put an upper constraint on the mass, $m < 10^{-22}$ eV [404, 405].

Here we investigate the possibility of depletion of the GW signal due to the decay of tensor modes to scalar ones. Our results agree with the analysis in [406], where it was showed that higher derivative corrections in the Horndeski effective field theory of dark energy are too small to modify the GW signal. Working in the decoupling limit of QDMG, outside the Vainsthein screening region, the Lagrangian reduces to that of linearised massive gravity, since the waves mostly travel through vacuum [407]. Validity of the decoupling limit for GWs detected by Advanced LIGO and Virgo is under debate, since the decoupling scale is close to the energies observed by the mentioned detectors [408], and we will discuss more in later sections. LISA, however, will probe scales that are well below the decoupling scale, and therefore the use of the decoupling limit is not a concern for this upcoming GW experiment. The relevant Lagrangian simplifies to [390]

$$\mathcal{L} = \frac{1}{2}h^{\mu\nu}\hat{\mathcal{E}}^{\alpha\beta}_{\mu\nu}h_{\alpha\beta} + \frac{1}{12}\pi\Box\pi - \frac{1}{2}m^2(h^2_{\mu\nu} - h^2) + \frac{1}{12}m^2\pi h + \frac{1}{6}m^2\pi^2. \quad (5.10)$$

Corrections to the above expression might come from higher order interactions in the decoupling limit. Generic interactions are of the form [390]

$$\mathcal{L}_{j,k,l} = m^2 M_{\rm Pl}^2 \left(\frac{h}{M_{\rm Pl}}\right)^j \left(\frac{\partial A}{m M_{\rm Pl}}\right)^{2k} \left(\frac{\partial^2\pi}{m^2 M_{\rm Pl}}\right)^l. \quad (5.11)$$

Constraints one should keep in mind are $j + 2k + l > 2$, with $j,k,l \in N$ [390]. We set $k = 0$ for the remainder of the calculation, since we are not interested in helicity-1 interactions, which leads to $j + l > 2$. The first interaction that arises at $\Lambda_3$ decoupling scale, $h(\partial^2\pi)^2$, can be removed by field diagonali-

sation. Therefore, the first correction term is of the form $h(\partial^2\pi)^3$ or $(\partial^2\pi)^4$. We are exploring the possibility of depletion of the tensorial gravitational waves by their decay into scalars, so we examine the first of the two terms. This additional interaction appears in the Lagrangian as

$$\mathcal{L}_{103} = m^2 M_{\rm Pl}^2 \left(\frac{h}{M_{\rm Pl}}\right)\left(\frac{\partial^2\pi}{m^2 M_{\rm Pl}}\right)^3 = \frac{1}{m^4 M_{\rm Pl}^2} h(\partial^2\pi)^3. \tag{5.12}$$

Despite a 3-body decay of this type being dynamically forbidden, it is possible in the presence of a background. Since $\Lambda_3^3 = m^2 M_{\rm Pl}$, this term reduces to $\mathcal{L}_{103} = \frac{1}{\Lambda_3^6} h(\partial^2\pi)^3$. The vertex factor contribution to the amplitude is

$$g_{103}^{\mu\nu} = \eta^{\mu\nu}\frac{1}{\Lambda_3^6} p_1^2 p_2^2 p_3^2 = \frac{1}{\Lambda_3^6}\eta^{\mu\nu}(m_\pi^2)^3, \tag{5.13}$$

where $p_i$s are the outgoing momenta of the scalar particles, and $m_\pi$ is the is the mass of the scalar degree of freedom. From (5.10), we see that $m_\pi^2 = \frac{1}{3}m^2$. The resulting amplitude squared is

$$\sum_{\rm spins} \overline{|M|^2} = 2\left(\frac{1}{\Lambda_3^6} m_\pi^6\right)^2 = \frac{2m_\pi^{12}}{m^8 M_{\rm Pl}^4}. \tag{5.14}$$

The expression for the differential decay probability reads

$$\mathrm{d}\Gamma = \frac{(2\pi)^4}{2m}\sum_{\rm spins}\overline{|M|^2} d\Phi_3(p; p_1, p_2, p_3), \tag{5.15}$$

where $d\Phi_3(p; p_1, p_2, p_3)$ is the phase space of a $1 \to 3$ body decay. We apply the treatment of 3-body decay in the centre of mass frame of the decaying particle found in the Particle Data Group Review [409]:

$$\mathrm{d}\Gamma = \frac{1}{(2\pi)^3}\frac{1}{32m^3}\sum_{\rm spins}\overline{|M|^2}\mathrm{d}m_{12}^2\mathrm{d}m_{23}^2, \tag{5.16}$$

where $m$ is the mass of the decaying particle and $m_{ij}^2 = p_{ij}^2 = (p_i + p_j)^2$ are

combinations of masses and momenta of the new particles. Taking the mass of the scalar to be of the order of the mass of the tensor [3], we find $\int dm_{12}^2 dm_{23}^2 \approx \mathcal{O}(m^4)$. Therefore

$$\Gamma \approx \frac{1}{(2\pi)^3}\frac{m^5}{M_{Pl}^4} \approx 10^{-225}\text{eV}. \tag{5.17}$$

An order of magnitude estimate implies that a detailed calculation is not worth pursuing. The decay width is too small to affect the signal. For comparison, the decay width of the $\tau$ lepton is of the order $\approx 10^{-3}$ eV [410]. We conclude that in QDMG there can be no observable depletion of the GW signal due to the decay of the tensor mode into the scalar one.

## Rotation Curves

In this section we move from GW signals to a regime that allows for astrophysical tests of quasi-dilaton massive gravity [399]. We are now interested in manifestations of the theory on galactic scales. Quasi-dilaton massive gravity exhibits Vainshtein screening, and within the Vainshtein radius the scalar graviton degree of freedom is heavily suppressed [392]. It has been suggested, however, that in beyond Horndeski theories, the Vainshtein screening is only partially effective when time-dependent cosmological fields are considered [401]. One would expect a similar phenomenon arising in QDMG. A promising direction of research is analysis of the shape of the galaxy rotation curves. In the following, we first find the evolution of the Bardeen potentials, and then compare the predictions of the theory to data taken by SPARC [411]. Comparing the QDMG predictions to astrophysical data, we set an upper limit to the graviton mass. As mentioned earlier, we work in the decoupling limit of QDMG and use (5.9) as our starting point.

[3] Reasonable assumption from (5.10).

The FLRW metric in the longitudinal gauge reads

$$ds^2 = a^2(\tau)\left[-(1+2\Psi(r,\tau))\,d\tau^2 + (1-2\Phi(r,\tau))\,\delta_{ij}dx^i dx^j\right], \tag{5.18}$$

with $\Psi$ and $\Phi$ scalar perturbations defined as the usual Bardeen potentials. We are concerned with equations of motion of the two Bardeen potentials, as well as of the two galileons. We split $\pi$ and $\sigma$ respectively into a background cosmological value and its perturbation: $\pi(r,t) = \pi_0(t) + \phi(r,t)$ and $\sigma(r,t) = \sigma_0(t) + \lambda(r,t)$. For the rest of this work, we work on small time scales where we neglect expansion; we ignore $a(t)$, $H(t)$ and time derivatives of all fields, focusing on the effects coming solely from $\pi$ and $\sigma$, not from the FLRW metric. Because of this, it is also appropriate to use the decoupling limit of QDMG from (5.9). Furthermore, we consider only terms up to the cubic galileon [412]. Higher-order terms containing the fields or their first derivatives are also neglected. Varying the action with respect to the perturbations we then obtain 4 equations in the presence of a non-relativistic source, $T_{\mu\nu} = \mathrm{diag}(\rho,0,0,0)$, given by:

$$\begin{aligned} &2\nabla^2\Phi - \frac{\alpha_3+4\alpha_4}{\Lambda_3^6}[(\nabla^2\phi)^3 - 3\nabla^2\phi(\nabla_i\nabla_j\phi)(\nabla^i\nabla^j\phi) \\ &+ 2(\nabla^i\nabla_j\phi)(\nabla^j\nabla_k\phi)(\nabla^k\nabla_i\phi)] = \frac{1}{M_{\rm Pl}}\rho\,, \end{aligned} \tag{5.19}$$

$$\nabla^2(\Psi - \Phi) = 0\,, \tag{5.20}$$

$$\begin{aligned} &\omega\nabla^2\lambda - 6\nabla^2\phi + \frac{2-3\alpha_3}{\Lambda_3^3}[(\nabla^2\phi)^2 - (\nabla_i\nabla_j\phi)(\nabla^i\nabla^j\phi)] + \frac{\alpha_3-4\alpha_4}{2\Lambda_3^6} \\ &[(\nabla^2\phi)^3 - 3\nabla^2\phi(\nabla_i\nabla_j\phi)(\nabla^i\nabla^j\phi) + 2(\nabla_i\nabla^j\phi)(\nabla_j\nabla^k\phi)(\nabla_k\nabla^i\phi)] = 0\,, \end{aligned} \tag{5.21}$$

$$\frac{3}{2}\nabla^2\phi+\frac{3}{4}\frac{(2+3\alpha_3)}{\Lambda_3^3}[(\nabla^2\phi)^2-(\nabla_i\nabla_j\phi)(\nabla^i\nabla^j\phi)]-\frac{3(\alpha_3+4\alpha_4)}{\Lambda_3^6}$$
$$[(\nabla^2\Psi)(\nabla^2\phi)^2-(\nabla^2\Psi)(\nabla_i\nabla_j\phi)(\nabla^i\nabla^j\phi)-2(\nabla^2\phi)(\nabla_i\nabla_j\phi)(\nabla^i\nabla^j\Psi)$$
$$+2(\nabla_i\nabla^j\Psi)(\nabla_j\nabla^k\phi)(\nabla_k\nabla^i\phi)]-6\nabla^2\lambda+\frac{2(2-3\alpha_3)}{\Lambda_3^3}[(\nabla^2\lambda)(\nabla^2\phi)$$
$$-(\nabla_i\nabla_j\lambda)(\nabla^i\nabla^j\phi)]+\frac{3(\alpha_3-4\alpha_4)}{2\Lambda_3^6}[(\nabla^2\lambda)(\nabla^2\phi)^2-(\nabla^2\lambda)(\nabla_i\nabla_j\phi)(\nabla^i\nabla^j\phi)$$
$$-2(\nabla^2\phi)(\nabla_i\nabla_j\phi)(\nabla^i\nabla^j\lambda)+2(\nabla_i\nabla^j\lambda)(\nabla_j\nabla^k\phi)(\nabla_k\nabla^i\phi)]=\frac{\rho}{2M_{\rm Pl}}. \tag{5.22}$$

It is straight-forward to notice that the typical Poisson's equation for the Bardeen potential $\Phi$ is altered by the presence of the scalar mode shown in (5.19). Interestingly, however, the Laplace's equation (5.20) remains the same as in the GR case, with $\Psi=\Phi$. Already at the level of the equations of motion, we can deduce that gravitational lensing tests are not an appropriate means of constraining this theory, since the quantity that we probe with lensing, $\frac{\Phi+\Psi}{2\Phi}=1$ is indistinguishable from the exact same GR prediction.

Assuming spherical symmetry, integrating the above expressions by parts and using variables

$$x\equiv\frac{\phi'}{r},\ y\equiv\frac{\Psi'}{r},\ z\equiv\frac{\Phi'}{r},\ A\equiv\frac{M(r)}{8\pi M_{\rm Pl}r^3},\ q\equiv\frac{\lambda'}{r}, \tag{5.23}$$

where the primes denote radial derivatives, we obtain the following set of simultaneous equations:

$$z-\frac{\alpha_3+4\alpha_4}{\Lambda_3^6}x^3=A, \tag{5.24}$$

$$y-z=0, \tag{5.25}$$

$$\omega q-6x+\frac{2(2-3\alpha_3)}{\Lambda_3^3}x^2+\frac{\alpha_3-4\alpha_4}{\Lambda_3^6}x^3=0, \tag{5.26}$$

$$\frac{3}{2}x + \frac{3(2+3\alpha_3)}{2\Lambda_3^3}x^2 - \frac{6(\alpha_3+4\alpha_4)}{\Lambda_3^6}x^2 y - 6q + \frac{4(2-3\alpha_3)}{\Lambda_3^3}qx + \frac{3(\alpha_3-4\alpha_4)}{\Lambda_3^6}x^2 q = A. \tag{5.27}$$

Combining the first three coupled equations and plugging into (5.27) gives a quintic for $x$, for which we give the full expression in Appendix F.2. Taking the quintic term to be the dominant one, we can approximate

$$-\frac{3}{\Lambda_3^{12}}\left[2(\alpha_3+4\alpha_4)^2 + \frac{1}{\omega}(\alpha_3-4\alpha_4)^2\right]x^5 = A. \tag{5.28}$$

We use this equation to find the form of $x$, which will then provide a prediction for the shape of rotation curves.

The velocity of objects within the galaxy undergoing circular motion is

$$\frac{v^2}{r} = \frac{\partial\Psi}{\partial r}, \tag{5.29}$$

which in terms of our new variables reads

$$v^2 = r^2 y. \tag{5.30}$$

Most of galaxy's mass is in its dark matter halo, and in this work we assume it to obey the Navarro-Frenk-White (NFW) profile [413]:

$$\rho_{\rm NFW} = \frac{\rho_{\rm s}}{\frac{r}{r_{\rm s}}\left(1+\frac{r}{r_{\rm s}}\right)^2}, \tag{5.31}$$

with $r_{\rm s}$ and $\rho_s$ as the typical halo parameters.

Using (5.24), (5.25) and (5.28), and assuming an NFW distribution, we

get the following equation for the dark matter velocity profile

$$v_{\rm dm}^2 = 4\pi G r_{\rm s}^2 \rho_{\rm s} \Bigg\{ \frac{1}{R} \left( \ln(1+R) - \left(1+\frac{1}{R}\right)^{-1} \right) - \gamma\, R^{\frac{1}{5}} \left( \ln(1+R) - \left(1+\frac{1}{R}\right)^{-1} \right)^{\frac{3}{5}} \Bigg\}, \tag{5.32}$$

where $R = r/r_{\rm s}$, with

$$\gamma = \left(4\pi G \rho_{\rm s}\right)^{-\frac{2}{5}} m^{\frac{4}{5}} \frac{\alpha_3 + 4\alpha_4}{[6(\alpha_3+4\alpha_4)^2 + \frac{3}{\omega}(\alpha_3 - 4\alpha_4)^2]^{\frac{3}{5}}}. \tag{5.33}$$

We can constrain the $\gamma$ parameter by fitting the theoretical predictions to the rotation curves data. We use best-fit values of $\omega$ and $\alpha$ coefficients from [399]. Since $\gamma$ is a function of $m$, by constraining $\gamma$ we can put an upper limit on the graviton mass.

We use the data from the SPARC galaxy catalogue [411] to reconstruct rotation curves. The observed speed is not only due to the dark matter present, but there are gas, disk and bulge (if applicable) contributions too:

$$v^2(r) = v_{\rm gas}^2(r) + \Upsilon_{\rm disk}\, v_{\rm disk}^2(r) + \Upsilon_{\rm bulge}\, v_{\rm bulge}^2(r) + v_{\rm dm}^2(r), \tag{5.34}$$

where $\Upsilon$ is the stellar-to-mass ratio. We must subtract all the matter contributions from the data to obtain $v_{\rm dm}$, and then compare against our predictions. We use $\Upsilon_{\rm disk}, \Upsilon_{\rm bulge}, r_{\rm s}$ and $\rho_{\rm s}$ values from Table 4 in [414]. Our results could be refined with a Monte Carlo Markov Chain simulation [415] to find posterior best-fit values of all the parameters: in this case the NFW parameters and the $\gamma$ parameter from QDMG, as well as $\Upsilon_{\rm disk}$ and $\Upsilon_{\rm bulge}$.

All of the galaxies in the SPARC catalogue are characterised by a quantity, $Q$, which refers to the quality of the galaxy's rotation curve. We consider galaxies with $Q = 1$, in other words galaxies with the best quality rotation curves. We also choose carefully high mass and high luminosity galaxies because the NFW profile provides the best fit for those types of

galaxies [415]. On a single plot (see for instance the case of two representative galaxies in Figure 5.1) we compare the NFW profile in the GR case and the corresponding one in the QDMG case fit for the data. The galaxies that we take show consistency in the value of $\gamma$ that fits the dark matter galaxy profile (5.32) to data. The constraint placed on the graviton mass from this is

$$m \leq 10^{-31}\,\text{eV}. \tag{5.35}$$

This bound satisfies all constraints hitherto imposed on the mass of the graviton from Advanced LIGO/Virgo and Solar System tests [416]. Typically, massive gravity theories are motivated with the aim of explaining the origin of Dark Energy, and indeed values of $m$ of the order of Hubble, $m \approx 10^{-33}$ eV, can accomplish this [385]. Our constraint does not disqualify such a *statement*, neither does it rule out massive gravity as a proposal for explaining the late-time accelerated expansion of the Universe. However, one may wonder whether one can come up with an astrophysical test that could falsify massive gravity. In other words, could such a tiny mass be ever detected? The most promising constraints we can hope to probe in the upcoming decades will be through LISA when we will be able to detect masses up to $10^{-25}$ eV [416]. At present, we do not see a way for the constraint derived in (5.35) to be tested with GW data.

However, one should keep in mind that our result comes with subtleties and caveats. Along the way, we made numerous approximations: we decided to take (scientifically motivated) limits of QDMG that allowed us to proceed with our analytical analysis. These approximations included going only up to the cubic galileon in the decoupling limit, as well as setting the background values of the scalar fields $\pi_0$ and $\sigma_0$ to 0. We anticipate opportunities for future work within going beyond these approximations.

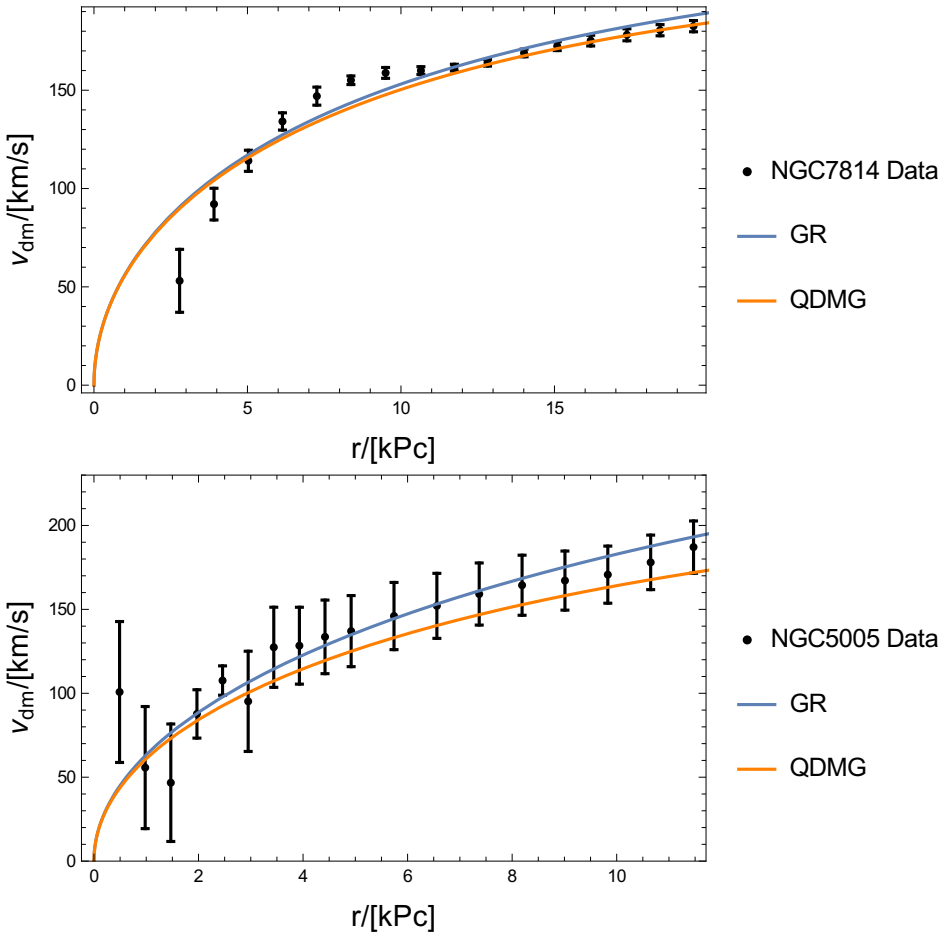


**Figure 5.1:** Dark Matter contribution to rotation curves, GR case and QDMG case, for 2 galaxies in the SPARC catalogue, NGC7814 (top panel) and NGC5005 (bottom panel). In the limit $m = 0$, the QDMG fit coincides with the GR fit. We have investigated what maximum graviton mass still keeps the theoretical QDMG fit within the error bars of the data.

## Discussion

We have looked for ways to lift the mathematical success of dRGT theory to a phenomenological level. The lack of stable cosmological solutions in massive gravity led us to extend the theory by adding a quasi-dilaton field, leading to quasi-dilaton massive gravity. Having resorted to this theory, we found a promising direction of study in analysing rotation curves of galaxies. The new scalar degrees of freedom in QDMG affect equations of motion of the dark matter within the galaxies and they are expected to alter the dark matter halo profile. The extent to which the dark matter profile can change is constrained by rotation curves data. We combine the

observations collected in the SPARC database with our theoretical prediction. In order for QDMG to agree with the data, the graviton mass must be $m \leq 10^{-31}\,\mathrm{eV}$. This result does not contradict any previous bounds on the mass of the graviton, and leaves massive gravity as a viable dark energy candidate theory.

We finalise this chapter with a discussion on frequency-dependent GW speed. In probing GW speed and studying modified gravity theories with the LISA detector, we argue there may be a new, independent, method for redshift mapping of sources.

## 5.4 LISA probe of gravitational-wave speed

The constraint from GW170817 [417, 418, 419, 420] is widely considered a major challenge to extended gravity theories predicting a non-standard GW propagation speed. However, it can also inform discussions on properties required for these gravity models to possess a healthy UV completion. This is the viewpoint of [408], which added a degree of subtlety to the interpretation of the data that has not yet been considered widely in the literature (though see e.g. [421] for further theoretical work on the topic). In [408], compelling arguments and examples are presented suggesting that the speed of propagation of GWs may vary as a function of the energy scale. The starting point is the observation that at low energies, most theories spontaneously break Lorentz invariance through a time-dependent vacuum expectation value of an additional field(s). Such a time-dependent vacuum expectation value is essential for driving cosmic acceleration, but it usually leads to a tensor speed $c_T < 1$ due to non-minimal couplings between extra fields and gravity. Explicit examples of this phenomenon arise in the context of Horndeski theories and their extensions, Beyond Horndeski or DHOST [422, 423, 424, 425, 426, 427, 428].

On the other hand, if the UV completion of an extended gravity theory is required to be Lorentz invariant (as is usually the case), then *nec-*

*essarily* the graviton speed becomes luminal at high energies. The transition between non-luminal and luminal speed is likely to occur well before (or at most, around) the strong-coupling scale of the theory, which for Horndeski-like theories is typically $\Lambda_3 = (M_{\rm Pl} H_0^2)^{1/3} \sim 260$ Hz. This is within the frequency band of ground-based GW detectors: as a consequence, ground measurements might correspond to the frequency range for which the Lorentz invariance of the theory has already enforced luminal propagation speed. At lower frequencies, for example in the LISA frequency band ($\sim 10^{-5} - 10^{-1}$ Hz), the speed of GWs may instead be different from one.

The relation between frequencies at source ($f_s$) and at detection ($f_o$), which scale as the inverse of time differences ($f \sim 1/\Delta t$), reads

$$\frac{f_o}{c_T(f_o)} = \frac{f_s}{(1+z)\, c_T(f_s)}, \tag{5.36}$$

where $z$ is the redshift of the source. Notice that, in the frequency regimes where $c_T(f)$ is frequency-independent, we find

$$f_s = (1+z)\, f_o, \tag{5.37}$$

which is the standard relation connecting frequencies at emission and at detection. In general, however, a frequency-dependent GW velocity requires to generalise (5.37) to (5.36).

It is convenient to define a dimensionless quantity $\Delta$ that measures the deviation from the standard relation (5.37) for GWs propagating through cosmological distances:

$$\Delta = \frac{f_s - (1+z)\, f_o(f_s, z)}{f_s} \tag{5.38}$$

$$= 1 - \frac{c_T(f_o)}{c_T(f_s)}. \tag{5.39}$$

The quantity $\Delta$ can be expressed as function of $f_s$, or of $f_o$, depending on

which is more convenient. A value $\Delta \neq 0$ indicates that $c_T$ is a non-constant function of frequency. In the following sections we study the spectrum of $\Delta$ for a particular effective field theory $c_T$ Ansatz, before briefly looking at how precise measurements of $c_T$ can help with redshift mapping of LISA sources.

### 5.4.1 Theoretical motivations for the GW speed Ansatz

We are motivated by the arguments of [408]: suppose there exists a scalar theory valid up to a strong coupling scale $\Lambda$, with new physics (e.g extra degrees of freedom) entering at the scale $M \leq \Lambda$. Let us assume a homogeneous scalar background $\phi_0(t)$ that spontaneously breaks Lorentz invariance, $\phi_0(t) = \alpha \Lambda t$, parameterised with a constant parameter $\alpha$ (although it may be mildly time-dependent, with $|\dot{\alpha}/\alpha| \leq H$). The spontaneous breaking of Lorentz invariance typically leads to a scalar speed different to that of light. We consider for example the partial UV completion of (6) in [408]. It leads to a dispersion relation,

$$\omega^2 = k^2 - \alpha^2 \frac{\omega^2 M^2}{M^2 - \omega^2 + k^2}. \tag{5.40}$$

The propagation speed is defined through the dispersion relation

$$\omega^2 = c^2(t,k)\, k^2. \tag{5.41}$$

Therefore (5.40) leads to a scalar speed given by

$$c_s^2(k) = 1 + \frac{k_\star^2}{k^2} - \frac{k_\star^2}{k^2}\sqrt{1 + 2\left(1 - c_0^2\right)\frac{k^2}{k_\star^2}}. \tag{5.42}$$

Although motivated by scalar theories, we adopt this expression in the tensor case for simplicity. Here

$$k_\star = \frac{M}{\sqrt{2}\, c_0} \qquad ; \qquad c_0^2 = \frac{1}{1+\alpha^2}. \tag{5.43}$$

Note that the function (5.42) has the properties

$$c_s(k \ll k_\star) = c_0, \tag{5.44}$$

$$c_s(k \gg k_\star) = 1, \tag{5.45}$$

showing consistency with GR at large scales. Rewriting tensor speed in (5.42) in terms of frequency ($f \equiv 2\pi k$), one obtains

$$c_T(f) = \left[1 + \frac{f_\star^2}{f^2} - \frac{f_\star^2}{f^2}\sqrt{1 + 2\left(1 - c_0^2\right)\frac{f^2}{f_\star^2}}\right]^{1/2}. \tag{5.46}$$

We can analytically compute the slope of the speed

$$\begin{aligned} n_T(f) &\equiv \frac{d\ln c_T}{d\ln f} \\ &= \frac{1 + \left(1 - c_0^2\right) f^2/f_\star^2 - \sqrt{1 + 2\left(1 - c_0^2\right) f^2/f_\star^2}}{\sqrt{1 + 2\left(1 - c_0^2\right) f^2/f_\star^2}\left(1 + f^2/f_\star^2 - \sqrt{1 + 2\left(1 - c_0^2\right) f^2/f_\star^2}\right)}. \end{aligned} \tag{5.47}$$

There exists an inflection point at

$$\frac{f_{\rm in}}{f_\star} = \sqrt{\frac{c_0\left(\sqrt{2} + c_0\right)}{1 - c_0^2}}, \tag{5.48}$$

which is an increasing function of $c_0$. At the inflection point the slope of $c_T(f)$ is maximal, resulting

$$n_T^{\rm max}(f_{\rm in}) = \frac{\left(1 - c_0^2\right)}{\left(1 + \sqrt{2}c_0\right)^2}, \tag{5.49}$$

which is a decreasing function of $c_0$.

The parameterisation (5.46) is controlled by two free parameters: a fiducial frequency $f_\star$ around which $c_T$ changes rapidly, and a low-frequency speed $c_0$ with $0 < c_0 \leq 1$. Ansatz (5.46) is motivated by the analysis in [408] of an UV completion of a scalar field theory, where the

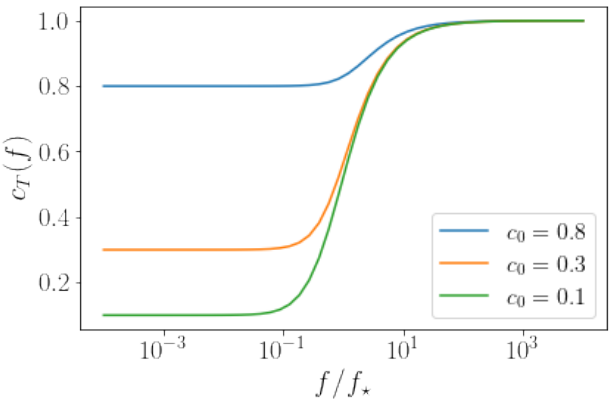


**Figure 5.2:** Plot of the effective field theory Ansatz for frequency-dependent $c_T(f)$, as given by (5.46).

scalar velocity depends on the energy, and smoothly (but rapidly) connects from $c_0$ to 1 as the energy increases. The transition from $c_0$ to unity occurs within a relatively small interval as the frequency increases (see Figure 5.2); the width of the transition is not a free parameter and depends entirely on $c_0$.

### 5.4.2 Identifying source redshift with precise measurements of GR deviations

A frequency profile for $c_T(f)$ as (5.46) implies that all the frequency-dependent effects occur in a relatively small frequency band centred around $f_\star$.

One can easily compute numerically the function $\Delta(f)$, introduced in (5.39), which is the important quantity that controls the deviations from GR. We plot $\Delta(f)$ in Figure 5.3 for representative choices of parameters. We notice that this function has a pronounced peak, whose maximal value $\Delta_{\max}$ depends on $c_0$, but also on the redshift $z$ at which the GW source event occurs. To understand better how $\Delta(f)$ evolves over the $z - c_0$ parameter space, we evaluate the amplitude and the position of the maximum of the function for redshifts log-uniformly distributed from 0.1 to 10, and values of $c_0$ uniformly distributed between 0.1 and 0.9, see Figure 5.4. We see that maximum deviation from GR occurs at frequencies of the order $f_\star$ and for

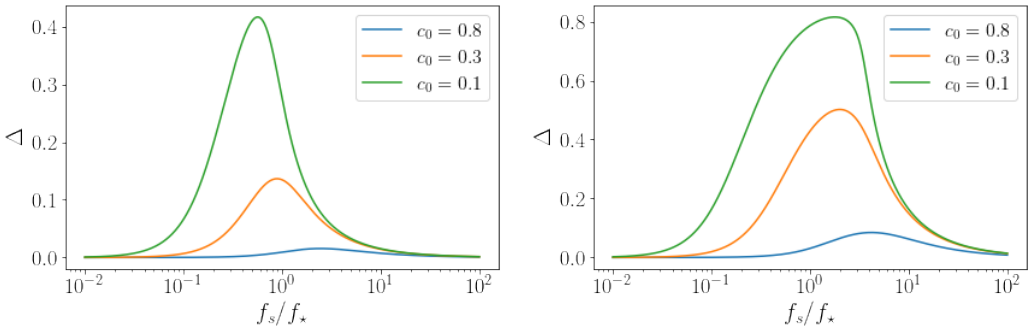


**Figure 5.3:** Plot of $\Delta$ for the EFT-inspired Ansatz, as defined in (5.39). Left panel: $z = 0.2$; Right panel: $z = 2$.

small $c_0$ and large $z$, as expected. We perform least squares polynomial fits to obtain a simple phenomenological fit relating $\Delta_{\rm max}$ to $c_0$ and $z$ that is valid up to large redshifts ($z = 15$):

$$\Delta_{\rm max}(c_0, z) = (1.07 - 1.04\, c_0) \left[1 - \frac{1}{(1+z)^{(1.07-0.84\, c_0)}}\right] . \tag{5.50}$$

This relation suggests that if we were able to measure with good precision deviations from GR induced by Ansatz (5.46), we might then be able to extract independent information on the *redshift* of the source, which might be helpful to build a Hubble diagram with GW sirens.

Recent work suggests that in a multiband scenario, e.g. with a merger event detected during the inspiral by LISA and during the merger by terrestrial detectors, we will be able to place constraints between graviton speed and speed of light to 1 part in $10^{-15}$ [429]. The two parameters $f_\star$ and $c_0$ controlling the location and height of the transition (with $c_0 = 1$ corresponding to the GR case) can indeed be constrained very well with LISA. Forecasting LISA capabilities to measure these quantities, one finds that both parameters influence considerably GW waveforms. We conclude that for massive-black-hole binaries in specific mass ranges (with total binary mass $M_{\rm tot} \sim 10^5 M_\odot$), the parameters $f_\star$ and $c_0$ characterising Ansatz (5.46), can be constrained to a fractional error of order percent level or better, with respect to their fiducial values.

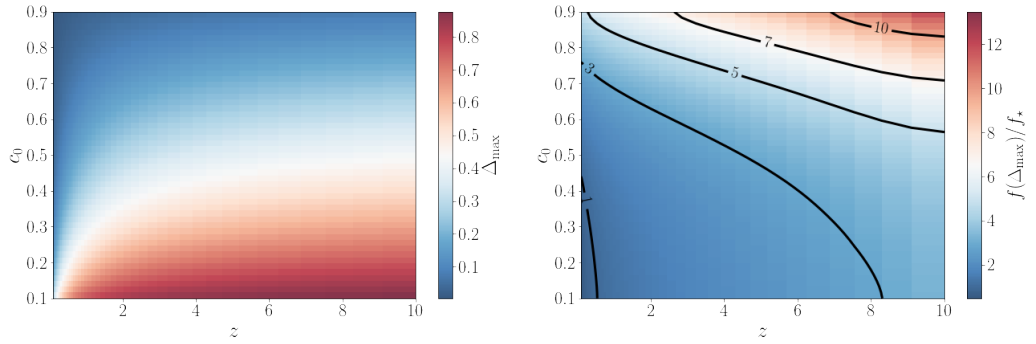


**Figure 5.4:** Variation of maximum value of $\Delta$ (left panel) and the position of the maximum (right panel) with redshift and $c_0$, for the EFT-inspired Ansatz of (5.46).

## 5.5 Afterword

General relativity has indisputably helped us understand gravitational effects in the Universe over the last 100 years, in both weak-field and more recently strong-field regimes. However, one cannot ignore its incompleteness at the UV scale and its incompatibility with Quantum Mechanics. Additionally, the dark energy and dark matter contents of the Universe are added ad-hoc, and their origin remains uncertain. Various modified gravity theories have been proposed to address these issues (for an extensive review, see [430]). Note that some of the models presented in [430] have since been constrained or ruled out completely by GW data, verifying once again the richness of information we can extract from GWs.

In this chapter we constrained a promising class of theories, massive gravity with an added quasi-dilaton field, with astrophysical data. We also discussed an effective field theory approach to gravity, and we demonstrated how one can use precision measurements with LISA as a novel and independent way to perform redshift mapping of CBC sources. The quest for a UV-complete theory of gravity that can explain dark energy and dark matter continues.

## Chapter 6

# Conclusions

Throughout this thesis we have covered various aspects of the gravitational-wave background: from detection methods, separation of sources to parameter estimation of physical models.

We presented the first careful treatment of correlated magnetic noise when searching for the background with the current detector network. The methods we developed for simultaneous estimation of correlated magnetic noise and GWB were used in the LVK O3 isotropic search, and these have now been integrated into the official collaboration pipeline, *pygwb*. The magnetic coupling should continue being monitored and work should be done to include any temporal variation in upcoming LVK observation runs. In the case of the proposed 3G Einstein Telescope, we estimated the magnetic noise that could contaminate the signal. We placed upper limits on the magnetic coupling functions of the detector that still allow it to achieve its science goals. Once its site has been confirmed, it remains to perform site-specific tests of magnetic noise sources.

Next we investigated source separation in 2G, 3G and space-based GW detectors. Separating astrophysical and cosmological background will prove difficult for current detectors, but with a network of Einstein Telescope and Cosmic Explorer we could reveal cosmological signals using CBC subtraction techniques. Source separation will rely heavily on the quality of subtraction of individual sources, and significant improvements

in this field are required. Furthermore, for LISA we applied a dictionary learning method that successfully reconstructed mergers of massive black holes in the presence of confusion noise due to the inspiral of millions of white dwarf binaries in the Milky Way. The success of this method certainly invites for future work and may be useful in studying detection of other GW sources.

The main aim of this thesis was to constrain physical models using GWB data. The astrophysical background from unresolved merger events is expected to be the dominant contribution to the GWB. We showed that with 3G detectors we may be able to observe the astrophysical background from the oldest, most distant pop III stars. Observing the background, and its characteristic peak frequency, could tell us about the population's macroscopic properties such as average redshifted binary mass. One can go further and study what the slope of the background reveals about the population, as well as consider attempts of disentangling the broken power law spectrum from other viable sources such as first-order phase transitions.

Symmetry breaking in the early Universe as it cools down and expands could have led to a first-order phase transition. Bubbles of true vacuum expanding into the false vacuum and eventually colliding leave a trace in the GWB. Symmetry breaking at energy scales inaccessible to particle colliders would lead to a signal in the terrestrial GW detector frequency range, e.g. Peccei-Quinn mechanism. We placed constraints on phase transition parameters from the most recent LVK run. In the special case of a supercooled phase transitions, we placed direct limits on particle couplings' of two representative symmetry-breaking models. This analysis will continue to be repeated with each subsequent LVK run, and it will probe increasingly more parameter space of Beyond Standard Model theories.

A possible signature of a first-order phase transition may be hiding in the polarisation of the GWB. Typically, the GWB is modelled under the assumptions that it is unpolarised. However, turbulent motion of the plasma

during the growth and collision of bubbles of true vacua may have a non-zero chirality, which could in turn lead to a polarised GWB spectrum. We search for signals of polarity in current GW data and consider how our results would change with future detector upgrades. Once site locations of next-generation detectors are selected, one will be able to estimate their overlap reduction functions, which will allow for studies of parity violation with 3G interferometers.

Finally we discuss modifications to GR, in search of a UV complete theory of gravity. We present astrophysical constraints on quasidilaton massive gravity arising from the rotation curves of galaxies. With LISA space-based detector we will be able to perform precision measurements of the speed of GWs. This could provide an independent and new avenue for redshift mapping of sources, helping to put tighter bounds on the Hubble constant. Work is also underway to combine multiband GW detections to study modified gravity theories at different energy scales.

The future of gravitational-wave physics is bright. With the improvement in detector sensitivity, we will continue to detect more coalescence events, as well as start to see the background from the unresolved mergers. Along with the advancements of data analysis and modelling, we will be able to subtract individual CBCs and reduce the astrophysical foreground. This is when we start to explore cosmological sources and probe the Universe beyond the surface of last scattering. With gravitational-wave data, we will being to paint a clearer picture of the physics of the early Universe.

# Appendix A

# Correlated magnetic noise

## A.1 Simulated magnetic noise properties

We use low noise magnetometers on-site at the Advanced LIGO and Advanced Virgo detectors and correlate them to deduce what $\gamma_{ij}^{M}$, defined in (2.1), looks like. A discussion of the magnetometers and their locations is given in [88]. We use the real part of complex coherence (RPCC), defined as

$$\gamma_{ij}^{M}(f;t) = \mathrm{Re}\left[\frac{\tilde{m}_i^*(f;t)\tilde{m}_j(f;t)}{\sqrt{\tilde{m}_i^*(f;t)\tilde{m}_i(f;t)}\sqrt{\tilde{m}_j^*(f;t)\tilde{m}_j(f;t)}}\right] \tag{A.1}$$

where $\tilde{m}_i(f;t)$ is the Fourier transform of the data from magnetometer $i$ starting at time $t$ evaluated at frequency $f$. We calculate the numerator and denominator of $\gamma_{ij}^{M}(f;t)$ separately over 4 s segments and average them separately over 1800 s of data to create an estimate of $\gamma_{ij}^{M}(f;t)$ for that 1800 s chunk of data. We do this for each 1800 s chunk of data available from from July 9, 2019 00:00 UTC – September 7 2019 00:00 UTC. We then take a histogram at each frequency over all of the 1800 s measurements. A heatmap of this histogram is shown in Figure A.1 for each possible detector pair. For the simulations discussed in 2.2.3, we use the median over the time chunks at each frequency, indicated by the white line in each panel in Figure A.1. This is indicated by the white line in Figure A.1.

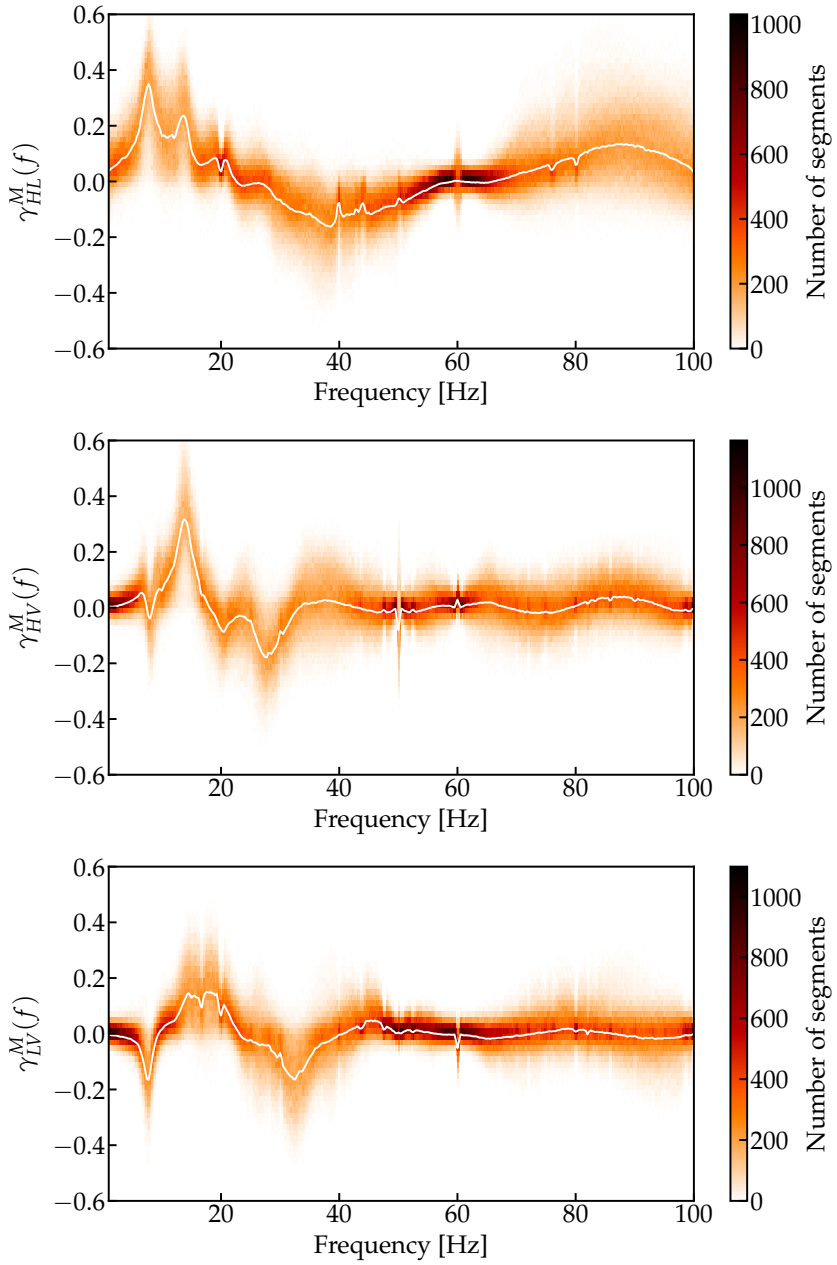


**Figure A.1:** Color indicates histogram of RPCC of Hanford-Livingston for each 1800 s chunk of data available for 60 days. The median value of all RPCC measurements taken at each frequency is shown in white.

The RPCC is not an exact measurement of $\gamma^{\mathrm{M}}_{ij}(f)$. It approximates this value only insofar as the the "signal", $M(f)$, dominates the noise in the individual magnetometers. However, in the absence of a reliable analytic calculation (which is available in the GW case, for example), it is a good heuristic for capturing the sign and general shape of $\gamma^{\mathrm{M}}_{ij}(f)$.

# Appendix B

# pyGWB

The isotropic background searches in the first three LVK observing runs have placed stringent constraints on the GWB amplitude. This was achieved using a hybrid frequentist-Bayesian approach where one defines a gaussian likelihood for $N$ pairs of baselines,

$$p(\hat{C}^{IJ}(f_k)|\mathbf{\Theta}) \propto \exp\left[-\frac{1}{2}\sum_{IJ}^{N}\sum_{k}\left(\frac{\hat{C}^{IJ}(f_k) - \Omega_{\rm M}(f_k|\mathbf{\Theta})}{\sigma^2_{IJ}(f_k)}\right)^2\right], \tag{B.1}$$

with $\Omega_{\rm M}(f_k|\mathbf{\Theta})$ as the GWB model and $\mathbf{\Theta}$ as its parameters. The likelihood defined in Eq. (B.1) is used to Bayesian update the priors on model parameters and output the posterior distributions of those parameters,

$$p(\mathbf{\Theta}|\hat{C}^{IJ}(f_k)) \propto p(\hat{C}^{IJ}(f_k)|\mathbf{\Theta})\, p(\mathbf{\Theta}). \tag{B.2}$$

Until now, the GW strain was analysed and processed with `stochastic.m` to give the data products $\hat{C}^{IJ}(f_k)$ and $\sigma_{IJ}(f_k)$, and a separate parameter estimation analysis followed. In `pygwb`, for the first time, we include parameter estimation as a part of the data handling and analysing process. The Parameter Estimation (PE) module implements Bayesian tools to search for a GWB in the data. In particular, this module represents a simple and user-friendly toolkit for any model builder to constrain their physical models with GW data.

The PE module is built on class inheritance, with `GWBModel` as the parent class. The class attributes are a list of `Baseline` objects $IJ$ the user wishes to include in the analysis, a label for the model in question, as well as a list of polarisations. The last of the attributes is set to *tensor* unless specified, giving the user the flexibility to change polarisation and explore models that predict a scalar or vector polarisation of the GWB. The methods of the parent class are functions shared between the different GWB models, e.g. the definition of likelihood in Eq. (B.1), as well as the definition of noise likelihood (Eq. (B.1) with $\Omega_{\rm M}(f_k|\mathbf{\Theta}) = 0$). If the *calibration_epsilon* attribute of the `Baseline` object is not set to 0, then the likelihoods include calibration uncertainty corrections [431]. The parent class also includes so-called abstract methods that must be defined in every child class, namely a dictionary of the model parameters $\mathbf{\Theta}$, as well as the definition of the model $\Omega_{\rm M}(f_k|\mathbf{\Theta})$.

Child classes in the PE module inherit attributes and methods of the `GWBModel` class. Each child class represents a single GWB model, and combined they form a catalogue of available GWB models to study with the LVK data. The inheritance structure of the module makes it straightforward to expand the catalogue, allowing users of the `pygwb` package to add their own $\Omega_{\rm M}(f_k|\mathbf{\Theta})$ models [1]. The `pygwb` documentation contains information on the existing models in the catalogue, with a description of the parameters and the dependence of the background on the parameters [432]. The documentation also covers a tutorial to assist the user with running PE on the data. Here we go through the example of searching for a power law GWB in the data with the `PowerLawModel` class. To search for a power law spectrum in the data,

$$\Omega_{\rm GW} = \Omega_{\rm ref} \left( \frac{f}{f_{\rm ref}} \right)^{\alpha} \tag{B.3}$$

it is sufficient to run the following command lines.

[1] Any changes to the PE module must be reviewed and approved by the assigned module lead via GitLab.

```
1 kwargs_pl = {"baselines":[HL,HV,LV], "model_name":'PL', "fref":25}
2 model_pl = PowerLawModel(**kwargs_pl)
3 priors_pl = {'omega_ref': bilby.core.prior.LogUniform(1e-13, 1e-5,
4              '$\\Omega_{\\rm ref}$'),
5              'alpha': bilby.core.prior.Gaussian(0, 3.5, '$\\alpha$')}
6 pl=bilby.run_sampler(likelihood=model_pl, priors=priors_pl, sampler='dynesty',
7 npoints=1000, walks=10, npool=10, outdir='./pe/', label='pl', resume=False)
```

In Line 1 we create a dictionary of the attributes relating to the model we would like to study. Note that in addition to the generic attributes that should be set for any model, i.e. the list of baselines and model label, the user must define the reference frequency for the power law model (B.3). Next, the PowerLawModel likelihood class is instantiated in Line 2. One more step before running parameter estimation is specifying the prior distributions of the model parameters, see Lines 3 and 4. Finally we let the `Bilby` sampler perform parameter estimation by specifying the previously-defined likelihood and priors. The user has flexibility in choosing the sampler as well as the sampler settings, which can be studied using the extensive `Bilby` documentation.

# Appendix C

# Dictionary learning: optimal hyperparameters

## C.1 Optimal regularisation parameter

In theory there exists an optimal regularisation parameter $\lambda_{\text{opt}}$ such that we retrieve the best reconstruction of a CBC signal. For each signal in the testing dataset, we vary $\lambda \in [10^{-8}, 10^{-1}]$ and reconstruct the CBC waveform. The calculated overlap between the reconstructed signal and the injected CBC, $\mathcal{O}$, can be seen in Figure C.1. For all reconstructions with $\lambda \lesssim 10^{-3}$, $\mathcal{O}$ plateaus. Some cases "dipped" to a minimum $\mathcal{O}$ before dramatically increasing as $\lambda$ increased. Regardless of the $\mathcal{O}$ behavior each CBC demonstrated, the optimal regularisation parameter $\lambda_{\text{opt}}$ took on a value between $10^{-3}$ and $10^{-2}$. This behavior was consistent over differing atom length $d$ and Galactic noise strength.

## C.2 Optimal atom length

The length of the columns of the dictionary significantly impacts quality of reconstruction. We fix $\lambda = 10^{-3}$ and vary dictionary size $d \in [2^2, 2^7]$ to find the value of atom length that results in best reconstruction of the CBC signals. In Table C.1 we report the change in the sum of $\mathcal{O}$s for all 50 individual testing samples as we alter the atom length. With this we

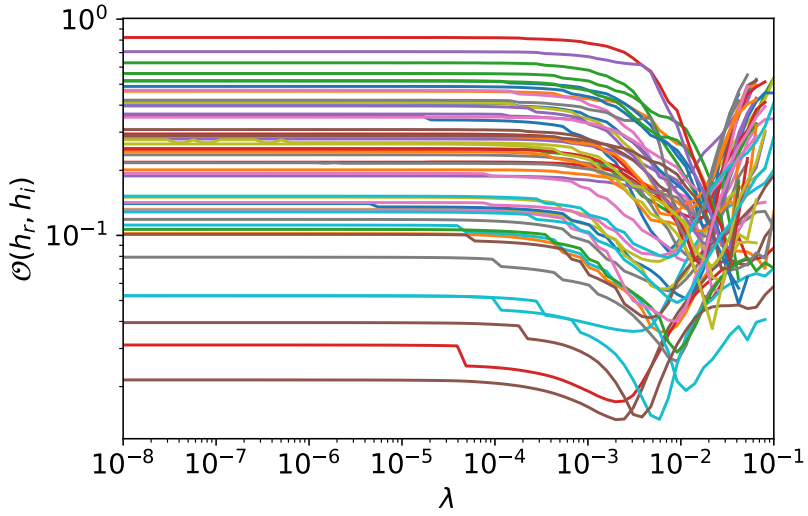


**Figure C.1:** Optimal value of the regularisation parameter is between $10^{-3}$ and $10^{-2}$. For $\lambda < 10^{-3}$ the $\mathcal{O}$ curve plateaus.

| atom length, $d$ | $\sum_i (\mathcal{O}_i)$ |
|---|---|
| 4 | 14.3 |
| 8 | 10.2 |
| 16 | 6.65 |
| 32 | 5.65 |
| 64 | 6.95. |
| 128 | 7.93 |

**Table C.1:** Variation in the total sum of overlaps as a function of atom length. The optimal atom length that gives best reconstruction is $d_{\text{opt}} = 4$.

identify the optimal atom length to be $d_{\text{opt}} = 4$.

# Appendix D

# Pop III suplemental material

## D.1 Residual background

To analytically calculate the residual background when individually detected sources are removed, one typically multiplies the total merger rate $R(z;\theta)$ by a factor $1-\epsilon(z,\theta)$, where the efficiency $\epsilon(z,\theta)$ is the probability for a source at redshift $z$ with parameters $\theta$ to be detected, integrated over inclination, polarisation and position in the sky (see [433]). In our analysis, however, the residual background catalogue is obtained by subtracting all sources individually detected by the interferometer network. For each source $k$ we calculate the individual signal-to-noise ratio $\rho^k$ assuming optimal-matched filtering and uncorrelated gaussian noise in the detectors as follows:

$$\left(\rho^k\right)^2 = \sum_{I=1}^{N} 4 \int_{f_{i,\min}}^{f_{i,\max}} \frac{\left|\tilde{H}^k\right|^2}{P_I(f)}\, df, \tag{D.1}$$

where

$$\tilde{H}^k = F_{+,I}(f,\Theta^k,\psi^k)\tilde{h}^k_+(f) + F_{\times,I}(f,\Theta^k,\psi^k)\tilde{h}^k_\times(f), \tag{D.2}$$

with $F_{+,I}$ and $F_{\times,I}$ the antenna factors of detector $I$ for polarisations $+$ and $\times$ that depend on source inclination $\Theta^k$ and position in the sky $\psi^k$, while $\tilde{h}^k_+$ and $\tilde{h}^k_\times$ are the Fourier transforms of the gravitational waveforms of the source $k$. $P_I(f)$ is the one-sided power spectral noise density of detector

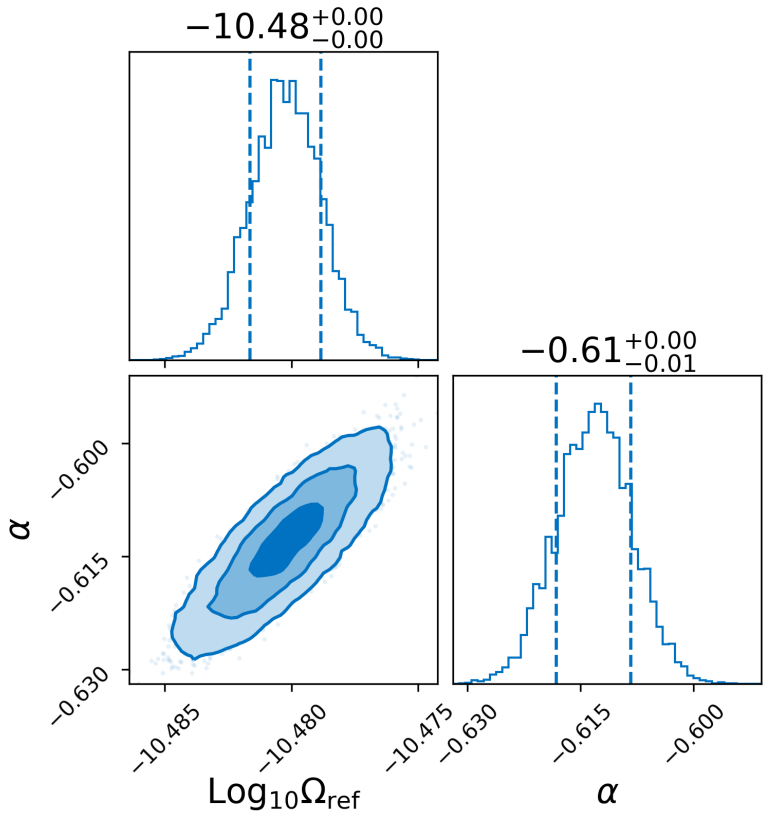


**Figure D.1:** Varying-$\alpha$ PL fit to residual GWB spectrum of pop I+II+III from the StarTrack simulation. We see that the $\alpha$ estimate is not 2/3 which would be expected for pop I/II.

*I*. A residual catalogue is computed by removing all sources with $\rho^k > 12$. Note that confusion noise, although an important issue for LISA due to the presence of e.g. white dwarves, early inspirals of stellar-mass black holes and monochromatic signals from supermassive black-hole binaries [151], does not pose a problem for the frequency range of terrestrial detectors that we consider. The SNR of individual compact binary sources above 5 Hz is not lowered due to overlapping signals, as was demonstrated in [182].

## D.2 Priors

All of the models for a population III signal have the same log-uniform prior distribution for the gravitational-wave background amplitude ranging between $10^{-13}$ and $10^{-5}$. As for the remaining parameters, we use

- power law (PL): $\alpha = \mathcal{N}(0,3.5)$,
- broken power law (BPL): $\alpha_1 = U(2/3,5/3), \alpha_2 = U(0,-8), f_{\rm peak} = U(10,100)$,
- smooth BPL: $\alpha_1 = U(2/3,5/3)$, $\alpha_2 = U(0,-8)$, $f_* = U(10,100), \Delta = U(0,10)$,
- triple BPL: $\alpha_1 = U(2/3,5/3)$, $\alpha_2 = U(0,-8), \alpha_3 = \delta(2/3), f^1_{\rm peak} = U(10,100), f^2_{\rm peak} = U(10,100)$.

Here $U(a,b)$ denotes a Uniform distribution between $a$ and $b$, and $\mathcal{N}(\mu,\sigma)$ is a normal distribution with mean $\mu$ and standard deviation $\sigma$. For models with a break frequency we use a uniform prior for the first power law index between 2/3 and 5/3, since this represents the inspiral/merger regime of the compact binary coalescence. Triple BPL has the third spectral index fixed to $\alpha_3 = 2/3$ since we expect the inspiral phase of population I/II signal to dominate at higher frequencies. In Figure D.1 we show the corner plot of the PL search, with strong support for $\alpha = -0.6$.

## D.3 Intrinsic mass distribution

We study the relation between peak frequency of population III GWB spectrum and the mass distribution of the sources. We fix the merger rate as a function of redshift to be the one of StarTrack FS1 model. For total mass, $M_{\rm tot} = m_1 + m_2$ varying between 10 and 90 $M_\odot$, we generate $\Omega_{\rm GW}$ spectra and record the frequency at which the spectra are maximum. We then find a best-fit curve for the data,

$$f_{\rm peak} = f_0 \left(\frac{90 M_\odot}{M_{\rm tot}}\right) \text{Hz}, \tag{D.3}$$

with $f_0 = 12.8$ Hz, see Figure D.2. However, changing the merger rate to the one from [236], we find a different best fit curve, with $f_0 = 53.7$ Hz, implying that the intrinsic mass may be difficult to extract from the

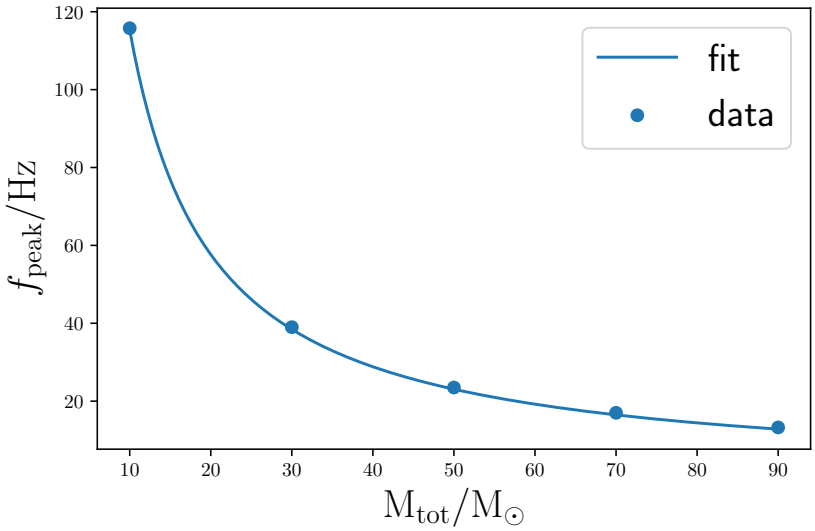


**Figure D.2:** StarTrack merger rate evolved, equal-mass binaries. We find a relationship between peak frequency and total intrinsic mass of the merger. This is a model-dependent statement.

estimate of the spectrum peak. We find more promising results if we study the redshifted total mass and its relation to peak frequency, as described in the main text.

Finally, the estimated $M^z_{\rm tot}$ can be depicted as a curve in the redshift-intrinsic total mass plane since $M^z_{\rm tot} = (1+z)M_{\rm tot}$, see Figure D.3. Note that we have included a 10% uncertainty error in matching of the ringdown and the peak frequency for consistency with our findings in Table 2 of the main text.

## D.4 Merger rate uncertainties

There are important differences in modelling pop III mergers [233, 246, 247, 248]. In some extreme cases pop III stars have lower redshifts, hence they would be more easily resolved individually and contribute less to the background. When this contribution goes below the pop I/II residual, its detection would not be straightforward. We use toy models close to ST to derive the background obtained as we shift the merger rate peak by $\Delta z$. The new catalogs are built using the merger rates shown in Figure D.4, primary

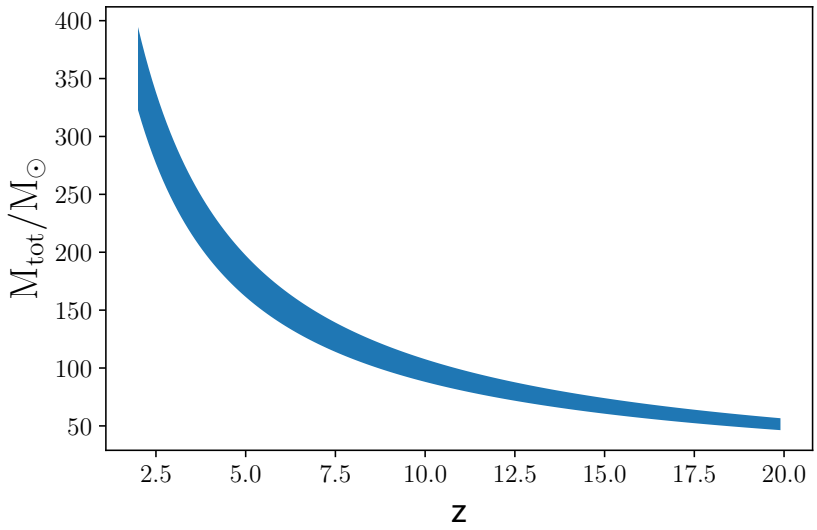


**Figure D.3:** $M^z_{\rm tot} = 1076 M_\odot$ constraint shown in the $M_{\rm tot}$-z plane, including 10% error bars accounting for the uncertainty of the estimate of $M^z_{\rm tot}$ from $f_{\rm peak}$.

masses similar to those in ST and uniform distribution for the mass ratio. Spins and eccentricities are neglected. We show in Figure D.5 the obtained background for each toy population. Residual backgrounds for negative $\Delta z$ exhibit lower amplitude as compared to the fiducial model ($\Delta z = 0$) due to the higher number of resolved binaries. The background obtained with higher redshifts, exhibits bumps with higher amplitude followed by a sharper decrease due to the absence of sources at low redshifts.

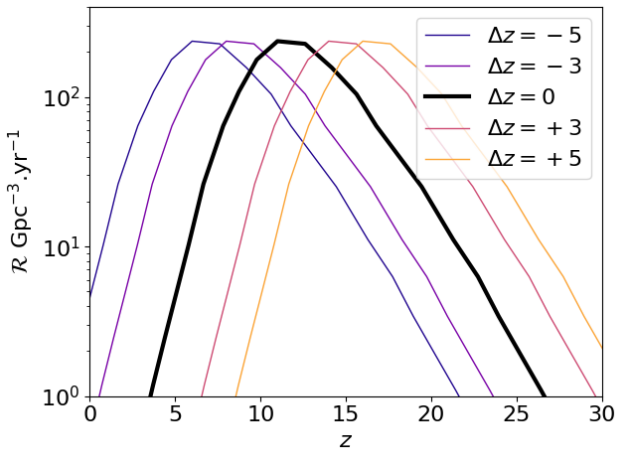


**Figure D.4:** Merger rates used to generate toy populations. The black line exhibits the merger rate of ST.

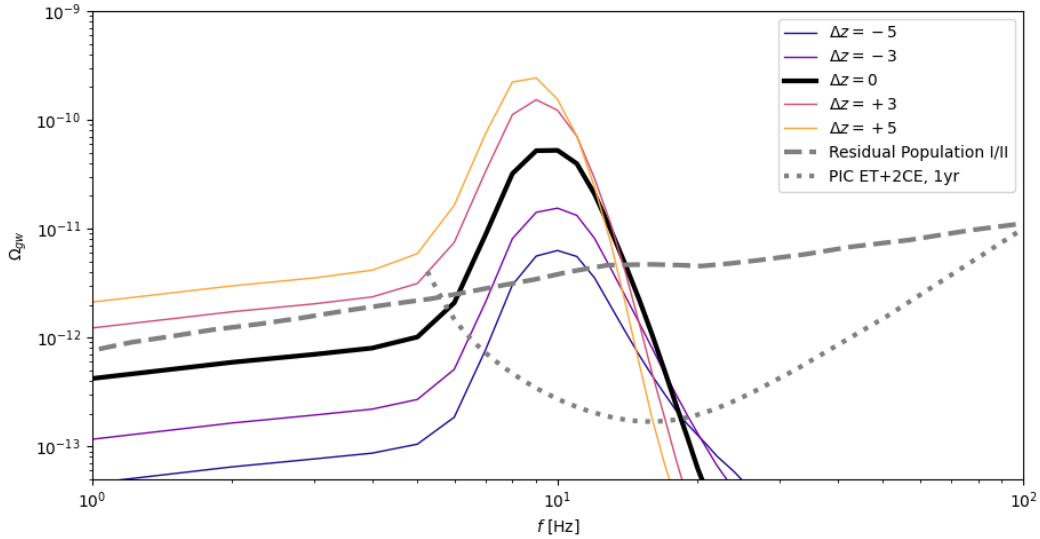


**Figure D.5:** Residual background obtained with toy populations close to ST model. The different colors correspond to different merger rates shown in Figure D.5. In grey we show the constraints for the residual detectability: for pop I/II in dashed line, and the PIC curve for ET+2CE in dotted line.

# Appendix E

# Supercooled first-order phase transition

## E.1 Gravitational waves from supercooled phase transitions

Several processes contribute to the GW signal from a supercooled FOPT. Those include bubble collisions, sound waves, and turbulence, the last of which will not be considered here, as it is generally subdominant [434, 191]. When calculating the contribution of bubble collisions to the GW signal, we assume that, in the limit of large $\alpha$, the fraction of the latent heat deposited into the bubble front $\kappa_{\rm bc} \sim 1$, leading to [435, 171, 191]

$$h^2\Omega_{\rm coll}(f) \approx \frac{(4.88\times10^{-6})\,(f/f_{\rm bc})^{2.8}}{1+2.8\,(f/f_{\rm bc})^{3.8}}\left(\frac{H_{\rm RH}}{\beta}\right)^2\left(\frac{100}{g_*}\right)^{\frac{1}{3}} \tag{E.1}$$

with the peak frequency $f_{\rm bc}$,

$$f_{\rm bc} \approx (3.7\times10^{-5}\ {\rm Hz})\left(\frac{g_*}{100}\right)^{\frac{1}{6}}\left(\frac{\beta}{H_{\rm RH}}\right)\left(\frac{T_{\rm RH}}{1\ {\rm TeV}}\right). \tag{E.2}$$

When considering cases in which the released energy can efficiently transfer to the plasma in the form of sound waves, we assume $\kappa_{\rm sw} \sim 1$, and the

resulting spectrum is [172, 191]

$$h^2\Omega_{\rm sw}(f) \approx \frac{(1.86\times10^{-5})\,(f/f_{\rm sw})^3}{\left[1+0.75\,(f/f_{\rm sw})^2\right]^{7/2}}\left(\frac{H_{\rm RH}}{\beta}\right)\left(\frac{100}{g_*}\right)^{\frac{1}{3}}, \tag{E.3}$$

where the peak frequency, $f_{\rm sw}$, is

$$f_{\rm sw} \approx (1.9\times10^{-4}\ {\rm Hz})\left(\frac{g_*}{100}\right)^{\frac{1}{6}}\left(\frac{\beta}{H_{\rm RH}}\right)\left(\frac{T_{\rm RH}}{1\ {\rm TeV}}\right). \tag{E.4}$$

Implicit in this spectrum is an infinite sound wave lifetime, $\tau_{\rm sw}$. Note that this is a good approximation only if turbulence and other damping processes are ignored, which is what we assume in this study [1]. Furthermore, in the supercooling limit, the $\alpha$ dependence vanishes from the spectra [2].

In the following we will consider the cases of bubble collision or of sound waves separately, assuming that one of the two mechanisms dominates the GW generation during the FOPT.

## E.2 Constraints on supercooled phase transitions using LVK data

To place constraints on model parameters using public data from LVK's third observing run O3 [331], we apply a Bayesian search following the methodology of [332]. Although a search for FOPT signals was already performed in [332], we now apply this search under the assumption that the signal comes from a supercooled phase transition. This allows for a simplification of the GW spectra, and therefore, less parameters in the Bayesian inference search, resulting in an increased ease of reusability of

[1] The finite sound wave lifetime, $\tau_{\rm sw}$, results in a multiplicative factor that is a function of $\tau_{\rm sw}$ and the expansion rate of the Universe when the sound waves were active [305, 301]. Currently, the value of $\tau_{\rm sw}$ remains highly uncertain, though an analytical estimate is usually adopted in the literature. Since this effect is simply an extra overall factor, it could be taken as an additional parameter in the Bayesian inference.

[2] The GW spectra in [435, 434, 171, 172, 191] are simulated for FOPTs not exhibiting large supercooling. In our analysis we assume that those results can be extrapolated to the region of large $\alpha$.

the obtained upper limits.

Below, two approaches will be explored parameterising the GW background signal as a broken power law and using the spectra provided in the previous section (see Eqs. (E.1) and (E.3)). In both cases, the contribution from the astrophysical background, i.e., from unresolved compact binary coalescences (CBCs), will be taken into account as well. This background is expected to follow a power law

$$\Omega_{\rm CBC}(f) = \Omega_{\rm ref} \left(\frac{f}{f_{\rm ref}}\right)^{2/3}, \tag{E.5}$$

where $f_{\rm ref}$ is a reference frequency taken, as usual, set to $f_{\rm ref} = 25$ Hz [331]. It is worth noting that the constraints obtained in this section are general and can be applied to any model exhibiting supercooling to constrain the underlying physical parameters.

### E.2.1 General broken power law search

To constraint a GW background from FOPTs, we model the GW spectrum by a broken power law as

$$\Omega_{\rm bpl}(f) = \Omega_* \left(\frac{f}{f_*}\right)^{n_1} \left[1 + \left(\frac{f}{f_*}\right)^{\Delta}\right]^{(n_2-n_1)/\Delta}, \tag{E.6}$$

where $n_1$ and $n_2$, respectively, denote the spectral indices before and after the peak, $\Delta$ is a peak smoothing parameter, and $\Omega_*$ and $f_*$ can be related to the peak amplitude and peak frequency of the spectrum. Note that the spectra introduced in Eqs. (E.1), (E.3), follow a broken power law with parameters $n_1 = 3$, $n_2 = -1$, $\Delta = 4$ and $n_1 = 3$, $n_2 = -4$, $\Delta = 2$ for bubble collisions and sound waves, respectively. We perform a parameter estimation search for both contributions separately, corresponding to the case where one of them dominates the GW spectrum. In each case, the values of $n_1$, $n_2$, and $\Delta$ are set to the relevant values of that contribution, as given above. Note that in [332], $n_2$ was allowed to vary.

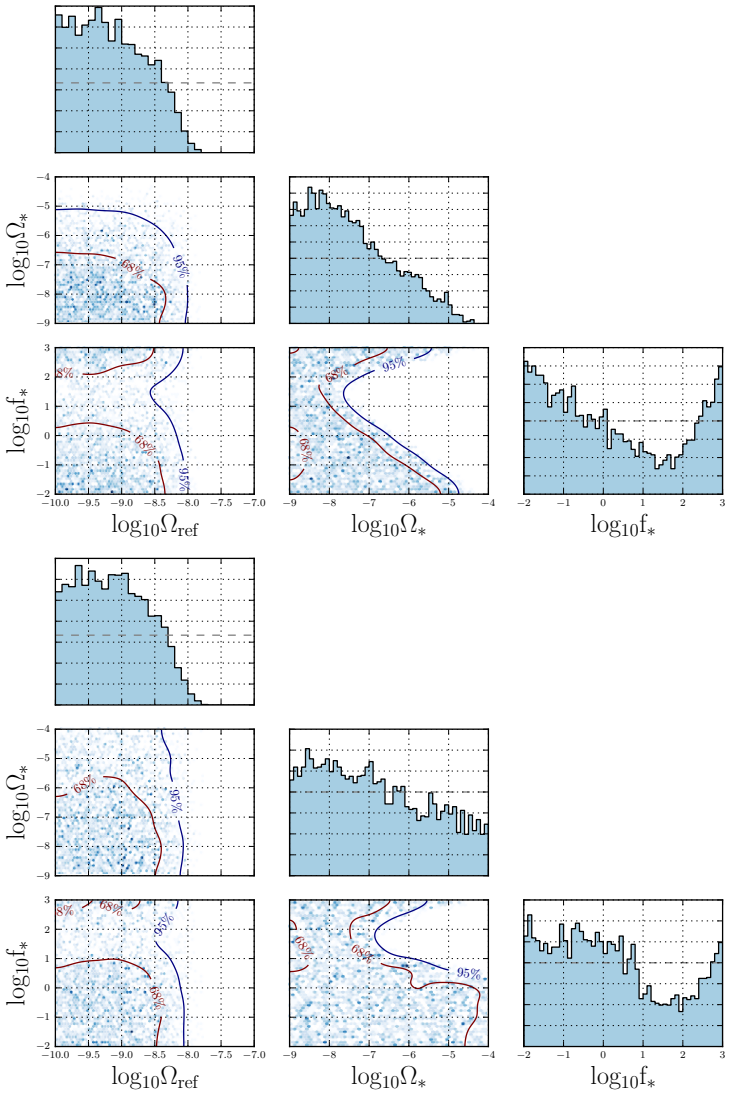


**Figure E.1:** Constraints from LVK O3 data on the broken power law parameters of a FOPT signal, together with the contribution from the CBC background, assuming dominant bubble collision spectrum (top) and a dominant sound waves spectrum (bottom).

The likelihood to perform this search is given by Eq. (3.4), where $\Omega_{\rm GW} = \Omega_{\rm CBC} + \Omega_{\rm bpl}$. The GW parameters to be constrained are $\boldsymbol{\theta}_{\rm GW} = (\Omega_{\rm ref},\ \Omega_*,\ f_*)$ with priors given in Table E.1 and results shown in Figure E.1 for bubble collisions (top panel) and sound waves (bottom panel). From the posteriors of the amplitude of the CBC background, $\Omega_{\rm ref}$, upper limits (ULs) at 95% confidence level (CL) are obtained. The value for the case in which bubble collisions dominate is $5.60 \times 10^{-9}$, which is consis-

| Broken power law | | Phenomenological | |
|---|---|---|---|
| $\Omega_{\rm ref}$ | LogU[$10^{-10}$, $10^{-7}$] | $\Omega_{\rm ref}$ | LogU[$10^{-10}$, $10^{-7}$] |
| $\Omega_*$ | LogU[$10^{-9}$, $10^{-4}$] | $\beta/H_{\rm RH}$ | LogU[1,$10^3$] |
| $f_*$ | LogU[$10^{-2}$, $10^3$] | $T_{\rm RH}$ | LogU[$10^5$,$10^{10}$] |

**Table E.1:** Summary of the priors used for parameter estimation for the broken power law model search and the phenomenological model search, where LogU stands for a log-uniform prior. The narrow prior on $\Omega_{\rm ref}$ stems from estimates of the CBC background [330]. The peak frequency is chosen such that it lies in the region of highest sensitivity in LIGO-Virgo. Values lower than 1 for fi/$H_{\rm RH}$ are not considered, since otherwise the phase transition would not take place.

tent with the upper limit obtained in [331, 332]. The UL in the case when sound waves dominate is also consistent with previous searches, with a value $5.70 \times 10^{-9}$. Similarly, 95% confidence level contours are obtained on the amplitude and peak frequency of the contribution from FOPTs, $\Omega_*$ and $f_*$, as depicted in Figure E.1. The values of the Bayes factor are $\log \mathcal{B}^{\rm CBC+BC}_{\rm noise} = -1.26$ and $\log \mathcal{B}^{\rm CBC+SW}_{\rm noise} = -0.80$, showing no evidence for a FOPT signal in the data.

### E.2.2 Phenomenological search

We now proceed with a different model assumption. Instead of the general broken power law model used above, we consider the GW spectra introduced in Section E.1, more specifically Eqs. (E.1) and (E.3), corresponding to bubble collisions and sound waves, respectively. The likelihood used to perform this search is given by Eq. (3.4), with $\Omega_{\rm GW} = \Omega_{\rm CBC} + \Omega_{\rm coll}$ and $\Omega_{\rm GW} = \Omega_{\rm CBC} + \Omega_{\rm sw}$ for bubble collisions and sounds waves, respectively. Therefore, the GW parameters to be constrained in this search are $\boldsymbol{\theta}_{\rm GW} = (\Omega_{\rm ref},\ \beta/H_{\rm RH},\ T_{\rm RH})$. We again highlight the difference with the search conducted in [332], where the $\alpha$ parameter was included. As discussed earlier, for supercooled FOPTs, for which $\alpha \gg 1$, neglecting this parameter is a valid assumption. The priors on the parameters used for parameter estimation are given in Table E.1, and the resulting posterior

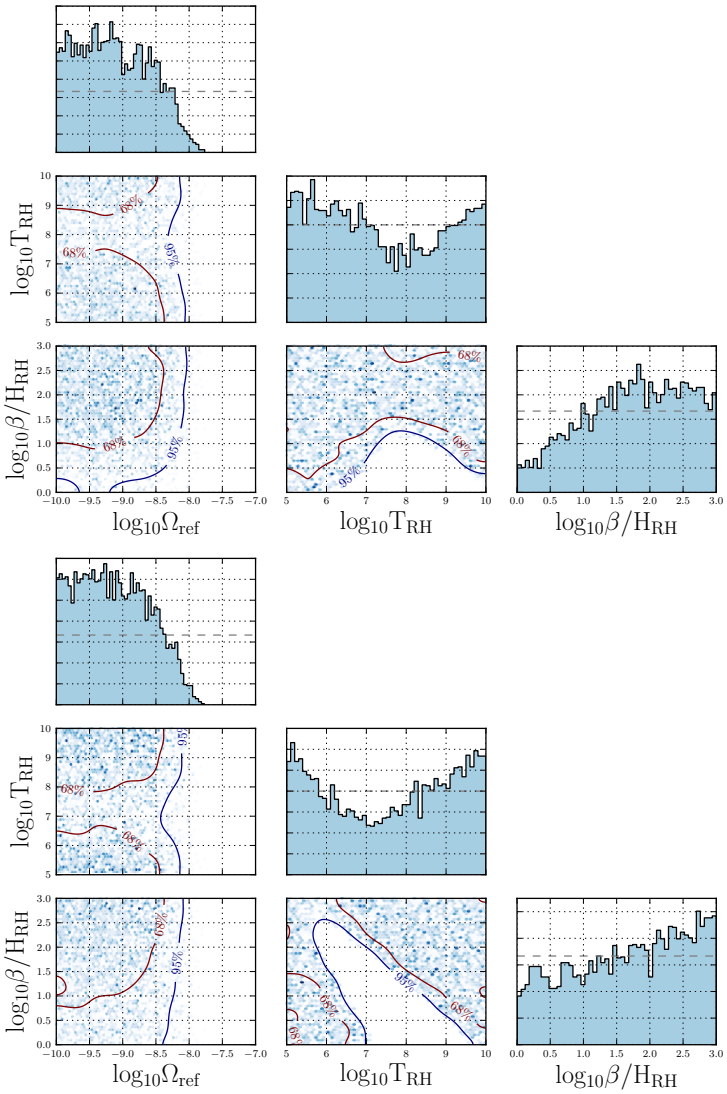


**Figure E.2:** Constraints from LVK O3 data on the phenomenological parameters $\beta/H_{\rm RH}$ and $T_{\rm RH}$ of a supercooled FOPT signal, together with the contribution from the CBC background, assuming a dominant bubble collision spectrum (top) and a dominant sound waves spectrum (bottom).

distributions are presented in Figure E.2. From the posteriors of the amplitude of the CBC background, $\Omega_{\rm ref}$, ULs at 95% CL are obtained. The value for the case in which bubble collisions or sound waves dominate is $5.89 \times 10^{-9}$ and $5.93 \times 10^{-9}$, respectively. They are consistent with the upper limit obtained in [331, 332]. Furthermore, exclusions at 95% CL for temperatures $T_{\rm RH}$ and inverse duration of the FOPT $\beta/H_{\rm RH}$ are depicted in Figure E.2.

Let us emphasise that the constraints derived above can be used in any model exhibiting supercooling. More precisely, once a model and its parameters are specified, one can compute the expected FOPT parameters $\beta/H_{\rm RH}$ and $T_{\rm RH}$ (or equivalently $\Omega_*$ and $f_*$) and compare them with the 95% confidence UL provided here. In this way, one uses GW data to exclude regions of the parameter space in concrete particle physics models. We will illustrate this in the next section for two particle physics models.

## E.3 Comparison of constraints on particle physics couplings

Let us now compare the exclusion regions obtained directly on the parameters of the models in Section 4.3.4 and the ones deduced from the analysis in E.2. Given a parameter choice for $(m_{Z'}, g)$ or $(F, \lambda)$, one can verify whether the corresponding $(\beta/H_{\rm RH}, T_{\rm RH})$ or $(f_*, \Omega_*)$ are excluded using the search analysis in E.2. The exclusion region comparison is shown in Figure E.3. Good agreement is found between the various exclusion regions, regardless of the search performed. This illustrates the reusability of the results obtained in E.2 to constrain any supercooled FOPT at a particle physics model level.

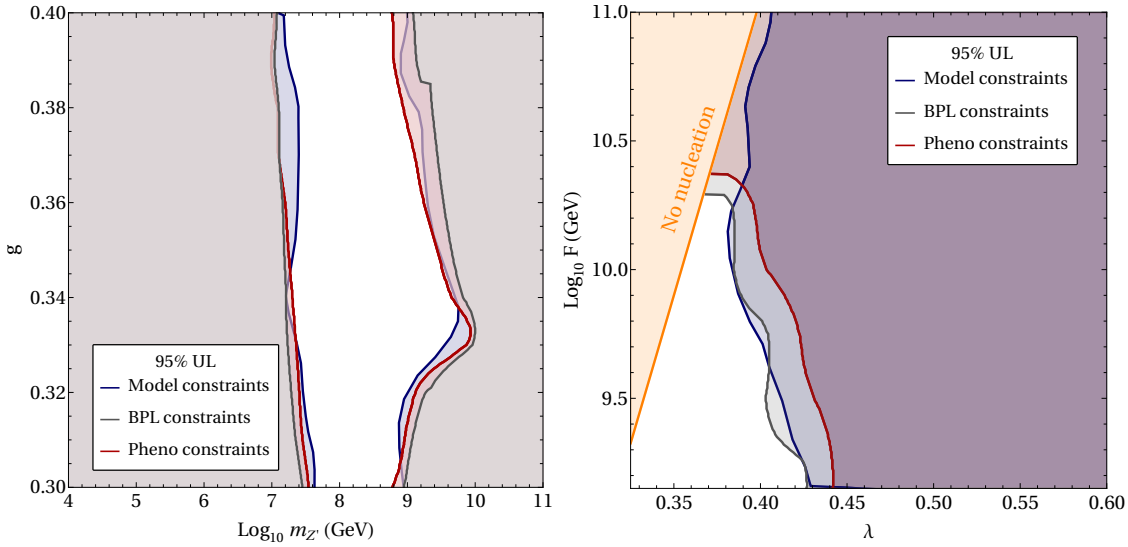


**Figure E.3:** Comparison of the constraints on the parameter space $(m_{Z'}, g)$ for Model I (top panel) and on $(\lambda, F)$ for Model II (bottom panel) obtained by constraining the model parameters directly as in Figure 4.8 (blue line), with those obtained by adopting the BPL model as given in Figure E.1 (gray line), and those adopting the phenomenological model in Figure E.2 (red line).

# Appendix F

# Quasidilaton massive gravity

## F.1 QDMG Lagrangian in the decoupling limit

We write below all terms in the Lagrangian of quasi-dilaton massive gravity in the decoupling limit,

$$\begin{aligned}\mathcal{L}^{\rm DL}_{\rm QDMG} = &-\frac{1}{4}\Big(h^{\mu\nu}\hat{\mathcal{E}}^{\alpha\beta}_{\mu\nu}h_{\alpha\beta} + \sum_{n=2}^{5}\frac{c_n}{\Lambda_3^{3(n-2)}}\mathcal{L}^{(n)}_{\rm Gal}[\pi] - \frac{2(\alpha_3+4\alpha_4)}{\Lambda_3^6}h^{\mu\nu}X^{(3)}_{\mu\nu}[\Pi]\Big)\\ &-\frac{\omega}{2}(\partial\sigma)^2 + \frac{1}{2}\sigma\sum_{n=1}^{4}\frac{(4-n)\alpha_n-(n+1)\alpha_{n+1}}{\Lambda_3^{3(n-1)}}\mathcal{L}_n[\Pi]\\ &+\frac{1}{2M_{\rm Pl}}h_{\mu\nu}T^{\mu\nu} + \frac{1}{2M_{\rm Pl}}\pi T - \frac{2+3\alpha_3}{4M_{\rm Pl}\Lambda_3^3}\partial_\mu\pi\partial_\nu\pi T^{\mu\nu}.\end{aligned} \tag{F.1}$$

The galileon Lagrangians are defined below:

$$\mathcal{L}^{(2)}_{\rm Gal}[\pi] = (\partial\pi)^2, \tag{F.2}$$

$$\mathcal{L}^{(3)}_{\rm Gal}[\pi] = (\partial\pi)^2\Box\pi, \tag{F.3}$$

$$\mathcal{L}^{(4)}_{\rm Gal}[\pi] = (\partial\pi)^2\Big((\Box\pi)^2 - \nabla_\mu\nabla_\nu\pi\nabla^\mu\nabla^\nu\pi\Big), \tag{F.4}$$

$$\mathcal{L}^{(5)}_{\rm Gal}[\pi] = (\partial\pi)^2\Big((\Box\pi)^3 - 3\Box\pi\nabla_\mu\nabla_\nu\pi\nabla^\mu\nabla^\nu\pi \\ +2\nabla^\mu\nabla_\nu\pi\nabla^\nu\nabla_\lambda\pi\nabla^\lambda\nabla_\mu\pi\Big). \tag{F.5}$$

Next, we define $X^{(3)}_{\mu\nu}$ as

$$X^{(3)}_{\mu\nu} = \Big([\Pi]^3 - 3[\Pi][\Pi^2] + 2[\Pi^3]\Big)\eta_{\mu\nu} \\ -3\Big([\Pi]^2\Pi_{\mu\nu} - 2[\Pi]\Pi^2_{\mu\nu} - [\Pi^2]\Pi_{\mu\nu} + 2\Pi^3_{\mu\nu}\Big), \tag{F.6}$$

where $\Pi_{\mu\nu} = \partial_\mu\partial_\nu\pi$. Finally, we explicitly write out the expressions for $\mathcal{L}_n[\Pi]$:

$$\mathcal{L}_1[\Pi] = 3![\Pi], \tag{F.7}$$

$$\mathcal{L}_2[\Pi] = 2\Big([\Pi]^2 - [\Pi^2]\Big), \tag{F.8}$$

$$\mathcal{L}_3[\Pi] = [\Pi]^3 - 3[\Pi][\Pi^2] + 2[\Pi^3]. \tag{F.9}$$

## F.2 Equation for $x$

We expand and show in full detail the equation for $x = \frac{\phi'}{r}$:

$$\left[\frac{3}{2} - \frac{36}{\omega}\right]x + \frac{3}{\Lambda_3^3}\left[\frac{2+3\alpha_3}{2} + \frac{12(2-3\alpha_3)}{\omega} - \frac{2(\alpha_3+4\alpha_4)}{\Lambda_3^3}A\right]x^2 \\ +\frac{8}{\Lambda_3^6}\left[\frac{3(\alpha_3-4\alpha_4)-(2-3\alpha_3)^2}{\omega}\right]x^3 - \frac{10}{\Lambda_3^9}\left[\frac{(2-3\alpha_3)(\alpha_3-4\alpha_4)}{\omega}\right]x^4 \\ -\frac{3}{\Lambda_3^{12}}\left[2(\alpha_3+4\alpha_4)^2 + \frac{1}{\omega}(\alpha_3-4\alpha_4)^2\right]x^5 = A \tag{F.10}$$

# Bibliography


[1] B. P. Abbott et al. Observation of Gravitational Waves from a Binary Black Hole Merger. *Phys. Rev. Lett.*, 116(6):061102, 2016.

[2] J. Aasi et al. Advanced LIGO. *Class. Quant. Grav.*, 32:074001, 2015.

[3] Emanuele Berti, Kent Yagi, and Nicolás Yunes. Extreme Gravity Tests with Gravitational Waves from Compact Binary Coalescences: (I) Inspiral-Merger. *Gen. Rel. Grav.*, 50(4):46, 2018.

[4] Emanuele Berti, Kent Yagi, Huan Yang, and Nicolás Yunes. Extreme Gravity Tests with Gravitational Waves from Compact Binary Coalescences: (II) Ringdown. *Gen. Rel. Grav.*, 50(5):49, 2018.

[5] R. Abbott et al. The population of merging compact binaries inferred using gravitational waves through GWTC-3. 11 2021.

[6] F. Acernese et al. Advanced Virgo: a second-generation interferometric gravitational wave detector. *Class. Quant. Grav.*, 32(2):024001, 2015.

[7] B. P. Abbott et al. GWTC-1: A Gravitational-Wave Transient Catalog of Compact Binary Mergers Observed by LIGO and Virgo during the First and Second Observing Runs. *Phys. Rev.*, X9(3):031040, 2019.

[8] `https://gracedb.ligo.org/superevents/public/O3/`.

[9] B.P. Abbott et al. GW190425: Observation of a Compact Binary Coalescence with Total Mass $\sim 3.4 M_{\odot}$. *Astrophys. J. Lett.*, 892(1):L3, 2020.

[10] R. Abbott et al. GW190814: Gravitational waves from the coalescence of a 23 solar mass black hole with a 2.6 solar mass compact object. *The Astrophysical Journal*, 896(2):L44, jun 2020.

[11] R. Abbott et al. Observation of Gravitational Waves from Two Neutron Star–Black Hole Coalescences. *Astrophys. J. Lett.*, 915(1):L5, 2021.

[12] R. Abbott et al. GWTC-2: Compact Binary Coalescences Observed by LIGO and Virgo During the First Half of the Third Observing Run. *Phys. Rev. X*, 11:021053, 2021.

[13] R. Abbott et al. GWTC-2.1: Deep Extended Catalog of Compact Binary Coalescences Observed by LIGO and Virgo During the First Half of the Third Observing Run. 8 2021.

[14] R. Abbott et al. GWTC-3: Compact Binary Coalescences Observed by LIGO and Virgo During the Second Part of the Third Observing Run. 11 2021.

[15] Eemeli Annala, Tyler Gorda, Aleksi Kurkela, and Aleksi Vuorinen. Gravitational-wave constraints on the neutron-star-matter Equation of State. *Phys. Rev. Lett.*, 120(17):172703, 2018.

[16] N. Aghanim et al. Planck 2018 results. VI. Cosmological parameters. *Astron. Astrophys.*, 641:A6, 2020. [Erratum: Astron.Astrophys. 652, C4 (2021)].

[17] Steven Weinberg. *The quantum theory of fields. Vol. 2: Modern applications*. Cambridge University Press, 2013.

[18] Ruth Durrer. *The Cosmic Microwave Background*. Cambridge University Press, Cambridge, 2008.

[19] Sean M. Carroll. *Spacetime and Geometry*. Cambridge University Press, 7 2019.

[20] Robert M. Wald. *General Relativity*. Chicago Univ. Pr., Chicago, USA, 1984.

[21] Charles W. Misner, K. S. Thorne, and J. A. Wheeler. *Gravitation*. W. H. Freeman, San Francisco, 1973.

[22] Nils Andersson et al. The Transient Gravitational-Wave Sky. *Class. Quant. Grav.*, 30:193002, 2013.

[23] Pierre Auclair et al. Probing the gravitational wave background from cosmic strings with LISA. *JCAP*, 04:034, 2020.

[24] Rachel Jeannerot, Jonathan Rocher, and Mairi Sakellariadou. How generic is cosmic string formation in supersymmetric grand unified theories. *Phys. Rev. D*, 68:103514, Nov 2003.

[25] R. Abbott et al. Constraints on Cosmic Strings Using Data from the Third Advanced LIGO–Virgo Observing Run. *Phys. Rev. Lett.*, 126(24):241102, 2021.

[26] R. Abbott et al. All-sky search for short gravitational-wave bursts in the third Advanced LIGO and Advanced Virgo run. *Phys. Rev. D*, 104(12):122004, 2021.

[27] B. P. Abbott et al. Observation of Gravitational Waves from a Binary Black Hole Merger. *Phys. Rev. Lett.*, 116(6):061102, 2016.

[28] R. A. Hulse and J. H. Taylor. Discovery of a pulsar in a binary system. *Astrophys. J.*, 195:L51–L53, 1975.

[29] Joel M. Weisberg and Joseph H. Taylor. Relativistic binary pulsar B1913+16: Thirty years of observations and analysis. *ASP Conf. Ser.*, 328:25, 2005.

[30] R. Abbott et al. Search for continuous gravitational waves from 20 accreting millisecond X-ray pulsars in O3 LIGO data. 9 2021.

[31] R. Abbott et al. Narrowband searches for continuous and long-duration transient gravitational waves from known pulsars in the LIGO-Virgo third observing run. 12 2021.

[32] Benjamin P. Abbott et al. GW170817: Implications for the Stochastic Gravitational-Wave Background from Compact Binary Coalescences. *Phys. Rev. Lett.*, 120(9):091101, 2018.

[33] Nelson Christensen. Stochastic Gravitational Wave Backgrounds. *Rept. Prog. Phys.*, 82(1):016903, 2019.

[34] B. P. Abbott et al. GW170814: A Three-Detector Observation of Gravitational Waves from a Binary Black Hole Coalescence. *Phys. Rev. Lett.*, 119(14):141101, 2017.

[35] Thomas Callister, A. Sylvia Biscoveanu, Nelson Christensen, Maximiliano Isi, Andrew Matas, Olivier Minazzoli, Tania Regimbau, Mairi Sakellariadou, Jay Tasson, and Eric Thrane. Polarization-based Tests of Gravity with the Stochastic Gravitational-Wave Background. *Phys. Rev.*, X7(4):041058, 2017.

[36] Benjamin P. Abbott et al. Search for Tensor, Vector, and Scalar Polarizations in the Stochastic Gravitational-Wave Background. *Phys. Rev. Lett.*, 120(20):201102, 2018.

[37] Thomas Callister, Maya Fishbach, Daniel Holz, and Will Farr. Shouts and Murmurs: Combining Individual Gravitational-Wave Sources with the Stochastic Background to Measure the History of Binary Black Hole Mergers. 3 2020.

[38] Joseph D. Romano and Neil J. Cornish. Detection methods for stochastic gravitational-wave backgrounds: a unified treatment. *Living Rev. Rel.*, 20(1):2, 2017.

[39] Albert Abraham Michelson and Edward Williams Morley. On the Relative Motion of the Earth and the Luminiferous Ether. *Am. J. Sci.*, 34:333–345, 1887.

[40] Aidan F. Brooks et al. Overview of Advanced LIGO Adaptive Optics. *Appl. Opt.*, 55:8256, 2016.

[41] Michele Maggiore. *Gravitational Waves. Vol. 1: Theory and Experiments*. Oxford Master Series in Physics. Oxford University Press, 2007.

[42] T. Akutsu et al. Construction of KAGRA: an Underground Gravitational Wave Observatory. *PTEP*, 2018(1):013F01, 2018.

[43] H. Grote and D. H. Reitze. First-Generation Interferometric Gravitational-Wave Detectors. In *46th Rencontres de Moriond on Gravitational Waves and Experimental Gravity*, pages 5–18, Paris, France, 2011. Moriond.

[44] M Punturo et al. The einstein telescope: a third-generation gravitational wave observatory. *Classical and Quantum Gravity*, 27:194002, 01 2010.

[45] David Reitze, Rana X Adhikari, Stefan Ballmer, Barry Barish, Lisa Barsotti, GariLynn Billingsley, Duncan A. Brown, Yanbei Chen, Dennis Coyne, Robert Eisenstein, Matthew Evans, Peter Fritschel, Evan D. Hall, Albert Lazzarini, Geoffrey Lovelace, Jocelyn Read, B. S. Sathyaprakash, David Shoemaker, Joshua Smith, Calum Torrie, Salvatore Vitale, Rainer Weiss, Christopher Wipf, and Michael Zucker. Cosmic explorer: The u.s. contribution to gravitational-wave astronomy beyond ligo, 2019.

[46] Pau Amaro-Seoane et al. Laser Interferometer Space Antenna. 2 2017.

[47] Evan D. Hall and Matthew Evans. Metrics for next-generation

gravitational-wave detectors. *Classical and Quantum Gravity*, 36(22):225002, November 2019.

[48] Patrick M. Meyers, Katarina Martinovic, Nelson Christensen, and Mairi Sakellariadou. Detecting a stochastic gravitational-wave background in the presence of correlated magnetic noise. *Phys. Rev. D*, 102(10):102005, 2020.

[49] Ssohrab Borhanian, Arnab Dhani, Anuradha Gupta, K. G. Arun, and B. S. Sathyaprakash. Dark sirens to resolve the hubble-lemaître tension, 2020.

[50] Evan D. Hall and Matthew Evans. Metrics for next-generation gravitational-wave detectors. *Class. Quant. Grav.*, 36(22):225002, 2019.

[51] Matthew Evans et al. A Horizon Study for Cosmic Explorer: Science, Observatories, and Community. 9 2021.

[52] L. Badurina et al. AION: An Atom Interferometer Observatory and Network. *JCAP*, 05:011, 2020.

[53] Yousef Abou El-Neaj et al. AEDGE: Atomic Experiment for Dark Matter and Gravity Exploration in Space. *EPJ Quant. Technol.*, 7:6, 2020.

[54] Maura A. McLaughlin. The North American Nanohertz Observatory for Gravitational Waves. *Class. Quant. Grav.*, 30:224008, 2013.

[55] Pablo A. Rosado. Gravitational wave background from binary systems. *Phys. Rev. D*, 84:084004, 2011.

[56] Joseph D. Romano and Neil. J. Cornish. Detection methods for stochastic gravitational-wave backgrounds: a unified treatment. *Living Reviews in Relativity*, 20(1), Apr 2017.

[57] David Alonso, Carlo R. Contaldi, Giulia Cusin, Pedro G. Ferreira, and Arianna I. Renzini. Noise angular power spectrum of gravitational wave background experiments. *Phys. Rev. D*, 101(12):124048, 2020.

[58] Arianna I. Renzini, Boris Goncharov, Alexander C. Jenkins, and Pat M. Meyers. Stochastic Gravitational-Wave Backgrounds: Current Detection Efforts and Future Prospects. *Galaxies*, 10(1):34, 2022.

[59] R. Abbott et al. Upper limits on the isotropic gravitational-wave background from Advanced LIGO and Advanced Virgo's third observing run. *Phys. Rev. D*, 104(2):022004, 2021.

[60] Nelson Christensen. Measuring the stochastic gravitational-radiation background with laser-interferometric antennas. *Phys. Rev. D*, 46:5250–5266, Dec 1992.

[61] Chiara M. F. Mingarelli, Stephen R. Taylor, B. S. Sathyaprakash, and Will M. Farr. Understanding $\Omega_{\rm gw}(f)$ in Gravitational Wave Experiments. *arXiv e-prints*, page arXiv:1911.09745, November 2019.

[62] N. Aghanim et al. Planck 2018 results. VIII. Gravitational lensing. *Astron. Astrophys.*, 641:A8, 2020.

[63] P. Ajith et al. Inspiral-merger-ringdown waveforms for black-hole binaries with non-precessing spins. *Phys. Rev. Lett.*, 106:241101, 2011.

[64] E. Vangioni, K. A. Olive, T. Prestegard, J. Silk, P. Petitjean, and V. Mandic. The Impact of Star Formation and Gamma-Ray Burst Rates at High Redshift on Cosmic Chemical Evolution and Reionization. *Mon. Not. Roy. Astron. Soc.*, 447:2575, 2015.

[65] R. Abbott et al. Population Properties of Compact Objects from the Second LIGO-Virgo Gravitational-Wave Transient Catalog. *Astrophys. J. Lett.*, 913(1):L7, 2021.

[66] W. O. Schumann. Über die strahlungslosen Eigenschwingungen einer leitenden Kugel, die von einer Luftschicht und einer Ionosphärenhülle umgeben ist. *Zeitschrift Naturforschung Teil A*, 7:149–154, February 1952.

[67] W. O. Schumann. Über die Dämpfung der elektromagnetischen Eigenschwingungen des Systems Erde - Luft - Ionosphäre. *Zeitschrift Naturforschung Teil A*, 7:250–252, March 1952.

[68] W. O. Schumann. Über die strahlungslosen Eigenschwingungen einer leitenden Kugel, die von einer Luftschicht und einer Ionosphärenhülle umgeben ist. *Zeitschrift Naturforschung Teil A*, 7(2):149–154, February 1952.

[69] W. O. Schumann and H. König. Über die Beobachtung von "atmospherics" bei geringsten Frequenzen. *Naturwissenschaften*, 41(8):183–184, January 1954.

[70] Colin Price. ELF Electromagnetic Waves from Lightning: The Schumann Resonances. *Atmosphere*, 7(9):116, Sep 2016.

[71] Eric Thrane, Nelson Christensen, and Robert Schofield. Correlated magnetic noise in global networks of gravitational-wave interferometers: observations and implications. *Phys. Rev.*, D87:123009, 2013.

[72] E. Thrane, N. Christensen, R. M. S. Schofield, and A. Effler. Correlated noise in networks of gravitational-wave detectors: subtraction and mitigation. *Phys. Rev.*, D90(2):023013, 2014.

[73] Irene Fiori et al. The hunt for environmental noise in virgo during the third observing run. *Galaxies*, 8(4), 2020.

[74] P Nguyen et al. Environmental noise in advanced LIGO detectors. *Classical and Quantum Gravity*, 38(14):145001, jun 2021.

[75] Yoshiaki Himemoto and Atsushi Taruya. Impact of correlated magnetic noise on the detection of stochastic gravitational waves: Estimation based on a simple analytical model. *Physical Review D*, 96(2):022004, Jul 2017.

[76] Yoshiaki Himemoto and Atsushi Taruya. Correlated magnetic noise from anisotropic lightning sources and the detection of stochastic gravitational waves. *Physical Review D*, 100(8):082001, Oct 2019.

[77] D.D. Sentman. *Handbook of Atmospheric Electrodynamics*, volume 1. CRC Press, Boca Raton, 1995.

[78] Colin Price and Alexander Melnikov. Diurnal, seasonal and inter-annual variations in the schumann resonance parameters. *Journal of Atmospheric and Solar-Terrestrial Physics*, 66(13):1179 – 1185, 2004. SPECIAL - Space Processes and Electrical Changes in Atmospheric L ayers.

[79] Hongjuan Zhou, Haiyan Yu, Bingxia Cao, and Xiaolin Qiao. Diurnal and seasonal variations in the schumann resonance parameters observed at chinese observatories. *Journal of Atmospheric and Solar-Terrestrial Physics*, 98:86 – 96, 2013.

[80] Michael W. Coughlin et al. Subtraction of correlated noise in global networks of gravitational-wave interferometers. *Class. Quant. Grav.*, 33(22):224003, 2016.

[81] Jennifer C. Driggers, Matthew Evans, Keenan Pepper, and Rana Adhikari. Active noise cancellation in a suspended interferometer. *Rev. Sci. Instrum.*, 83:024501, 2012.

[82] M. Coughlin, J. Harms, D. C. Bowden, P. Meyers, V. C. Tsai, V. Mandic, G. Pavlis, and T. Prestegard. Coherence-based approaches for estimating the composition of the seismic wavefield. 11 2019.

[83] Sukanta Bose, Bernard Hall, Nairwita Mazumder, Sanjeev Dhurandhar, Anuradha Gupta, and Andrew Lundgren. Tackling excess noise from bilinear and nonlinear couplings in gravitational-wave interferometers. *J. Phys. Conf. Ser.*, 716(1):012007, 2016.

[84] Rich Ormiston, Tri Nguyen, Michael Coughlin, Rana X. Adhikari, and Erik Katsavounidis. Noise Reduction in Gravitational-wave Data via Deep Learning. *Phys. Rev. Res.*, 2(3):033066, 2020.

[85] Thomas Callister, M.W. Coughlin, and J.B. Kanner. Gravitational-wave Geodesy: A New Tool for Validating Detection of the Stochastic Gravitational-wave Background. *Astrophys. J. Lett.*, 869(2):L28, 2018.

[86] Kamiel Janssens, Thomas A. Callister, Nelson Christensen, Michael W. Coughlin, Ioannis Michaloliakos, Jishnu Suresh, and Nick van Remortel. Gravitational-Wave Geodesy: Defining False Alarm Probabilities with Respect to Correlated Noise. 12 2021.

[87] B. P. Abbott et al. Search for the isotropic stochastic background using data from Advanced LIGO's second observing run. *Physical Review D*, 100(6):061101, Sep 2019.

[88] Michael W. Coughlin et al. Measurement and subtraction of Schumann resonances at gravitational-wave interferometers. *Phys. Rev.*, D97(10):102007, 2018.

[89] `https://alog.ligo-wa.caltech.edu/aLOG/index.php?callRep=39199`.

[90] `https://logbook.virgo-gw.eu/virgo/?r=40025`.

[91] Giancarlo Cella, Carlo Nicola Colacino, Elena Cuoco, Angela Di Virgilio, Tania Regimbau, Emma L. Robinson, and John T Whelan. Prospects for stochastic background searches using Virgo and LSC interferometers. *Class. Quant. Grav.*, 24:S639–S648, 2007.

[92] B. P. Abbott et al. Prospects for observing and localizing gravitational-wave transients with Advanced LIGO, Advanced Virgo and KAGRA. *Living Reviews in Relativity*, 21(1):3, April 2018.

[93] V. Mandic, E. Thrane, S. Giampanis, and T. Regimbau. Parameter Estimation in Searches for the Stochastic Gravitational-Wave Background. *Physical Review Letters*, 109(17):171102, October 2012.

[94] W.R. Gilks, S. Richardson, and D.J. Spiegelhalter. *Markov Chain Monte Carlo in Practice*, 1996.

[95] Nelson Christensen and Renate Meyer. Markov chain Monte Carlo methods for Bayesian gravitational radiation data analysis. *Phys. Rev. D*, 58:082001, Sep 1998.

[96] John Skilling. Nested sampling for general Bayesian computation. *Bayesian Anal.*, 1(4):833–859, 12 2006.

[97] John Veitch, Walter Del Pozzo, Cody, Matt Pitkin, and ed1d1a8d. johnveitch/cpnest: Minor optimisation, July 2017.

[98] Gregory Ashton et al. BILBY: A user-friendly Bayesian inference library for gravitational-wave astronomy. *Astrophys. J. Suppl.*, 241(2):27, 2019.

[99] Samantha R Cook, Andrew Gelman, and Donald B Rubin. Validation of software for bayesian models using posterior quantiles. *Journal of Computational and Graphical Statistics*, 15(3):675–692, 2006.

[100] Kara Merfeld et al. aLIGO LHO Logbook. `https://alog.ligo-wa.caltech.edu/aLOG/index.php?callRep=48212`.

[101] M. Punturo et al. The Einstein Telescope: A third-generation gravitational wave observatory. *Class. Quant. Grav.*, 27:194002, 2010.

[102] Florian Amann et al. Site-selection criteria for the Einstein Telescope. *Rev. Sci. Instrum.*, 91(9):9, 2020.

[103] Izabela Kowalska-Leszczynska et al. Globally coherent short duration magnetic field transients and their effect on ground based gravitational-wave detectors. *Class. Quant. Grav.*, 34(7):074002, 2017.

[104] Matthew Ball, Robert Schofield, and Raymond Frey. Intersite Magnetic Signals from Lightning. Technical Report T2000634, LSC, 2020.

[105] S. Hild et al. Sensitivity Studies for Third-Generation Gravitational Wave Observatories. *Class. Quant. Grav.*, 28:094013, 2011.

[106] Nils Andersson et al. Einstein telescope design study: Vision document. 2009.

[107] B. P. Abbott et al. Search for the isotropic stochastic background using data from Advanced LIGO's second observing run. *Phys. Rev.*, D100(6):061101, 2019.

[108] Eric Thrane and Joseph D. Romano. Sensitivity curves for searches for gravitational-wave backgrounds. *Phys. Rev. D*, 88(12):124032, 2013.

[109] L. Naticchioni et al. Characterization of the Sos Enattos site for the Einstein Telescope. *J. Phys. Conf. Ser.*, 1468(1):012242, 2020.

[110] Renato Romero. Radio waves below 22 khz.

[111] S. Atsuta, T. Ogawa, S. Yamaguchi, K. Hayama, A. Araya, N. Kanda, O. Miyakawa, S. Miyoki, A. Nishizawa, K. Ono, Y. Saito, K. Somiya, T. Uchiyama, M. Uyeshima, and K. Yano. Measurement of schumann resonance at kamioka. *Journal of Physics: Conference Series*, 716:012020, may 2016.

[112] A Cirone, I Fiori, F Paoletti, M M Perez, A R Rodríguez, B L Swinkels, A M Vazquez, G Gemme, and A Chincarini. Investigation of magnetic noise in advanced virgo. *Classical and Quantum Gravity*, 36(22):225004, oct 2019.

[113] S Hild, S Chelkowski, A Freise, J Franc, N Morgado, R Flaminio, and R DeSalvo. A xylophone configuration for a third-generation gravitational wave detector. *Classical and Quantum Gravity*, 27(1):015003, dec 2009.

[114] Ashish Sharma and Jan Harms. Searching for cosmological gravitational-wave backgrounds with third-generation detectors in the presence of an astrophysical foreground. *Phys. Rev. D*, 102:063009, Sep 2020.

[115] Michael W. Coughlin et al. Measurement and subtraction of Schumann resonances at gravitational-wave interferometers. *Phys. Rev. D*, 97(10):102007, 2018.

[116] A. Cirone, A. Chincarini, M. Neri, S. Farinon, G. Gemme, I. Fiori, F. Paoletti, E. Majorana, P. Puppo, P. Rapagnani, and et al. Magnetic coupling to the advanced virgo payloads and its impact on the low frequency sensitivity. *Review of Scientific Instruments*, 89(11):114501, Nov 2018.

[117] D Davis, J S Areeda, et al. *Classical and Quantum Gravity*, 38(13):135014, jun 2021.

[118] P Nguyen. aLIGO LHO Logbook. 57672, 2021.

[119] Philippe Nguyen et al. aLIGO LHO Logbook. 49521, 2019.

[120] Dipongkar Talukder, Eric Thrane, Sukanta Bose, and Tania Regimbau. Measuring neutron-star ellipticity with measurements of

the stochastic gravitational-wave background. *Phys. Rev. D*, 89(12):123008, 2014.

[121] R. Abbott et al. Gravitational-wave Constraints on the Equatorial Ellipticity of Millisecond Pulsars. *Astrophys. J. Lett.*, 902(1):L21, 2020.

[122] Michele Maggiore et al. Science Case for the Einstein Telescope. *JCAP*, 03:050, 2020.

[123] Mohammad Amin Shoaie, Stefano Meroli, Simao Machado, and Daniel Ricci. Evolution of optical fibre cabling components at cern: Performance and technology trends analysis. *Optical Fiber Technology*, 42:69–74, 2018.

[124] Jan Harms and Ho Jung Paik. Newtonian-noise cancellation in full-tensor gravitational-wave detectors. *Phys. Rev. D*, 92:022001, Jul 2015.

[125] F Badaracco and J Harms. Optimization of seismometer arrays for the cancellation of newtonian noise from seismic body waves. *Classical and Quantum Gravity*, 36(14):145006, jun 2019.

[126] Nelson Christensen. Stochastic gravitational wave backgrounds. *Reports on Progress in Physics*, 82(1):016903, nov 2018.

[127] Bruce Allen. The Stochastic gravity wave background: Sources and detection. In *Relativistic gravitation and gravitational radiation. Proceedings, School of Physics, Les Houches, France, September 26-October 6, 1995*, pages 373–417, 1996.

[128] Michele Maggiore. Stochastic backgrounds of gravitational waves. *ICTP Lect. Notes Ser.*, 3:397–414, 2001.

[129] Chiara Caprini and Daniel G. Figueroa. Cosmological Backgrounds of Gravitational Waves. *Class. Quant. Grav.*, 35(16):163001, 2018.

[130] Tania Regimbau. The astrophysical gravitational wave stochastic background. *Res. Astron. Astrophys.*, 11:369–390, 2011.

[131] L. Boco, A. Lapi, S. Goswami, F. Perrotta, C. Baccigalupi, and L. Danese. Merging Rates of Compact Binaries in Galaxies: Perspectives for Gravitational Wave Detections. 7 2019.

[132] Xing-Jiang Zhu, Eric J. Howell, David G. Blair, and Zong-Hong Zhu. On the gravitational wave background from compact binary coalescences in the band of ground-based interferometers. *Mon. Not. Roy. Astron. Soc.*, 431(1):882–899, 2013.

[133] Rory Smith and Eric Thrane. Optimal Search for an Astrophysical Gravitational-Wave Background. *Phys. Rev. X*, 8(2):021019, 2018.

[134] Colm Talbot and Eric Thrane. Measuring the binary black hole mass spectrum with an astrophysically motivated parameterization. *Astrophys. J.*, 856(2):173, 2018.

[135] Jose J. Blanco-Pillado, Ken D. Olum, and Xavier Siemens. New limits on cosmic strings from gravitational wave observation. *Phys. Lett. B*, 778:392–396, 2018.

[136] Christophe Ringeval and Teruaki Suyama. Stochastic gravitational waves from cosmic string loops in scaling. *JCAP*, 12:027, 2017.

[137] Vitor Cardoso and Paolo Pani. Testing the nature of dark compact objects: a status report. *Living Rev. Rel.*, 22(1):4, 2019.

[138] Tania Regimbau and Jose Antonio de Freitas Pacheco. Gravitational wave background from magnetars. *Astron. Astrophys.*, 447:1, 2006.

[139] B.P. Abbott et al. An Upper Limit on the Stochastic Gravitational-Wave Background of Cosmological Origin. *Nature*, 460:990, 2009.

[140] M.C. Guzzetti, N. Bartolo, M. Liguori, and S. Matarrese. Gravitational waves from inflation. *Riv. Nuovo Cim.*, 39(9):399–495, 2016.

[141] Mark Hindmarsh, Stephan J. Huber, Kari Rummukainen, and David J. Weir. Shape of the acoustic gravitational wave power spectrum from a first order phase transition. *Phys. Rev. D*, 96(10):103520, 2017. [Erratum: Phys.Rev.D 101, 089902 (2020)].

[142] Tania Regimbau and Scott A. Hughes. Gravitational-wave confusion background from cosmological compact binaries: Implications for future terrestrial detectors. *Phys. Rev. D*, 79:062002, 2009.

[143] T. Regimbau, M. Evans, N. Christensen, E. Katsavounidis, B. Sathyaprakash, and S. Vitale. Digging deeper: Observing primordial gravitational waves below the binary black hole produced stochastic background. *Phys. Rev. Lett.*, 118(15):151105, 2017.

[144] Sylvia Biscoveanu, Colm Talbot, Eric Thrane, and Rory Smith. Measuring the primordial gravitational-wave background in the presence of astrophysical foregrounds. *arXiv e-prints*, 2020.

[145] Suvodip Mukherjee and Joseph Silk. Time-dependence of the astrophysical stochastic gravitational wave background. *Mon. Not. Roy. Astron. Soc.*, 491(4):4690–4701, 2020.

[146] Surabhi Sachdev, Tania Regimbau, and B. S. Sathyaprakash. Subtracting compact binary foreground sources to reveal primordial gravitational-wave backgrounds. *Phys. Rev. D*, 102(2):024051, 2020.

[147] Haowen Zhong, Rich Ormiston, and Vuk Mandic. Detecting cosmological gravitational waves background after removal of compact binary coalescences in future gravitational wave detectors. 9 2022.

[148] Matthew R. Adams and Neil J. Cornish. Detecting a stochastic grav-

itational wave background in the presence of a galactic foreground and instrument noise. *Phys. Rev. D*, 89:022001, Jan 2014.

[149] Mauro Pieroni and Enrico Barausse. Foreground cleaning and template-free stochastic background extraction for LISA. *JCAP*, 07:021, 2020. [Erratum: JCAP 09, E01 (2020)].

[150] Guillaume Boileau, Nelson Christensen, Renate Meyer, and Neil J. Cornish. Spectral separation of the stochastic gravitational-wave background for LISA: Observing both cosmological and astrophysical backgrounds. *Phys. Rev. D*, 103(10):103529, 2021.

[151] Nikolaos Karnesis, Stanislav Babak, Mauro Pieroni, Neil Cornish, and Tyson Littenberg. Characterization of the stochastic signal originating from compact binary populations as measured by LISA. *Phys. Rev. D*, 104(4):043019, 2021.

[152] Bei Zhou, Luca Reali, Emanuele Berti, Mesut Çalışkan, Cyril Creque-Sarbinowski, Marc Kamionkowski, and B. S. Sathyaprakash. Compact Binary Foreground Subtraction in Next-Generation Ground-Based Observatories. 9 2022.

[153] Bei Zhou, Luca Reali, Emanuele Berti, Mesut Çalışkan, Cyril Creque-Sarbinowski, Marc Kamionkowski, and B. S. Sathyaprakash. Subtracting Compact Binary Foregrounds to Search for Subdominant Gravitational-Wave Backgrounds in Next-Generation Ground-Based Observatories. 9 2022.

[154] V. Mandic, E. Thrane, S. Giampanis, and T. Regimbau. Parameter Estimation in Searches for the Stochastic Gravitational-Wave Background. *Physical Review Letters*, 109(17):171102, October 2012.

[155] Thomas Callister, A. Sylvia Biscoveanu, Nelson Christensen, Maximiliano Isi, Andrew Matas, Olivier Minazzoli, Tania Regimbau, Mairi

Sakellariadou, Jay Tasson, and Eric Thrane. Polarization-Based Tests of Gravity with the Stochastic Gravitational-Wave Background. *Physical Review X*, 7(4):041058, October 2017.

[156] Leo Tsukada, Thomas Callister, Andrew Matas, and Patrick Meyers. First search for a stochastic gravitational-wave background from ultralight bosons. *Physical Review D*, 99(10):103015, May 2019.

[157] T. Regimbau, M. Evans, N. Christensen, E. Katsavounidis, B. Sathyaprakash, and S. Vitale. Digging deeper: Observing primordial gravitational waves below the binary-black-hole-produced stochastic background. *Phys. Rev. Lett.*, 118:151105, Apr 2017.

[158] Curt Cutler and Jan Harms. Big bang observer and the neutron-star-binary subtraction problem. *Phys. Rev. D*, 73:042001, Feb 2006.

[159] Jan Harms, Christoph Mahrdt, Markus Otto, and Malte Prieß. Subtraction-noise projection in gravitational-wave detector networks. *Phys. Rev. D*, 77:123010, Jun 2008.

[160] Thomas Callister, Letizia Sammut, Shi Qiu, Ilya Mand el, and Eric Thrane. Limits of Astrophysics with Gravitational-Wave Backgrounds. *Physical Review X*, 6(3):031018, July 2016.

[161] Alexander Saffer and Kent Yagi. Parameter Estimation for Tests of General Relativity with the Astrophysical Stochastic Gravitational Wave Background. *Phys. Rev. D*, 102(2):024001, 2020.

[162] Rachel Jeannerot, Jonathan Rocher, and Mairi Sakellariadou. How generic is cosmic string formation in SUSY GUTs. *Phys. Rev. D*, 68:103514, 2003.

[163] Thibault Damour and Alexander Vilenkin. Gravitational wave bursts from cusps and kinks on cosmic strings. *Phys. Rev. D*, 64:064008, 2001.

[164] Thibault Damour and Alexander Vilenkin. Gravitational radiation from cosmic (super)strings: Bursts, stochastic background, and observational windows. *Phys. Rev. D*, 71:063510, 2005.

[165] L. Lentati et al. European Pulsar Timing Array Limits On An Isotropic Stochastic Gravitational-Wave Background. *Mon. Not. Roy. Astron. Soc.*, 453(3):2576–2598, 2015.

[166] Xavier Siemens, Vuk Mandic, and Jolien Creighton. Gravitational wave stochastic background from cosmic (super)strings. *Phys. Rev. Lett.*, 98:111101, 2007.

[167] Yann Gouttenoire, Géraldine Servant, and Peera Simakachorn. Beyond the Standard Models with Cosmic Strings. 12 2019.

[168] Larissa Lorenz, Christophe Ringeval, and Mairi Sakellariadou. Cosmic string loop distribution on all length scales and at any redshift. *JCAP*, 10:003, 2010.

[169] Benedict Von Harling, Alex Pomarol, Oriol Pujolàs, and Fabrizio Rompineve. Peccei-Quinn Phase Transition at LIGO. *JHEP*, 04:195, 2020.

[170] Chiara Caprini, Mark Hindmarsh, Stephan Huber, Thomas Konstandin, Jonathan Kozaczuk, Germano Nardini, Jose Miguel No, Antoine Petiteau, Pedro Schwaller, Géraldine Servant, and David J. Weir. Science with the space-based interferometer eLISA. II: gravitational waves from cosmological phase transitions. *Journal of Cosmology and Astroparticle Physics*, 2016(04):001–001, apr 2016.

[171] Stephan J. Huber and Thomas Konstandin. Gravitational Wave Production by Collisions: More Bubbles. *JCAP*, 09:022, 2008.

[172] Mark Hindmarsh, Stephan J. Huber, Kari Rummukainen, and

David J. Weir. Gravitational waves from the sound of a first order phase transition. *Phys. Rev. Lett.*, 112:041301, 2014.

[173] Mark Hindmarsh, Stephan J. Huber, Kari Rummukainen, and David J. Weir. Numerical simulations of acoustically generated gravitational waves at a first order phase transition. *Phys. Rev. D*, 92(12):123009, 2015.

[174] Chiara Caprini, Ruth Durrer, and Geraldine Servant. Gravitational wave generation from bubble collisions in first-order phase transitions: An analytic approach. *Phys. Rev. D*, 77:124015, 2008.

[175] Ryusuke Jinno and Masahiro Takimoto. Gravitational waves from bubble collisions: An analytic derivation. *Phys. Rev. D*, 95(2):024009, 2017.

[176] David J. Weir. Gravitational waves from a first order electroweak phase transition: a brief review. *Phil. Trans. Roy. Soc. Lond. A*, 376(2114):20170126, 2018.

[177] Abhishek Parida, Sanjit Mitra, and Sanjay Jhingan. Component Separation of a Isotropic Gravitational Wave Background. *JCAP*, 04:024, 2016.

[178] Sachiko Kuroyanagi, Takeshi Chiba, and Tomo Takahashi. Probing the Universe through the stochastic gravitational wave background. *Journal of Cosmology and Astroparticle Physics*, 2018(11):038, November 2018.

[179] B. P. Abbott et al. Prospects for Observing and Localizing Gravitational-Wave Transients with Advanced LIGO, Advanced Virgo and KAGRA. *Living Rev. Rel.*, 21(1):3, 2018.

[180] Benjamin P Abbott et al. Exploring the Sensitivity of Next Generation Gravitational Wave Detectors. *Class. Quant. Grav.*, 34(4):044001, 2017.

[181] Duncan Meacher, Eric Thrane, and Tania Regimbau. Statistical properties of astrophysical gravitational-wave backgrounds. *Phys. Rev. D*, 89(8):084063, 2014.

[182] Duncan Meacher, Kipp Cannon, Chad Hanna, Tania Regimbau, and B.S. Sathyaprakash. Second Einstein Telescope Mock Data and Science Challenge: Low Frequency Binary Neutron Star Data Analysis. *Phys. Rev. D*, 93(2):024018, 2016.

[183] Jose J. Blanco-Pillado, Ken D. Olum, and Benjamin Shlaer. The number of cosmic string loops. *Phys. Rev. D*, 89(2):023512, 2014.

[184] B P Abbott et al. Exploring the sensitivity of next generation gravitational wave detectors. *Classical and Quantum Gravity*, 34(4):044001, jan 2017.

[185] David Reitze et al. The US Program in Ground-Based Gravitational Wave Science: Contribution from the LIGO Laboratory. *Bull. Am. Astron. Soc.*, 51:141, 3 2019.

[186] M. Gasperini and M. Giovannini. Dilaton contributions to the cosmic gravitational wave background. *Phys. Rev. D*, 47:1519–1528, Feb 1993.

[187] Chiara Caprini, Daniel G. Figueroa, Raphael Flauger, Germano Nardini, Marco Peloso, Mauro Pieroni, Angelo Ricciardone, and Gianmassimo Tasinato. Reconstructing the spectral shape of a stochastic gravitational wave background with LISA. *JCAP*, 2019(11):017, 2019.

[188] Matthew R. Adams and Neil J. Cornish. Discriminating between a stochastic gravitational wave background and instrument noise. *Physical Review D*, 82(2), Jul 2010.

[189] Pau Amaro-Seoane et al. eLISA/NGO: Astrophysics and cosmology in the gravitational-wave millihertz regime. *GW Notes*, 6:4–110, 2013.

[190] Travis Robson, Neil J. Cornish, and Chang Liu. The construction and use of LISA sensitivity curves. *Class. Quant. Grav.*, 36(10):105011, 2019.

[191] Chiara Caprini et al. Science with the space-based interferometer eLISA. II: Gravitational waves from cosmological phase transitions. *JCAP*, 1604(04):001, 2016.

[192] Ashley J. Ruiter, Krzysztof Belczynski, Matthew Benacquista, Shane L. Larson, and Gabriel Williams. The LISA Gravitational Wave Foreground: A Study of Double White Dwarfs. *Astrophys. J.*, 717:1006–1021, 2010.

[193] Seth E. Timpano, Louis J. Rubbo, and Neil J. Cornish. Characterizing the galactic gravitational wave background with LISA. *Phys. Rev. D*, 73:122001, 2006.

[194] Pau Amaro-Seoane et al. Laser interferometer space antenna, 2017.

[195] Samaya Nissanke, Michele Vallisneri, Gijs Nelemans, and Thomas A. Prince. GRAVITATIONAL-WAVE EMISSION FROM COMPACT GALACTIC BINARIES. *The Astrophysical Journal*, 758(2):131, oct 2012.

[196] Naoki Seto. Annual modulation of the galactic binary confusion noise background and LISA data analysis. *Phys. Rev. D*, 69:123005, 2004.

[197] Quentin Baghi. The LISA Data Challenges. *arXiv e-prints*, page arXiv:2204.12142, April 2022.

[198] Guillaume Boileau, Astrid Lamberts, Nelson Christensen, Neil J Cornish, and Renate Meyer. Spectral separation of the stochastic gravitational-wave background for iLISA/i in the context of a modulated galactic foreground. *Monthly Notices of the Royal Astronomical Society*, 508(1):803–826, sep 2021.

[199] Leor Barack and Curt Cutler. Confusion noise from LISA capture sources. *Physical Review D*, 70(12), dec 2004.

[200] Guillaume Boileau, Alexander C. Jenkins, Mairi Sakellariadou, Renate Meyer, and Nelson Christensen. Ability of LISA to detect a gravitational-wave background of cosmological origin: The cosmic string case. *Physical Review D*, 105(2), jan 2022.

[201] Alejandro Torres-Forné, Elena Cuoco, José A. Font, and Antonio Marquina. Application of dictionary learning to denoise LIGO's blip noise transients. *Phys. Rev. D*, 102(2):023011, 2020.

[202] Neil J. Cornish and Edward K. Porter. The Search for supermassive black hole binaries with LISA. *Class. Quant. Grav.*, 24:5729–5755, 2007.

[203] Antoine Klein et al. Science with the space-based interferometer eLISA: Supermassive black hole binaries. *Phys. Rev.*, D93(2):024003, 2016.

[204] Alberto Sesana. Black Hole Science With the Laser Interferometer Space Antenna. *Front. Astron. Space Sci.*, 8:601646, 2021.

[205] Mostafa Sadeghi, Massoud Babaie-Zadeh, and Christian Jutten. Dictionary learning for sparse representation: A novel approach. *IEEE Signal Processing Letters*, 20(12):1195–1198, 2013.

[206] Scott Shaobing Chen, David L. Donoho, and Michael A. Saunders. Atomic decomposition by basis pursuit. *SIAM Review*, 43(1):129–159, 2001.

[207] Robert Tibshirani. Regression shrinkage and selection via the lasso. *Journal of the Royal Statistical Society. Series B (Methodological)*, 58(1):267–288, 1996.

[208] Julien Mairal, Francis Bach, Jean Ponce, and Guillermo Sapiro. Online dictionary learning for sparse coding. In *Proceedings of the 26th*

*Annual International Conference on Machine Learning*, ICML '09, page 689–696, New York, NY, USA, 2009. Association for Computing Machinery.

[209] Sebastian Khan, Sascha Husa, Mark Hannam, Frank Ohme, Michael Pürrer, Xisco Jiménez Forteza, and Alejandro Bohé. Frequency-domain gravitational waves from nonprecessing black-hole binaries. II. A phenomenological model for the advanced detector era. *Phys. Rev. D*, 93(4):044007, 2016.

[210] Seth E. Timpano, Louis J. Rubbo, and Neil J. Cornish. Characterizing the galactic gravitational wave background with lisa. *Phys. Rev. D*, 73:122001, Jun 2006.

[211] Curt Cutler. Angular resolution of the LISA gravitational wave detector. *Physical Review D*, 57(12):7089–7102, jun 1998.

[212] Astrid Lamberts, Sarah Blunt, Tyson B. Littenberg, Shea Garrison-Kimmel, Thomas Kupfer, and Robyn E. Sanderson. Predicting the LISA white dwarf binary population in the Milky Way with cosmological simulations. *Mon. Not. Roy. Astron. Soc.*, 490(4):5888–5903, 2019.

[213] Curt Cutler and Eanna E. Flanagan. Gravitational waves from merging compact binaries: How accurately can one extract the binary's parameters from the inspiral wave form? *Phys. Rev. D*, 49:2658–2697, 1994.

[214] Neil J. Cornish and Tyson B. Littenberg. BayesWave: Bayesian Inference for Gravitational Wave Bursts and Instrument Glitches. *Class. Quant. Grav.*, 32(13):135012, 2015.

[215] Benjamin P Abbott et al. A guide to LIGO-Virgo detector noise and extraction of transient gravitational-wave signals. 2019.

[216] Neil J. Cornish, Tyson B. Littenberg, Bence Bécsy, Katerina Chatziioannou, James A. Clark, Sudarshan Ghonge, and Margaret Millhouse. BayesWave analysis pipeline in the era of gravitational wave observations. *Phys. Rev. D*, 103(4):044006, 2021.

[217] Fabio Pacucci, Abraham Loeb, and Stefania Salvadori. Gravitational Wave Sources from Pop III Stars are Preferentially Located within the Cores of their Host Galaxies. *Mon. Not. Roy. Astron. Soc.*, 471(1):L72–L76, 2017.

[218] Volker Bromm, Paolo S. Coppi, and Richard B. Larson. Forming the first stars in the universe: the fragmentation of primordial gas. *Astrophys. J. Lett.*, 527:L5–8, 1999.

[219] Volker Bromm and Richard B. Larson. The First stars. *Ann. Rev. Astron. Astrophys.*, 42:79–118, 2004.

[220] Naoki Yoshida, Tom Abel, Lars Hernquist, and Naoshi Sugiyama. Simulations of early structure formation: Primordial gas clouds. *Astrophys. J.*, 592:645–663, 2003.

[221] Rafael S de Souza, Naoki Yoshida, and Kunihito Ioka. Population III.1 and III.2 Gamma-Ray Bursts: Constraints on the Event Rate for Future Radio and X-ray Surveys. *Astron. Astrophys.*, 533:A32, 2011.

[222] R. A. A. Bowler, R. J. McLure, J. S. Dunlop, D. J. McLeod, E. R. Stanway, J. J. Eldridge, and M. J. Jarvis. No evidence for Population III stars or a direct collapse black hole in the z = 6.6 Lyman $\alpha$ emitter 'CR7'. *Mon. Not. Roy. Astron. Soc.*, 469(1):448–458, 2017.

[223] Rogier A. Windhorst et al. On the observability of individual Population III stars and their stellar-mass black hole accretion disks through cluster caustic transits. *Astrophys. J. Suppl.*, 234(2):41, 2018.

[224] Jonathan P. Gardner et al. The James Webb Space Telescope. *Space Sci. Rev.*, 123:485, 2006.

[225] B. J. Carr, J. R. Bond, and W. D. Arnett. Cosmological consequences of Population III stars. *The Astrophysical Journal*, 277:445–469, February 1984.

[226] Naoki Yoshida, Volker Bromm, and Lars Hernquist. The era of massive population III stars: cosmological implications and self-termination. *Astrophys. J.*, 605:579–590, 2004.

[227] M. Trenti and M. Stiavelli. The Formation Rates of Population III Stars and Chemical Enrichment of Halos during the Reionization Era. *Astrophys. J.*, 694:879–892, 2009.

[228] Sunmyon Chon, Takashi Hosokawa, and Naoki Yoshida. Radiation hydrodynamics simulations of the formation of direct-collapse supermassive stellar systems. *Monthly Notices of the Royal Astronomical Society*, 475(3):4104–4121, 01 2018.

[229] Shingo Hirano, Takashi Hosokawa, Naoki Yoshida, Kazuyuki Omukai, and Harold W. Yorke. Primordial star formation under the influence of far ultraviolet radiation: 1540 cosmological haloes and the stellar mass distribution. *Mon. Not. Roy. Astron. Soc.*, 448(1):568–587, 2015.

[230] Alexander Heger, C. L. Fryer, S. E. Woosley, N. Langer, and D. H. Hartmann. How massive single stars end their life. *Astrophys. J.*, 591:288–300, 2003.

[231] Pau Amaro-Seoane et al. Laser Interferometer Space Antenna. *arXiv e-prints*, page arXiv:1702.00786, February 2017.

[232] Krzysztof Belczynski, Vassiliki Kalogera, and Tomasz Bulik. A Comprehensive study of binary compact objects as gravitational wave

sources: Evolutionary channels, rates, and physical properties. *Astrophys. J.*, 572:407–431, 2001.

[233] K. Belczynski, T. Ryu, R. Perna, E. Berti, T. L. Tanaka, and T. Bulik. On the likelihood of detecting gravitational waves from Population III compact object binaries. *Mon. Not. Roy. Astron. Soc.*, 471(4):4702–4721, 2017.

[234] Ken K. Y. Ng, Salvatore Vitale, Will M. Farr, and Carl L. Rodriguez. Probing multiple populations of compact binaries with third-generation gravitational-wave detectors. *Astrophys. J. Lett.*, 913(1):L5, 2021.

[235] Yudai Suwa, Tomoya Takiwaki, Kei Kotake, and Katsuhiko Sato. Gravitational Wave Background from Population III Stars. *Astrophys. J. Lett.*, 665:L43–L46, 2007.

[236] Kohei Inayoshi, Kazumi Kashiyama, Eli Visbal, and Zoltán Haiman. Gravitational wave background from Population III binary black holes consistent with cosmic reionization. *Mon. Not. Roy. Astron. Soc.*, 461(3):2722–2727, 2016.

[237] C. Périgois, C. Belczynski, T. Bulik, and T. Regimbau. StarTrack predictions of the stochastic gravitational-wave background from compact binary mergers. *Phys. Rev. D*, 103(4):043002, 2021.

[238] Jan Harms, Christoph Mahrdt, Markus Otto, and Malte Priess. Subtraction-noise projection in gravitational-wave detector networks. *Phys. Rev. D*, 77:123010, 2008.

[239] Tania Regimbau, Duncan Meacher, and Michael Coughlin. Second Einstein Telescope mock science challenge: Detection of the gravitational-wave stochastic background from compact binary coalescences. *Phys. Rev. D*, 89(8):084046, 2014.

[240] Krzystof Belczynski, Vassiliki Kalogera, Frederic A. Rasio, Ronald E. Taam, Andreas Zezas, Tomasz Bulik, Thomas J. Maccarone, and Natalia Ivanova. Compact object modeling with the startrack population synthesis code. *Astrophys. J. Suppl.*, 174:223, 2008.

[241] T. Regimbau and V. Mandic. Astrophysical Sources of Stochastic Gravitational-Wave Background. *Class. Quant. Grav.*, 25:184018, 2008.

[242] K. Belczynski, A. Romagnolo, A. Olejak, J. Klencki, D. Chattopadhyay, S. Stevenson, M. Coleman Miller, J. P. Lasota, and Paul A. Crowther. The Uncertain Future of Massive Binaries Obscures the Origin of LIGO/Virgo Sources. *Astrophys. J.*, 925(1):69, 2022.

[243] Taeho Ryu, Takamitsu L. Tanaka, and Rosalba Perna. Formation, disruption and energy output of Population III X-ray binaries. *Monthly Notices of the Royal Astronomical Society*, 456(1):223–238, 12 2015.

[244] Carole Périgois, Filippo Santoliquido, Yann Bouffanais, Ugo N. Di Carlo, Nicola Giacobbo, Sara Rastello, Michela Mapelli, and Tania Regimbau. Gravitational background from dynamical binaries and detectability with 2G detectors. *arXiv e-prints*, page arXiv:2112.01119, December 2021.

[245] Davide Gerosa, Salvatore Vitale, and Emanuele Berti. Astrophysical implications of GW190412 as a remnant of a previous black-hole merger. *Phys. Rev. Lett.*, 125(10):101103, 2020.

[246] Kotaro Hijikawa, Ataru Tanikawa, Tomoya Kinugawa, Takashi Yoshida, and Hideyuki Umeda. On the population III binary black hole mergers beyond the pair-instability mass gap. *Mon. Not. Roy. Astron. Soc.*, 505(1):L69–L73, 2021.

[247] Ataru Tanikawa, Gen Chiaki, Tomoya Kinugawa, Yudai Suwa, and Nozomu Tominaga. Can Population III stars be major origins of both

merging binary black holes and extremely metal poor stars? *Publ. Astron. Soc. Jap.*, 74(3):521–532–532, 2022.

[248] Ataru Tanikawa, Hajime Susa, Takashi Yoshida, Alessandro A. Trani, and Tomoya Kinugawa. Merger rate density of Population III binary black holes below, above, and in the pair-instability mass gap. *Astrophys. J.*, 910(1):30, 2021.

[249] Anupam Mazumdar and Graham White. Review of cosmic phase transitions: their significance and experimental signatures. *Rept. Prog. Phys.*, 82(7):076901, 2019.

[250] Mark B. Hindmarsh, Marvin Lüben, Johannes Lumma, and Martin Pauly. Phase transitions in the early universe. 8 2020.

[251] Edward Witten. Cosmic Separation of Phases. *Phys. Rev. D*, 30:272–285, 1984.

[252] C.J. Hogan. Gravitational radiation from cosmological phase transitions. *Mon. Not. Roy. Astron. Soc.*, 218:629–636, 1986.

[253] K. Kajantie, M. Laine, K. Rummukainen, and Mikhail E. Shaposhnikov. Is there a hot electroweak phase transition at $m_H \gtrsim m_W$? *Phys. Rev. Lett.*, 77:2887–2890, 1996.

[254] Jose R. Espinosa, Thomas Konstandin, and Francesco Riva. Strong Electroweak Phase Transitions in the Standard Model with a Singlet. *Nucl. Phys.*, B854:592–630, 2012.

[255] Djuna Croon, Tomás E. Gonzalo, Lukas Graf, Nejc Koˇ snik, and Graham White. GUT Physics in the era of the LHC. *Front. in Phys.*, 7:76, 2019.

[256] Nobuchika Okada, Osamu Seto, and Hikaru Uchida. Gravitational waves from breaking of an extra $U(1)$ in $SO(10)$ grand unification. 6 2020.

[257] Wei-Chih Huang, Francesco Sannino, and Zhi-Wei Wang. Gravitational Waves from Pati-Salam Dynamics. 4 2020.

[258] Stephan J. Huber, Thomas Konstandin, Germano Nardini, and Ingo Rues. Detectable Gravitational Waves from Very Strong Phase Transitions in the General NMSSM. *JCAP*, 03:036, 2016.

[259] Mateo Garcia-Pepin and Mariano Quiros. Strong electroweak phase transition from Supersymmetric Custodial Triplets. *JHEP*, 05:177, 2016.

[260] Ligong Bian, Huai-Ke Guo, and Jing Shu. Gravitational Waves, baryon asymmetry of the universe and electric dipole moment in the CP-violating NMSSM. 2017.

[261] S.V. Demidov, D.S. Gorbunov, and D.V. Kirpichnikov. Gravitational waves from phase transition in split NMSSM. *Phys. Lett. B*, 779:191–194, 2018.

[262] Naoyuki Haba and Toshifumi Yamada. Gravitational waves from phase transition in minimal SUSY $U(1)_{B-L}$ model. *Phys. Rev. D*, 101(7):075027, 2020.

[263] Nathaniel Craig, Noam Levi, Alberto Mariotti, and Diego Redigolo. Ripples in Spacetime from Broken Supersymmetry. 11 2020.

[264] Hao Yu, Zi-Chao Lin, and Yu-Xiao Liu. Gravitational waves and extra dimensions: a short review. *Commun. Theor. Phys.*, 71(8):991–1006, 2019.

[265] Eugenio Megias, Germano Nardini, and Mariano Quiros. Gravitational Imprints from Heavy Kaluza-Klein Resonances. 5 2020.

[266] Hooman Davoudiasl, Pier Paolo Giardino, Ethan T. Neil, and Enrico Rinaldi. Unified Scenario for Composite Right-Handed Neutrinos and Dark Matter. *Phys. Rev. D*, 96(11):115003, 2017.

[267] Sebastian Bruggisser, Benedict Von Harling, Oleksii Matsedonskyi, and Géraldine Servant. Electroweak Phase Transition and Baryogenesis in Composite Higgs Models. *JHEP*, 12:099, 2018.

[268] Ligong Bian, Yongcheng Wu, and Ke-Pan Xie. Electroweak phase transition with composite Higgs models: calculability, gravitational waves and collider searches. *JHEP*, 12:028, 2019.

[269] Stefania De Curtis, Luigi Delle Rose, and Giuliano Panico. Composite Dynamics in the Early Universe. *JHEP*, 12:149, 2019.

[270] Ke-Pan Xie, Yongcheng Wu, and Ligong Bian. Electroweak baryogenesis and gravitational waves in a composite Higgs model with high dimensional fermion representations. 5 2020.

[271] Kaustubh Agashe, Peizhi Du, Majid Ekhterachian, Soubhik Kumar, and Raman Sundrum. Cosmological Phase Transition of Spontaneous Confinement. *JHEP*, 05:086, 2020.

[272] Wei-Chih Huang, Manuel Reichert, Francesco Sannino, and Zhi-Wei Wang. Testing the dark SU(N) Yang-Mills theory confined landscape: From the lattice to gravitational waves. *Phys. Rev. D*, 104(3):035005, 2021.

[273] Peisi Huang, Andrew J. Long, and Lian-Tao Wang. Probing the Electroweak Phase Transition with Higgs Factories and Gravitational Waves. *Phys. Rev.*, D94(7):075008, 2016.

[274] Michael J. Ramsey-Musolf. The electroweak phase transition: a collider target. *JHEP*, 09:179, 2020.

[275] Arthur Hebecker, Joerg Jaeckel, Fabrizio Rompineve, and Lukas T. Witkowski. Gravitational Waves from Axion Monodromy. *JCAP*, 11:003, 2016.

[276] P.S. Bhupal Dev, Francesc Ferrer, Yiyang Zhang, and Yongchao Zhang. Gravitational Waves from First-Order Phase Transition in a Simple Axion-Like Particle Model. *JCAP*, 11:006, 2019.

[277] Luigi Delle Rose, Giuliano Panico, Michele Redi, and Andrea Tesi. Gravitational Waves from Supercool Axions. *JHEP*, 04:025, 2020.

[278] Anish Ghoshal and Alberto Salvio. Gravitational Waves from Fundamental Axion Dynamics. 6 2020.

[279] Ryusuke Jinno and Masahiro Takimoto. Probing a classically conformal B-L model with gravitational waves. *Phys. Rev. D*, 95(1):015020, 2017.

[280] Taiki Hasegawa, Nobuchika Okada, and Osamu Seto. Gravitational waves from the minimal gauged $U(1)_{B-L}$ model. *Phys. Rev. D*, 99(9):095039, 2019.

[281] Ligong Bian, Wei Cheng, Huai-Ke Guo, and Yongchao Zhang. Gravitational waves triggered by $B - L$ charged hidden scalar and leptogenesis. 7 2019.

[282] Wei Chao, Wen-Feng Cui, Huai-Ke Guo, and Jing Shu. Gravitational Wave Imprint of New Symmetry Breaking. 2017.

[283] Vedran Brdar, Lukas Graf, Alexander J. Helmboldt, and Xun-Jie Xu. Gravitational Waves as a Probe of Left-Right Symmetry Breaking. *JCAP*, 12:027, 2019.

[284] Alejandro Lopez and Katherine Freese. First Test of High Frequency Gravity Waves from Inflation using ADVANCED LIGO. *JCAP*, 01:037, 2015.

[285] P. S. Bhupal Dev and A. Mazumdar. Probing the Scale of New Physics by Advanced LIGO/VIRGO. *Phys. Rev.*, D93(10):104001, 2016.

[286] R.D. Peccei and Helen R. Quinn. Constraints Imposed by CP Conservation in the Presence of Instantons. *Phys. Rev. D*, 16:1791–1797, 1977.

[287] James D. Wells. Implications of supersymmetry breaking with a little hierarchy between gauginos and scalars. In *11th International Conference on Supersymmetry and the Unification of Fundamental Interactions*, 6 2003.

[288] Asimina Arvanitaki, Nathaniel Craig, Savas Dimopoulos, and Giovanni Villadoro. Mini-Split. *JHEP*, 02:126, 2013.

[289] Nima Arkani-Hamed, Arpit Gupta, David E. Kaplan, Neal Weiner, and Tom Zorawski. Simply Unnatural Supersymmetry. 12 2012.

[290] *Fundamental Physics at the Intensity Frontier*, 5 2012.

[291] A. D. Linde. *Decay of the False Vacuum at Finite Temperature*. *Nuclear Physics B*, 216(2):421 – 445, 1983.

[292] Rong-Gen Cai, Zhoujian Cao, Zong-Kuan Guo, Shao-Jiang Wang, and Tao Yang. The Gravitational-Wave Physics. 2017.

[293] Tina Kahniashvili, Arthur Kosowsky, Grigol Gogoberidze, and Yurii Maravin. Detectability of Gravitational Waves from Phase Transitions. *Phys. Rev. D*, 78:043003, 2008.

[294] Tina Kahniashvili, Leonardo Campanelli, Grigol Gogoberidze, Yurii Maravin, and Bharat Ratra. Gravitational Radiation from Primordial Helical Inverse Cascade MHD Turbulence. *Phys. Rev.*, D78:123006, 2008. [Erratum: Phys. Rev.D79,109901(2009)].

[295] Tina Kahniashvili, Leonard Kisslinger, and Trevor Stevens. Gravitational Radiation Generated by Magnetic Fields in Cosmological Phase Transitions. *Phys. Rev. D*, 81:023004, 2010.

[296] Chiara Caprini, Ruth Durrer, and Geraldine Servant. The stochastic gravitational wave background from turbulence and magnetic fields generated by a first-order phase transition. *JCAP*, 0912:024, 2009.

[297] Leonard Kisslinger and Tina Kahniashvili. Polarized Gravitational Waves from Cosmological Phase Transitions. *Phys. Rev. D*, 92(4):043006, 2015.

[298] Alberto Roper Pol, Sayan Mandal, Axel Brandenburg, Tina Kahniashvili, and Arthur Kosowsky. Numerical Simulations of Gravitational Waves from Early-Universe Turbulence. 3 2019.

[299] Mark Hindmarsh. Sound shell model for acoustic gravitational wave production at a first-order phase transition in the early Universe. *Phys. Rev. Lett.*, 120(7):071301, 2018.

[300] Mark Hindmarsh and Mulham Hijazi. Gravitational waves from first order cosmological phase transitions in the Sound Shell Model. *JCAP*, 1912(12):062, 2019.

[301] Huai-Ke Guo, Kuver Sinha, Daniel Vagie, and Graham White. Phase Transitions in an Expanding Universe: Stochastic Gravitational Waves in Standard and Non-Standard Histories. *JCAP*, 01:001, 2021.

[302] Daniel Cutting, Mark Hindmarsh, and David J. Weir. Vorticity, kinetic energy, and suppressed gravitational wave production in strong first order phase transitions. *Phys. Rev. Lett.*, 125(2):021302, 2020.

[303] Jose R. Espinosa, Thomas Konstandin, Jose M. No, and Geraldine Servant. Energy Budget of Cosmological First-order Phase Transitions. *JCAP*, 06:028, 2010.

[304] Felix Giese, Thomas Konstandin, and Jorinde van de Vis. Model-independent energy budget of cosmological first-order phase transitions. 4 2020.

[305] John Ellis, Marek Lewicki, and José Miguel No. Gravitational waves from first-order cosmological phase transitions: lifetime of the sound wave source. 3 2020.

[306] John Ellis, Marek Lewicki, José Miguel No, and Ville Vaskonen. Gravitational wave energy budget in strongly supercooled phase transitions. *JCAP*, 06:024, 2019.

[307] Chiara Caprini et al. Detecting gravitational waves from cosmological phase transitions with LISA: an update. *JCAP*, 03:024, 2020.

[308] Arthur Kosowsky and Michael S. Turner. Gravitational radiation from colliding vacuum bubbles: envelope approximation to many bubble collisions. *Phys. Rev.*, D47:4372–4391, 1993.

[309] Arthur Kosowsky, Michael S. Turner, and Richard Watkins. Gravitational waves from first order cosmological phase transitions. *Phys. Rev. Lett.*, 69:2026–2029, 1992.

[310] Chiara Caprini, Ruth Durrer, Thomas Konstandin, and Geraldine Servant. General Properties of the Gravitational Wave Spectrum from Phase Transitions. *Phys. Rev.*, D79:083519, 2009.

[311] Michele Maggiore. *Gravitational Waves. Vol. 2: Astrophysics and Cosmology*. Oxford University Press, 3 2018.

[312] Daniel Cutting, Mark Hindmarsh, and David J. Weir. Gravitational waves from vacuum first-order phase transitions: from the envelope to the lattice. *Phys. Rev. D*, 97(12):123513, 2018.

[313] Daniel Cutting, Elba Granados Escartin, Mark Hindmarsh, and David J. Weir. Gravitational waves from vacuum first order phase transitions II: from thin to thick walls. 5 2020.

[314] Marek Lewicki and Ville Vaskonen. Gravitational wave spectra from strongly supercooled phase transitions. *Eur. Phys. J. C*, 80(11):1003, 2020.

[315] Marek Lewicki and Ville Vaskonen. Gravitational waves from colliding vacuum bubbles in gauge theories. *Eur. Phys. J. C*, 81(5):437, 2021. [Erratum: Eur.Phys.J.C 81, 1077 (2021)].

[316] Yuefeng Di, Jialong Wang, Ruiyu Zhou, Ligong Bian, Rong-Gen Cai, and Jing Liu. Magnetic Field and Gravitational Waves from the First-Order Phase Transition. *Phys. Rev. Lett.*, 126(25):251102, 2021.

[317] B.P. Abbott et al. Upper Limits on the Isotropic Gravitational-Wave Background from Advanced LIGO's and Advanced Virgo's Third Observing Run. *LIGO-DCC:P2000314*, 2020.

[318] Patrick M. Meyers, Katarina Martinovic, Nelson Christensen, and Mairi Sakellariadou. Detecting a stochastic gravitational-wave background in the presence of correlated magnetic noise. *Phys. Rev. D*, 102:102005, Nov 2020.

[319] B. P. Abbott et al. GW150914: Implications for the stochastic gravitational wave background from binary black holes. *Phys. Rev. Lett.*, 116(13):131102, 2016.

[320] John Ellis, Marek Lewicki, and José Miguel No. On the Maximal Strength of a First-Order Electroweak Phase Transition and its Gravitational Wave Signal. *JCAP*, 04:003, 2019.

[321] Sidney Coleman and Erick Weinberg. Radiative corrections as the origin of spontaneous symmetry breaking. *Phys. Rev. D*, 7:1888–1910, Mar 1973.

[322] Benedict von Harling and Geraldine Servant. QCD-induced Electroweak Phase Transition. *JHEP*, 01:159, 2018.

[323] Pietro Baratella, Alex Pomarol, and Fabrizio Rompineve. The Supercooled Universe. *JHEP*, 03:100, 2019.

[324] Tomislav Prokopec, Jonas Rezacek, and Bogumił a Świeżewska. Gravitational waves from conformal symmetry breaking. *JCAP*, 02:009, 2019.

[325] Carlo Marzo, Luca Marzola, and Ville Vaskonen. Phase transition and vacuum stability in the classically conformal B-L model. 2018.

[326] Ryusuke Jinno, Hyeonseok Seong, Masahiro Takimoto, and Choong Min Um. Gravitational waves from first-order phase transitions: Ultra-supercooled transitions and the fate of relativistic shocks. *JCAP*, 10:033, 2019.

[327] John Ellis, Marek Lewicki, and Ville Vaskonen. Updated predictions for gravitational waves produced in a strongly supercooled phase transition. *JCAP*, 11:020, 2020.

[328] Kaustubh Agashe, Peizhi Du, Majid Ekhterachian, Soubhik Kumar, and Raman Sundrum. Phase Transitions from the Fifth Dimension. *JHEP*, 02:051, 2021.

[329] Marek Lewicki, Oriol Pujolàs, and Ville Vaskonen. Escape from supercooling with or without bubbles: gravitational wave signatures. *Eur. Phys. J. C*, 81(9):857, 2021.

[330] B. P. Abbott et al. Gw170817: Implications for the stochastic gravitational-wave background from compact binary coalescences. *Phys. Rev. Lett.*, 120:091101, Feb 2018.

[331] R. Abbott et al. Upper limits on the isotropic gravitational-wave background from advanced ligo and advanced virgo's third observing run. *Phys. Rev. D*, 104:022004, 2021.

[332] Alba Romero, Katarina Martinovic, Thomas A. Callister, Huai-Ke Guo, Mario Martí nez, Mairi Sakellariadou, Feng-Wei Yang, and Yue Zhao. Implications for first-order cosmological phase transitions from the third LIGO-virgo observing run. *Physical Review Letters*, 126(15), apr 2021.

[333] Luca Di Luzio, Maurizio Giannotti, Enrico Nardi, and Luca Visinelli. The landscape of QCD axion models. *Phys. Rept.*, 870:1–117, 2020.

[334] Alberto Roper Pol, Sayan Mandal, Axel Brandenburg, Tina Kahniashvili, and Arthur Kosowsky. Numerical simulations of gravitational waves from early-universe turbulence. *Phys. Rev. D*, 102(8):083512, 2020.

[335] Peter Niksa, Martin Schlederer, and Günter Sigl. Gravitational Waves produced by Compressible MHD Turbulence from Cosmological Phase Transitions. *Class. Quant. Grav.*, 35(14):144001, 2018.

[336] R. Abbott et al. Upper Limits on the Isotropic Gravitational-Wave Background from Advanced LIGO's and Advanced Virgo's Third Observing Run. 1 2021.

[337] R. Abbott et al. `https://dcc.ligo.org/G2001287/public`.

[338] Stephon H. S. Alexander, Michael E. Peskin, and M. M. Sheikh-Jabbari. Leptogenesis from gravity waves in models of inflation. *Physical Review Letters*, 96(8), Feb 2006.

[339] Masaki Satoh, Sugumi Kanno, and Jiro Soda. Circular polarization of primordial gravitational waves in string-inspired inflationary cosmology. *Physical Review D*, 77(2), Jan 2008.

[340] Nicola Bartolo, Luca Caloni, Giorgio Orlando, and Angelo Ricciardone. Tensor non-Gaussianity in chiral scalar-tensor theories of gravity. *JCAP*, 03:073, 2021.

[341] Tomohiro Takahashi and Jiro Soda. Chiral Primordial Gravitational Waves from a Lifshitz Point. *Phys. Rev. Lett.*, 102:231301, 2009.

[342] Neil Barnaby and Marco Peloso. Large non-gaussianity in axion inflation. *Physical Review Letters*, 106(18), May 2011.

[343] Marc Kamionkowski, Arthur Kosowsky, and Michael S. Turner. Gravitational radiation from first-order phase transitions. *Physical Review D*, 49(6):2837–2851, Mar 1994.

[344] Edward Witten. Cosmic separation of phases. *Phys. Rev. D*, 30:272–285, Jul 1984.

[345] C. J. Hogan. Gravitational radiation from cosmological phase transitions. *MNRAS*, 218:629–636, Feb 1986.

[346] Axel Brandenburg, Kari Enqvist, and Poul Olesen. Large-scale magnetic fields from hydromagnetic turbulence in the very early universe. *Physical Review D*, 54(2):1291–1300, Jul 1996.

[347] Mattias Christensson, Mark Hindmarsh, and Axel Brandenburg. Inverse cascade in decaying three-dimensional magnetohydrodynamic turbulence. *Physical Review E*, 64(5), Oct 2001.

[348] Tina Kahniashvili, Axel Brandenburg, Alexander G. Tevzadze, and Bharat Ratra. Numerical simulations of the decay of primordial magnetic turbulence. *Physical Review D*, 81(12), Jun 2010.

[349] Axel Brandenburg, Tina Kahniashvili, Sayan Mandal, Alberto Roper Pol, Alexander G. Tevzadze, and Tanmay Vachaspati. Dynamo effect in decaying helical turbulence. *Physical Review Fluids*, 4(2), Feb 2019.

[350] Axel Brandenburg, Yutong He, Tina Kahniashvili, Matthias Rheinhardt, and Jennifer Schober. Relic gravitational waves from the chiral magnetic effect. 1 2021.

[351] S.G. Crowder, R. Namba, V. Mandic, S. Mukohyama, and M. Peloso. Measurement of parity violation in the early universe using gravitational-wave detectors. *Physics Letters B*, 726(1-3):66–71, Oct 2013.

[352] An upper limit on the stochastic gravitational-wave background of cosmological origin. *Nature*, 460(7258):990–994, Aug 2009.

[353] Naoki Seto. Quest for circular polarization of gravitational wave background and orbits of laser interferometers in space. *Phys. Rev. D*, 75:061302, 2007.

[354] Angelo Ricciardone. Primordial gravitational waves with lisa. *Journal of Physics: Conference Series*, 840:012030, May 2017.

[355] Giorgio Orlando, Mauro Pieroni, and Angelo Ricciardone. Measuring parity violation in the stochastic gravitational wave background with the lisa-taiji network. *Journal of Cosmology and Astroparticle Physics*, 2021(03):069, Mar 2021.

[356] Valerie Domcke, Juan Garcia-Bellido, Marco Peloso, Mauro Pieroni, Angelo Ricciardone, Lorenzo Sorbo, and Gianmassimo Tasinato. Measuring the net circular polarization of the stochastic gravitational wave background with interferometers. *JCAP*, 05:028, 2020.

[357] Peng Xu, Zhi Wang, and Li-E Qiang. Towards constraining parity-violations in gravity with satellite gradiometry. *Phys. Lett. B*, 789:378–386, 2019.

[358] Marcel Lesieur. *Turbulence in Fluids*. Springer Netherlands, 1997.

[359] S. S. Moiseev and O. Chkhetiani. Helical scaling in turbulence. *Journal of Experimental and Theoretical Physics*, 83:192–198, 01 1996.

[360] Naoki Seto and Atsushi Taruya. Measuring a parity-violation signature in the early universe via ground-based laser interferometers. *Phys. Rev. Lett.*, 99:121101, Sep 2007.

[361] Bruce Allen and Joseph D. Romano. Detecting a stochastic background of gravitational radiation: Signal processing strategies and sensitivities. *Phys. Rev. D*, 59:102001, Mar 1999.

[362] Andrew Matas and Joseph D. Romano. Frequentist versus Bayesian analyses: Cross-correlation as an (approximate) sufficient statistic for LIGO-Virgo stochastic background searches. 12 2020.

[363] Andrew J. Long, Eray Sabancilar, and Tanmay Vachaspati. Leptogenesis and primordial magnetic fields. *Journal of Cosmology and Astroparticle Physics*, 2014(02):036–036, Feb 2014.

[364] G.C. Dorsch, S.J. Huber, T. Konstandin, and J.M. No. A second higgs doublet in the early universe: baryogenesis and gravitational waves. *Journal of Cosmology and Astroparticle Physics*, 2017(05):052–052, May 2017.

[365] Tina Kahniashvili. Gravitational radiation from primordial helical turbulence. 2005.

[366] David J. Weir. Gravitational waves from a first-order electroweak phase transition: a brief review. *Philosophical Transactions of the Royal Society A: Mathematical, Physical and Engineering Sciences*, 376(2114):20170126, Jan 2018.

[367] Arthur Kosowsky, Andrew Mack, and Tinatin Kahniashvili. Gravitational radiation from cosmological turbulence. *Physical Review D*, 66(2), Jul 2002.

[368] Tina Kahniashvili, Grigol Gogoberidze, and Bharat Ratra. Polarized

cosmological gravitational waves from primordial helical turbulence. *Physical Review Letters*, 95(15), Oct 2005.

[369] Tina Kahniashvili, Axel Brandenburg, Grigol Gogoberidze, Sayan Mandal, and Alberto Roper Pol. Circular polarization of gravitational waves from early-universe helical turbulence. 2020.

[370] Leonard Kisslinger and Tina Kahniashvili. Polarized gravitational waves from cosmological phase transitions. *Phys. Rev. D*, 92:043006, Aug 2015.

[371] Serge Reynaud and Marc-Thierry Jaekel. Tests of general relativity in the solar system. *Proc. Int. Sch. Phys. Fermi*, 168:203–217, 2009.

[372] Thomas E. Collett, Lindsay J. Oldham, Russell J. Smith, Matthew W. Auger, Kyle B. Westfall, David Bacon, Robert C. Nichol, Karen L. Masters, Kazuya Koyama, and Remco van den Bosch. A precise extragalactic test of General Relativity. *Science*, 360:1342, 2018.

[373] B. P. Abbott et al. Tests of general relativity with GW150914. *Phys. Rev. Lett.*, 116(22):221101, 2016. [Erratum: Phys. Rev. Lett.121,no.12,129902(2018)].

[374] M. Kramer et al. Tests of general relativity from timing the double pulsar. *Science*, 314:97–102, 2006.

[375] Sean M. Carroll, Antonio De Felice, Vikram Duvvuri, Damien A. Easson, Mark Trodden, and Michael S. Turner. Cosmology of generalized modified gravity models. *Phys. Rev. D*, 71:063513, Mar 2005.

[376] B. P. Abbott et al. GW170817: Observation of Gravitational Waves from a Binary Neutron Star Inspiral. *Phys. Rev. Lett.*, 119(16):161101, 2017.

[377] B. P. Abbott et al. Gravitational Waves and Gamma-rays from a Binary Neutron Star Merger: GW170817 and GRB 170817A. *Astrophys. J.*, 848(2):L13, 2017.

[378] T. Baker, E. Bellini, P. G. Ferreira, M. Lagos, J. Noller, and I. Sawicki. Strong constraints on cosmological gravity from GW170817 and GRB 170817A. *Phys. Rev. Lett.*, 119(25):251301, 2017.

[379] Jose María Ezquiaga and Miguel Zumalacárregui. Dark Energy After GW170817: Dead Ends and the Road Ahead. *Phys. Rev. Lett.*, 119(25):251304, 2017.

[380] Jeremy Sakstein and Bhuvnesh Jain. Implications of the neutron star merger gw170817 for cosmological scalar-tensor theories. *Phys. Rev. Lett.*, 119:251303, Dec 2017.

[381] Henri Ruegg and Marti Ruiz-Altaba. The Stueckelberg field. *Int. J. Mod. Phys.*, A19:3265–3348, 2004.

[382] M. Fierz and W. Pauli. On relativistic wave equations for particles of arbitrary spin in an electromagnetic field. *Proc. Roy. Soc. Lond. A*, 173:211–232, 1939.

[383] Kurt Hinterbichler. Theoretical Aspects of Massive Gravity. *Rev. Mod. Phys.*, 84:671–710, 2012.

[384] Eugeny Babichev and Cédric Deffayet. An introduction to the Vainshtein mechanism. *Class. Quant. Grav.*, 30:184001, 2013.

[385] Claudia de Rham, Gregory Gabadadze, and Andrew J. Tolley. Resummation of Massive Gravity. *Phys. Rev. Lett.*, 106:231101, 2011.

[386] G. R. Dvali, Gregory Gabadadze, and Massimo Porrati. 4-D gravity on a brane in 5-D Minkowski space. *Phys. Lett.*, B485:208–214, 2000.

[387] Malcolm Fairbairn and Ariel Goobar. Supernova limits on brane world cosmology. *Phys. Lett.*, B642:432–435, 2006.

[388] B. P. et al Abbott. Tests of general relativity with gw170817. *Phys. Rev. Lett.*, 123:011102, Jul 2019.

[389] Mikhail S. Volkov. Self-accelerating cosmologies and hairy black holes in ghost-free bigravity and massive gravity. *Class. Quant. Grav.*, 30:184009, 2013.

[390] Claudia de Rham. Massive Gravity. *Living Rev. Rel.*, 17:7, 2014.

[391] Furqan Dar, Claudia De Rham, J. Tate Deskins, John T. Giblin, and Andrew J. Tolley. Scalar Gravitational Radiation from Binaries: Vainshtein Mechanism in Time-dependent Systems. *Class. Quant. Grav.*, 36(2):025008, 2019.

[392] Guido D'Amico, Gregory Gabadadze, Lam Hui, and David Pirtskhalava. Quasidilaton: Theory and cosmology. *Phys. Rev.*, D87:064037, 2013.

[393] Ruth Durrer. Cosmological perturbation theory. *Lect. Notes Phys.*, 653:31–70, 2004.

[394] Clifford Cheung and Grant N. Remmen. Positive Signs in Massive Gravity. *JHEP*, 04:002, 2016.

[395] Michael Kenna-Allison, A. Emir Gümrükçüoğlu, and Kazuya Koyama. Viability of bigravity cosmology. *Phys. Rev. D*, 99:104032, May 2019.

[396] Yi-Fu Cai and Emmanuel N. Saridakis. Cosmology of F(R) nonlinear massive gravity. *Phys. Rev.*, D90(6):063528, 2014.

[397] T. Damour and Alexander M. Polyakov. The String dilaton and a least coupling principle. *Nucl. Phys.*, B423:532–558, 1994.

[398] Nicholas A. Ondo and Andrew J. Tolley. Complete Decoupling Limit of Ghost-free Massive Gravity. *JHEP*, 11:059, 2013.

[399] Radouane Gannouji, Md. Wali Hossain, M. Sami, and Emmanuel N. Saridakis. Quasidilaton nonlinear massive gravity: Investigations of background cosmological dynamics. *Phys. Rev.*, D87:123536, 2013.

[400] Rajeev Kumar Jain, Chris Kouvaris, and Niklas Grønlund Nielsen. White Dwarf Critical Tests for Modified Gravity. *Phys. Rev. Lett.*, 116(15):151103, 2016.

[401] Kazuya Koyama and Jeremy Sakstein. Astrophysical Probes of the Vainshtein Mechanism: Stars and Galaxies. *Phys. Rev.*, D91:124066, 2015.

[402] Vincenzo Salzano, David F. Mota, Salvatore Capozziello, and Megan Donahue. Breaking the Vainshtein screening in clusters of galaxies. *Phys. Rev.*, D95(4):044038, 2017.

[403] A. Emir Gumrukcuoglu, Chunshan Lin, and Shinji Mukohyama. Cosmological perturbations of self-accelerating universe in nonlinear massive gravity. *JCAP*, 1203:006, 2012.

[404] B. P. Abbott et al. Tests of General Relativity with the Binary Black Hole Signals from the LIGO-Virgo Catalog GWTC-1. 2019.

[405] Claudia de Rham, J. Tate Deskins, Andrew J. Tolley, and Shuang-Yong Zhou. Graviton Mass Bounds. *Rev. Mod. Phys.*, 89(2):025004, 2017.

[406] Paolo Creminelli, Matthew Lewandowski, Giovanni Tambalo, and Filippo Vernizzi. Gravitational Wave Decay into Dark Energy. *JCAP*, 1812(12):025, 2018.

[407] Claudia de Rham, Andrew J. Tolley, and Daniel H. Wesley. Vainshtein Mechanism in Binary Pulsars. *Phys. Rev.*, D87(4):044025, 2013.

[408] Claudia de Rham and Scott Melville. Gravitational Rainbows: LIGO and Dark Energy at its Cutoff. *Phys. Rev. Lett.*, 121(22):221101, 2018.

[409] Particle Data Group. Review of particle physics. *Phys. Rev. D*, 98:030001, Aug 2018.

[410] Antonio Pich. Precision Tau Physics. *Prog. Part. Nucl. Phys.*, 75:41–85, 2014.

[411] Federico Lelli, Stacy S. McGaugh, and James M. Schombert. SPARC: Mass Models for 175 Disk Galaxies with Spitzer Photometry and Accurate Rotation Curves. *Astron. J.*, 152:157, 2016.

[412] Shun Arai and Atsushi Nishizawa. Generalized framework for testing gravity with gravitational-wave propagation. ii. constraints on horndeski theory. *Phys. Rev. D*, 97:104038, May 2018.

[413] Julio F. Navarro, Carlos S. Frenk, and Simon D. M. White. The Structure of cold dark matter halos. *Astrophys. J.*, 462:563–575, 1996.

[414] Álefe O. F. de Almeida, Luca Amendola, and Viviana Niro. Galaxy rotation curves in modified gravity models. *JCAP*, 1808(08):012, 2018.

[415] Harley Katz, Federico Lelli, Stacy S. McGaugh, Arianna Di Cintio, Chris B. Brook, and James M. Schombert. Testing feedback-modified dark matter haloes with galaxy rotation curves: estimation of halo parameters and consistency with ΛCDM scaling relations. *Monthly Notices of the Royal Astronomical Society*, 466(2):1648–1668, 12 2016.

[416] Clifford M. Will. Solar system versus gravitational-wave bounds on the graviton mass. *Classical and Quantum Gravity*, 35(17):17LT01, Sep 2018.

[417] B. P. Abbott et al. GW170817: Observation of Gravitational Waves from a Binary Neutron Star Inspiral. *Phys. Rev. Lett.*, 119(16):161101, 2017.

[418] B. P. Abbott et al. Gravitational Waves and Gamma-rays from a Binary Neutron Star Merger: GW170817 and GRB 170817A. *Astrophys. J. Lett.*, 848(2):L13, 2017.

[419] B. P. Abbott et al. Multi-messenger Observations of a Binary Neutron Star Merger. *Astrophys. J. Lett.*, 848(2):L12, 2017.

[420] LIGO Scientific Collaboration and Virgo Collaboration. GW170817: Observation of Gravitational Waves from a Binary Neutron Star Inspiral. *Physical Review Letters*, 119(16):161101, October 2017.

[421] Johannes Noller. Cosmological constraints on dark energy in light of gravitational wave bounds. *Phys. Rev. D*, 101(6):063524, 2020.

[422] Gregory Walter Horndeski. Second-order scalar-tensor field equations in a four-dimensional space. *Int. J. Theor. Phys.*, 10:363–384, 1974.

[423] C. Deffayet, Xian Gao, D. A. Steer, and G. Zahariade. From k-essence to generalised Galileons. *Phys. Rev. D*, 84:064039, 2011.

[424] Miguel Zumalacárregui and Juan García-Bellido. Transforming gravity: from derivative couplings to matter to second-order scalar-tensor theories beyond the Horndeski Lagrangian. *Phys. Rev. D*, 89:064046, 2014.

[425] Jérôme Gleyzes, David Langlois, Federico Piazza, and Filippo Vernizzi. Healthy theories beyond Horndeski. *Phys. Rev. Lett.*, 114(21):211101, 2015.

[426] David Langlois and Karim Noui. Degenerate higher derivative theories beyond Horndeski: evading the Ostrogradski instability. *JCAP*, 02:034, 2016.

[427] Marco Crisostomi, Kazuya Koyama, and Gianmassimo Tasinato. Extended Scalar-Tensor Theories of Gravity. *JCAP*, 04:044, 2016.

[428] Jibril Ben Achour, Marco Crisostomi, Kazuya Koyama, David Langlois, Karim Noui, and Gianmassimo Tasinato. Degenerate higher order scalar-tensor theories beyond Horndeski up to cubic order. *JHEP*, 12:100, 2016.

[429] Tessa Baker, Enrico Barausse, Anson Chen, Claudia de Rham, Mauro Pieroni, and Gianmassimo Tasinato. Testing gravitational wave propagation with multiband detections. 9 2022.

[430] Timothy Clifton, Pedro G. Ferreira, Antonio Padilla, and Constantinos Skordis. Modified Gravity and Cosmology. *Phys. Rept.*, 513:1–189, 2012.

[431] `https://stochastic-alog.ligo.org/aLOG//index.php?callRep=339711`.

[432] `https://pygwb.docs.ligo.org/pygwb/api/pygwb.pe.html`.

[433] T. Regimbau, K. Siellez, D. Meacher, B. Gendre, and M. Boër. Revisiting coincidence rate between Gravitational Wave detection and short Gamma-Ray Burst for the Advanced and third generation. *Astrophys. J.*, 799(1):69, 2015.

[434] Marc Kamionkowski, Arthur Kosowsky, and Michael S. Turner. Gravitational radiation from first order phase transitions. *Phys. Rev. D*, 49:2837–2851, 1994.

[435] Arthur Kosowsky, Michael S. Turner, and Richard Watkins. Gravitational radiation from colliding vacuum bubbles. *Phys. Rev.*, D45:4514–4535, 1992.